Extremely low frequency electromagnetic properties in marine environments with non-parallel interfaces

Bhakta, Nitin

EXTREMELY LOW FREQUENCY ELECTROMAGNETIC PROPAGATION IN MARINE ENVIRONMENTS WITH NON-PARALLEL INTERFACES

by

NITIN BHAKTA

Thesis submitted to the University
of London for the degree of
Doctor of Philosophy

Department of Physics
King's College London

November 2001

Abstract

This thesis is concerned with the development of propagation models for low frequency electromagnetic (EM) radiation in ocean environments where the air-sea and sea-seabed interfaces are not parallel (because the seabed is sloping). The sources considered are Hertzian electric dipoles radiating in seawater in the extremely low frequency (ELF) portion of the electromagnetic spectrum.

This study includes a detailed review of an existing 3-layer (i.e. air-sea-seabed) model based on the Hertz vector formulation. This analytical model applies to parallel boundaries. New work includes the experimental validation of this formulation and an extension to include 5-layers (i.e. ionosphere-air-sea-seabed1-seabed2).

The focus of the work is the development of two propagation models for a sloping seabed environment. The special case when both the source and observer are in the sea layer is addressed within a 3-dimensional problem space. Both analytical and numerical formulations are developed. The analytical formulation addresses environments where the seabed has a constant gradient. It is computationally efficient and thus suited to 'real-time' applications such as source modelling. This is most accurate at higher frequencies and for deeper waters, when the interaction between the air-sea and sea-seabed interfaces is negligible. The numerical formulation is based on the finite-difference time-domain (FDTD) method and can be applied to most arbitrary seabed profiles. This model exploits co-ordinate transformations to simplify the process of applying the boundary conditions.

Results are presented showing the field characteristics in various sloping seabed environments compared to their horizontally stratified counterparts. The results show that the impact of the sloping seabed is greatest for higher frequency sources situated near the seabed. The results also show that the greatest changes in the total field level occur at large distances from the source, with the EM field increasing when the sea depth decreases.

Acknowledgements

I wish to thank my supervisor Dr David Llanwyn Jones for all his help over the years. I am especially grateful for his support and feedback while writing my thesis. I wish you all the best in your retirement.

I am indebted to the research team at the Swedish Defence Research Agency (FOI), for all their help and support. Personal thanks goes to Leif Abrahamsson for developing the air-sea interface formulation and for all his help with the development of the FDTD model.

I would also like to thank the Ministry of Defence for funding this research and all the researchers from DERA (now QinetiQ and DSTL) who have helped me over the years.

Finally, I would like to thank all my family and friends for their support over the years.

Contents

List of figures

List of tables

Chapter 1

Introduction

Extremely low frequency electromagnetic (ELFE) radiation (i.e. radio waves) is of significant interest in several marine applications, including submarine communication systems and naval stealth. The ELFE band is defined as 1Hz-3kHz in this study (officially, it is 3Hz-3kHz). These applications are made possible owing to the low attenuation rates experienced by the ELFE radiation in conducting media such as seawater. This allows the radiation to propagate over significant distances.

The propagation characteristics of ELFE radiation in littoral environments with a sloping seabed will be investigated in this thesis. Two propagation models have been developed. A numerical model based on the finite-difference time-domain (FDTD) method and an approximate analytical formulation. These models are considered more representative of the real environment compared to traditional propagation models that only take account of flat seabed profiles in a plane-stratified model. The models developed in this thesis will be the first 3-dimensional sloping seabed models to investigate applications when both the source and observer are situated in the sea.

1.1 Nature of the problem

ELFE propagation models can be formulated to predict the electromagnetic field levels in a marine environment. These can be exploited in the 'forward' sense to make field predictions for a specified source and a set of environmental parameters. Alternatively, they can be used in the 'inverse' sense to predict the source and/or environmental parameters for a given field distribution. Owing to the complexity involved in obtaining inverse formulations, forward models are always used in conjunction with optimisation algorithms to produce inverse models. Forward

propagation models are essential in applications that require field predictions or in source and environmental characterisation applications (see Section 1.4 and 1.9).

Propagation models are usually formulated for a specific idealised source and environmental geometry. The idealised nature of the source (e.g. a point dipole) does not pose any significant problems, since actual complex sources can be represented by a number of appropriately distributed simpler dipole sources. In fact, this is one of the important applications of propagation models, usually referred to as 'source modelling'. The constraint on the environmental geometry does however pose some problems. An analytical solution only appears possible when the air, sea and seabed mediums are horizontally stratified (i.e. the interfaces are parallel). Virtually all propagation models are formulated for this simple environmental geometry.

The geometry of the marine environment is much more complicated and does not usually conform to the horizontally stratified case. Geological features on the ocean floor (e.g. trenches and ridges) and the transition from the deep ocean floor to the continental bank usually gives rise to a geometry where the sea-seabed interface is no longer parallel to the air-sea interface. This is commonly referred to as the 'sloping seabed' problem and constitutes a 'range-dependent' propagation problem. Range-dependent problems are complicated by changing environmental or media parameters with distance from the source. The transition from sea to land at the coastline also complicates matters greatly due to the intersection of the interfaces. This is usually referred to as the 'coastline' or 'wedge' problem.

The need for a sloping seabed propagation model is greatest in the littoral environments where shallow waters dictate the use of 3-layer air-sea-seabed models. Coastal propagation models are also essential in the littoral environment when near a coastline. In contrast, deep waters often permit simple 2-layer air-sea models to be exploited due to the remote nature of the seabed, which means it has a negligible effect on the propagation of ELFE radiation near the sea surface.

Despite the importance of the littoral environment and the prevalence of non-parallel interfaces, very few propagation models address underwater applications where the source and observer are situated in the sea. This configuration is particularly

important for naval applications involving submarines. Existing models that address this configuration are restricted to a 2-dimensional geometry, thus cannot model complex source distributions composed of arbitrary orientated dipoles. The models developed in this study will overcome these problems, thus ensuring widespread applicability, including inverse problems.

1.2 Overview of thesis

This thesis will focus on the development of ELFE propagation models for a sloping seabed environment, for the case when both the source and observer are situated in the sea layer. A fast approximate analytical model will be developed for inverse applications where a 'wedge-like' geometry is applicable, and a numerical FDTD model has been implemented for application in environments with an arbitrary seabed profile. The validity of the models will also be demonstrated using various tests cases involving alternative models and cross-validation between the two sloping seabed models.

Chapter 2 will present a detailed description of what will be referred to as the King's College London (KCL) ELFE propagation model. This formulation can be used to predict the electromagnetic fields from a horizontal electric dipole (HED), embedded in the sea layer, in a 3-layer horizontally plane-stratified medium (i.e. air-sea-seabed). An extension of the 3-layer KCL model to a 5-layer model for an ionosphere-air-sea-sediment-bedrock is also presented.

Chapter 3 details the experimental validation of the KCL formulation implemented in the *LAYER* FORTRAN77 program. The experimental validation was performed using a mobile calibrated source (i.e. fixed to a boat) and a seabed mounted electric sensor system. The trial was conducted in the shallow waters of Weymouth Bay (approximately 20m water depth).

Chapter 4 investigates the problems associated with producing an exact analytical solution for the sloping seabed problem. The problems are illustrated by examining 2-layer models (i.e. sea-seabed) for vertical electric dipole (VED) sources. The investigation highlights the problem associated with the application of the boundary

conditions and indicates the way forward is to use different co-ordinate systems for each of the interfaces. Then attempt to couple the two solutions together in an appropriate manner.

Chapter 5 details the development of an approximate analytical 3-layer model for a seabed with a constant gradient (i.e. wedge geometry). The model is a combination of two simple 2-layer models describing propagation in the air-sea and sea-seabed environments respectively. 'Geometrical-optical' approximations have been employed and new 'geometrical-imaging' techniques have been developed to take account of the interaction of the two interfaces, thus coupling the solutions from the two models.

Chapter 6 details the development of a 3-dimensional ELFE propagation model for a sloping seabed environment with up to ten layers for both magnetic and electric dipole sources. Each of the layers can be stratified with an arbitrary profile provided the interfaces do not intersect each other. The model is implemented numerically using the finite-difference time-domain method. The application of the boundary conditions is simplified by transforming the sloping seabed environment into a horizontally stratified environment within a new co-ordinate system using a one-to-one mapping. The model also incorporates a special analytical air-sea interface formulation, specially developed for this study by L. Abrahamsson, thus negating the need to model the air volume.

Chapter 7 details the validation of the two sloping seabed models developed in this study. The geometrical-imaging technique is validated using analytical formulations. The geometrical-optical modelling approach is validated using a horizontally plane-stratified propagation model. Similarly, the boundary conditions implemented within the FDTD model for the air-sea and sea-seabed interfaces are validated using horizontally plane-stratified models. The co-ordinate transformation employed to map the FDTD model's geometry is cross-validated using results from the analytical sloping seabed model. The results successfully demonstrate the validity of the models.

Chapter 8 contains a number of predictions obtained using the approximate analytical sloping seabed model. The results investigate the impact of the sloping seabed with variations in the slope angle of the seabed, the frequency of the source and the depth of the source. The results show that large field enhancements can be observed near coastlines as the sea depth decreases. The impact of the sloping seabed is also greater at higher frequencies and for sources near the seabed.

1.3 Historical background

The first application of low frequency electromagnetic radiation was in radio communication systems. Tesla first proposed the concept of a global communication system using a single radio transmitter during the late 19th Century. His work generated significant interest and it was not long before the commercial benefits of a wireless communication system over conventional submarine (i.e. under-water) cables were realised.

The first viable 'wireless' telegraph link was Marconi's in 1906 between Clifden, Ireland and Glace Bay, Newfoundland; operating at 45kHz over a distance of 3,750km (Pickworth, 2000). Messages were relayed from Glace Bay to New York and Montreal, and from Clifden to England via landlines and submarine cables.

In 1906, Fessenden also established his Brant Rock, USA link with Machrihanish, Scotland on 60kHz, distance 5,000km (Pickworth, 2000). Fessenden made the first transatlantic broadcast on Christmas Eve in 1906.

The long range of these so-called superstations can be attributed to a combination of high power transmitters and the relatively low absorption of very long waves by the ionosphere's D region. This allowed sufficient energy to reach the higher E region from where it was reflected back to Earth.

Commercial superstations provided an attractive alternative to submarine cables from 1906 until around 1925 when they were made redundant by short wave systems. However, there was an obvious strategic benefit to be gained from wireless systems, since submarine cables were easily cut during times of war.

In 1925 Britain commissioned station GBR at Rugby; this station radiated waves at 16kHz supposedly to transmit signals simultaneously to all our overseas territories. As overseas territories did not have superstations, return messages were transmitted via short wave stations. The role of GBR, like all second-generation systems (i.e. built after 1925) was primarily strategic (i.e. used for communicating with naval submarines).

The first third generation system was built in the 1980s by the US Navy. The Seafarer system was developed by the navy during the 'Cold War' to send signals to nuclear powered submarines, at their operational depth (Jones, 1985). The Seafarer antenna is composed of two horizontal wires (each 150km long) configured in a cross-shape. The ends of the wires are in electrical contact with the ground, thus forming an earth loop antenna that behaves as a horizontal magnetic dipole. The Seafarer system consists of two transmitter-sites, one in Wisconsin and one in Michigan. The transmitters are driven simultaneously at a frequency of 76Hz, with an effective radiating power of 10W (Jones, 1985).

Communication systems prior to Seafarer relied on the submarine coming near the sea surface to receive the signals. The signals could now be received by submerged submarines towing an antenna consisting of a long transmission line with an electrode at one end; the submarine hull would act as the second electrode.

Fessenden's success in demonstrating the transatlantic transmission of radio waves posed a problem to the physicists of the day. In 1878, Stuart had tried to demonstrate the existence of a conducting layer in the upper atmosphere from periodic variations in the geomagnetic field. However, more interest was generated in 1902, when Kennelly and later Heaviside proposed the existence of a concentric conducting layer in the atmosphere that reflected radio waves. Sommerfeld carried out extensive calculations in 1909 to show that diffraction theory was responsible for the observed reflections, but the measured field amplitudes were significantly greater than diffraction theory could account for.

In 1925, Appleton and Barnett provided the first experimental proof for the existence of a reflecting 'ionospheric' layer. Appleton and Barnett varied the frequency of a transmitter so that the interactions between the direct and reflected waves resulted in interference effects being observed at a remote site. Appleton termed the reflection layer the E layer.

The first important attempt at a theoretical model of the ionosphere was made by S. Chapman in 1931. In the late 1950s, Budden and Wait showed that the Earth and the ionosphere could be regarded as a waveguide. This resulted in the 'waveguide-mode theory'. Early ionospheric research made use of atmospherics (or spherics), in particular lightning strikes, which are the most dominant natural source of radio waves in the ELF band.

Even before the beginning of the twentieth century, interference effects were noticed on long distance telegraph communications and these were associated with lightning flashes. Early research was carried out using a simple earpiece and the interfering atmospheric was classified according to the audio sound it produced. Eccles and Airey made the first simultaneous measurements of atmospherics from two separate stations in 1911 and Eccles was the first to realise that a reflecting layer in the upper atmosphere was needed to explain the results.

Research into ELF atmospherics entered a new phase when Schumann suggested that global electromagnetic resonances might be observable when the radio frequency is equal to the natural frequency of the Earth-ionosphere's spherical cavity, (i.e. the region enclosed by the concentric spheres formed by the Earth's surface and the lower region of the ionosphere). For a cavity formed between two perfectly conducting boundaries the resonance frequencies (f_m) are given by $f_m = 7.49\sqrt{m(m+1)}$, where m=0,1,2...etc. Balsner and Wagner provided the first experimental evidence to confirm the existence of the 'Schumann' resonances in 1960.

The first ELFE propagation model was developed by Sommerfeld in the early 1900s for a horizontal electric dipole (HED) located above a conducting medium. The

resulting solution was very complicated and involved highly oscillatory integrals (now called Sommerfeld Integrals) that can only be evaluated numerically. Numerous authors such as Bannister and Wait have developed approximate solutions based on 'quasi-static' approximations that allow a closed form solution to be obtained (Kraichman, 1976). More recently, Burke and Jones, (1994) developed an exact analytical solution for the 3-layer model comprising of air-sea-seabed layers; evaluating the complex equations using full numerical integration.

ELF radio waves are still considered valuable and essential tools for investigating various atmospheric and ionospheric phenomena. However, the exploitation of ELF radio waves is dominated by military applications. In addition to submarine communication systems, the possibility of detecting submarines by their stray ELFE 'signatures' and the possible mine threat posed to naval vessels by these stray fields has caused an escalation in research. This potential threat has been driven by advancements in sensor technologies and signal-processing techniques.

Readers with a general interest in ELF research are urged to read an excellent review paper by Barr, Llanwyn Jones and Rodgers (2000). This covers developments in ELF and VLF research over the last 50 years and contains hundreds of useful references.

1.4 Naval stealth

Naval stealth is primarily concerned with avoiding detection for tactical gain or for survivability. Hostile platforms (i.e. submarines) or threat devices (i.e. sea mines) are designed to identify the presence of naval platforms by exploiting a broad range of influences. These can include radar cross-section, infrared, acoustics, magnetics, electromagnetics and hydrodynamics influences. These influences are usually referred to as 'signatures' in the context of naval stealth, since they can provide a means for identifying naval platforms.

All naval platforms produce signatures that can be exploited for detection purposes. In most cases, these signatures are generated directly by the platform and are unavoidable. In other cases, the signatures are a response to an active detection system such as sonar or radar, where the platform is detected by the reflected signals.

A significant amount of military research is focused on minimising the signatures for both submarines and surface ships. This research addresses a broad range of factors including the design of platforms, the materials used for construction, special coatings and novel signature reduction technologies.

It is worth noting that the avoidance of detection is only part of the story. The localisation and classification of naval platforms can also be important before weapons can be deployed. Once detected, a platform can always attempt to confuse her opponents weapon systems by using decoys or countermeasures. However, once engaged in battle, the platform with the most superior weapons and countermeasures will most likely be victorious.

As technology improves, detection systems and weapon systems become increasingly more sophisticated and 'intelligent'. Intelligent in this context refers to the ability to undertake complex computations to discriminate between real signals and possible decoys or background noise sources in real-time. Some weapons or detection systems will also exploit more than one signature, thus reducing the false alarm rate when making detections or reducing the effectiveness of countermeasures.

1.4.1 Electromagnetic signatures

As mentioned earlier, there is a broad range of signatures that can be exploited for detection purposes. This study is primarily focused on low frequency electromagnetic signatures in 1Hz to 3kHz range. These signatures are collectively referred to as ELFE signatures in naval applications (Hubbard *et al.*, 1997). Non-acoustic signatures are particularly important in shallow water environments where acoustic signatures become increasing difficult to detect or exploit due to scattering from the interfaces. Alternating EM signatures also have advantages over static magnetic or static electric signatures due to the lower background noise levels, which typically falls off as $1/f$, where f is the frequency.

ELFE signatures can be important in naval applications due to the relatively large propagation ranges possible in seawater. ELFE signatures can be exploited by both airborne and underwater systems. Submarines can be detected by aircraft equipped

with magnetic anomaly detection (MAD) systems (Ash, 1997) or underwater surveillance systems (Certenais *et al.*, 1997) and sea mines (Hubbard *et al.*, 1997). Surface ships are also at threat from underwater systems, particularly sea mines. However, some airborne systems can exploit much higher frequencies (i.e. radar and infrared) since there is no need for the electromagnetic radiation to propagate through the highly attenuating seawater.

1.4.2 Signature sources

There are numerous sources of ELFE signatures on naval platforms. The most common sources are referred to as the 'shaft-related' and 'power frequency' ELFE signatures. The shaft-related ELFE signature is generated by the modulation of corrosion currents due to the varying electrical resistance between the rotating propeller shaft and the hull. The currents are generated by the galvanic corrosion of the dissimilar metals used to construct the submarine i.e. the steel hull (anode) and the nickel-aluminium-bronze (NAB) propeller (cathode). This corrosion can be slowed down using a cathodic protection system. This can consist of passive sacrificial zinc anodes or an active impressed current cathodic protection (ICCP) system. The ICCP anodes can generate a power frequency ELFE signature if they are fed with a poorly rectified current. All other power frequency sources can be attributed to onboard electrical systems such as motors and power distribution systems (Le Coat *et al.*, 1997).

The corrosion-related ELFE signatures are generated by electric sources and the ELFE signatures due to onboard electrical systems are generated by magnetic sources. The electric sources tend to be more important for submarine applications, since the onboard magnetic sources are heavily shielded by the thick pressure hull. Both sources tend to be important for surface ships, due to the limited amount of shielding.

The shaft-related ELFE signature can be reduced by grounding the shaft using active shaft grounding (ASG) or a passive system based on slip ring or brushes around shaft, electrically bounded to the hull (Holtham *et al.*, 1996). In both cases, the aim is to provide an electrical path for the current that has a constant resistance. The corrosion-

related power frequency signature can be reduced by filtering or smoothing the rectified anode currents; thus minimising the superimposed AC ripple. The power frequency signature due to onboard electric systems can be reduced by adopting good wiring practices (i.e. minimise loops in current carrying cables, twisted pairs, screening and shielding) and shielding large sources of EM fields. In practice, no signature reduction technique is perfect, hence there will be a residual signature.

1.4.3 Measuring platform signatures

The measurement of submarine and surface ship signatures is a crucial step in assessing the vulnerability of a platform to detection. The measurements are also used to optimise (i.e. minimise) the signature if suitable signature reduction systems are installed or for identifying the sources of emissions. The latter is the most important aspect for ELFE signatures, since the signature reduction systems typically fitted cannot be optimised. They are hardware systems that achieve a fixed reduction, based on the specification of the equipment. However, rangings can be useful to ensure the hardware systems are functioning correctly (i.e. within the specifications quoted by the manufacturer).

Signature measurements are made on what is historically referred to as an 'open sea degaussing[1] range' (OSDGR). An OSDGR typically consists of a line of magnetic and electric sensors that can measure the static and alternating magnetic and electric signatures of a platform. The position of the platform is tracked as is sails over the sensors using either optical tracker points or GPS antennas on the platform. At least two reference points are required on the platform to deduce heading, pitch and roll.

An OSDGR is typically situated on a site that has been surveyed to ensure the seabed is flat and free of ferrous materials that can contaminate measurements. A flat seabed is critical for static electric and ELFE measurements. The source models employed during rangings are only valid when the seabed is flat. The source model is used to determine an equivalent distribution of Hertzian dipoles (see Section 1.8) that can

[1] Degaussing is a term used to describe a method of compensating for a platforms ferromagnetic signature using a 3-axis coil system. The coil currents are optimised to produce a magnetic field that cancels the platform's signature.

accurately describe the signature of the platform being ranged (Rawlins *et al.*, 1999). The dipole distribution can then be used to predict the signature at any other desired location, provided the prediction is made at distances greater than the measurement distance. It can also be used to determine the most probable source of the ELFE signature.

Some countries also employ portable ranges (equivalent to an OSDGR) that can be employed when required in 'forward operating areas'. This can be near a war zone, where platforms may require periodic rangings to ensure the signatures are within acceptable limits, thus minimising the mine threat. This applies to all platforms, particularly mine countermeasure vessels (MCMV). In practice, it can be difficult to find a suitable site that meets all the requirements of an OSDGR, particularly a flat seabed.

1.4.4 Environmental effects on signatures

As indicated above, the ELFE signatures of naval platforms can be highly sensitive to the local environment. The shift of emphasis in naval warfare from 'blue' waters to 'littoral' waters has been a critical factor in the drive to understanding how the environment affects signatures. Deep blue waters present a relatively simple 2-layer problem for ELFE propagation with a relatively predictable sea conductivity (close to the global average σ=4S/m). This predictability gives rise to a well-defined assessment of the threat posed to naval platforms and a clear understanding on how to exploit ELFE signatures in these types of environment.

In contrast, littoral waters are much more complex in terms of the environmental geometry and the range of sea and seabed conductivities. The large number of variables leads to uncertainty in the threat posed to platforms and makes it difficult to make good tactical decisions.

2-layer models are inadequate in littoral environments. 3-layer propagation models are required as a minimum. In practice, more layers are needed to model the conductivity profiles that exist within the sea and seabed layers (see Section 2.3).

Furthermore, models that account for real seabed profiles are required to provide more realistic field predictions; thus allowing accurate threat assessments to be made. In some cases, models that can account for the coastline are also required.

1.4.5 Summary

In summary, propagation models play a crucial role in assessing the detection threat posed to naval platforms. Weapon systems can also exploit propagation models to allow them to discriminate against countermeasures and decoys. Applications such as source modelling also require accurate and efficient propagation models to allow signature levels to be predicted and to identify sources of signatures. The emphasis on littoral warfare has also increased the demand for more advanced propagation models that account for complex coastal environments.

1.5 Properties of the marine environment

The environment can play a significant role in determining the propagation characteristics of ELFE radiation. Both the geometry of the environment and the physical properties (e.g. salinity and temperature) of the media can affect the field levels.

Both temperature and salinity determine the conductivity of seawater. The conductivity is critical in determining the propagation range of EM radiation in conducting mediums. The EM radiation suffers an exponential attenuation that increases with increasing frequency and conductivity. This is the reason why only ELF radiation propagates into seawater; all the higher frequency bands are severely attenuated. In fact, the only exception is the visible portion of the EM spectrum where atomic effects (involving the absorption/emission of energy by electron transitions between different atomic energy levels) allow light to propagate in seawater.

1.5.1 Electromagnetic properties of seawater

A medium can be characterised for ELFE propagation purposes by its conductivity (σ), permittivity (ε) and its magnetic permeability (μ).

Seawater is a relatively good conductor of electricity due to its ionic composition. Salts such as sodium chloride and magnesium sulphate are fully dissociated into positive and negative ions by water. These ions are therefore free to conduct electricity though ionic conduction.

Seawater is a diamagnetic liquid. Its magnetic permeability μ is very close to that of free space $\mu_0 = 4\pi \times 10^{-7}$ H/m. The permeability is essentially a constant and only experiences negligible changes compared with other seawater parameters (Akindinov *et al.*, 1978). Seawater has a relative permittivity of approximately $\varepsilon_r = 81$ and can be regarded as a constant for ELF application (Akindinov *et al.* 1978).

The sea conductivity varies from 2S/m in the Arctic Ocean (e.g. cold waters with low salinity) to 8S/m in the Red Sea (warm water with high salinity). The conductivity can fall below 2S/m near to fresh water sources such as estuaries or in enclosed seas (e.g. the Baltic Sea). The conductivity typically changes by 2% – 3% for every 1°C (Akindinov, 1978), hence will vary with depth due to the temperature profile that exists in seawater.

1.5.2 Attenuation of electromagnetic waves in seawater

As mentioned earlier, electromagnetic waves experience an exponential attenuation in a conducting medium. The electric field, E(R) is given by

$$E(R) = E_0 e^{-\frac{R}{\delta}} \tag{1.1}$$

where E_0 is the initial field at R=0, R is the distance over which the wave has propagated and δ is the skin depth. The skin depth is defined as

$$\delta = \sqrt{\frac{2}{\omega\mu\sigma}} \tag{1.2}$$

for a good electrical conductor (Kraichman, 1970), where σ is the electrical conductivity, ω is the angular frequency and μ is the magnetic permeability. The skin depth is the distance over which the field amplitude decreases to 1/e of its original value. The wavelength of the radiation is also given by $2\pi\delta$ (Kraichman, 1970). It is interesting to note that the wavelength of ELF radiation is several orders of magnitude smaller in conducting media than in air. For example, the free-space wavelength at 1Hz is 300,000km compared with just 1580m in seawater (with a conductivity of 4S/m)!

1.5.3 Properties of the seabed

The electrical conductivity of the seabed can range from 10^{-4} S/m to 1 S/m (Burrows, 1978). The seabed is typically composed of several layers of varying thickness and conductivity. Layers of sediment are often found on the ocean floor; these tend to be water saturated, hence have a relatively high conductivity. The underlying bedrock can be permeable or impermeable, where the latter has a significantly lower conductivity.

The low conductivity of the seabed can affect the propagation of ELFE radiation by providing a low attenuation path for the radiation to propagate in, compared to the highly attenuating seawater.

1.5.4 Seabed profiles and geometry

The geometry of the seabed is generally very complex and variable. It has been shaped by billions of years of volcanic activity, erosion by seawater and the deposition of sediments. Figure 1.1 (taken from WWW.NGDC.NOAA.gov) shows a colour coded contour plot of the ocean floor and Earth's surface. Even on a global scale, vast areas of the seabed are sloping, particularly near fault lines, such as the mid-Atlantic ridge. The seabed depth can exceed 10km below sea level in the deepest oceans. Each of the world's oceans may be divided into three regions. The continental bank, the continental slope and the deep ocean.

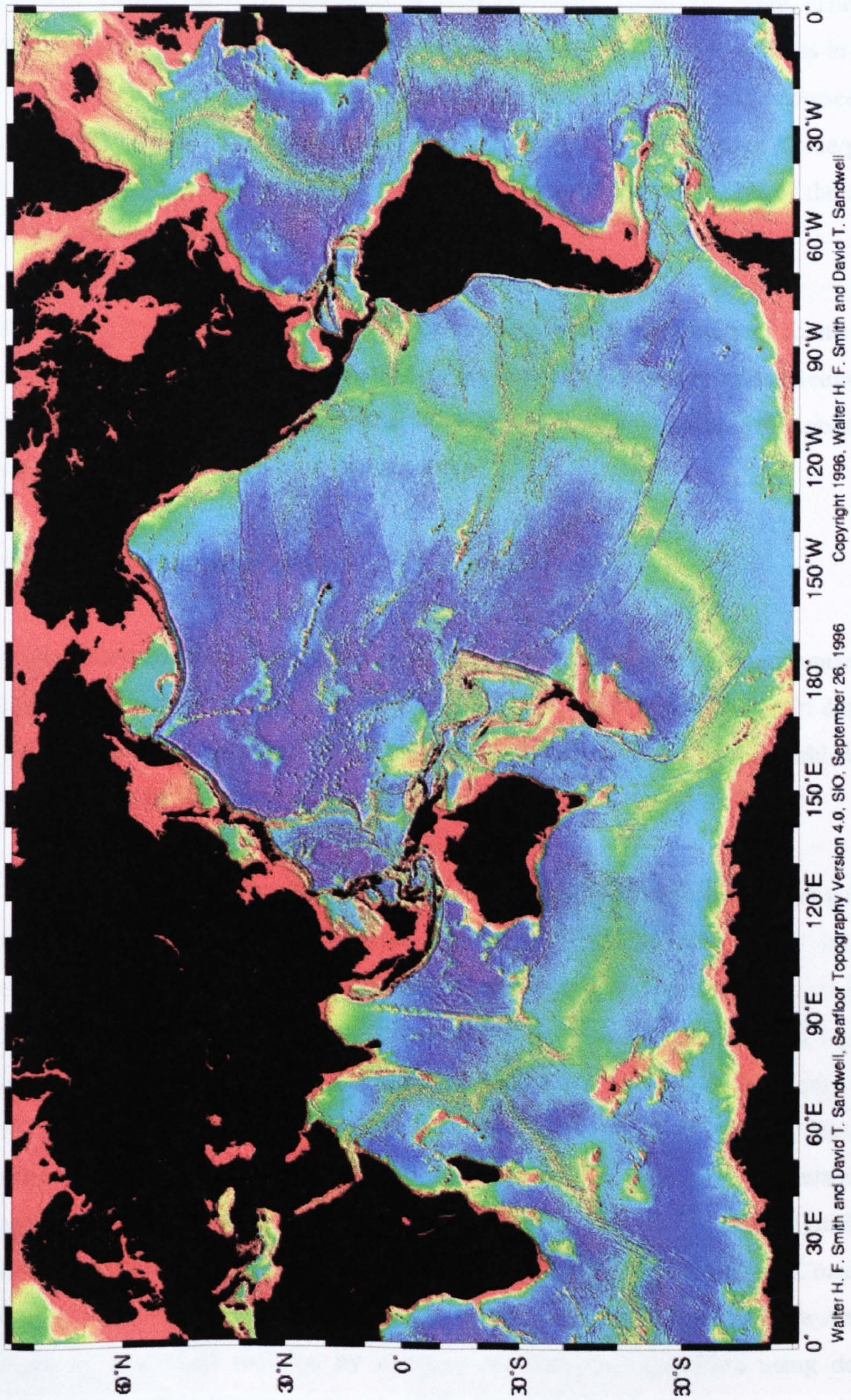

Figure 1.1: Colour contour plot of ocean depths

The continental bank has a depth of approximately 150m to 200m. These are relatively shallow waters and make up 7.6% of the oceans ('orange' regions in Figure 1.1). The continental slope ('yellow/green' regions in Figure 1.1) represents the transition from the shallow waters to the deep ocean. The deep ocean ('blue/purple' regions in Figure 1.1) has depths of 3km to 11km and represents 77% of the area of the oceans (Akindinov, 1978).

This study is largely concerned with the sloping seabed environment found in the continental bank and the continental slope regions, where sea depths are below 2km. In deeper waters, the seabed becomes less significant when dealing with applications near the sea surface (e.g. naval applications).

1.6 ELF noise sources

A significant barrier to the useful exploitation of EM signals in many underwater applications is the background electromagnetic noise level. False alarms in detection algorithms and the corruption of communications data are some of the problems that can be caused by background noise sources.

The ocean is also a difficult environment in which to perform signal processing for signal to noise (SNR) ratios of less than unity. This difficulty arises from the problems applying noise cancellation techniques or correlation techniques. Cancellation techniques rely on the coherence of noise over large distances, such that two sensor readings can be subtracted from each other. Ideally, both sensors would see the same noise, but only one sensor would see the signal of interest. The signal coherence is normally affected by the differences in the properties of seawater over large distances (i.e. temperature and salinity). This problem is made significantly worse by ocean currents mixing different layers of seawater together. Correlation techniques are difficult to implement due to the dispersive nature of seawater. The degree of dispersion suffered by a signal can only be quantified using detailed propagation models that accurately describe the ELFE propagation characteristics.

There are several distinct noise sources in the oceans; some of which are man-made,

but the majority have their origins in naturally occurring phenomena. These can range from atmospheric events to magnetohydrodynamic (MHD) effects in the ocean itself. This section will give a brief overview of some relevant noise sources that influence electromagnetic field measurements within the ocean environment.

1.6.1 Atmospheric sources

Lightning discharges from the thousands of thunderstorms occurring around the world at any give time are by far the most significant source of ELF noise in the 5-100Hz range. Cloud-to-ground lightning discharges can be many kilometres long (i.e. 2-14km) with currents ranging from 1-250kA (Ogawa, 1982), thus making them good ELF transmitters.

Lightning activity is responsible for exciting the Earth-ionosphere wave-guide, producing strong resonance effects in the ELF band. These are usually referred to as the Schumann resonances, and form well defined peaks in the background noise spectrum. The resonance peaks do however change slightly with time, due to the height and conductivity variations of the lower ionosphere with night and day.

ELFE radiation from lightning discharge also permeates the seas, oceans and the continents. Littoral environments suffer the most since radiation can easily penetrate the shallow waters. Furthermore, radiation incident upon land is also channelled into the seabed, thus bypassing the highly attenuating seawater.

Global lightning activity is a constant nuisance, but local lightning discharges can cause significant problems. The EM field levels from local discharges will dwarf the Schumman resonances and contain a broader range of frequencies.

1.6.2 Ionospheric sources

The ionosphere is also an abundant source of ELF noise. Magnetic storms caused by major solar eruptions (e.g. solar flares) produce significant noise and can affect communication systems and power distribution systems on Earth. Magnetic sub-

storms caused by instabilities in the magnetosphere are more common and can regularly disrupt communications.

The 'solar quiet daily variation' is caused by fluctuations in the electric currents flowing in the ionosphere (i.e. the polar electrojet current). These fluctuations influence the Earth's geomagnetic field, thus imposing a time-varying component to the otherwise 'static' field levels. The geomagnetic noise also permeates the oceans where it can induce electric fields.

1.6.3 Magnetohydrodynamic (MHD) effects in seawater

An electric current will tend to flow in any conductor moving relative to a magnetic field. This current flow will generate a magnetic field such that it acts to oppose the motion of the conductor. This mechanism also applies to seawater moving in the Earth's geomagnetic field. MHD effects can therefore generate electromagnetic noise in the ocean environment.

Surface waves and ocean swells are created by the action of the wind on the sea surface. The magnitude and velocity of the waves and swells (i.e. the sea-state) is directly proportional to the wind speed.

Tide changes and underwater earthquakes can generate internal waves in the world's seas and oceans. These can also result in strong MHD effects, albeit at very low frequencies (e.g. below 1Hz).

1.6.4 Man made sources

National power grid:

The national power grid used to supply electricity to domestic/commercial and industrial users effectively forms a long array of ELFE transmitters. This produces a significant spike in the EM background spectrum at 50Hz in the UK (or 60Hz elsewhere) with associated harmonics. This signal is unmistakably present in virtually

all ELFE field measurements made in the UK. In most cases, the EM signals extend out to hundreds of miles from the coastlines of all industrialised countries.

The ELFE emissions from power lines do not propagate globally since they are predominantly from horizontal electric sources. Much of the energy from the horizontal electric sources is directed vertically, thus simply bounces to-and-fro between the ground and the ionosphere. Vertical electric sources (e.g. lightning) would be required to excite the Earth-ionosphere wave-guide effectively. Nevertheless, power-frequency noise can be a big problem but it is easily removed from field measurements using a suitable 'notch' filter.

Industrial activity / electrical systems:

Some industrial processes use high current systems that can generate significant ELF emissions, usually at power frequencies. However, these are not considered a significant contributor to EM noise in the marine environment.

Communication systems:

ELF communication systems are still used in the 21st century for strategic communications with submarines. These systems affect ELF measurements anywhere in the world at the transmitting frequency (i.e. 76Hz for the US Seafarer system).

Ionospheric heaters:

ELFE signals can be generated in the ionosphere by perturbing the polar electroject currents using amplitude modulated high frequency radio waves. Ionospheric heaters, such as the HAARP facility in Alaska, USA, have been investigated to determine if they can provide a viable alternative to land based ELFE transmitters.

Techniques such as dual frequency heating may provide an alternative to perturbing the polar electrojet, thus allowing ionospheric heating applications to be exploited at lower latitudes. Dual frequency heating uses two slightly different high frequency

signals to exploit non-linear heating mechanisms. The low frequency radiation generated will be equal to twice the difference between the two frequencies used.

1.7 Electromagnetic propagation through seawater

This section of the report aims to provide a qualitative and graphical representation of the most significant propagation modes in an ocean environment. The distinct paths taken by the radiation as it travels from the source to the observer (e.g. sensors) are usually referred to as propagation modes and these can be useful for developing an understanding of how the observed field levels correspond to the environment and the geometry of the problem.

1.7.1 Propagation modes

There are essentially three distinct propagation modes; these are usually referred to as the direct wave, reflected waves (both primary and secondary) and lateral waves, see Figure 1.2.

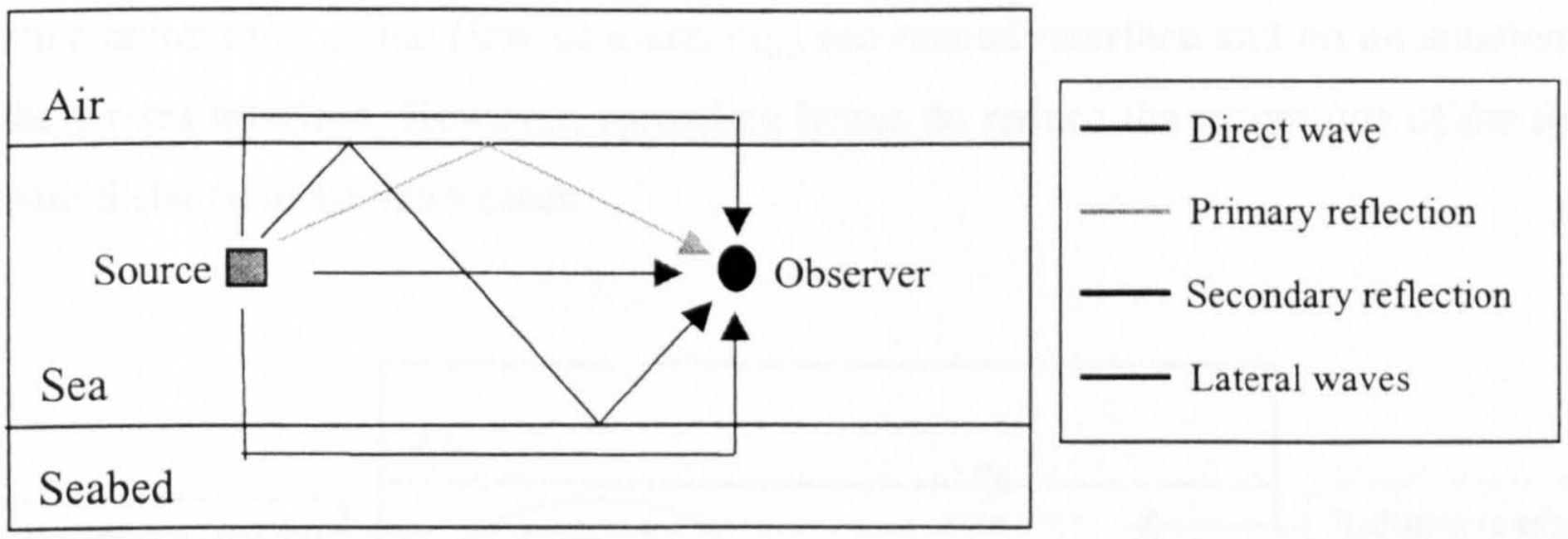

Figure 1.2: Propagation modes

1.7.2 Direct wave

The direct path describes the radiation that propagates directly from the source to the observer and is the solution that would be obtained in an infinite medium (i.e. without boundary effects). This mode is dominant in the near field and in deep waters where the air-sea and sea-seabed interfaces are far from the region of interest in-relation to the source-observer separation.

1.7.3 Reflections

The reflections are usually separated into two categories, the primary reflections relate to waves that reach the observer after one reflection from either the air-sea or sea-seabed boundary. Secondary reflections account for all other reflections that reach the observer after reflecting off both interfaces at least once. The reflected modes are always smaller in magnitude than the direct mode (having a longer path length), provided propagation is exclusively within the sea layer, but they can be important because they can constructively or destructively interfere with the direct mode, thus affecting the near-field solution.

1.7.4 Lateral waves

Lateral waves are rather more complicated and correspond to waves that appear to propagate vertically in the sea layer and horizontally along the interfaces, see Figure 1.3. Lateral waves are usually denoted as 'up-down' or 'down-up' depending on whether they propagate via the air-sea or sea-seabed interfaces, respectively. The lateral waves only suffer significant attenuation in the sea layer, with lower attenuation rates at the (low conductivity) sea-seabed interface and no attenuation at the air-sea interface. However, spreading losses do reduce the magnitude of the field with distance in all these cases.

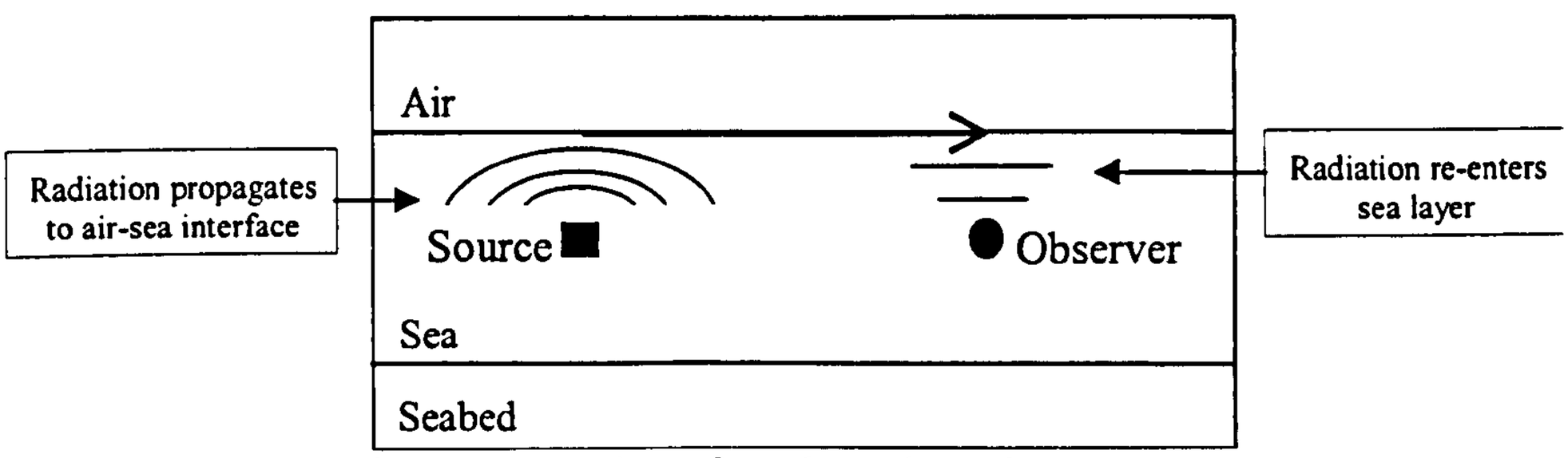

Figure 1.3: Schematic representation of up-down lateral wave

The mechanism that gives rise to lateral waves can be described as follows. Refraction effects cause the direction of propagation to change as the radiation passes through an interface between two different media. Snell's Law can be used to show

that a critical angle (ϕ_c) exists below which refraction effects are possible. For angles greater than ϕ_c, only reflections are possible, no field is transmitted. When the angle of incidence is equal to ϕ_c, the transmitted wave propagates along the interface with characteristics (i.e. velocity, attenuation and phase) governed by the least lossy medium (i.e. air or seabed). This surface wave is usually referred to as the lateral wave. The energy from the surface wave will continuously leak into the more lossy medium (i.e. the seawater), thus propagates back to the observer point (Kraichman, 1976).

Lateral waves tend to give rise to large propagation ranges in shallow waters. Since the majority of attenuation is experienced during the short vertical paths in the sea, with spreading losses dominant over the remainder of the horizontal path. However, there will be both spreading and attenuation losses for the down-up mode.

It is worth noting that not all sources produce lateral waves efficiently. Significant lateral waves will only be launched in the air or seabed if the transmission[2] coefficients for the interfaces permit radiation to pass through them. For example, the transmission coefficients for the air-sea interface will not let vertically polarisation radiation through, hence vertical electric dipoles (VED) to not produce up-down lateral waves. However, they can produce a small down-up lateral wave component.

1.7.5 Geometry of environment

The propagation modes detailed above can be used to describe propagation in any environment. However, there will be differences or complications depending on the geometry of the environment.

For example, the key difference between the horizontally stratified medium and a sloping seabed environment is with the reflections. If the interfaces are parallel, there can be an infinite number of multiple reflections between the interfaces. However, for the non-parallel case, there will only be a finite number of multiple reflections due to

---

[2] Snell's Law can be used to show that small angles of incidence are required to launch lateral waves. Hence, the critical factors will be the transmission coefficients and the field polarisation directly above or below the source.

the slope angle. This limits the number of propagation paths that allow radiation to reach the observer for any given geometry, see Figure 1.4.

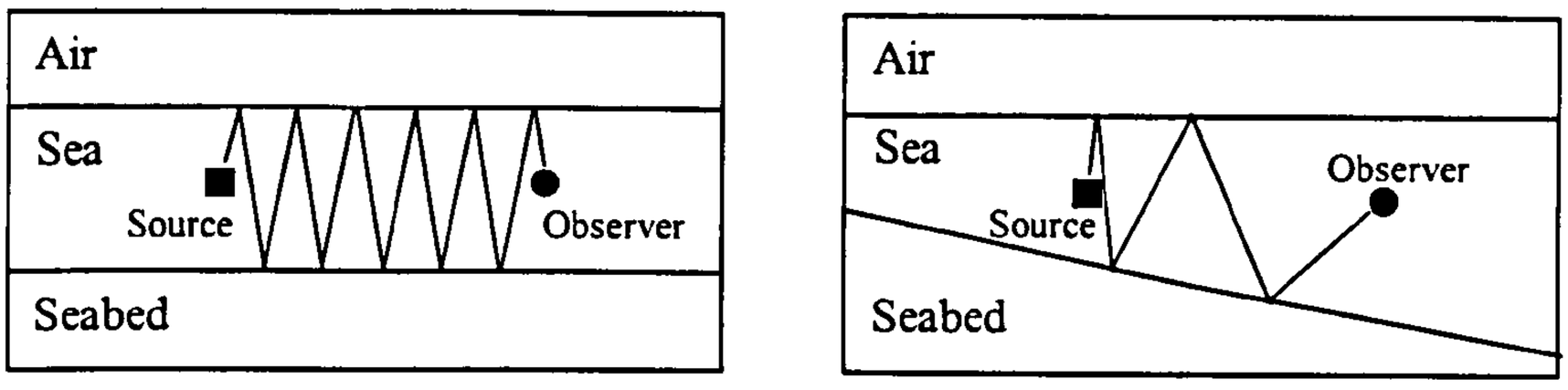

Figure 1.4. Secondary reflections based on seabed geometry

The same picture can be applied to the multiple reflections of the lateral waves. Once the lateral waves have re-entered the sea layer, they can reflect off the air-sea and sea-seabed boundaries. However, this effect is only significant at low frequencies, where the attenuation in the sea layer is relatively small. Furthermore, this effect is only significant at large distances from the source where the propagation is dominated by lateral waves.

A sloping seabed can also influence the number of lateral waves 'launched' into the air and seabed layers. Lateral waves only tend to occur when the angle of incidence of the wave front with the interfaces is very close to zero; this only happens directly above and below a source in a horizontally stratified medium. However, a sloping seabed will cause the angle of reflection to change with every reflection off the sloping seabed interface, hence there are more opportunities for the angles to approach zero, thus potentially launching more lateral waves. However, the 'resonance' condition (Wait, 1996) that exists above and below a source will no longer exist for the sloping seabed environment, thus reducing the number of lateral waves. The relative importance of these two competing effects needs to be quantified. This problem will be investigated in more detail in Chapter 5.

1.8 Dipole sources

The four fundamental sources of electromagnetic radiation are the horizontal electric dipole (HED), the vertical electric dipole (VED), the horizontal magnetic dipole (HMD) and the vertical magnetic dipole (HMD), see Figure 1.5.

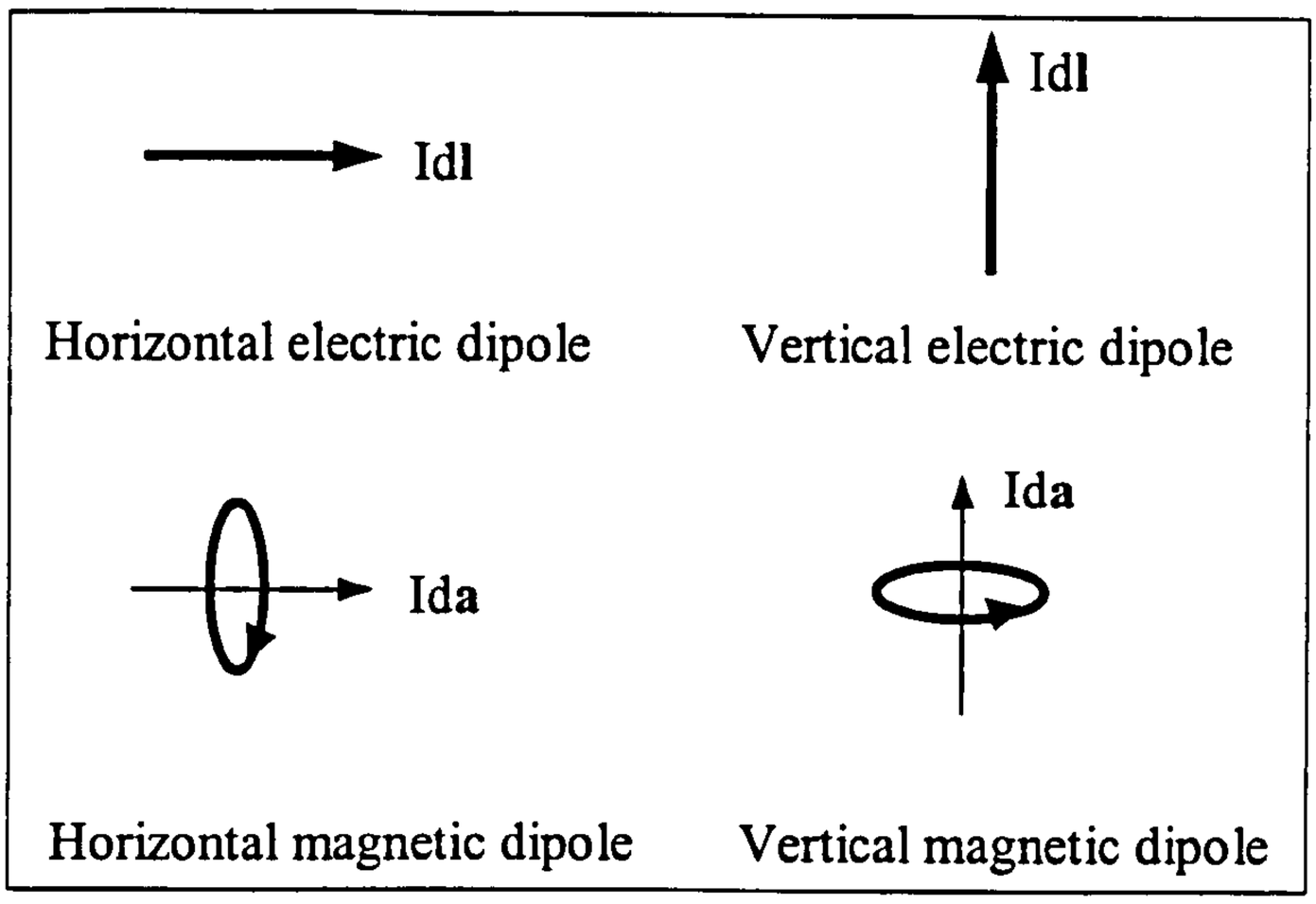

Figure 1.5: The four fundamental Hertzian dipole sources

An electric dipole is defined as a current element with an infinitesimal length. The electric dipole moment is given by the multiplication of these two factors and is denoted by Idl. A magnetic dipole is defined as a current loop with an infinitesimal area. The magnetic dipole moment is similarly given by the multiplication of these two factors and is denoted by Ida. Point sources of this nature are usually referred to as Hertzian dipoles. The orientation of the dipoles is defined by the direction of the vectors **l** or **a** in the source strengths.

Although Hertzian dipoles are mathematical idealisations, they can be useful for describing more complex real sources. For example, a complicated antenna can be modelled using the superposition of an equivalent configuration of point sources that replicates the geometry of the antenna (Dunbar, 1997).

The radiation patterns from the vertical and horizontal electric dipoles are equivalent, albeit rotated, in an infinite medium. However, the dipoles behave very differently when in a stratified medium. For example, the HED is an efficient radiator in seawater since it gives rise to lateral waves, whereas the VED does not generate significant lateral waves, hence is a poor radiator. The reason being that a vertically polarised field is fully reflected from the air-sea interface. In contrast, a horizontally polarised field is transmitted through the air-sea interface, thus can propagate as a

lateral wave suffering no attenuation whilst in the air. Similar arguments can also be applied to the magnetic dipoles.

1.9 Other applications of the ELFE propagation models

1.9.1 Strategic communications with submarines

As mentioned earlier, the fact that ELF waves penetrated the oceans and could be detected by submarines towing underwater antennas was of enormous military and strategic importance. The Seafarer transmitter in the US and the GBR transmitter in the UK are thus primarily for signalling to naval submarines, especially during an impending war (Jones, 1985; Pickworth, 2000).

Propagation models are required to model the field levels reaching submarines in various environments. A global propagation model is required to determine the how the fields propagate from the antenna in the Earth-ionosphere wave-guide to the submarine in the seawater.

1.9.2 Geophysical prospecting

Geophysical prospecting is largely concerned with the detection of mineral deposits, reservoirs of oil and gas, water-bearing formations and in the evaluation of civil engineering sites. The application of ELF radiation in geophysical prospecting is aimed at identifying the conductivity anomaly created by these mineral deposits in the surrounding rock. The low attenuation rates of ELF radiation in the Earth's crust means that depths over 10km can be probed or surveyed.

ELF based prospecting techniques work by inducing electric currents in the rock/mineral deposits. This can be achieved using natural sources of radiation (e.g. background EM noise) or by using active sources. The induced electric currents will generate electromagnetic fields that can be detected at the Earth's surface and interpreted to determine the underlying structure. Different frequencies can be used to probe to different depths; hence a full picture of the underlying structure can be

obtained. ELF propagation models are considered essential to interpret the field information received at the Earth's surface.

Magnetotellurics is another prospecting technique that maps the impedance of buried anomalies using changes in the polarisation of the scattered magnetic and electric fields (Peddell and Garnett, 1997). The incident field used to probe the ground can be from natural or artificial sources.

Prospecting using active sources can be carried out using a pair of electric electrodes inserted into the ground. The electrodes induce currents in the underlying rock, the depth of which is governed by the frequency used to drive the electrodes. The resulting fields can be surveyed at the Earth's surface and interpreted using propagation models. This would require inverse propagation models that aim to determine the environmental profile (e.g. conductivity with depth) for a given source and receiver configuration and using the measured field values.

1.9.3 ELFE Scattering

ELF scattering uses the same principles as geophysical prospecting. Possible applications include the search for metal objects in seawater such as submarines and ship wrecks, or objects buried in the Earth such as mines and pipes.

ELF scattering in seawater is feasible since the wavelength of the radiation is only a small fraction of its free-space wavelength; thus, the ELF wavelengths are comparable to the dimensions of the objects under investigation.

Modelling the scattered field from complex geometrical bodies is currently beyond the scope of analytical modelling techniques. However, numerical methods such as the finite element method have been shown to be useful (Ireland, 1997).

1.10 Overview of other sloping seabed models

ELFE propagation models tend to be predominantly formulated for horizontally plane-stratified environments; however, there are a number of sloping seabed and coastline models. These are all based on either numerical or iterative methods, owing to the complexity of obtaining an analytical solution. A summary of each model is provided below to indicate their main differences and intended applications.

(Weaver and Agarwal, 1997) details the development of a finite-difference (FD) model for investigating electromagnetic induction in coastal regions from low frequency excitations originating in the upper atmosphere (i.e. generated by ionospheric sources or solar events). The geometry considered includes both a coastline and a sloping seabed. The exciting signal is a plane wave emanating from the upper atmosphere.

This model solves directly for the magnetic field components to simplify the application of the boundary condition at the air-sea interface. All three components of the magnetic field are continuous across the air-sea interface, due to the absence of magnetic permeability discontinuities across the interface. This allows the integral relationship for the horizontal and vertical magnetic fields at the air-sea interface to be exploited.

Electric field components can be obtained using Maxwell's equations if required, albeit with increased numerical errors. The model also uses a 'staircase' approximation to model the geometry of the problem (i.e. even curved surfaces are constructed from rectangular blocks). The results presented by Weaver *et al.* (1997) showed that the induction effects were greatest at the coastline.

Schlak and Wait (1967) produced the earliest known sloping seabed model. They considered the electromagnetic response of a shallow water environment with a constant slope seabed (i.e. wedge geometry) to an electric dipole source situated in the air. The response of the seabed was modelled by using an analytically based geometrical approach to account for all the multiple reflections within the sea layer. The model was used to calculate the effective impedance of the sea surface due to the

underlying sloping seabed. This model was developed for application in geophysical prospecting.

A qualitative treatment of ELF propagation in the coastal environment was presented in (Tyler and Sanford, 1999). This paper attempted to predict ELFE propagation characteristics in the coastal environment by considering the attenuation and phase change of the radiation over the different geometrical path lengths. A matched phase condition for the 'beach mode' was derived, where the up-down and down-up lateral waves interfered constructively with each other at the beach (i.e. the coastline).

Quantitative results from a 2-dimensional finite-element (FE) model were also presented in (Tyler and Sanford, 1999) to validate their results. An infinitely long current line source was modelled for various seabed profiles. The results also investigated the influence of the source depth and source frequency.

The results showed the presence of a standing wave in the air as predicted when the matched phase condition is met. The results also showed that the fields were enhanced near the coastline, particularly at higher frequencies and for source near the seabed.

The University of Lille, France, has produced a coastal propagation model based on the finite-difference method. This model has been summarised in (Bruxelle, 1997). The mathematical formulation is based on Helmholtz relations. The general solution is obtained by minimising the mean power dissipated through the computational domain.

The results presented in (Bruxelle, 1997) for an infinite current line source showed there was a large increase in the EM field at the coastline, where the air-sea and sea-seabed interfaces meet. This is in agreement with results presented in (Weaver *et al.*, 1997 and Tyler *et al.*, 1999).

Chapter 2

Mathematical model for a HED embedded in a 3-layer medium

A detailed derivation of the electromagnetic field equations for a horizontal electric dipole (HED) in a horizontally stratified medium is presented in this chapter. The general case of a 3-layer medium consisting of air, sea and seabed layers is considered; the formulation is limited to the case when both the source and observer are situated in the sea layer.

This derivation is originally taken from Burke and Jones, (1994) and is referred to here as the 'KCL' model. It has since been reviewed and reported by Bhakta, (1998) and Orr, (2000) and is included here for completeness. This formulation and its interpretation is considered essential for developing an understanding of the different modes of ELFE propagation, (see Section 1.7); furthermore, it is the logical starting point for developing a sloping seabed solution based on analytical techniques.

2.1 Propagation models

Figure 2.1 shows a schematic representation of a 3-layer propagation model with the Cartesian co-ordinate system defined. Each layer is assumed to be homogeneous and isotropic and of infinite extent in the horizontal *xy*-plane; with both the air and seabed layers extending out to infinity in the negative and positive *z*-directions, respectively. The electrical conductivity (σ), electrical permittivity (ε) and magnetic permeability (μ) are used to characterise the properties of each medium throughout the model. The co-ordinate system is centred above the source at the air-sea interface. The source depth is thus given by $(0,0,h)$. The observer can be at any point (x,y,z) within the sea layer which has a depth, d.

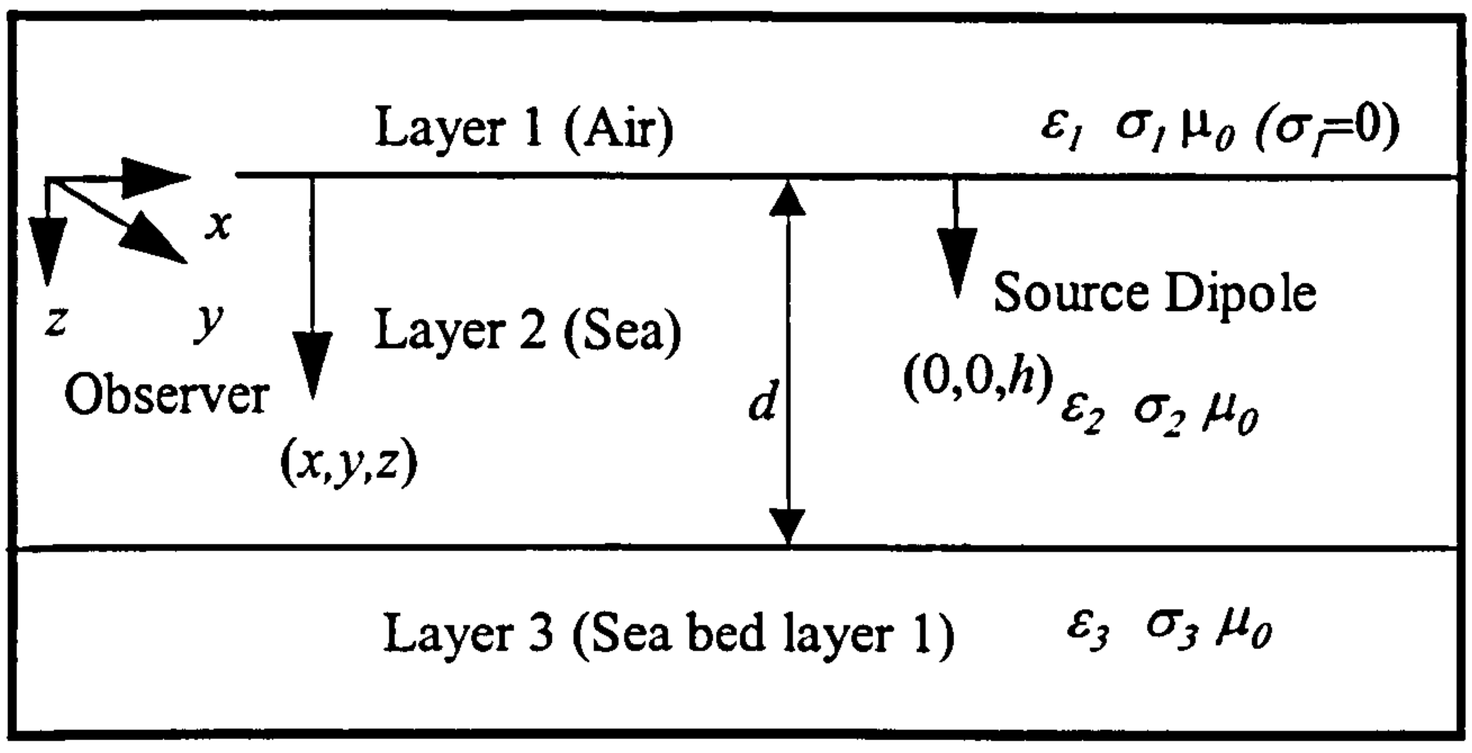

Figure 2.1: Schematic representation of a 3-layer propagation model

KCL opted to used the Hertz vector (Π) formulation to derive the ELFE field equations. This is a vector function from which both the electric scalar and magnetic vector potentials (and hence the electric and magnetic fields) can be derived. The Hertz vector is defined to satisfy the Lorentz condition identically. As a result, for Maxwell's equations to hold Π, must satisfy

$$\nabla \times \nabla \times \Pi - \nabla\nabla \cdot \Pi + \mu\varepsilon \frac{\partial^2 \Pi}{\partial^2} + \mu\sigma \frac{\partial \Pi}{\partial} = \mathbf{0}. \tag{2.1}$$

Equation (2.1) can be rewritten to give the more familiar vector Helmholtz equation

$$\nabla^2 \Pi - \mu\varepsilon \frac{\partial^2 \Pi}{\partial^2} - \mu\sigma \frac{\partial \Pi}{\partial} = \mathbf{0}. \tag{2.2}$$

The magnetic and electric fields can then be determined from

$$\mathbf{H} = \varepsilon\nabla \times \frac{\partial \Pi}{\partial t} + \sigma\nabla \times \Pi \tag{2.3}$$

and

$$\mathbf{E} = \nabla\nabla \cdot \Pi - \mu\varepsilon \frac{\partial^2 \Pi}{\partial t^2} - \mu\sigma \frac{\partial \Pi}{\partial t}. \tag{2.4}$$

Equations (2.2)-(2.4) can be simplified by considering plane (linearly polarized) wave propagation with an assumed time dependence of $e^{i\omega t}$ to give

$$\nabla^2 \Pi + k^2 \Pi = 0, \tag{2.5}$$

$$\mathbf{H} = \sigma^* \nabla \times \Pi = -\frac{k^2}{i\omega\mu} \nabla \times \Pi, \tag{2.6}$$

and

$$\mathbf{E} = \nabla\nabla \cdot \Pi + k^2 \Pi \tag{2.7}$$

where ω is the angular frequency, $\mathrm{i} = \sqrt{-1}$, ik is the propagation constant, $\sigma^* = \sigma + i\omega\varepsilon$ is the complex electrical conductivity and $k^2 = -i\omega\mu\sigma^*$. It is worth noting that the Hertz vector is related to the more commonly used magnetic vector potential **A** by

$$\Pi = -\frac{\mathrm{i}\omega}{k^2} \mathbf{A} \tag{2.8}$$

To find a solution to the 3-layer problem described above, the Hertz vector satisfying Equation (2.5) is found in each of the 3-layers. The overall solution is then obtained by 'joining' these three solutions using the boundary conditions at each interface and at infinity.

2.2 The HED model

For a dipole located in a linear, homogeneous and infinite medium, Π consists of only the primary excitation, Π^P. However when there is more than one medium, a perturbation to this solution is required to take account of the reflections from the boundaries between the media. Hence, the complete solution would comprise both a primary (Π^P) and secondary (Π^S) excitation;

$$\Pi = \Pi^P + \Pi^S, \tag{2.9}$$

where Π^S must be finite throughout space, be a solution of Equation (2.5) and satisfy the radiation conditions.

The HED is constructed from an infinitesimal current element with a dipole moment of Idl directed in the positive x-direction. It is initially assumed this will result in a Hertz vector possessing only an x-component, (Π_x,0,0). For an infinite linear, homogeneous medium, the solution to Equation (2.5) gives

$$\Pi_x^p = \frac{Idl}{4\pi\sigma_2^*}\frac{e^{-ikR}}{R} \tag{2.10}$$

where Idl is the dipole moment, σ_2^* is the complex conductivity of layer two and $R^2=x^2+y^2+(z-h)^2$ with h as the distance along the z axis where the dipole is located. Equation (2.10) can be rewritten in a more convenient form by using the Sommerfeld integral representation

$$\frac{e^{-ikR}}{R} = \int_0^\infty \frac{\lambda}{u_2} e^{-u_2|z-h|} J_0(\lambda\rho)d\lambda \tag{2.11}$$

to give

$$\Pi_x^p = \frac{Idl}{4\pi\sigma_2^*}\int_0^\infty \frac{\lambda}{u_2} e^{-u_2|z-h|} J_0(\lambda\rho)d\lambda \tag{2.12}$$

where J_0 is a Bessel function, $\rho^2 = x^2 + y^2$, $u_n = \sqrt{\lambda^2 - k_n^2}$ and λ is a separation (or dummy) variable.

To find Π_x^s, solutions are to be obtained to satisfy the scalar form of Equation (2.5). The scalar solution is preferred since the exact form for each of the Hertz vector components will depend on the source type and the boundary conditions.

$$\nabla^2 \Pi_x^s + k^2 \Pi_x^s = 0 \tag{2.13}$$

Using cylindrical geometry and taking advantage of the azimuthal symmetry, Equation (2.13) becomes

$$\frac{1}{\rho}\frac{\partial}{\partial\rho}\left(\rho\frac{\partial\Pi_x^s}{\partial\rho}\right)+\frac{\partial^2\Pi_x^s}{\partial z^2}+k^2\Pi_x^s=0. \tag{2.14}$$

Solving Equation (2.14) using the separation of variables yields

$$\Pi_x^s=\left(\alpha_1 e^{uz}+\beta_1 e^{-uz}\right)\left(\gamma_1 J_0(\rho\lambda)+\delta_1 Y_0(\rho\lambda)\right), \tag{2.15}$$

where α_1, β_1, γ_1 and δ_1 are constants, λ is the separation variable (a positive real number) and $u=\sqrt{\lambda^2-k^2}$. Since $Y_0(\rho\lambda)$ is singular at $\rho=0$; $\delta_1=0$ and the required solution becomes

$$\Pi_x^s=\left(\alpha_2 e^{uz}+\beta_2 e^{-uz}\right)J_0(\rho\lambda), \tag{2.16}$$

where $\alpha_2=\alpha_1\gamma_1$ and $\beta_2=\beta_1\gamma_1$. Since λ is a free parameter, Equation (2.16) can be written as a combination of all λ's:

$$\Pi_x^s=\frac{Idl}{4\pi\sigma^*}\int_0^\infty\left(\alpha e^{uz}+\beta e^{-uz}\right)J_0(\rho\lambda)d\lambda, \tag{2.17}$$

where α and β have been defined to allow the integral to have a $\pm\frac{Idl}{4\pi\sigma^*}$ factor introduced.

Equations (2.12) and (2.17) can now be used to determine Π_{x_j}, the x-component of Π in the j^{th} layer.

In layer 1 (the air) there is only a contribution from Π_x^s. For the solution to be finite everywhere, $\beta = 0$ in Equation (2.17) and

$$\Pi_{x1} = \frac{Idl}{4\pi\sigma_2^*} \int_0^\infty A_1 e^{u_1 z} J_0(\rho\lambda) d\lambda . \tag{2.18}$$

Similarly, for layer 3 (the seabed) $\alpha = 0$ in equation (2.17) to give

$$\Pi_{x3} = \frac{Idl}{4\pi\sigma_2^*} \int_0^\infty A_4 e^{-u_3 z} J_0(\rho\lambda) d\lambda . \tag{2.19}$$

In layer 2 (the sea), contributions from both the primary and secondary Hertz vector are taken into account to give

$$\Pi_{x2} = \frac{Idl}{4\pi\sigma_2^*} \int_0^\infty \left(\frac{\lambda}{u_2} e^{-u_2|z-h|} + A_2 e^{-u_2 z} + A_3 e^{u_2 z} \right) J_0(\rho\lambda) d\lambda \tag{2.20}$$

In Equations (2.18)-(2.20), $u_j = \sqrt{\lambda^2 - k_j^2}$, and the electrical conductivities σ_1^* and σ_3^* have been absorbed into the constants A_1 and A_4 respectively.

Equations (2.18) and (2.20) describe the dipole's field transmitted into the air and seabed media, respectively. Equation (2.19) represents the direct path (primary excitation) of the dipole and its reflection (secondary excitation) between both the upper and lower boundaries of the sea medium. It will also include the contribution from the up-down and down-up lateral wave components.

The boundary conditions at the interface can now be applied to obtain the 'transmission' coefficients A_1 and A_4 and the 'reflection' coefficients A_2 and A_3. From Faraday's law, it can be shown that the tangential components of **E** are continuous across the interfaces. Similarly, from Ampere's law, tangential components of **H** are continuous across the interfaces providing there are no surface currents.

However, Sommerfeld (1949) showed that these boundary conditions cannot be met for a HED, if the Hertz vector possesses only an x-component. Therefore a z-component of Π is introduced such that $\Pi = (\Pi_x, 0, \Pi_z)$. This gives rise to the following three equations for Π_z in each layer

$$\Pi_{z1} = \frac{Idl}{4\pi\sigma_2^*}\frac{\partial}{\partial x}\int_0^\infty B_1 e^{u_1 z} J_0(\rho\lambda)d\lambda, \tag{2.21}$$

$$\Pi_{z2} = \frac{Idl}{4\pi\sigma_2^*}\frac{\partial}{\partial x}\int_0^\infty \left(B_2 e^{u_2 z} + B_3 e^{-u_2 z}\right) J_0(\rho\lambda)d\lambda \tag{2.22}$$

and

$$\Pi_{z3} = \frac{Idl}{4\pi\sigma_2^*}\frac{\partial}{\partial x}\int_0^\infty B_4 e^{-u_3 z} J_0(\rho\lambda)d\lambda \tag{2.23}$$

where B_1, B_2, B_3 and B_4 are coefficients that need to be determined. This form of the solution with $\frac{\partial}{\partial x}$ in front of the integral is needed to satisfy the boundary conditions. The magnetic permeability (μ) is assumed to be equal to μ_0, the permeability of free space, in the following formulation.

The boundary conditions can now be applied to determine all these unknown coefficients. Using Equation (2.6) the tangential components of **H** are given by

$$H_x = \sigma^* \frac{\partial \Pi_z}{\partial y} \tag{2.24}$$

and

$$H_y = \sigma^*\left(\frac{\partial \Pi_x}{\partial z} - \frac{\partial \Pi_z}{\partial x}\right) \tag{2.25}$$

$k_j^2 = -i\omega\mu\sigma_j^*$ can now be used to show that $k^2\Pi_z$ must be continuous for H_x to be continuous and $k^2\frac{\partial\Pi_x}{\partial z}$ must be continuous for H_y to be continuous. Similarly, the tangential components of **E** can be derived using Equation (2.7) such that

$$E_x = k^2\Pi_x + \frac{\partial}{\partial x}\nabla\cdot\Pi \tag{2.26}$$

and

$$E_y = \frac{\partial}{\partial y}\nabla\cdot\Pi \tag{2.27}$$

where

$$\nabla\cdot\Pi = \frac{\partial\Pi_x}{\partial x} + \frac{\partial\Pi_z}{\partial z}. \tag{2.28}$$

This suggests that $\nabla\cdot\Pi$ and $k^2\Pi_x$ will be continuous across the boundaries.

To calculate the fields when the source and observer are both in the sea (layer 2) requires that the coefficients A_2, A_3, B_2 and B_3 are found. Using the continuity of $k^2\Pi_x$ across the sea/seabed interface at $z=d$ gives

$$\frac{Idl}{4\pi\sigma_2^*}k_3^2\int_0^\infty A_4 e^{-u_3 d}J_0(\lambda\rho)d\lambda =$$

$$\frac{Idl}{4\pi\sigma_2^*}k_2^2\int_0^\infty\left(\frac{\lambda}{u_2}e^{-u_2(d-h)} + A_2e^{-u_2 d} + A_3e^{u_2 d}\right)J_0(\lambda\rho)d\lambda \tag{2.29}$$

$$\Rightarrow \quad A_4k_3^2e^{-u_3 d} = k_2^2\left(\frac{\lambda}{u_2}e^{-u_2|d-h|} + A_2e^{-u_2 d} + A_3e^{u_2 d}\right). \tag{2.30}$$

Similarly, at the air-sea boundary $z=0$, giving

$$A_1 k_1^2 = k_2^2\left(\frac{\lambda}{u_2}e^{-u_2 h} + A_2 + A_3\right). \tag{2.31}$$

From the continuity of $k^2 \frac{\partial \Pi_x}{\partial z}$ across the sea-seabed boundary $z=d$

$$-k_3^2 u_3 e^{-u_3 d} A_4 = k_2^2\left(-\lambda e^{-u_2(d-h)} - u_2 A_2 e^{-u_2 d} + u_2 A_3 e^{u_2 d}\right). \tag{2.32}$$

Similarly continuity of the air-sea boundary $z=0$ gives

$$A_1 u_1 k_1^2 = k_2^2\left(\lambda e^{-u_2 h} - u_2 A_2 + u_2 A_3\right) \tag{2.33}$$

resulting in four equations which can be used to solve for the four unknown coefficients. Eliminating A_1 and A_4 from the equations and solving for A_2 and A_3 gives

$$A_2 = \frac{\lambda}{u_2}e^{-u_2 h} R_1\left(\frac{1 + R_3 e^{-2u_2(d-h)}}{1 - R_1 R_3 e^{-2u_2 d}}\right) \tag{2.34}$$

and

$$A_3 = \frac{\lambda}{u_2}e^{-u_2(2d-h)} R_3\left(\frac{1 + R_1 e^{-2u_2 h}}{1 - R_1 R_3 e^{-2u_2 d}}\right) \tag{2.35}$$

where

$$R_j = \frac{u_2 - u_j}{u_j + u_2} \tag{2.36}$$

for j=1,3.

The continuity of $k^2 \Pi_z$ can be applied to Equations (2.21), (2.22) and (2.23) to give

$$B_1 = \frac{k_2^2}{k_1^2}(B_2 + B_3) \tag{2.37}$$

and

$$\mathrm{B}_4 = \frac{k_2^2}{k_3^2} e^{u_3 d}\left(B_2 e^{u_2 d} + B_3 e^{-u_2 d}\right) \tag{2.38}$$

for the air-sea (z=0) and sea/seabed (z=d) interfaces, respectively. Finally applying the continuity of $\nabla \cdot \Pi$ at the same interfaces yields

$$A_1 + u_1 B_1 = \left(\frac{\lambda}{u_2} e^{-u_2 h} + A_2 + A_3\right) + u_2\left(B_2 - B_3\right) \tag{2.39}$$

and

$$e^{-u_3 d}\left(A_4 - u_3 B_4\right) = \left(\frac{\lambda}{u_2} e^{-u_2 (d-h)} + A_2 e^{-u_2 d} + A_3 e^{u_2 d}\right) + \left(B_2 e^{u_2 d} - B_3 e^{-u_2 d}\right). \tag{2.40}$$

Solving Equations (2.37)-(2.40) for B_2 and B_3 gives

$$B_3 = \frac{M - N R_1^{||} e^{-u_2 d}}{1 - R_{21}^{||} R_3^{||} e^{-2u_2 d}}, \tag{2.41}$$

$$B_2 = \frac{M R_3^{||} e^{-u_2 d} - N e^{-u_2 d}}{1 - R_1^{||} R_3^{||} e^{-2u_2 d}}, \tag{2.42}$$

$$R_j^{||} = \frac{k_1^2 u_2 - k_2^2 u_j}{k_1^2 u_2 + k_2^2 u_j} \tag{2.43}$$

for j=1,3 where

$$N = \left(\frac{\lambda}{u_2} e^{-u_2 (d-h)} + A_2 e^{-u_2 d} + A_3 e^{u_2 d}\right)\left(\frac{k_3^2 - k_2^2}{k_2^2 u_3 + k_3^2 u_2}\right) \tag{2.44}$$

and

$$M = \left(\frac{\lambda}{u_2} e^{-u_2 h} + A_2 + A_3 \right) \left(\frac{k_1^2 - k_2^2}{k_2^2 u_1 + k_1^2 u_2} \right). \tag{2.45}$$

The complete solution for Π has now been found for the HED, for the case when both the source and observer are in the sea medium. Equations (2.6) and (2.7) can now be used to determine the corresponding magnetic and electric fields. These field expressions can be found in Burke and Jones, (1994) and Orr, (2000).

2.3 A new 5-Layer model

The 3-layer KCL model detailed above is a very useful tool for analysing ELFE propagation in both deep and shallow waters. However, there are situations when more layers are required to accurately model environments with complex conductivity profiles. This can include shallow coastal waters, particularly if fresh water sources are nearby.

Coastal waters tend to have relatively high conductivity sedimentary layers deposited on a low conductivity layer of bedrock. The depth of sedimentary layers can vary significantly. The influence of the sedimentary layer on ELFE propagation will largely depend on its thickness. For a thick sediment layer, the bedrock will have a negligible role. For a thin sediment layer, the bedrock will dominate propagation effects. However, there will also be circumstances when the sediment layer thickness is such that both layers play a crucial role. There will also be situations when the water column contains different conductivity layers due to temperature profiles with depth or the uneven mixing of fresh and salt water.

Orr (2000) presented an extension of the KCL model to include an additional seabed layer, thus accounting for the sedimentary layer and the underlying bedrock (i.e. 4-layers, air-sea-sediment-bedrock). This thesis describes a further extension of the KCL model and the 4-layer model developed by Orr (2000) to produce a new 5-layer formulation (Bhakta, 1998). This formulation includes an additional upper layer to represent the ionosphere, see Figure 2.2. In practice, the additional layer can be used

to model an extra layer within the seabed or sea layer, rather than the ionosphere. The role of the extra layer will be determined by the location of the source and observer.

The 5-layer formulation presented in this thesis assumes the environment is stratified such that an ionosphere-air-sea-sediment-bedrock model is applicable; when both the source and observer are within the sea layer. This model also assumes the conductivity of the ionosphere is isotropic.

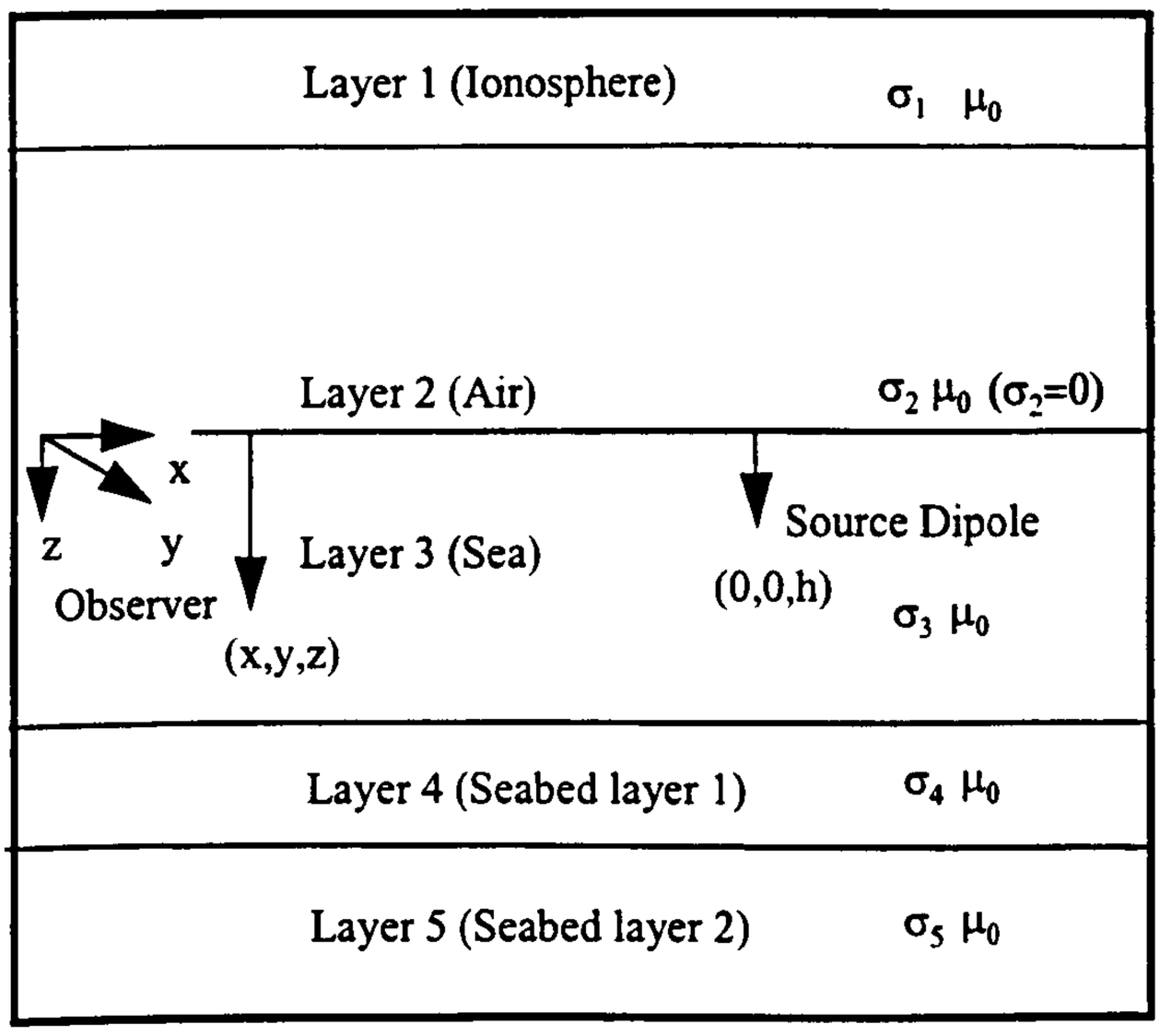

Figure 2.2: Schematic representation of a 5-layer propagation model

The derivation of the 5-layer model is summarised below. The derivation follows the same methodology used for the 3-layer KCL model. It is worth noting that this formulation was never implemented. The *NLAYER* propagation model acquired from FOI (Sweden) could model an arbitrary number of layers (i.e. 1000's of layers), thus negated its need. However, it may still be of interest to other authors.

The form of the Hertz vectors for the ionosphere, air, sea, seabed1 (i.e. sediment) and seabed2 (i.e. bedrock) layers are presented below in Equations (2.46) to (2.55). The subscripts used on the variables denote the layer number (i.e. d_2=depth of air layer).

$$\Pi_{x_1} = \frac{Idl}{4\pi\sigma_2^*}\int_0^\infty A_1 e^{u_1 z} J_0(\rho\lambda)d\lambda \tag{2.46}$$

$$\Pi_{z_1} = \frac{Idl}{4\pi\sigma_2^*}\frac{\partial}{\partial x}\int_0^\infty B_1 e^{u_1 z} J_0(\rho\lambda)d\lambda \tag{2.47}$$

$$\Pi_{x_2} = \frac{Idl}{4\pi\sigma_2^*}\int_0^\infty \left[A_2 e^{u_2 z} + A_3 e^{-u_2 z}\right] J_0(\rho\lambda)d\lambda \tag{2.48}$$

$$\Pi_{z_2} = \frac{Idl}{4\pi\sigma_2^*}\frac{\partial}{\partial x}\int_0^\infty \left[\mathrm{B}_2 e^{u_2 z} + B_3 e^{-u_2 z}\right] J_0(\rho\lambda)d\lambda \tag{2.49}$$

$$\Pi_{x_3} = \frac{Idl}{4\pi\sigma_2^*}\int_0^\infty \left[\frac{\lambda}{u_3} e^{-u_3|z-h|} + A_4 e^{-u_3 z} + A_5 e^{u_3 z}\right] J_0(\rho\lambda)d\lambda \tag{2.50}$$

$$\Pi_{z_3} = \frac{Idl}{4\pi\sigma_2^*}\frac{\partial}{\partial x}\int_0^\infty \left[\mathrm{B}_4 e^{-u_3 z} + B_5 e^{u_3 z}\right] J_0(\rho\lambda)d\lambda \tag{2.51}$$

$$\Pi_{x_4} = \frac{Idl}{4\pi\sigma_2^*}\int_0^\infty \left[A_6 e^{-u_4 z} + A_7 e^{u_4 z}\right] J_0(\rho\lambda)d\lambda \tag{2.52}$$

$$\Pi_{z_4} = \frac{Idl}{4\pi\sigma_2^*}\frac{\partial}{\partial x}\int_0^\infty \left[\mathrm{B}_6 e^{-u_4 z} + B_7 e^{u_4 z}\right] J_0(\rho\lambda)d\lambda \tag{2.53}$$

$$\Pi_{x_5} = \frac{Idl}{4\pi\sigma_2^*}\int_0^\infty A_8 e^{-u_5 z} J_0(\rho\lambda)d\lambda \tag{2.54}$$

$$\Pi_{z_5} = \frac{Idl}{4\pi\sigma_2^*}\frac{\partial}{\partial x}\int_0^\infty B_8 e^{-u_5 z} J_0(\rho\lambda)d\lambda \tag{2.55}$$

Applying the continuity requirement $k^2\Pi_x$ across the interfaces gives

$$k_1^2 A_1 e^{u_1 d_2} = k_2^2 \left(A_2 e^{u_2 d_2} + A_3 e^{-u_2 d_2} \right), \tag{2.56}$$

$$k_2^2 (A_2 + A_3) = k_3^2 \left(\frac{\lambda}{u_3} e^{-u_3 h} + A_4 + A_5 \right), \tag{2.57}$$

$$k_3^2 \left(\frac{\lambda}{u_3} e^{-u_3 |d_3 - h|} + A_4 e^{-u_3 d_3} + A_5 e^{u_3 d_3} \right) = k_4^2 \left(A_6 e^{-u_4 d_3} + A_7 e^{u_4 d_3} \right), \tag{2.58}$$

and

$$k_4^2 \left(A_6 e^{-u_4 (d_3 + d_4)} + A_7 e^{u_4 (d_3 + d_4)} \right) = k_5^2 A_8 e^{-u_5 (d_3 + d_4)}. \tag{2.59}$$

Applying the continuity requirement $k^2 \frac{\partial \Pi_x}{\partial z}$ across the interfaces gives

$$u_1 k_1^2 A_1 e^{u_1 d_2} = u_2 k_2^2 \left(A_2 e^{u_2 d_2} - A_3 e^{-u_2 d_2} \right), \tag{2.60}$$

$$u_2 k_2^2 (A_2 - A_3) = u_3 k_3^2 \left(\frac{\lambda}{u_3} e^{-u_3 h} - A_4 + A_5 \right), \tag{2.61}$$

$$u_3 k_3^2 \left(-\frac{\lambda}{u_3} e^{-u_3 |d_3 - h|} - A_4 e^{-u_3 d_3} + A_5 e^{u_3 d_3} \right) =$$

$$u_4 k_4^2 \left(- A_6 e^{-u_4 d_3} + A_7 e^{u_4 d_3} \right) \tag{2.62}$$

and

$$u_4 k_4^2 \left(- A_6 e^{-u_4 (d_3 + d_4)} + A_7 e^{u_4 (d_3 + d_4)} \right) = -u_5 k_5^2 A_8 e^{-u_5 (d_3 + d_4)}. \tag{2.63}$$

Applying the continuity requirement $k^2 \Pi_z$ across the interfaces gives

$$k_1^2 B_1 e^{u_1 d_2} = k_2^2 \left(B_2 e^{u_2 d_2} + B_3 e^{-u_2 d_2} \right), \tag{2.64}$$

$$k_2^2 (B_2 + B_3) = k_3^2 (B_4 + B_5), \tag{2.65}$$

$$k_3^2 \left(B_4 e^{-u_3 d_3} + B_5 e^{u_3 d_3} \right) = k_4^2 \left(B_6 e^{-u_4 d_3} + B_7 e^{u_4 d_3} \right) \tag{2.66}$$

and

$$k_4^2 \left(B_6 e^{-u_4 (d_3 + d_4)} + B_7 e^{u_4 (d_3 + d_4)} \right) = k_5^2 B_8 e^{-u_5 (d_3 + d_4)}. \tag{2.67}$$

Finally, applying the continuity requirement, $\nabla \cdot \Pi$ across the interfaces gives

$$A_1 e^{u_1 d_2} + u_1 B_1 e^{u_1 d_2} = A_2 e^{u_2 d_2} + A_3 e^{-u_2 d_2} + u_2 \left(B_2 e^{u_2 d_2} - B_3 e^{-u_2 d_2} \right) \tag{2.68}$$

$$A_2 + A_3 + u_2 (B_2 - B_3) = \frac{\lambda}{u_3} e^{-u_3 h} + A_4 + A_5 - u_3 (B_4 - B_5) \tag{2.69}$$

$$\frac{\lambda}{u_3} e^{-u_3 |d_3 - h|} + A_4 e^{-u_3 d_3} + A_5 e^{u_3 d_3} - u_3 \left(B_4 e^{-u_3 d_3} - B_5 e^{u_3 d_3} \right) =$$

$$A_6 e^{-u_4 d_3} + A_7 e^{u_4 d_3} - u_4 \left(B_6 e^{-u_4 d_3} - B_7 e^{u_4 d_3} \right) \tag{2.70}$$

and

$$A_6 e^{-u_4 (d_3 + d_4)} + A_7 e^{u_4 (d_3 + d_4)} - u_4 \left(B_6 e^{-u_4 (d_3 + d_4)} - B_7 e^{u_4 (d_3 + d_4)} \right) =$$

$$A_8 e^{-u_5 (d_3 + d_4)} - u_5 B_8 e^{-u_5 (d_3 + d_4)} \tag{2.71}$$

The application of the boundary conditions has thus produced sixteen equations, which can be solved simultaneously to determine the sixteen unknown coefficients. However, if field predictions are only required in the sea layer, only A_4, A_5, B_4 and B_5 need to be determined for substitution into Equations (2.5) and (2.6). Therefore,

the sixteen equations above can be reduced to four equations with four unknowns using substitution to eliminate the remaining coefficients, see Equations (2.72) to (2.75).

$$-\frac{\lambda}{u_3}e^{-u_3 h}R'_{23} + A_4 - A_5 R'_{23} = 0 \tag{2.72}$$

$$-\frac{\lambda}{u_3}e^{-u_3|d_3-h|}R'_{45} - A_4 e^{-u_3 d_3}R'_{45} + A_5 e^{u_3 d_3} = 0 \tag{2.73}$$

$$B_4 - B_5 R'^{||}_{34} - P^{||}_{21}S'_3 + S_2 T_1 = 0 \tag{2.74}$$

$$-B_4 e^{-u_3 d_3}R'^{||}_{34} + B_5 e^{u_3 d_3} + S_4 T_2 + S_3 = 0 \tag{2.75}$$

This gives

$$A_4 = \frac{\lambda}{u_3}e^{-u_3 h}\frac{\left(1 + R'_{45}e^{-2u_3(d_3-h)}\right)}{\left(1 - R'_{23}R'_{45}e^{-2u_3 d_3}\right)}, \tag{2.76}$$

$$A_5 = \frac{\lambda}{u_3}e^{-u_3(2d_3-h)}R'_{45}\frac{\left(1 + R'_{23}e^{-2u_3 h}\right)}{\left(1 - R'_{23}R'_{45}e^{-2u_3 d_3}\right)}, \tag{2.77}$$

$$B_4 = \frac{\left(P^{||}_{21}S'_3 - S_2 T_1\right) - \left(S_4 T_2 + S_3\right)e^{-u_3 d_3}R'^{||}_{23}}{\left(1 - R'^{||}_{23}R'^{||}_{34}e^{-2u_3 d_3}\right)} \tag{2.78}$$

and

$$B_5 = \frac{\left(P^{||}_{21}S'_3 - S_2 T_1\right)e^{-2u_3 d_3}R'^{||}_{34} - \left(S_4 T_2 + S_3\right)e^{-u_3 d_3}}{\left(1 - R'^{||}_{23}R'^{||}_{34}e^{-2u_3 d_3}\right)} \tag{2.79}$$

for the coefficients, where

$$R_{21} = \frac{u_2 - u_1}{u_2 + u_1}, \tag{2.80}$$

$$R_{45} = \frac{u_4 - u_5}{u_4 + u_5}, \tag{2.81}$$

$$R'_{23} = \frac{u_3 - P_{21}u_2}{u_3 + P_{21}u_2}, \tag{2.82}$$

$$R'_{45} = \frac{u_3 - P_{45}u_4}{u_3 + P_{45}u_4}, \tag{2.83}$$

$$P_{21} = \frac{1 - R_{21}e^{2u_2d_2}}{1 + R_{21}e^{2u_2d_2}}, \tag{2.84}$$

$$P_{45} = \frac{1 - R_{45}e^{-2u_4d_4}}{1 + R_{45}e^{-2u_4d_4}}, \tag{2.85}$$

$$R^{||}_{21} = \frac{u_1k_2^2 - u_2k_1^2}{u_1k_2^2 + u_2k_1^2}, \tag{2.86}$$

$$R^{||}_{45} = \frac{u_4k_5^2 - u_5k_4^2}{u_4k_5^2 + u_5k_4^2}, \tag{2.87}$$

$$P^{||}_{21} = \frac{1 - R^{||}_{21}e^{2u_2d_2}}{1 + R^{||}_{21}e^{2u_2d_2}}, \tag{2.88}$$

$$P^{||}_{45} = \frac{1 - R^{||}_{45}e^{-2u_4d_4}}{1 + R^{||}_{45}e^{-2u_4d_4}}, \tag{2.89}$$

$$R'^{||}_{23} = \frac{k_3^2 u_2 - k_2^2 u_3 P^{||}_{21}}{k_3^2 u_2 + k_2^2 u_3 P^{||}_{21}}, \tag{2.90}$$

$$R'^{||}_{34} = \frac{k_4^2 u_3 - k_3^2 u_4 P^{||}_{45}}{k_4^2 u_3 - k_3^2 u_4 P^{||}_{45}}, \tag{2.91}$$

$$T_1 = \frac{k_2^2 u_2 \left(1 - P^{||}_{21}\right) e^{u_2 d_2}}{k_3^2 u_2 + k_2^2 u_3 P^{||}_{21}}, \tag{2.92}$$

$$T_2 = \frac{k_4^2 u_4 \left(P^{||}_{45} - 1\right)}{k_4^2 u_3 + k_3^2 u_4 P^{||}_{45}}, \tag{2.93}$$

$$S_3 = \frac{k_4^2 - k_3^2}{k_4^2 u_3 + k_3^2 u_4 P^{||}_{45}} \left(\frac{\lambda}{u_3} e^{-u_3 |d_3 - h|} + A_4 e^{-u_3 d_3} + A_5 e^{u_3 d_3} \right), \tag{2.94}$$

$$S'_3 = \frac{k_2^2 - k_3^2}{k_3^2 u_2 + k_2^2 u_3 P^{||}_{21}} \left(\frac{\lambda}{u_3} e^{-u_3 h} + A_4 + A_5 \right), \tag{2.95}$$

$$S_2 = \frac{k_3^2}{k_2^2} e^{u_2 d_2} \left(\frac{k_2^2 - k_1^2}{k_2^2 u_1 + k_1^2 u_2} \right) \left(\frac{1 + R_{21}}{1 + R_{21} e^{2 u_2 d_2}} \right) \left(\frac{\lambda}{u_3} e^{-u_3 h} + A_4 + A_5 \right) \tag{2.96}$$

and

$$S_4 = \frac{k_3^2}{k_2^2} e^{-u_4 d_4} \left(\frac{k_5^2 - k_4^2}{k_5^2 u_4 + k_4^2 u_5} \right) \left(\frac{1 + R_{45}}{1 + R_{45} e^{-2 u_4 d_4}} \right)$$

$$* \left(\frac{\lambda}{u_3} e^{-u_3 |d_3 - h|} + A_4 e^{-u_3 d_3} + A_5 e^{u_3 d_3} \right). \tag{2.97}$$

Chapter 3

Experimental validation of the HED formulation

This Chapter describes the experimental validation of the KCL ELFE propagation model presented in Chapter 2 and its implementation in the *LAYER* program (see below). The validation was carried out in a shallow water environment using a calibrated electric source and a seabed-mounted sensor system. This Chapter is based on the work detailed in (Bhakta, 1997, 1998).

3.1 Introduction

The author would like to acknowledge and thank the research team at DERA Bincleaves for conducting the sea trial and for making the ELFE field data available.

Section 1.4 discussed a number of military applications that exploited ELFE propagation models including the evaluation of the mine threat posed to surface ships and submarines. It is not difficult to see that this type of application requires exceptionally accurate propagation models. Propagation models like the formulation detailed in Chapter 2 are mathematically complex and difficult to implement in computer programs.

LAYER is a FORTRAN program that was developed by King's College London to numerically evaluate the exact field equations for a number of sources using gaussian quadrature (Burke and Jones, 1994). The data from the DERA Bincleaves trial was used to validate the HED model implemented within *LAYER*.

All the experimental work was carried out in Weymouth Bay, a shallow water environment consisting of a relatively flat seabed, thus making a good approximation to the propagation model. However, the homogeneity of Weymouth Bay is

questionable owing to mixing between high salinity waters, particularly with the incoming tide and fresh water flowing into the Bay from the River Wey. It is anticipated that 'pockets' of different salinity waters can persist in this complex environment for long periods depending on the sea state.

3.2 Experimental procedure

A calibrated source with precisely known characteristics is essential for validating propagation models. The calibrated source used in this trial was a 2m long battery powered electric dipole with a maximum source strength (i.e. Idl) of 10Am. The bandwidth of the source ranged from 2kHz down to DC. The source could be driven by sinusoidal and square wave forms.

A small rigid inflatable boat (RIB) was used to perform the 'rangings' (see Section 1.4.3). The source was securely fixed to the hull of the RIB in a direction parallel to the keel line, thus representative of a HED, see Figure 3.1. The position of the RIB was continuously tracked in real-time using differential GPS (global positioning system).

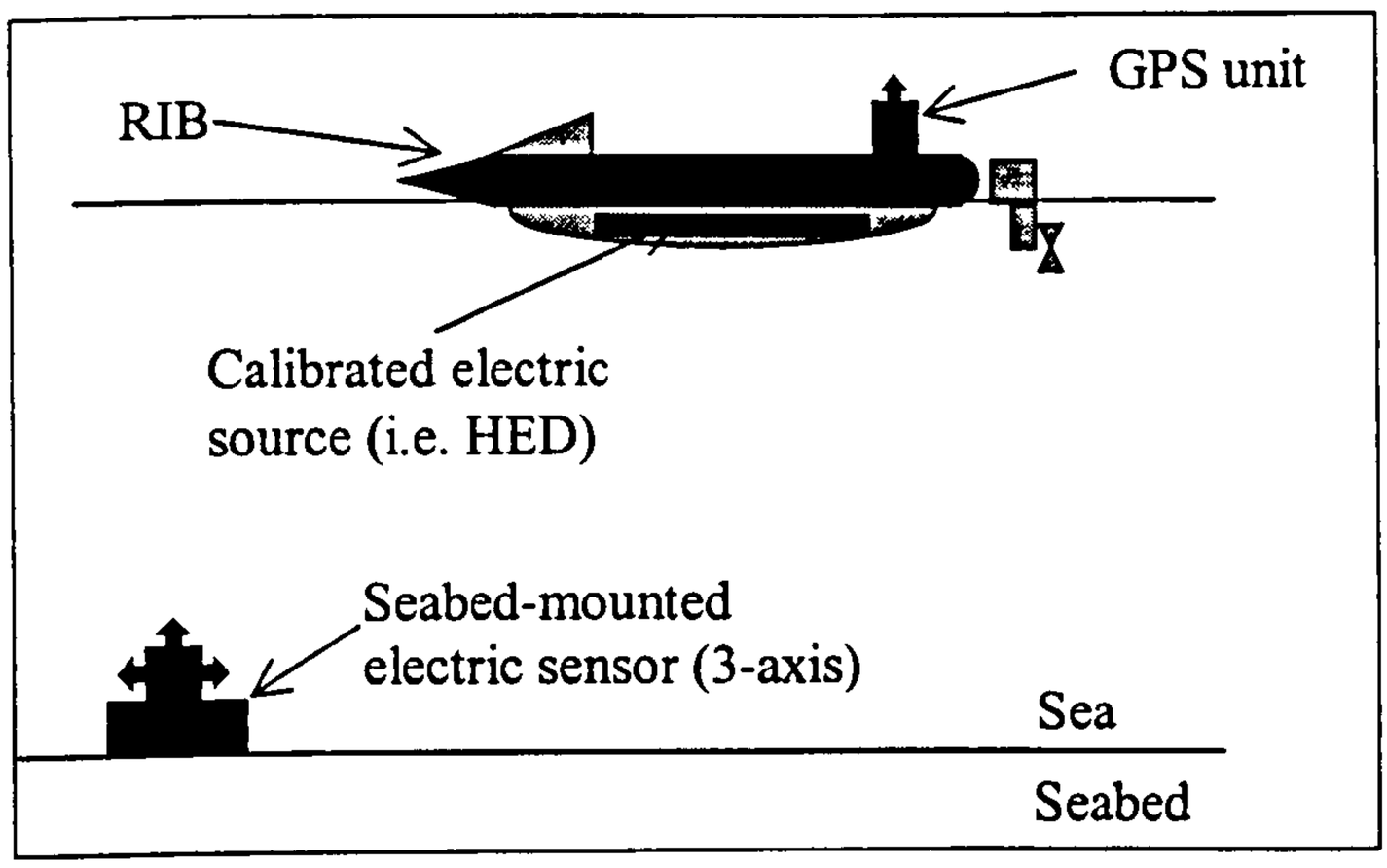

Figure 3.1: Schematic representation of experimental set-up

A seabed-mounted sensor was used to measure all three components of the HED's alternating electric field. All the measurements included a time-stamp for referencing

back to the differential GPS (D-GPS) readings. This was essential for calculating the relative source to sensor separations throughout the trial.

The sea conductivity was measured directly using a conductivity probe and the sea depth was determined using a pressure sensor fixed to the seabed sensor. Unfortunately the seabed conductivity was not measured; it was anticipated that this could be deduced from the experimental data. The seabed conductivity was going to be estimated by using an iterative process to match the predicted and measured fields (i.e. by manually varying the seabed conductivity). The success criteria would be to get agreement in both the near field (which would be dominated by the direct wave and the primary and secondary reflections) and agreement in the far field (which would be dominated by the propagation of the lateral waves).

The sensor was deployed at the start of the trial where its co-ordinates (or rather the co-ordinates of the RIB during deployment) were logged using the D-GPS system.

In practice, small differences in the recorded position of the sensor and its true position arose from the effects of the sea currents causing the RIB and sensor to drift during deployment. These differences needed to be reconciled if accurate results of the peak electric field were to be obtained. The peak electric field values were important for determining the sea conductivity. Localisation of the sensor was achieved by using the characteristics of the electric field data to confirm when the dipole source passed through the vertical plane centred on the sensor and perpendicular to the direction of the source. This resulted in an electric field that had a peak in the sensor x-component, with both the y- and z-components at zero (in the source's frame of reference where x is parallel to the source). The sensor co-ordinates in the xy-plane could be deduced using the D-GPS data by performing two orthogonal rangings on north-south and east-west headings, see Figure 3.2. Unfortunately, experimental uncertainties made it virtually impossible to accurately locate the sensor. These uncertainties arose from the fact field measurements were only made every 3 seconds (this equated to an average distance of 8m) and the heading of the RIB changed continuously during the rangings. The latter caused problems because it was impossible to determine the heading of the RIB using one D-GPS mast alone on

the platform. Two masts would be required to accurately determine heading, pitch and roll.

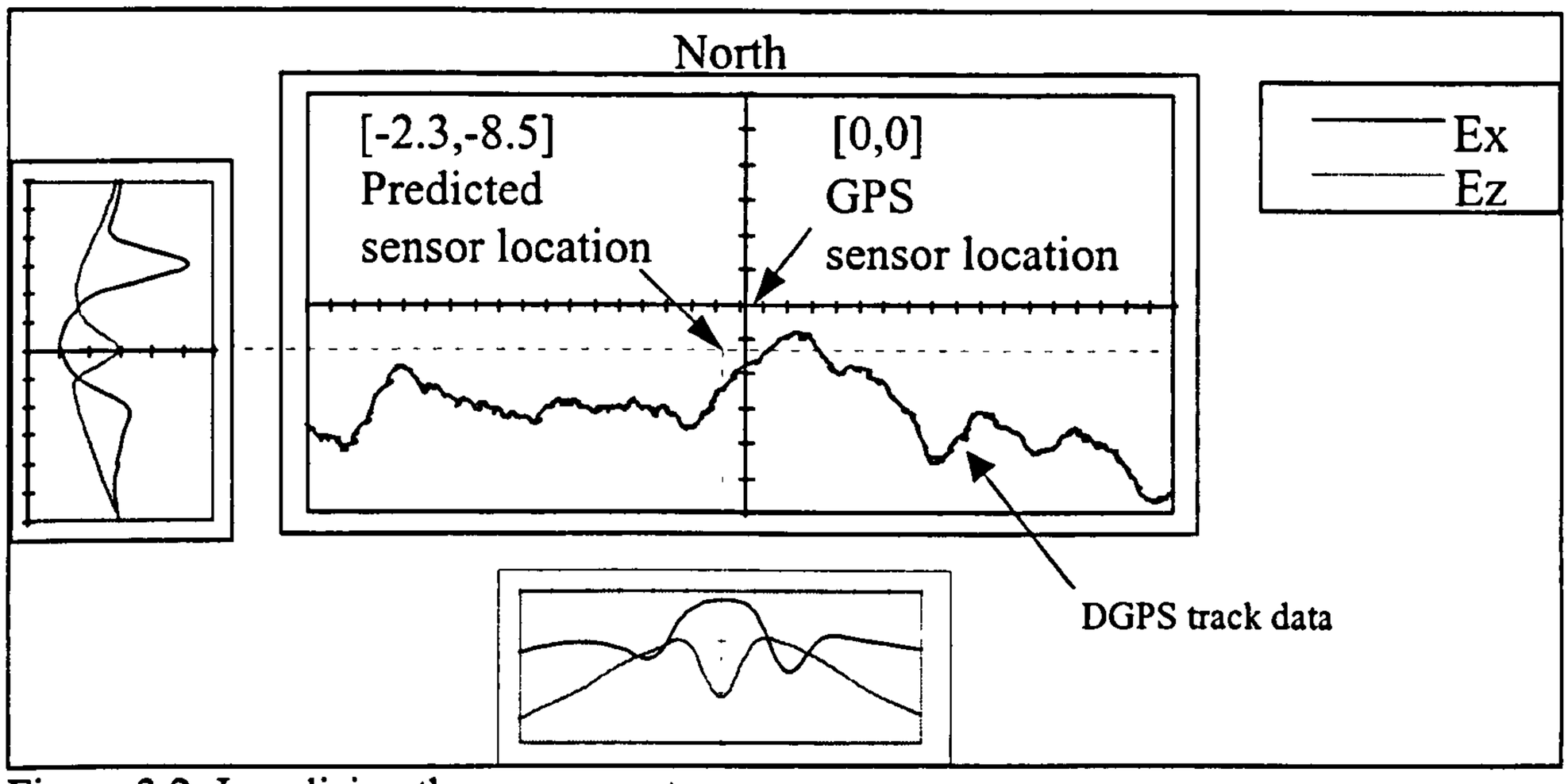

Figure 3.2: Localising the sensor system

The sensor location was predicted to be at [-2.3m, -8.5m] in the *xy*-plane. This location was determined using rangings performed on a north-south heading (run 24 South) and on an east-west heading (run 4 East). Runs 24 South and 4 East were both performed at 10Hz.

3.3 Sea and seabed conductivities

During the data analysis phase, low frequency runs were used to match the predicted and measured fields on several rangings for both north-south and east-west runs to find the most representative value for the seabed conductivity.

The matching process involved manually adjusting parameters to obtain the best fit between the experimentally measured and predicted field levels. Only the sea (see below) and seabed conductivity values were varied during this matching process. A manual process was favoured over an automated process (i.e. using a least squares optimisation routine) for the following reasons. Firstly, to artificially weight the matching process towards data in the far-field, thus minimising the problems with the uncertainty in the sensor location. Secondly, to make the most of the far-field data

where the down-up lateral wave mode contribution was significant. Finally, to allow the fitting process to use the 'noisy' portion of the data that is above the noise floor.

During this matching process, it was found that it was difficult to get agreement between the measured and predicted electric fields (in both the near-field and the far-field) unless the sea water conductivity was also changed from the measured value. The estimated conductivities from the matching process were 3.4S/m for the sea layer and 0.05S/m for the seabed layer. The estimated sea conductivity was therefore significantly lower than the 4.5S/m measured directly using the conductivity probe.

There is very little doubt that the measured value was correct, especially since the measurement was made using a calibrated probe and this value was confirmed using a second probe (albeit un-calibrated). However, this discrepancy could be attributed to the assumption that Weymouth bay can be approximated by a 3-layer model with homogeneous layers. It is anticipated that more layers were required to accurately describe conductivity variations within both the sea and seabed layers. Hence, the estimated values may have been 'effective' conductivity values that would have matched the approximate 3-layer model to the real environment.

A detailed analysis of this data has recently been undertaken in (Orr, 2000) using an automated optimisation algorithm for predicting the sea and seabed conductivity. The sea conductivity is in relatively good agreement with the findings in this study, the average value quoted in (Orr, 2000) was 3.2S/m +/-0.16S/m for the data relevant to this study. However, the seabed conductivity differed significantly. Orr (2000) quoted an average value of 0.2S/m +/-0.04S/m. This large difference can be explained by the limited far-field data used in the optimisation process by Orr, due to its contamination by noise. Orr used a cut-off threshold of –125dB, below which data was omitted. This far-field data was considered essential for fixing the seabed conductivity. This noise is most likely generated by surface waves and moving seawater disturbed by the passage of the RIB near the sensor.

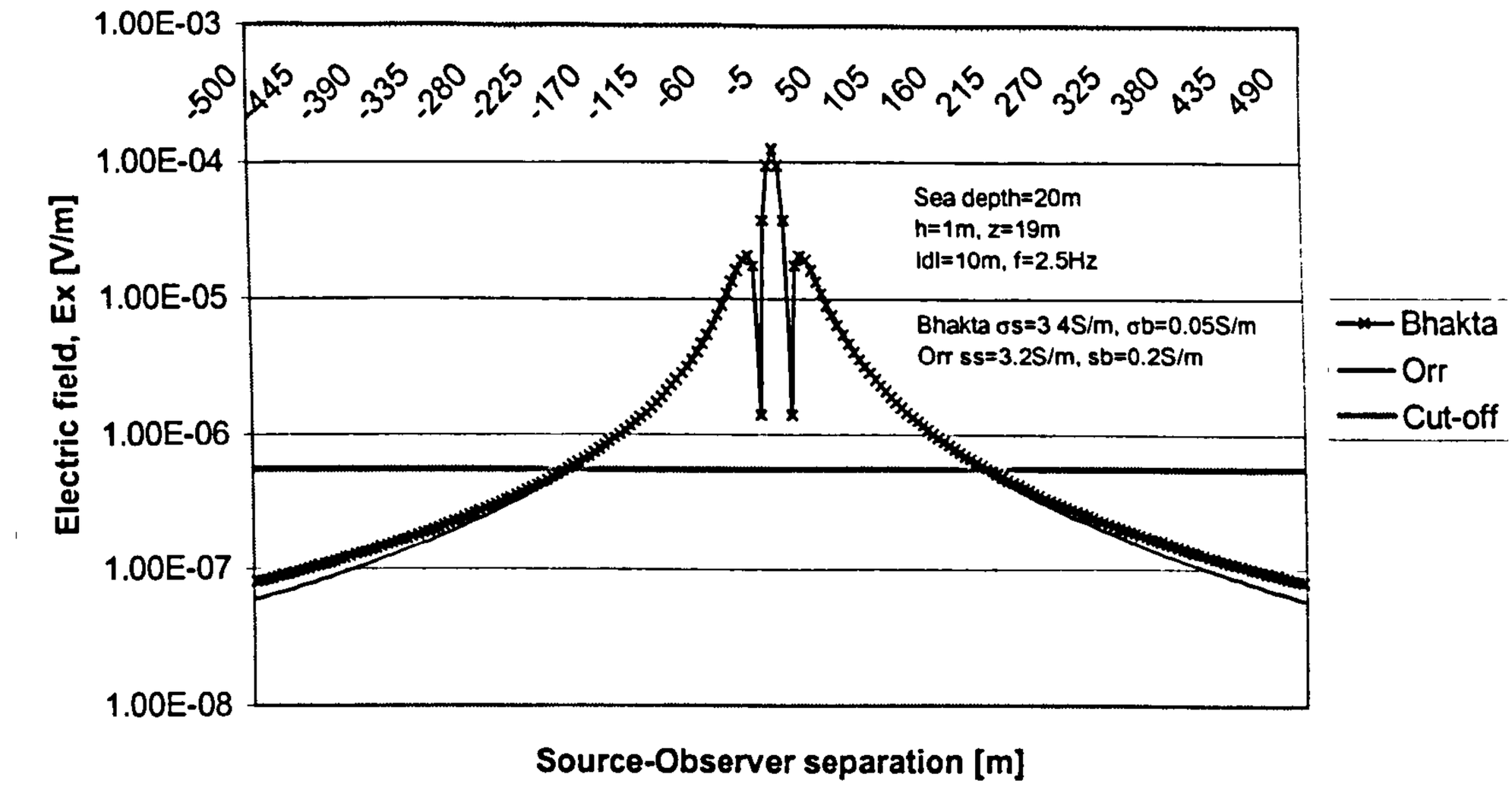

Figure 3.3: Comparison between results by Bhakta and Orr

Figure 3.3 shows a comparison between field predictions made using the conductivity values estimated by Orr (2000) and Bhakta (1998). The –125dB data cut-off threshold used by Orr is also marked (equivalent to 5.6E-07V/m). The peak fields agree very well with a percentage difference of 1.5% (i.e. 100*[(Bhakta-Orr)/Bhakta]). The spatial locations of the field nulls (due to the cancellation of different propagation modes) are also in very good agreement. The field difference increases to 6.3% near the –125dB cut-off threshold at approximately 200m from the source. The difference increases significantly to 26% at 500m from the source. As expected, the magnitude of the field predictions produced by Orr attenuate more rapidly due to the higher seabed conductivity. This result illustrates the importance of far-field data to estimate the seabed conductivity. The relative importance of the different propagation modes is shown in Figure 3.4.

It is hoped that future trials will carry out extensive measurements to determine the presence of any conductivity profiles within the sea layer. Although equivalent conductivity data for the seabed would be extremely desirable, it is acknowledged that this is unlikely to be available due to the difficulty and financial costs involved. Hence more rigorous experiments need to be planned to determine the seabed conductivity profile and simultaneously validate future propagation models.

3.4 Model validation results

Figure 3.4 shows a field comparison between the measured experimental data and various field predictions obtained using the *LAYER* ELFE propagation model. The 'infinite' solution is obtained by assuming the source is in an infinite sea medium. This only contains the direct wave contribution. The 'air-sea' and 'sea-seabed' solutions are obtained using *LAYER* to mimic a 2-layer model. These only include the direct wave contributions and all the interactions with either the air-sea or the sea-seabed interface, respectively. The 'modular' solution is obtained using an approximate 3-layer model (i.e. air-sea + sea-seabed) and includes all the different propagation modes, except those that involve interactions with both the interfaces. The method used to obtain the modular solution is described in Section 5.3 along with details about interface interactions. The 'predicted' solution includes all the propagation modes and constitutes the full numerical solution to the ELFE equations presented in Chapter 2 (i.e. the KCL model).

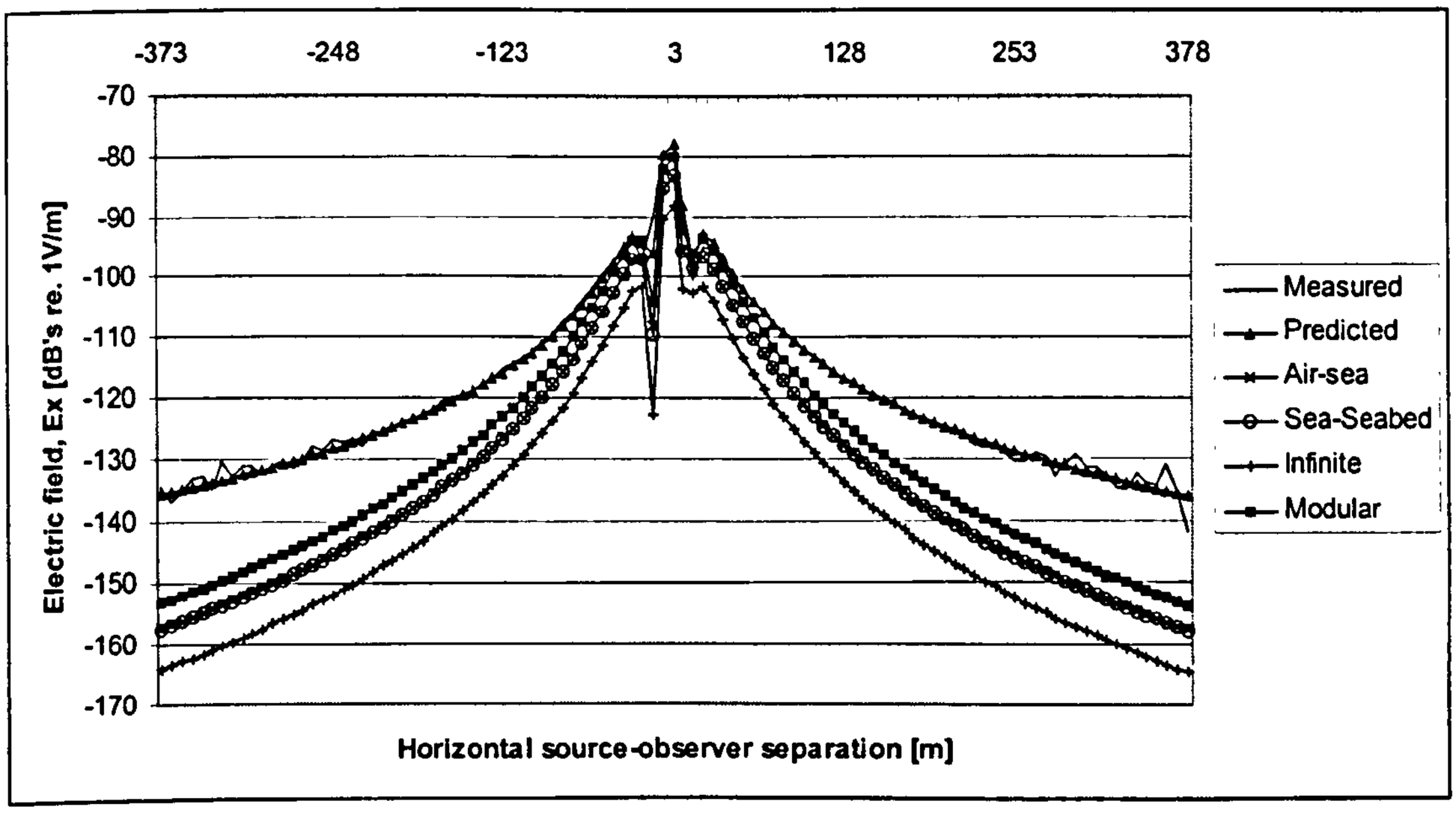

Figure 3.4: Run 13West; Field comparisons for different propagation modes

Figure 3.4 shows that the full numerical solution from *LAYER* is required to get agreement with the experimental data. The intermediate solutions obtained using the infinite medium or 2-layer[1] models are inadequate for addressing this shallow water

[1] Even the approximate 3-layer 'modular' solution is obtained using (two) 2-layer models.

problem. It is also worth noting that it is impossible to get agreement between any of the intermediate solutions and the experimental data over the entire source-observer range, for any given conductivity values. A propagation model that takes account of all the different propagation modes is essential in conjunction with the correct conductivities. The probability of producing an erroneous ELFE propagation model[2] that will give the desired answer by using arbitrary conductivity values is considered highly improbable.

The validity of KCL formulation and its implementation in the *LAYER* program will be judged on its ability to accurately predict the field levels obtained from the experimental trial over the entire source-observer range.

The experimental runs used for the validation process are summarised in Table 3.1. All the runs in Table 3.1 were all collected on the same day (i.e. 9th August 1996) and all have frequencies ranging from 1-10Hz. Higher frequency runs were intentionally not used.

Run	Frequency
4 East	10.0Hz
9 West	5.0Hz
11 West	2.75Hz
12 East	2.0Hz
13 West	1.0Hz

Table 3.1: Experimental data from 9th August 1996

Data from the same day was used to minimise the impact of conductivity changes in the seawater due to tide cycles and the influx of fresh water from the River Wey. The low frequency runs were chosen to allow data to be analysed for large source-observer separations. As mentioned earlier, this far-field data was considered useful for two reasons: Firstly, the large source-observer separation would ensure that the errors in the sensor's location would become less significant. Secondly, the far-field

[2] This includes either incorrect formulations or incorrectly implemented formulations (i.e. coding bugs).

data would contain a greater[3] contribution from the lateral waves, particularly the 'down-up' mode that propagates through the seabed.

Figures 3.5 to 3.9 (top) show comparisons between the measured and predicted field levels. All the field predictions were obtained by assuming the source maintained a constant heading along the x-axis with y=0.0 for the entire run. Figures 3.5 to 3.9 (bottom) shows the actual tracking data for the source. Some of the discrepancies between the field predictions and the measured data can be directly correlated with the tracking (i.e. when $y \neq 0$).

Table 3.2 summarises the percentage misfit between the measured and predicted field levels.

Run	% Misfit
4 East	1.161
9 West	0.723
11 West	0.716
12 East	0.606
13 West	0.687

Table 3.2: Percentage misfit between measured and predicted fields

The percentage error was calculated using the following expression with all the field values expressed in dB's:

$$\%Misfit = 100 * \left(\frac{Measured - Predicted}{Measured} \right)$$

The field predictions are generally in good agreement with the experimental measurements. The average percentage misfit was 0.78% when calculated using dB's, or approximately 8% if calculated using field values. This value is considered more than satisfactory considering no attempt was made to optimise the conductivity values

[3] The lateral wave components would be less significant at higher frequencies due to the attenuation experienced within the sea layer, prior to the arrival of the lateral waves at the source.

for each run individually. Furthermore, no attempts were made to correct for the true sensor position or the tracking offsets.

Rawlins *et al* (1999) quotes percentage misfit errors between 4-7% for a similar experiment. However, Rawlins *et al* (1999) used a source model (i.e. inverse propagation model) specially developed for ranging applications. This source model explicitly made use of the tracking data when making the field predictions.

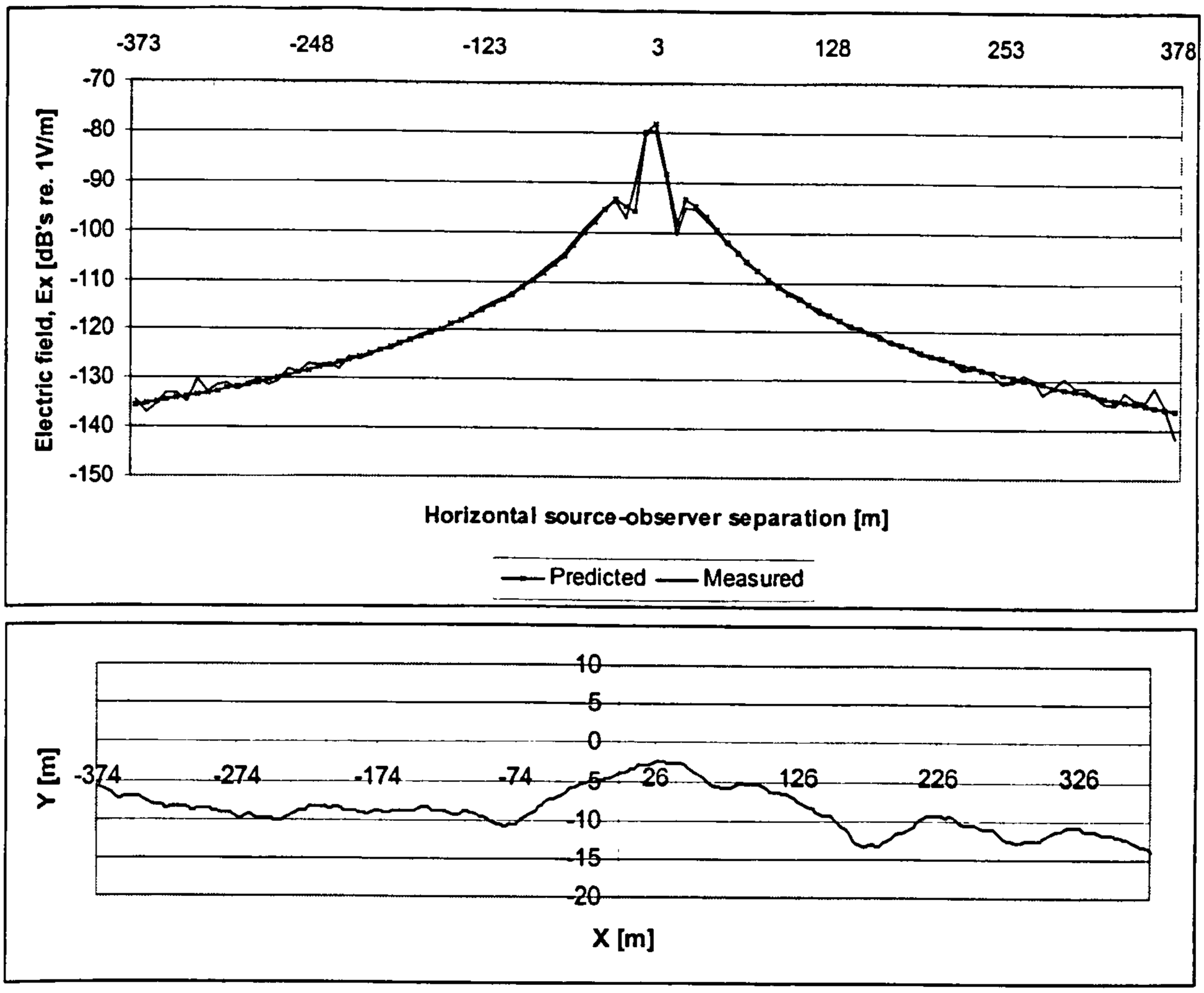

Figure 3.5: Run 13West; Field comparison (top), tracking (bottom)

	Start	CPA	Finish
Time	17:37:33	17:40:01	17:42:30

	Start	Increment	Finish
Distance	-373.326m	7.3697	378.39

Average speed
2.531022m/s

Sea depth	Source depth	Sensor depth	Frequency
19.4m	1.0m	18.65m	1.0Hz

Sea conductivity	Seabed conductivity
3.4S/m	0.05S/m

Table 3.3: Parameters for run 13West

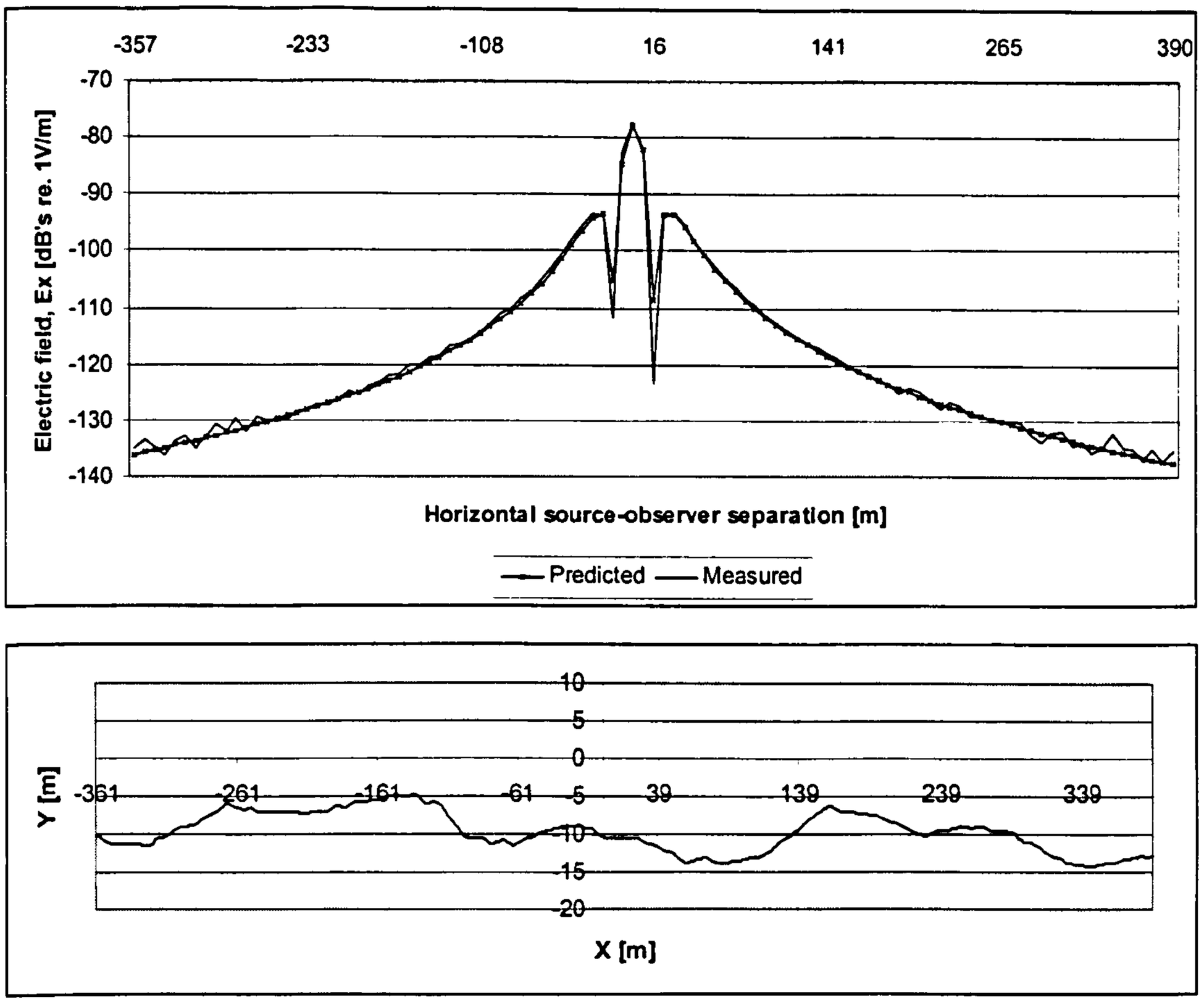

Figure 3.6: Run 9West; Field comparison (top), tracking (bottom)

	Start	CPA	Finish
Time	17:02:07	17:04:30	17:07:04

	Start	Increment	Finish
Distance	-361.46m	7.36m	389.266m

Average speed
2.5277m/s

Sea depth	Source depth	Sensor depth	Frequency
19.6m	1.0m	18.85m	5.0Hz

Sea conductivity	Seabed conductivity
3.4S/m	0.05S/m

Table 3.4: Parameters for run 9West

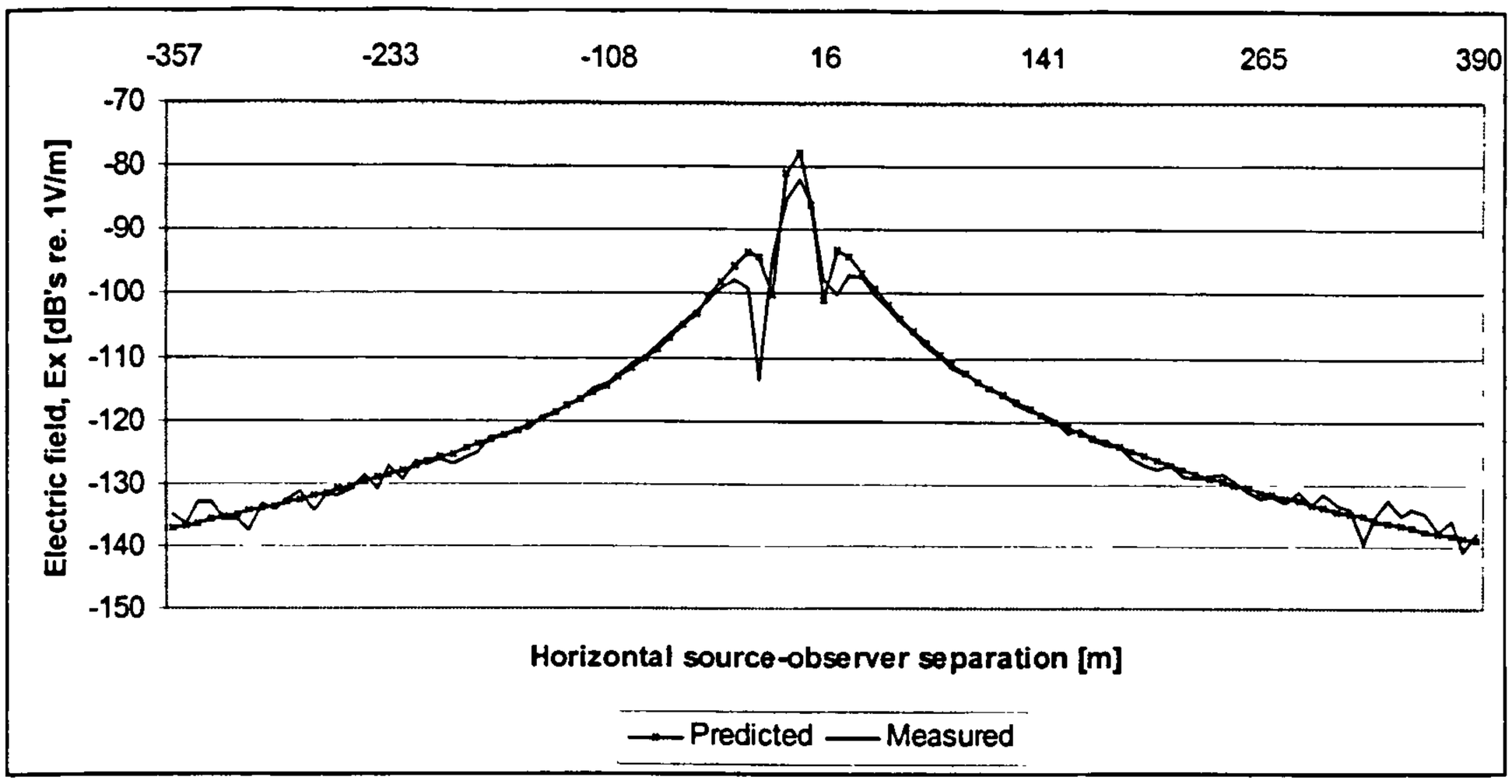

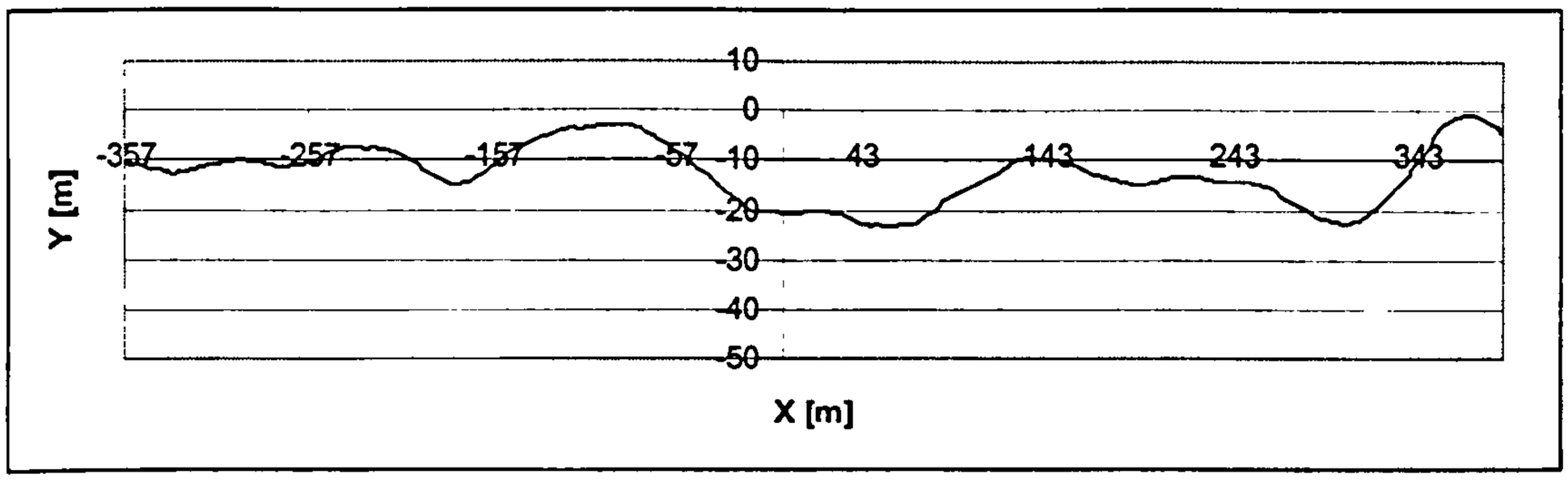

Figure 3.7: Run 4East; Field comparison (top), tracking (bottom)

	Start	CPA	Finish
Time	13:09:42	13:12:05	13:14:39

	Start	Increment	Finish
Distance	-357.2m	7.322m	389.68m

Average speed
2.49794m/s

Sea depth	Source depth	Sensor depth	Frequency
19.55m	1.0m	18.8m	10.0Hz

Sea conductivity	Seabed conductivity
3.4S/m	0.05S/m

Table 3.5: Parameters for run 4East

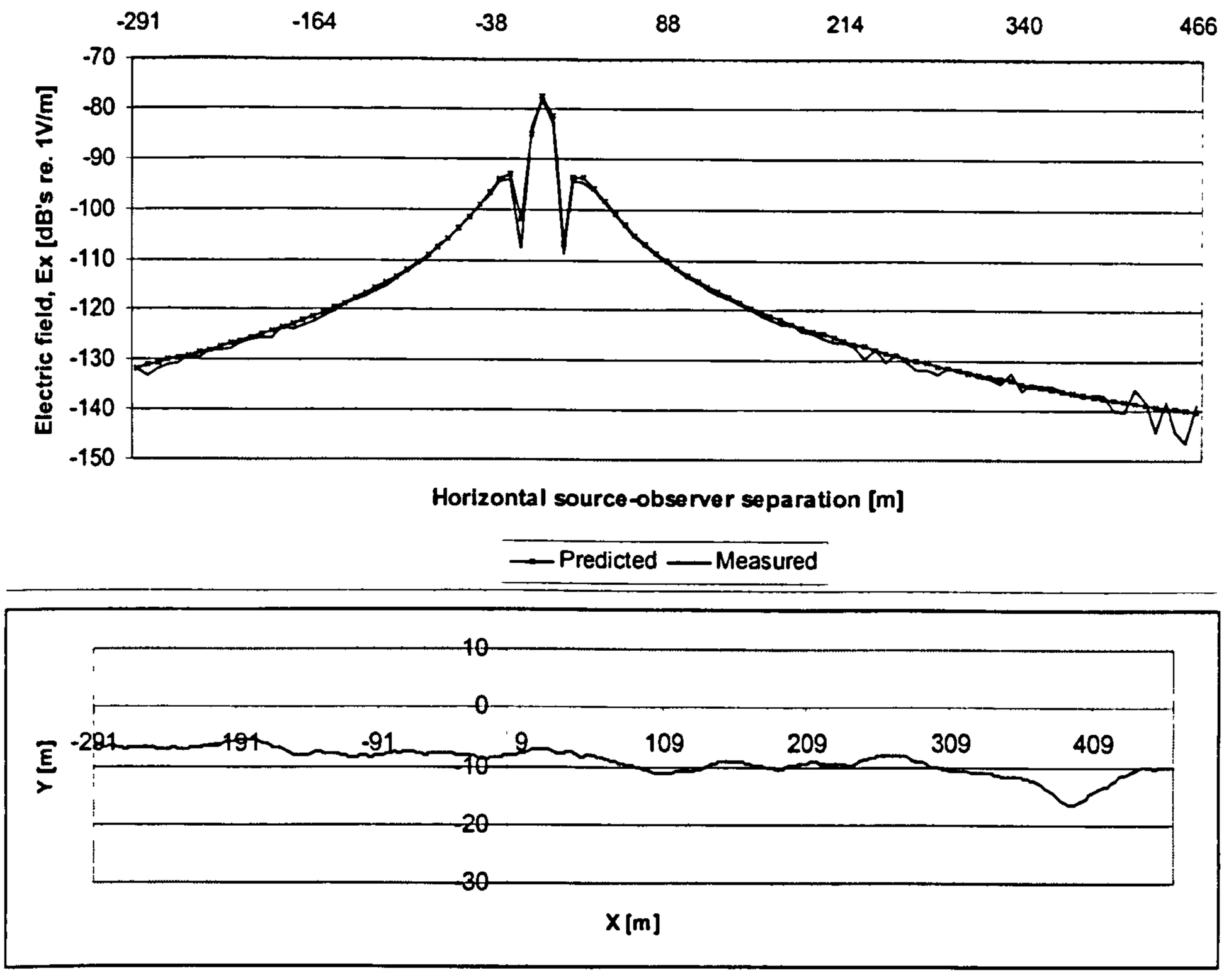

Figure 3.8: Run 11West; Field comparison (top), tracking (bottom)

	Start	CPA	Finish
Time	17:20:32	17:22:26	17:25:29

	Start	Increment	Finish
Distance	-290.454m	7.419m	466.255m

Average speed
2.547839m/s

Sea depth	Source depth	Sensor depth	Frequency
19.5m	1.0m	18.75m	2.75Hz

Sea conductivity	Seabed conductivity
3.4S/m	0.05S/m

Table 3.6: Parameters for run 11West

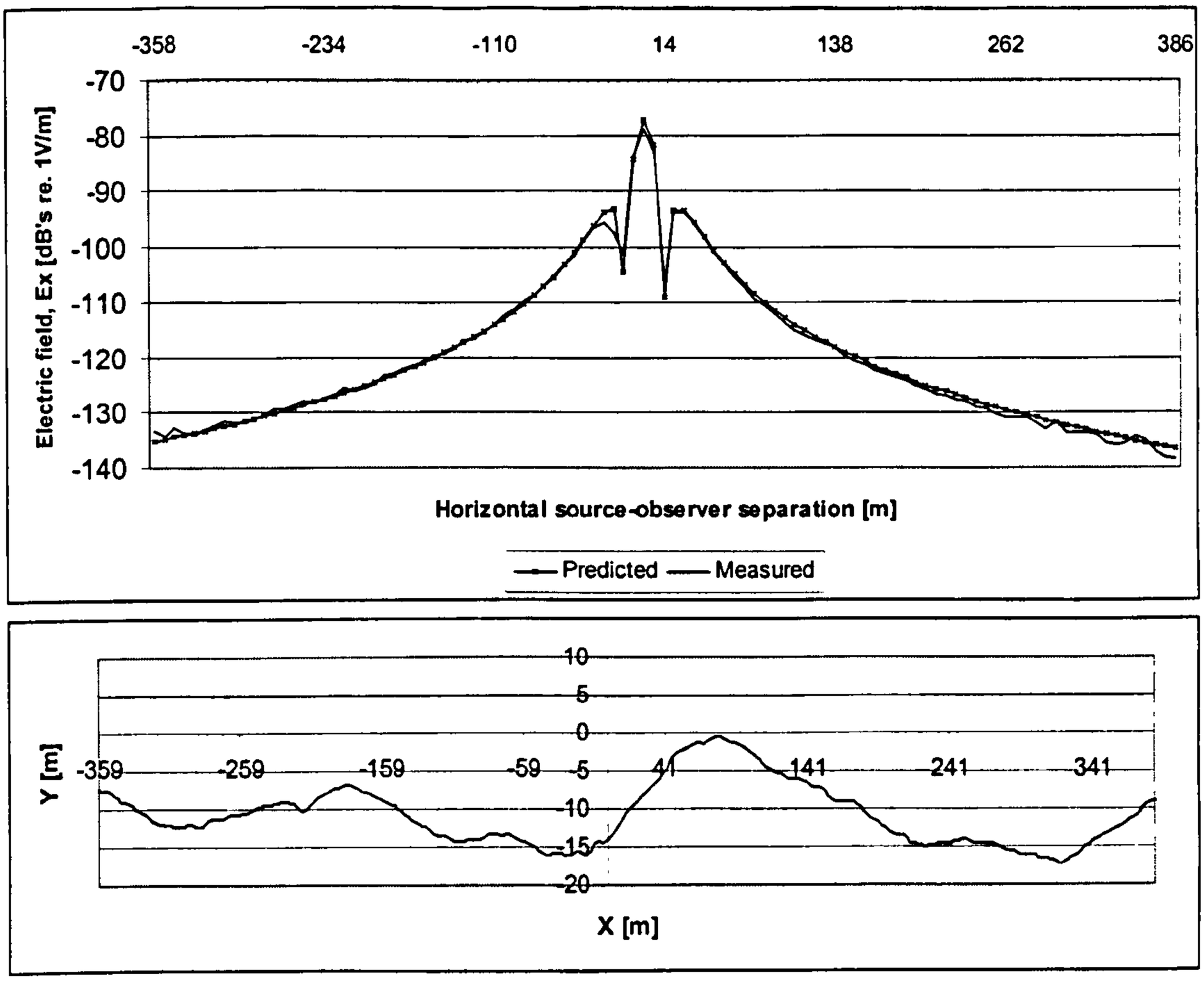

Figure 3.9: Run 12East; Field comparison (top), tracking (bottom)

	Start	CPA	Finish
Time	17:29:01	17:31:24	17:33:58

	Start	Increment	Finish
Distance	-358.351m	7.297m	385.916m

Average speed
2.50595m/s

Sea depth	Source depth	Sensor depth	Frequency
19.4m	1.0m	18.65m	2.0Hz

Sea conductivity	Seabed conductivity
3.4S/m	0.05S/m

Table 3.7: Parameters for run 12East

3.5 Conclusions

The validation of the KCL HED formulation implemented within the *LAYER* program was carried out using experimental data from a calibrated source. The shallow water trial was considered ideal for validating the field contributions from all the different propagation modes.

Most of the parameters required to carry out the experimental validation were measured at the start of the trial or were recorded continuously throughout the trial. The only parameter not measured was the seabed conductivity due to time and cost restrictions. A manual fitting procedure was used to determine the conductivity value that would allow the measured and predicted field values to be matched. This approach was considered valid because arbitrary sea or seabed conductivity values cannot make a propagation model give a 'correct' answer over a large range of source-observer separations. The different propagation modes use the conductivity information differently.

The sea and seabed conductivity values were estimated to be 3.4S/m and 0.05S/m, respectively. These conductivity values were considered optimum values for approximating Weymouth Bay with a 3-layer propagation model. In practice, the stratification of Weymouth Bay is likely to be far more complicated owing to the conductivity layers within both the sea and seabed layers.

The comparison between the predicted and measured field values showed that the KCL ELFE propagation model could accurately describe the behaviour of ELFE radiation over the entire source-observer range considered. The measured and predicted fields were in good[4] agreement with an average percentage-misfit error less than 1.0% (when the fields are expressed as dB's). This value was considered more than adequate to validate *LAYER* and demonstrate it could model all the propagation modes encountered in shallow water environments.

[4] The discrepancies between the measured and predicted fields at the nulls in the field distributions were attributed to inadequate sampling of the minima. These differences were significant in some cases, but sufficiently localised, thus not affecting the average percentage misfits.

Chapter 4

Boundary conditions

This Section illustrates the inherent complexity involved in solving the sloping seabed problem using analytical techniques by examining a simple deep-sea model (i.e. 2-layer). This is considered a useful exercise for understanding the problem at hand and a useful starting point to generate ideas for making further progress.

The difficulty of deriving an exact analytical solution for the sloping seabed problem is largely associated with the application of the boundary conditions across the media interfaces. This can be demonstrated by investigating the derivation of two solutions for the vertical electric dipole (VED) above a seabed. The derivation is carried out using the Hertz vector formulation detailed in Chapter 2 and experimentally validated in Chapter 3. The derivation for the VED will follow the same procedure to that used for the HED.

4.1 2-layer sloping seabed

The two cases examined are shown schematically in Figures 4.1. Case 1 corresponds to a horizontally plane-stratified environment, and Case 2 can be considered a sloping seabed environment.

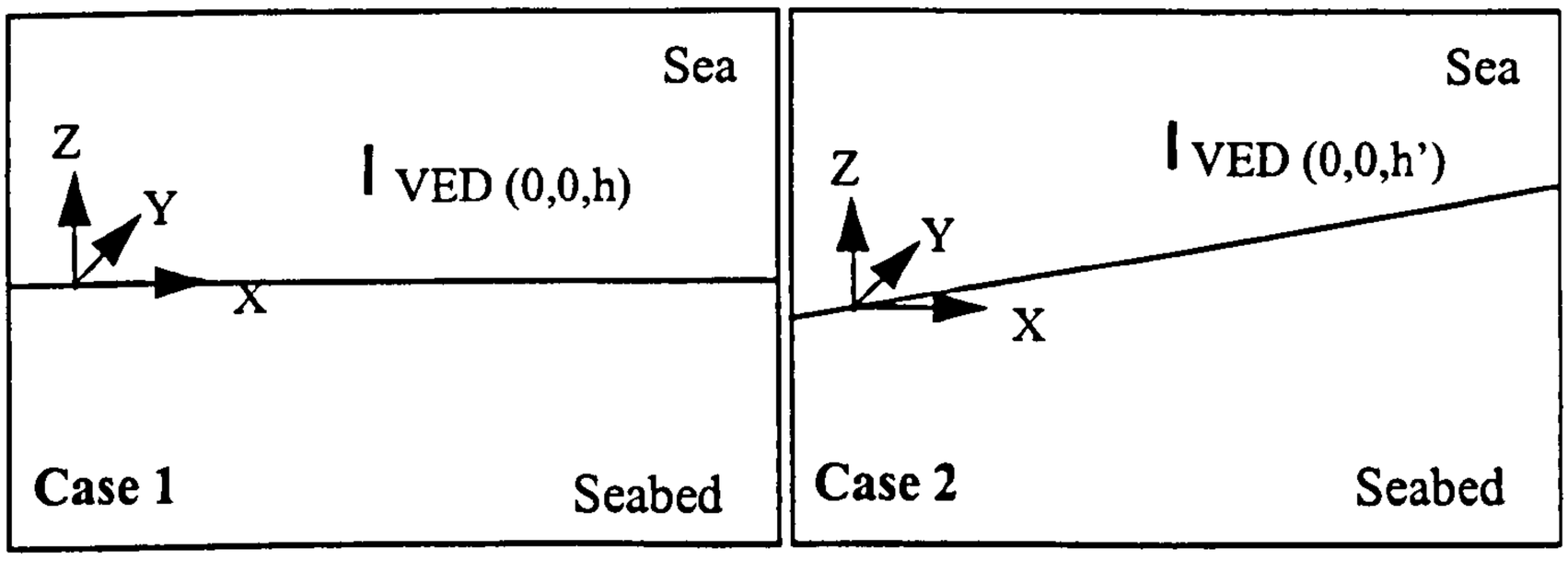

Figure 4.1: Horizontally plane-stratified (left) and sloping seabed (right) schematics

The boundary conditions resulting from the continuity of the tangential **E** and **H** field components across the interface can be deduced using

$$(\mathbf{E}_2 - \mathbf{E}_1)\times \hat{n} = 0 \tag{4.1}$$

and

$$(\mathbf{H}_2 - \mathbf{H}_1)\times \hat{n} = 0, \tag{4.2}$$

where the subscripts 1 and 2 refer to the sea and seabed layers, respectively.

For Case 1, the unit vector ($\hat{n}$) normal to the interface only has a *z*-component. Hence, the following boundary conditions need to be met:

$$E_{y_2} = E_{y_1} \tag{4.3}$$

and

$$E_{x_2} = E_{x_1}\,. \tag{4.4}$$

The Hertz vector only has a *z*-component for a VED directed in the positive z-direction i.e. $\Pi(0,0,\Pi_z)$, thus using Equations (4.5) and (4.6),

$$\mathbf{E} = k^2\Pi + \nabla\nabla\cdot\Pi \tag{4.5}$$

$$\mathbf{H} = \sigma^*\nabla\times\Pi \tag{4.6}$$

the boundary conditions can then be reduced to the continuity of $k^2\Pi_z$ and $\frac{\partial\Pi_z}{\partial z}$ across the sea-seabed interface. If the Hertz vector is postulated to be in the form

$$\Pi_{z_1} = \frac{Idl}{4\pi\sigma^*}\int_0^\infty\left(\frac{\lambda}{u_1}e^{-u_1|z-h|} + a_1e^{-u_1z}\right)J0(\rho\lambda)d\lambda \tag{4.7}$$

for the sea layer where the a_1 is a reflection coefficient, and in the form

$$\Pi_{z_2} = \frac{Idl}{4\pi\sigma^*}\int_0^\infty a_2 e^{u_2 z} J0(\rho\lambda)d\lambda \tag{4.8}$$

for the seabed layer where a_2 is a transmission coefficient. The application of the boundary conditions $k^2\Pi_z$ and $\frac{\partial \Pi_z}{\partial z}$ at z=0 will yield two equations which can be solved simultaneously to determine the two unknown coefficients, a_1 and a_2. This will lead to the exact formal solution to this problem.

For Case 2, the unit vector normal to the sea-seabed interface has both an x- and z-component, hence the following condition

$$E_{x_2} - E_{z_2}\tan\theta = E_{x_1} - E_{z_1}\tan\theta \tag{4.9}$$

must also be met in conjunction with Equation (4.3), where θ is the slope angle relative to the x-axis.

Assuming[1] the Hertz vector has both a x- and z-component, $\Pi(\Pi_x, 0, \Pi_z)$ for this new sloping geometry, Equations (4.5) and (4.6) gives rise to the following continuity requirements: - $\tan\theta \cdot k^2\Pi_z$, $\nabla\cdot\Pi$, $\frac{\partial}{\partial x}\nabla\cdot\Pi$, $\tan\theta\cdot\frac{\partial}{\partial z}\nabla\cdot\Pi$, $k^2\frac{\partial \Pi_z}{\partial x}$, $k^2\frac{\partial \Pi_x}{\partial z}$, $k^2\Pi_x\tan\theta$, $k^2\Pi_x$ and $k^2\Pi_z$ where $\nabla\cdot\Pi = \left(\frac{\partial \Pi_x}{\partial x} + \frac{\partial \Pi_z}{\partial z}\right)$.

The form of the Hertz vector is now substantially more difficult to postulate, but one possible form may be

$$\Pi_{x_1} = \frac{Idl}{4\pi\sigma^*}\sin\theta\int_0^\infty \left(b_1 e^{-u_1|z-h|} + b_2 e^{-u_1 z}\right)J0(\rho\lambda)d\lambda \tag{4.10}$$

[1] This is based on prior knowledge of the solution obtained using other means, see Section 5.2.

$$\Pi_{z_1} = \frac{Idl}{4\pi\sigma^*}\frac{\partial}{\partial x}\int_0^\infty\left(\frac{\lambda}{u_1}e^{-u_1|z-h|}\left(b_3\cos\theta + b_4\sin\theta\right) + \left(b_5\cos\theta + b_6\sin\theta\right)e^{-u_1 z}\right)J0(\rho\lambda)d\lambda \tag{4.11}$$

in the upper sea layer and

$$\Pi_{x_2} = \frac{Idl}{4\pi\sigma^*}\sin\theta\int_0^\infty b_7 e^{u_2 z}J0(\rho\lambda)d\lambda \tag{4.12}$$

$$\Pi_{z_2} = \frac{Idl}{4\pi\sigma^*}\frac{\partial}{\partial x}\int_0^\infty\left(b_8\sin\theta + b_9\cos\theta\right)e^{u_2 z}J0(\rho\lambda)d\lambda \tag{4.13}$$

in the lower seabed layer. It is worth noting that this postulated form will collapse to the form given by Equations (4.7) and (4.8) when θ tends to zero, as expected.

The application of the boundary conditions is now at $z(x)=x\tan\theta$ if the co-ordinate system is centred at the interface, directly below the source. This will result in nine equations with nine unknowns, which should be solvable in theory, albeit extremely laboriously. In fact, the complexity of the resulting simultaneous equations is usually sufficient justification for seeking alternative means of solving this problem. This extra complexity simply arises from the mixed and second order derivatives in the continuity boundary conditions. In addition, the fact that the exponents (containing the sea depth) in the equations are now a function of x greatly complicates matters, thus making the application of the x-derivatives very cumbersome.

4.2 3-layer sloping seabed

Although the 2-layer problem is solvable, it does highlight the difficulty in solving problems where the co-ordinate system is not ideal for the application of the boundary conditions. This suggests that the 3-layer sloping seabed model will be significantly more difficult to solve. The complexity of the simultaneous equations for the 3-layer case may provide an unsurpassable barrier to the search for a solution. However, there are other problem areas to consider before a set of equations can be formulated. These include: -

i) The form in which to postulate the Hertz vector is largely based on guesswork. Ideally, the form is chosen such that the number of unknowns and the number of equations (after the application of the boundary conditions) match, thus making it theoretically possible to obtain a closed form solution.

ii) There is also the problem of what happens when the interfaces meet if a coastline model is developed.

In summary, the sloping seabed problem for the 3-layer case is extremely difficult 'if not impossible' to solve exactly using analytical techniques, due to the reasons mentioned above. Hence, most authors have opted for alternative methods that are predominantly based on numerical techniques.

4.3 Discussion

This investigation has shown how a relatively simply problem can become virtually intractable if the co-ordinate system is not suitable for applying the boundary conditions.

This type of problem is widespread in physics and has a simple solution that is applicable in some circumstances. To put it simply, use a more suitable co-ordinate system. For Case 2, a rotated Cartesian co-ordinate system with the x-axis parallel to the sea-seabed interface and the z-axis perpendicular to the sea-seabed interface would be ideal. The source could then be resolved into components parallel and perpendicular to the sea-seabed interface and solved using the same approach adopted for Case 1.

Unfortunately, there is no way of selecting a useful co-ordinate system that will be convenient for both the air-sea and sea-seabed interfaces in a 3-layer sloping seabed model. The only option would be to address each of the interfaces separately using a different co-ordinate system and adding the solutions together. This would shift the problem from the application of the boundary conditions to the modelling of the interactions between the interfaces. The latter option is deemed more feasible,

provided the interfaces have a constant gradient, hence, this thesis will attempt to explore this possibility for obtaining an analytical solution.

For more complex seabed profiles, a numerical approach will be employed. Co-ordinate transformations will also be investigated to reduce problems of applying boundary conditions across the interfaces.

It is worth noting that a commercial finite-element method (FEM) was investigated as a possible tool for analysing ELFE propagation in complex environments; before deciding to develop a new model from scratch. However, the FEM package investigated was unable to model alternating electric dipoles in seawater. The results produced to date have only examined static sources.

A summary of this work is included in Appendix A for completeness. The static result presented should give a useful insight into the propagation characteristics for ELFE radiation when approaching the DC limit (i.e. 1Hz and below).

Chapter 5

Analytical sloping seabed model

Sloping seabed models are essential for examining ELFE propagation in littoral environments where the geometry of the seabed is not horizontally plane-stratified. The propagation characteristic of the electromagnetic fields in this type of environment has not been quantified for a 3-dimensional problem space and need investigating, especially for critical applications such as mine threat analysis for naval vessels. Mine threat analysis requires the field distribution to be mapped over a plane underneath the platform. Existing 2-dimensional models only consider infinite line sources with the results predicted in the vertical plane parallel to the platform's keel line.

Chapters 5 and 6 detail the development of two different approaches for addressing this problem. A numerical model based on the finite-difference time-domain (FDTD) method (see Chapter 6) and an approximate analytical model that uses a new imaging technique in this chapter. Two different approaches were considered essential to provide some means of cross-validating the models using independent techniques; thus gaining confidence in the results. The models are also developed to address complementary environmental geometries, thus improving the computational efficiency of each model in their region of applicability.

5.1 Introduction

Chapter 4 showed that analytical sloping seabed models are extremely difficult to formulate owing to the problems encountered applying the boundary conditions. The review in Section 1.10 reinforced this view by showing that only one model exploited analytical methods. However, this model required the resulting integrals to be evaluated using iterative techniques (Schlak *et al.*, 1967).

This chapter details the development of an exact 2-layer formulation that can be exploited for applications in deep waters and an approximate 3-layer formulation for shallow waters. The approximate 3-layer model exploits a new 'imaging' technique specially developed for the sloping seabed problem, thus resulting in a fully analytical method, (albeit approximate in nature).

Both the analytical models developed assume the seabed has a constant gradient slope with no additional features. This reduces the generality of the models compared to the FDTD model developed in Chapter 6, but is compensated for by a large increase in computational efficiency. This efficiency is critical for potential future applications such as source modelling where thousands of field predictions are required in a few seconds.

5.2 Exact 2-Layer sloping seabed model

A 2-layer sloping seabed model has been developed as the starting point for the 3-layer model. This model is considered useful for investigating the propagation characteristics of ELFE radiation in 'deep' waters, where the air-sea boundary is sufficiently far from the region of interest. In ELFE applications, deep or shallow waters can be defined relative to the electrical skin depth (see Section 1.5.2). Waters are considered to be deep if the air-sea and sea-seabed interfaces are about five skin[1] depths (δ) apart.

Chapter 4 showed that it is extremely difficult to solve the 2-layer sloping seabed problem if a standard Cartesian co-ordinate system is used, due to the problems applying the boundary conditions across the sea-seabed interface, see Figure 5.1 (left). However, the problem can be relatively straight forward to solve if the Cartesian co-ordinate system is rotated such that the vertical axis is normal to the sea-seabed interface as shown in Figure 5.1 (right).

[1] 200m of water can be considered deep at power frequencies (i.e. 50Hz).

This problem can be solved using a horizontally plane-stratified 2-layer propagation model, if the source is resolved into components parallel and perpendicular to the sea-seabed interface. This will result in a solution composed of both horizontal (HED′) and vertical (VED′) electric dipoles. The primes indicate they are the solution in the new transformed co-ordinate system.

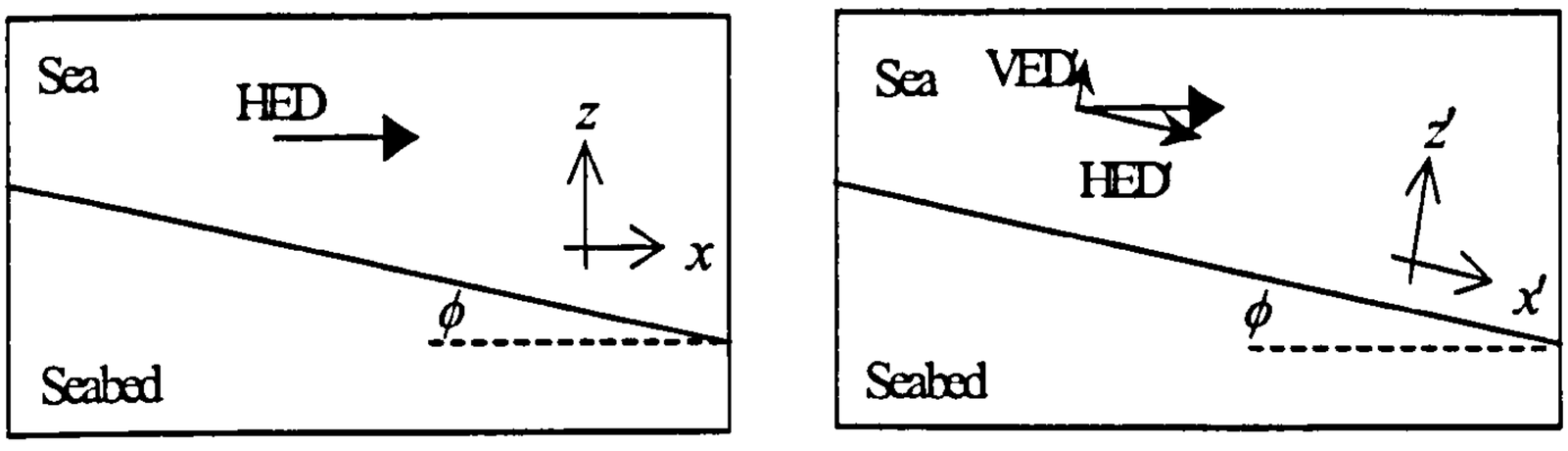

Figure 5.1: 2-layer sloping seabed problem

Surprisingly, this simple approach to solving the problem has given a deep insight into the form of the solution that was previously unknown. The solution for either a HED or VED above a sloping seabed is composed of both HED′ and VED′ source terms.

Both types of sources behave differently when in a stratified medium and will therefore produce a field distribution that is significantly more complicated than the individual dipoles alone. The solution for HED and VED sources in a 2-layer horizontally stratified medium is readily derivable and well documented by several authors e.g. Kraichman (1970). It can also be derived from the formulation presented in Chapter 2[2], by letting the sea depth (d) tend to infinity.

When implementing this model, it is important to ensure all the relevant parameters are transformed into the new rotated co-ordinate system for the purpose of the calculations. This transformation can be achieved using a matrix operator in the following form

$$\begin{pmatrix} x' \\ z' \end{pmatrix} = \begin{pmatrix} \cos\phi & \sin\phi \\ -\sin\phi & \cos\phi \end{pmatrix} \begin{pmatrix} x \\ z \end{pmatrix}. \tag{5.1}$$

[2] It is worth noting that the formulation in Chapter 2 assumed the vertical axis is positive down, hence some care must be exercise if using this formulation.

This gives the new x' and z' co-ordinates after the Cartesian co-ordinate system has been rotated by an angle ϕ, (i.e. the seabed's slope angle).

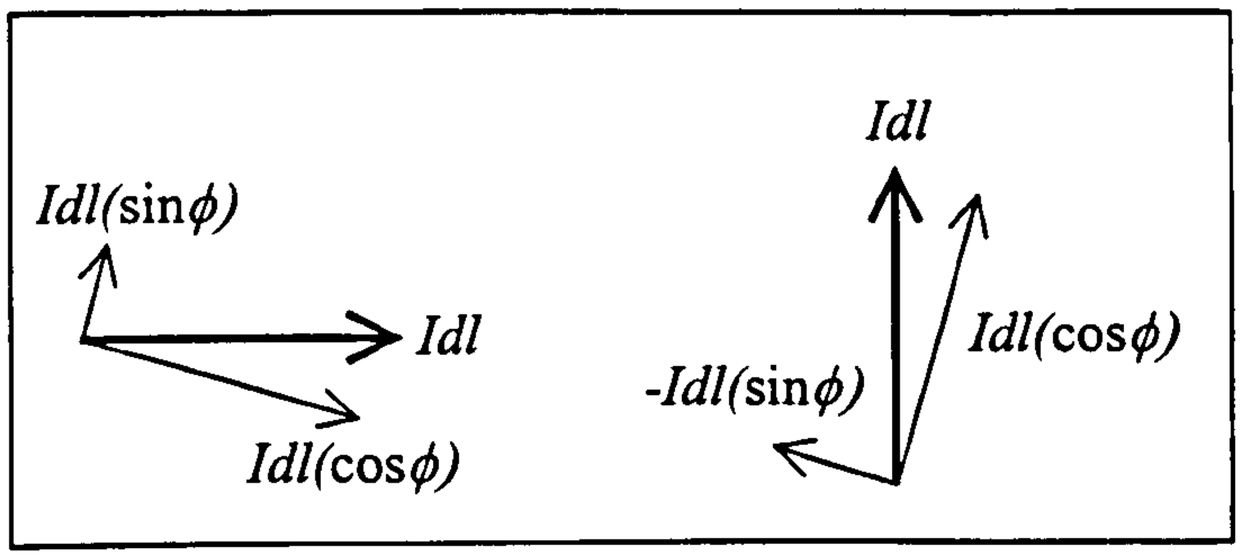

Figure 5.2: Resolved source components

The solution to the 2-layer sloping seabed problem is thus simply composed of combinations of the solution for a HED′ and a VED′ source with the appropriate source strengths that are functions of the slope angle, see Figure 5.2. If H and V are used to denote the solution from a HED′ and VED′ within the new rotated co-ordinate system (i.e. x',y and z') and F denotes any field component. Equation (5.2) gives the field values for a HED above a sloping seabed (denoted by the superscript S_H) with a slope angle ϕ.

$$F^{S_H}(x',y,z') = (\cos\phi)F^{H}(x',y,z') + (\sin\phi)F^{V}(x',y,z') \tag{5.2}$$

Similarly, Equation (5.3) gives the field values for a VED above a sloping seabed (denoted by the superscript S_V) with a slope angle ϕ.

$$F^{S_V}(x',y,z') = (\cos\phi)F^{V}(x',y,z') - (\sin\phi)F^{H}(x',y,z') \tag{5.3}$$

The solution given by Equations (5.2) and (5.3) can be transformed backed into the original co-ordinate system (x,y,z) using the following Equations for S_H. The same equations can also be used for S_V.

$$F_x^{SH}(x,y,z) = F_x^{SH}(x',y,z')\cos(\phi) + F_z^{SH}(x',y,z')\sin(\phi) \tag{5.4}$$

$$F_y^{SH}(x,y,z) = F_y^{SH}(x',y,z') \tag{5.5}$$

$$F_z^{SH}(x,y,z) = F_z^{SH}(x',y,z')\cos(\phi) - F_x^{SH}(x',y,z')\sin(\phi) \tag{5.6}$$

The same approach is also valid for alternating magnetic sources, thus resulting in a solution composed of both horizontal (HMD′) and vertical (VMD′) magnetic dipoles.

5.3 Approximate 3-layer sloping seabed model (wedge geometry)

This section of the report details the development of a 3-layer model for littoral waters where both the influences of the air-sea and sea-seabed interfaces must be accounted for. This is the first analytical sloping seabed model for addressing applications where both the source and observer are located in the sea layer.

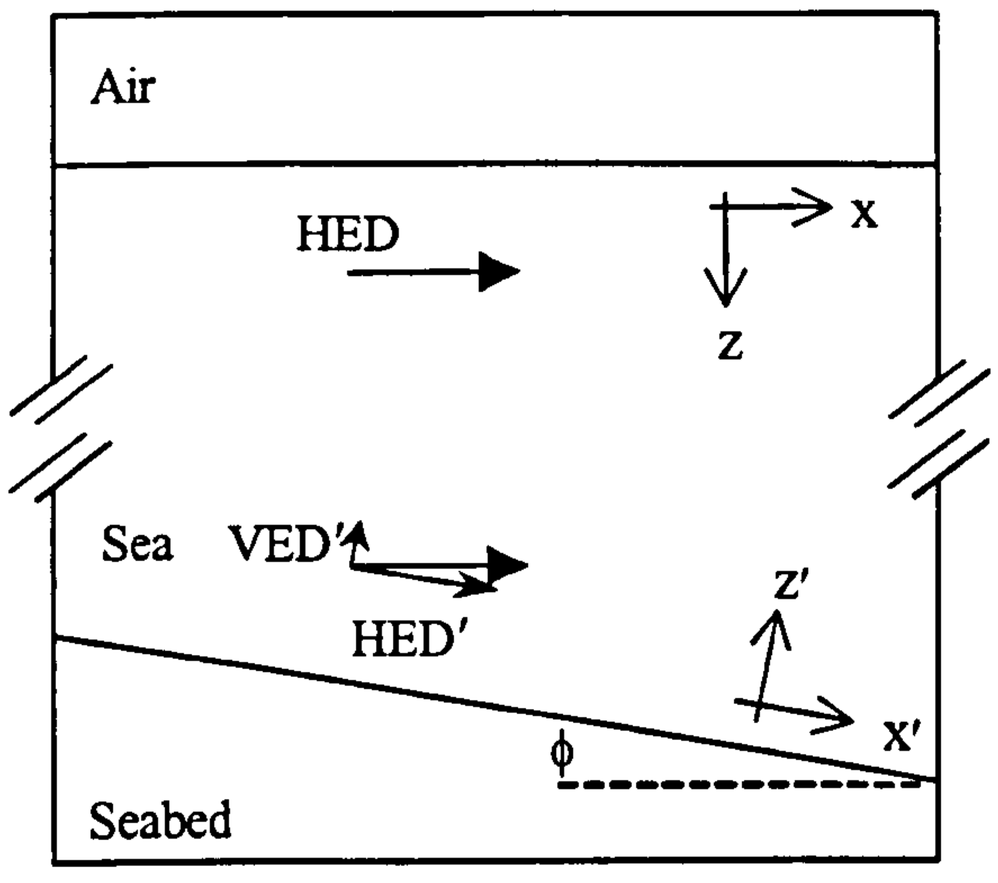

Figure 5.3: Schematic representation of approximate 3-layer model

The 3-layer model is formulated using the 2-layer sloping seabed model presented in Section 5.2 with a superimposed 2-layer model to account for the source's interaction with the air-sea interface, see Figure 5.3. The addition of the second model will ensure that the propagation of the up-down lateral wave via the air-sea interface, and the primary reflections off the air-sea interface are both included within the overall solution. There is no minimum or maximum depth for this method to work, provided the air-sea and sea-seabed interfaces do not intersect each other. This model thus works by calculating the solution using a 2-layer model for the air-sea interface (i.e.

assume there is no seabed layer) and adding this to the solution obtained using the 2-layer sea-seabed model (i.e. assume there is no air layer). In fact, the direct wave solution of the second model must be subtracted to ensure that this mode is only included once within the calculations. The relative positions of the interfaces and all the source and observer points must be maintained during these calculations.

This 'modular' approach to the 3-layer problem takes account of all the different propagation modes, except those associated with the interaction of the two interfaces with each other. The two approximations in the model are thus: -

- The exclusion of the secondary reflections (i.e. the reflections that take place off both the air-sea and sea-seabed interfaces);
- Lateral wave interactions that involve reflections (e.g. the up-down lateral wave reflecting off the sea-seabed interface before reaching the observer).

The interaction of the interfaces can be quantified by comparing the solution for the horizontally plane stratified problem solved using this modular approach and the full solution of the exact field equations obtained using *NLAYER*, see Figures 5.4 to 5.7.

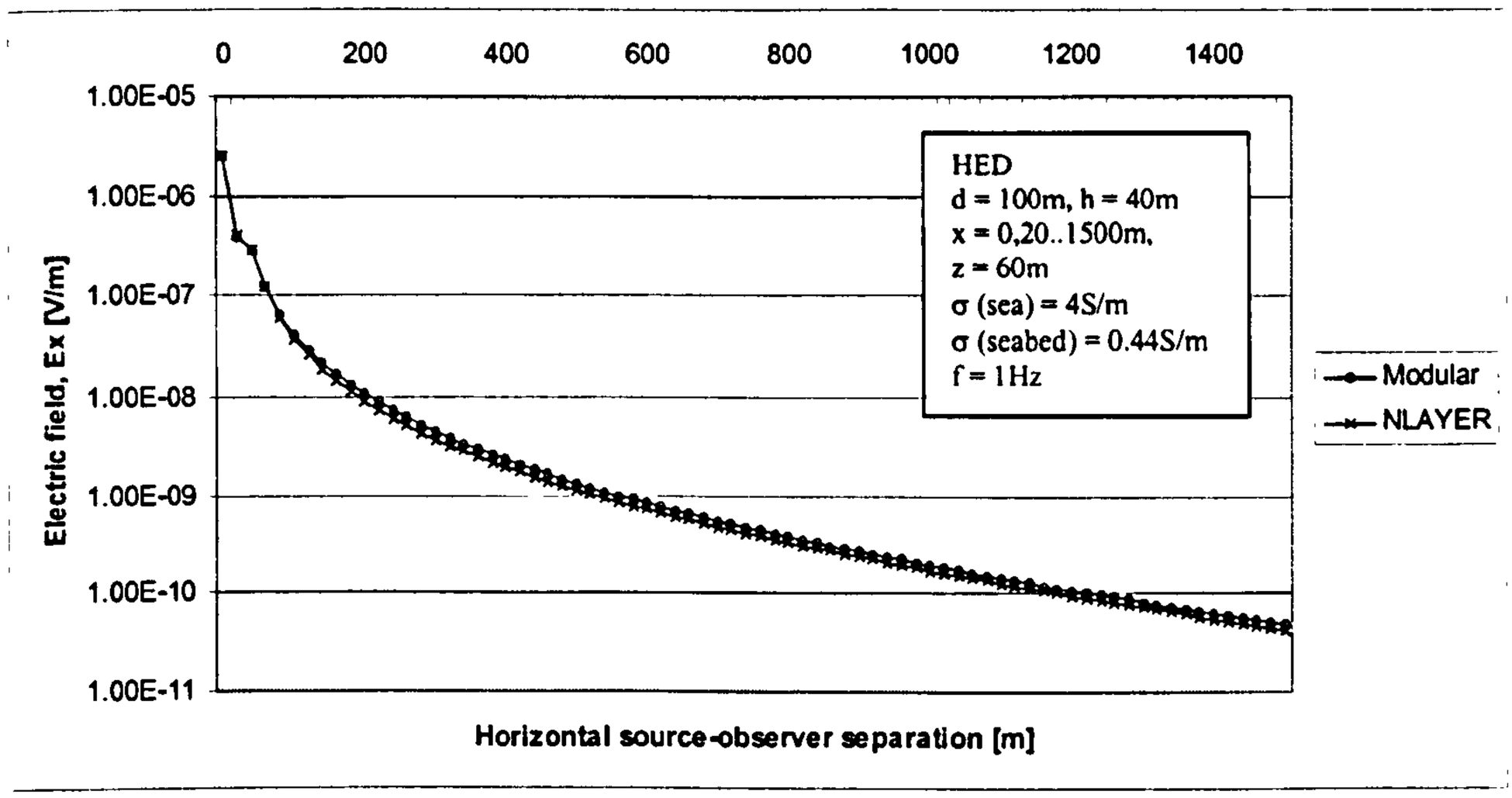

Figure 5.4: Comparison between *NLAYER* and modular solution for HED at 1Hz

Figure 5.4 shows that the low frequency (i.e. 1Hz) modular field predictions are greater than the exact solution. This can be attributed to the lack of interference

effects from the interface interactions. The mismatch between the two field predictions is 21% at 250m due to the exclusion of secondary reflections. The mismatch falls to 16% at 1500m from the source. This far-field difference is due to the omission of additional lateral wave contributions from reflected radiation.

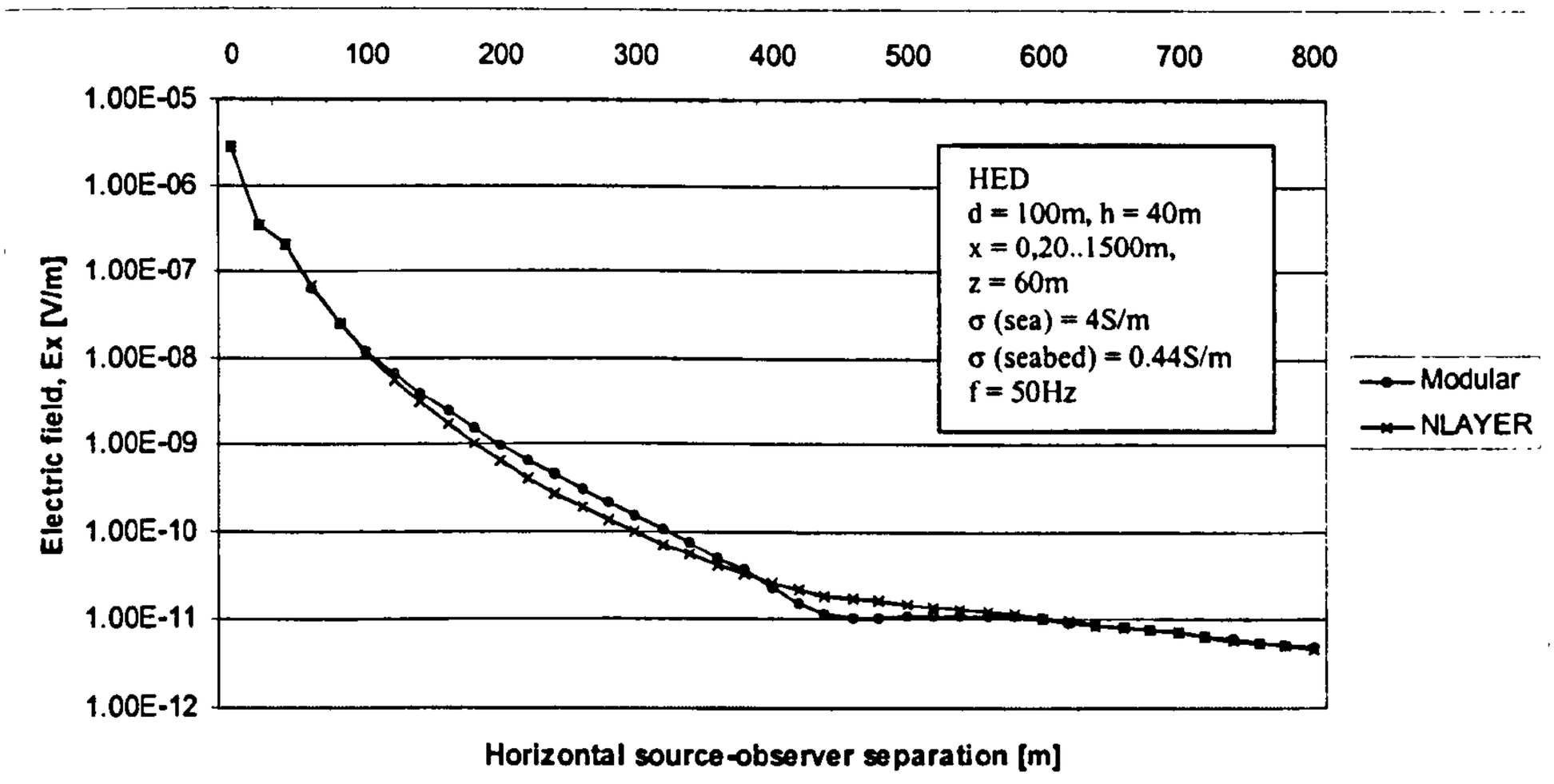

Figure 5.5: Comparison between *NLAYER* and modular solution for HED at 50Hz

Figure 5.5 shows a similar result obtained at 50Hz. The key difference is that there is a crossover point, after which the modular solution is smaller than the exact solution. The mismatch between the field predictions ranges from 60% at 250m to 4% at 800m. These near to medium range differences are attributed to the omission of secondary reflections[3] and multiple reflections of lateral waves[4]. The low far-field mismatch indicates that the contribution from additional lateral waves is small.

Figure 5.6 shows a similar comparison for 100Hz. The mismatch between the field predictions ranges from 60% at 200m to 3% at 500m and is attributed to the omission of secondary reflections and multiple reflections of lateral waves, respectively.

[3] This can be inferred because the differences occur in the region were the fields are falling exponentially.
[4] This can be inferred because the differences occur just as the $1/R^3$ spreading losses associated with lateral waves start to dominate.

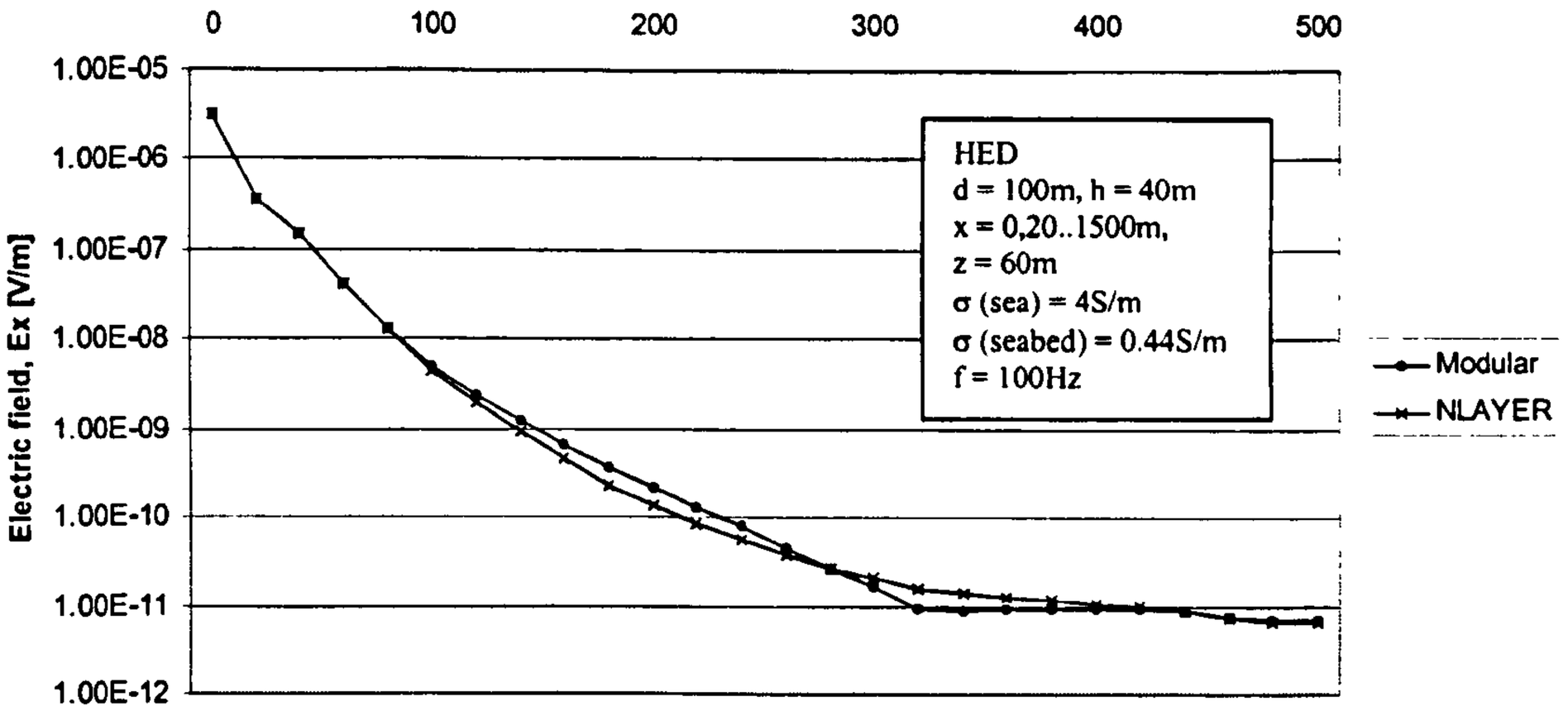

Figure 5.6: Comparison between *NLAYER* and modular solution for HED at 100Hz

Figure 5.7 also corresponds to 100Hz, but the sea depth has been increased from 100m to 300m. The field predictions are now virtually identical since the interface interactions are negligible for this particular configuration.

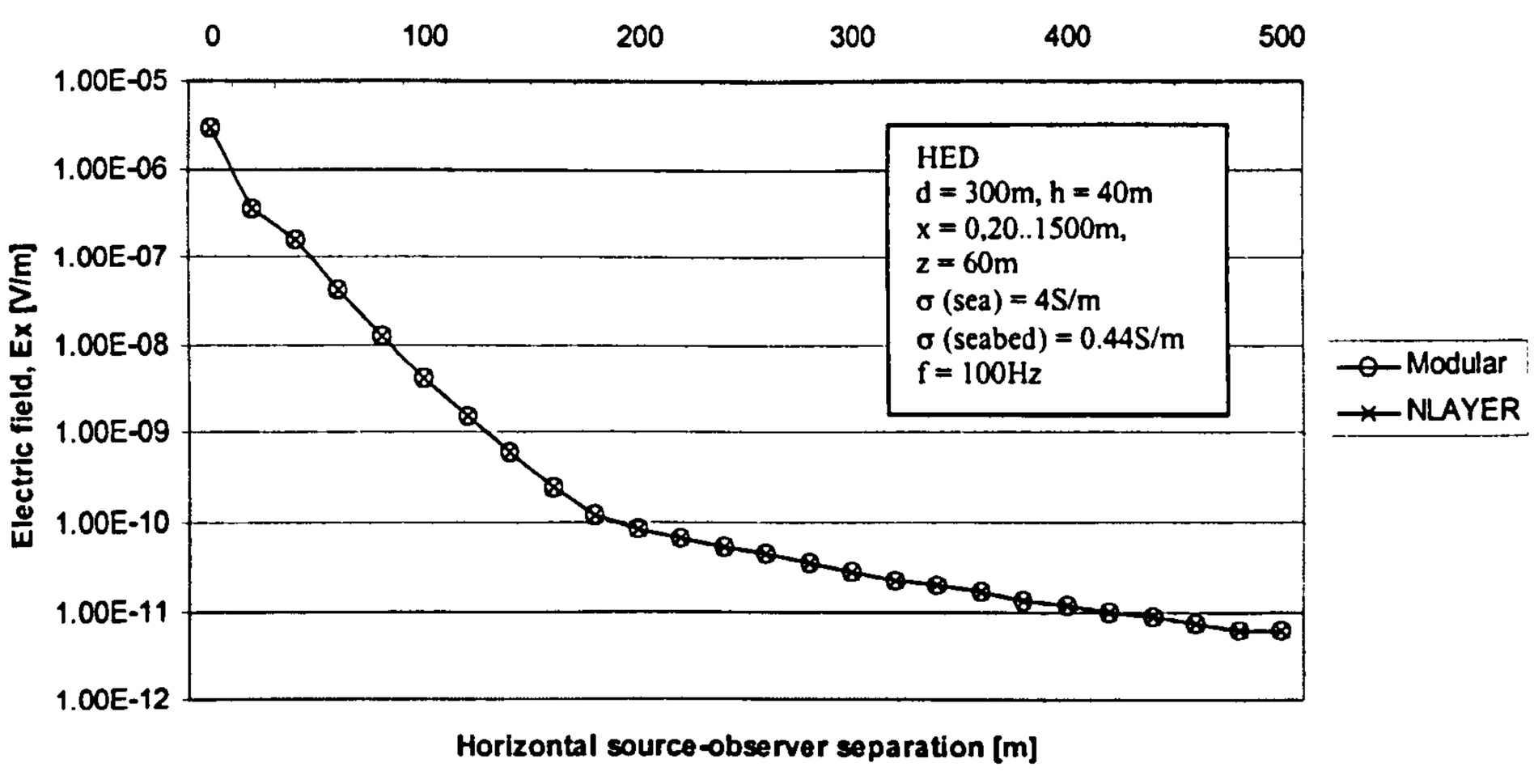

Figure 5.7: Deep-water comparison between *NLAYER* and modular solution for HED

For most practical applications and typical operating frequencies, this model will produce reasonably accurate results. For very shallow water application between 30m to 200m and low frequencies, the approximations become an issue and need to be corrected or compensated for in some way.

5.4 Secondary reflections - approximate correction factor

In order to increase the accuracy of this model, a method of including the contributions from the secondary reflections was formulated. This section details the techniques developed using a 'geometrical-optical' approach to the problem. This correction factor only needs to be applied for shallow waters and for low frequency problems i.e. seas that are electrically shallow ($d<5\delta$).

The secondary reflections are modelled using a 'geometrical-optical' approximation (Wait, 1996). The geometrical-optical approximation in this context refers to modelling the secondary reflections by taking into account the attenuation and phase change of the radiation over the geometrical path travelled. The interaction between the radiation and the interfaces is also approximated using plane wave theory (i.e. Fresnel reflection coefficients).

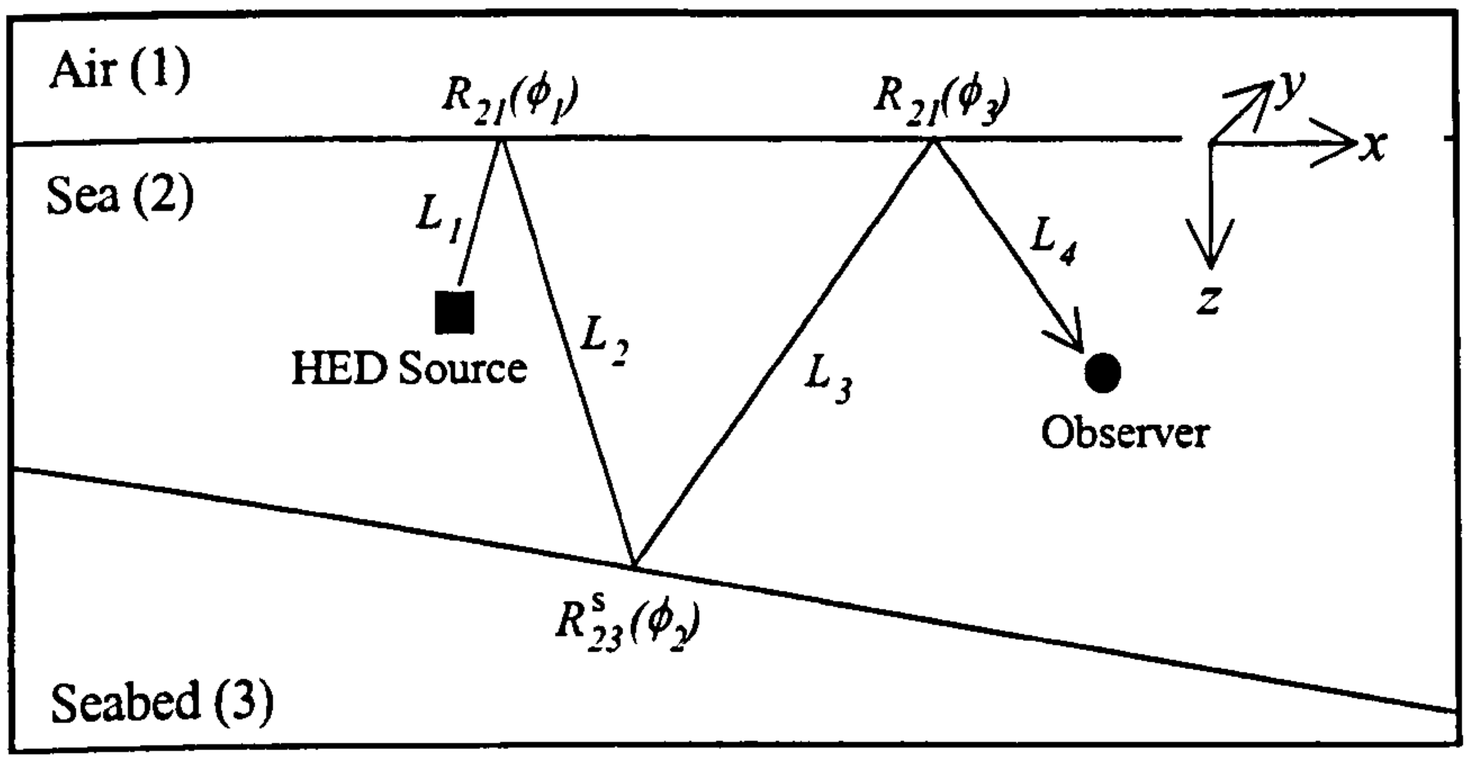

Figure 5.8: Modelling secondary reflections

This approach can be illustrated using the secondary reflection depicted in Figure 5.8. The longitudinal (x-direction) electric field from a HED is calculated at the observer using

$$E_x = E_0 R_{21}(\phi_1) R^s_{23}(\phi_2) R_{21}(\phi_3) \tag{5.7}$$

where E_0 is the infinite medium solution given by $E_0 = \left(\frac{\partial^2}{\partial x^2} . \Pi_x + k^2 \Pi_x \right)$ with

$\Pi_x = \frac{Idl}{4\pi\sigma^*} \frac{e^{-ikR}}{R}$, R is the path length given by $R = L_1 + L_2 + L_3 + L_4$, $R_{21}(\phi_1)$, $R_{23}^s(\phi_2)$ and $R_{21}(\phi_3)$ are Fresnel reflection coefficients and ϕ_1, ϕ_2 and ϕ_3 are the angles of incidence for each path of the secondary reflection.

The exact form of the reflection coefficients will depend on the polarisation of the field component being evaluated. The Fresnel reflection coefficients for transverse electric (TE) and transverse magnetic (TM) fields are

$$R_{21}(\phi) = \frac{k_2 \cos\phi - \left(k_1^2 - k_2^2 \sin^2\phi\right)^{\frac{1}{2}}}{k_2 \cos\phi + \left(k_1^2 - k_2^2 \sin^2\phi\right)^{\frac{1}{2}}} \tag{5.8}$$

and

$$R_{21}^{||}(\phi) = \frac{k_1^2 \cos\phi - ik_2 \left(k_1^2 - k_2^2 \sin^2\phi\right)^{\frac{1}{2}}}{k_1^2 \cos\phi + ik_2 \left(k_1^2 - k_2^2 \sin^2\phi\right)^{\frac{1}{2}}} \tag{5.9}$$

respectively, for reflections off the air-sea interface. These expressions can be easily derived using Equations (2.36) and (2.43) and making use of Snell's Law of refraction (i.e. $k_1 \sin\phi_1 = k_2 \sin\phi_2$) and the relationship $\lambda = k_1 \sin\phi_1$ (Wait, 1996).

The reflection coefficient for the sea-seabed interface requires special treatment owing to the rotated co-ordinate system used. The rotated co-ordinate system means that radiation with either a TE or TM polarisation relative to the air-sea interface will appear to have both a TE and TM polarisation in the sea-seabed's frame of reference. The reflection coefficient for the sea-seabed interface is thus dependent on the slope angle of the seabed, see Equations (5.10) and (5.11). The incidence angle (ϕ) is also transformed into the sloping seabed's frame of reference, since the Fresnel coefficients (or more precisely, Maxwell's equations) demand that the angle of

incidence is equal to the angle of reflection. The TE and TM reflection coefficients are denoted by $R_{23}^{s}(\phi)$ and $R_{23}^{s\|}(\phi)$ respectively for the sea-seabed interface.

$$R_{23}^{s}(\phi) = R_{23}(\phi + \phi_s)\cos(\phi_s) - R_{23}^{\|}(\phi + \phi_s)\sin(\phi_s) \tag{5.10}$$

$$R_{23}^{s\|}(\phi) = R_{23}^{\|}(\phi + \phi_s)\cos(\phi_s) + R_{23}(\phi + \phi_s)\sin(\phi_s) \tag{5.11}$$

5.5 Imaging technique

One of the problems associated with using geometrical-optical techniques is that all the propagation paths must be found in order to determine the geometrical path lengths and the angles of incidence with the interfaces. Although this can be done analytically using the geometry of the source, the observer and the interfaces, this can be very time consuming if all the modes are to be found. This study has therefore relied on developing a new 'imaging' technique to identify all the secondary reflections for a sloping seabed environment.

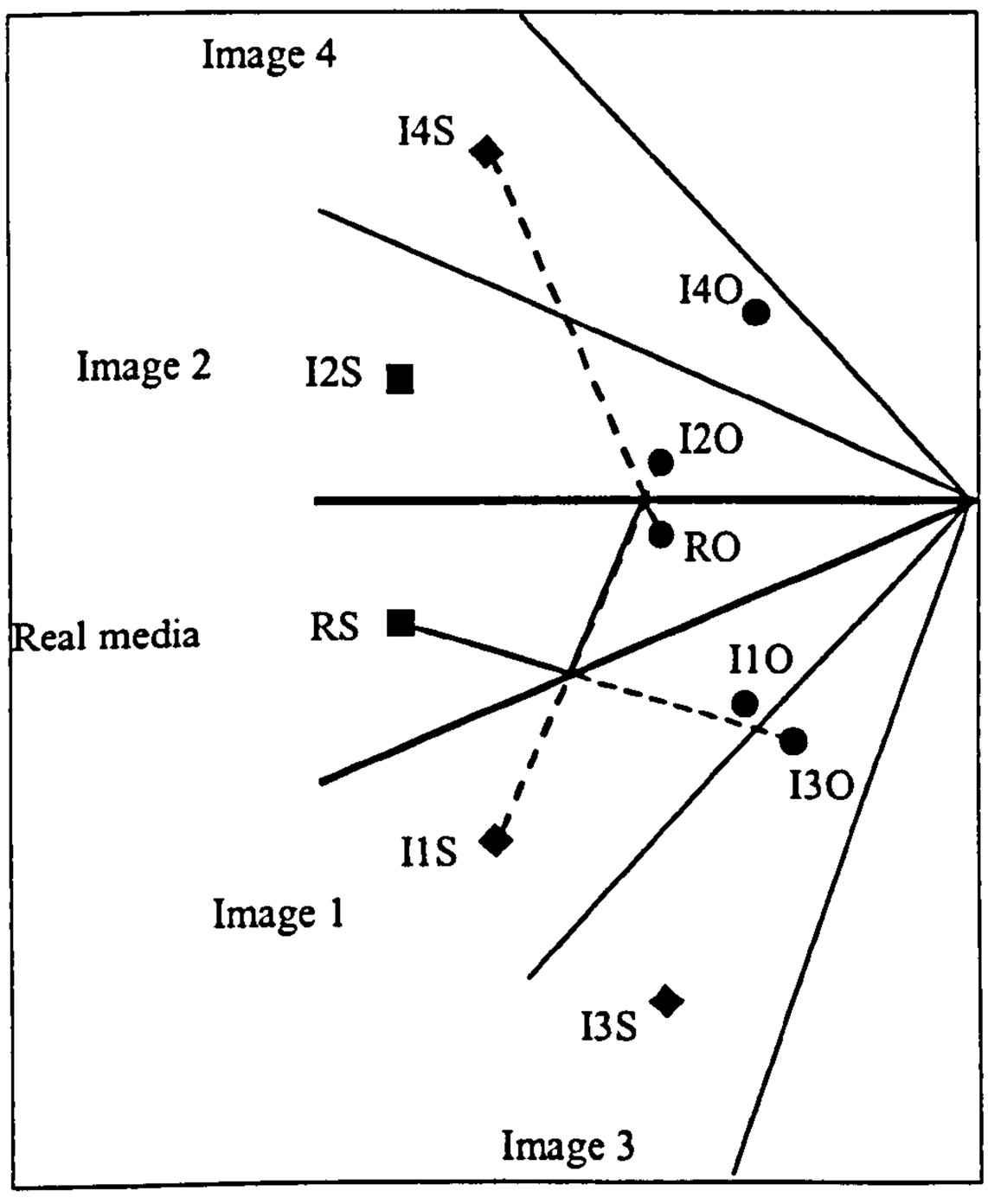

Figure 5.9: Imaging technique for secondary reflections

Figure 5.9 shows how images are generated for a given sloping seabed configuration. The images are generated by 'mirroring' the wedge geometry about the interfaces. The geometrical path length for the reflections is given by the image-source to real-observer separation. It can also be seen that if a line is drawn between the image-source and the real-observer, this can be used to determine the final angle at which the radiation reaches the observer. The final angle of incidence can be used to deduce all the previous angles of incidence on each of the interfaces. This is possible because the seabed has a known influence on the angle (i.e. $\phi_r = \phi_i \pm 2\phi_s$).

For example, given that RO and RS denote the real-observer and real-source. I1O, I2O, I1S, I2S denote the 1st image-observer, 2nd image-observer, 1st image-source and the 2nd image-source, respectively, and so on. The distance between I2S and RO gives the path length for the primary reflection off the air-sea interface. The distance between I4S and RO gives the path-length for the 1st secondary reflection. The angle between the line I4S-RO and the vertical axis (i.e. the normal to the air-sea interface) can also be used to deduce all the angles of incidence. The propagation path can also be generated by drawing construction lines between I4S-RO, I1S-I2O and RS-I3O and by tracing over the construction lines connecting RO and RS, whilst remaining in the real environment.

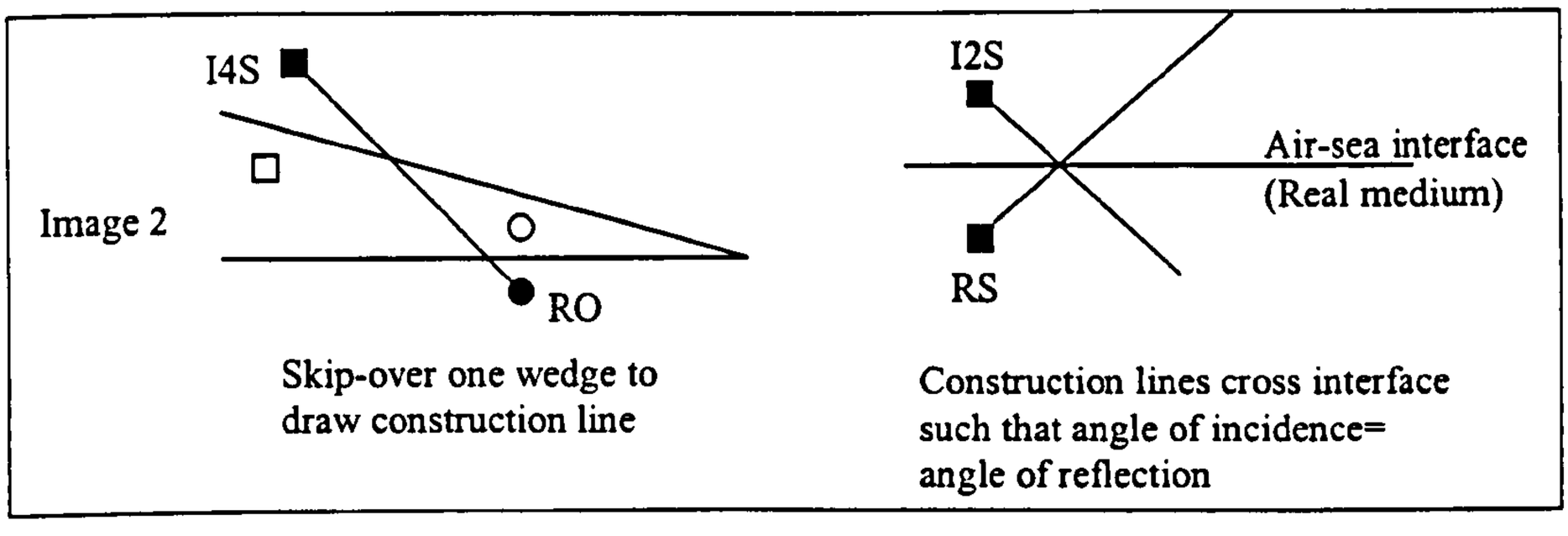

Figure 5.10: Procedure for drawing construction lines

The procedure for drawing the construction lines follows two simple rules, see Figure 5.10. Firstly, all the construction lines for each secondary reflection 'skip-over' the same number of 'wedges' when connecting source and observer points (e.g. all the construction lines for the 1st secondary reflection in Figure 5.9 skip-over one wedge. All the construction lines for the 2nd secondary reflection will skip-over two wedges).

Secondly, all the construction lines cross the air-sea and sea-seabed interfaces of the real environment such that the angle of incidence equal the angle of reflection in the reference frame of the interface. A simplified version of Figure 5.9 is presented below to highlight this procedure.

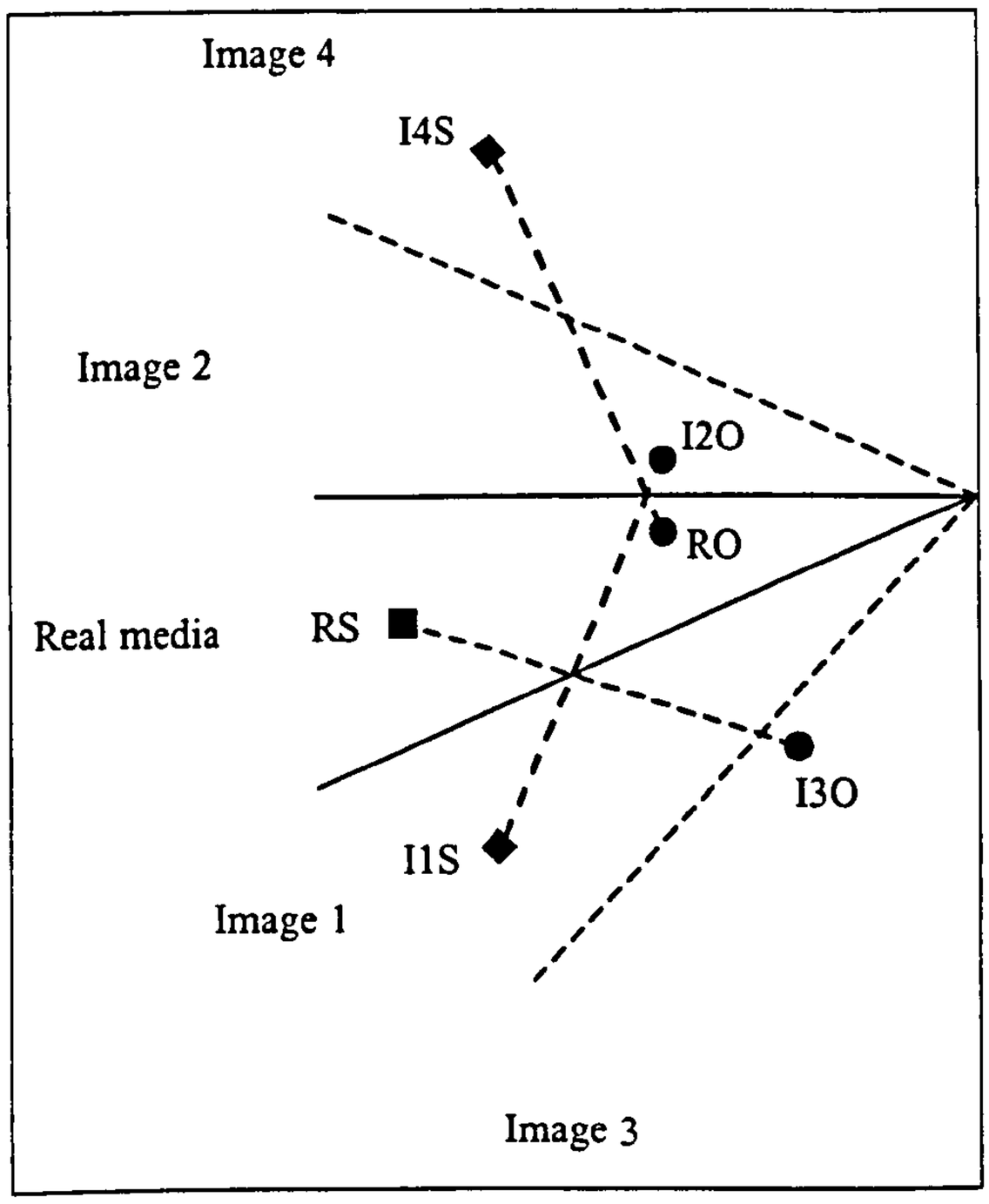

Figure 5.11: Simplified representation of imaging technique for secondary reflections

The image-source and image-observer co-ordinates can be determined mathematically by rotating the original source and observer co-ordinates using the following scheme. Figure 5.12 illustrates an example case for the source. An identical approach can be used for the observer.

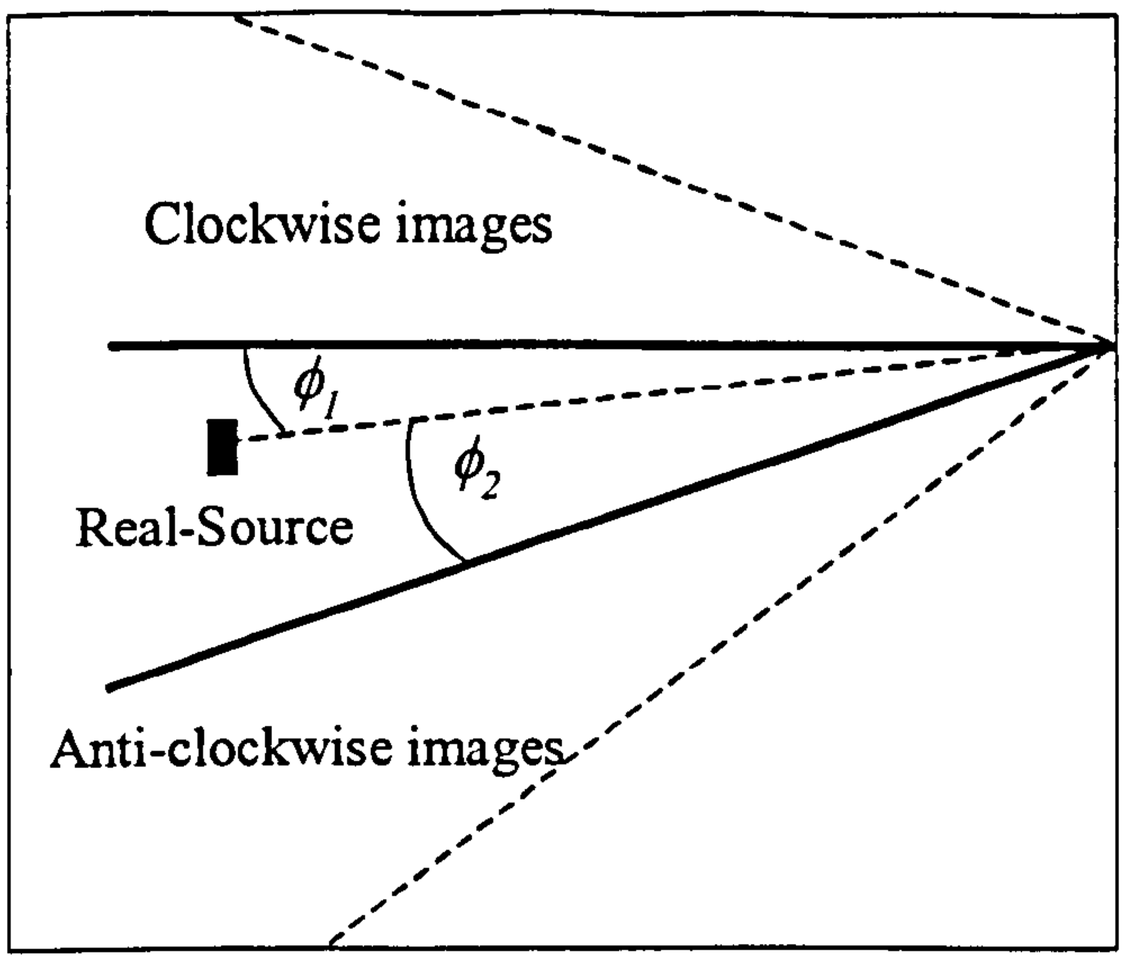

Figure 5.12: Rotation angles for observer

Given that the integer n denotes the image number, the rotation angles for the 'clockwise' images is given by

$$\phi_n = (n+1)\phi_1 + (n-1)\phi_2 \tag{5.12}$$

when n is odd, and by

$$\phi_n = n(\phi_1 + \phi_2) \tag{5.13}$$

when n is even. Similarly, the rotation angles for the 'anti-clockwise' images are given by

$$\phi_n = -(n+1)\phi_2 - (n-1)\phi_1 \tag{5.14}$$

when n is odd, and by

$$\phi_n = -n(\phi_1 + \phi_2) \tag{5.15}$$

when n is even. The image-source co-ordinates are then given using

$$x'_n = x_s \cos(\phi_n) + z_s \sin(\phi_n) \tag{5.16}$$

$$z'_n = x_s \sin(\phi_n) - z_s \cos(\phi_n) \tag{5.17}$$

where x_s and z_s are the real-source co-ordinates, see Equation (5.1). The image-source to real-observer separation (e.g. path length) is given by

$$L_n = \sqrt{(x_o - x'_n)^2 + (z_o - z'_n)^2} \tag{5.18}$$

where x_o and z_o are the real-observer co-ordinates. This expression can be used to provide a useful criterion for determining the relative importance of the contribution from the secondary reflections. If the direct path length between the source and observer is defined to be L_d, then the secondary reflections will be negligible if

$$\frac{L_n}{L_d} \geq 5 . \tag{5.19}$$

This simply indicates that the attenuation experienced by the secondary reflection is much larger than the attenuation experienced by the direct wave. For some applications, the parameter on the right hand side of Equation (5.19) could be relaxed to 3, thus limiting the error to below 5% (i.e. e^{-3}), rather than below 1% (i.e. e^{-5}).

The final angle of incidence is calculated from the right-angled triangle formed between horizontal and vertical construction lines, and the line between the image-source to real-observer, where the latter is the hypotenuse. This gives

$$\phi_n^i = \tan^{-1}\left(\frac{x_o - x'_n}{z_o - z'_n}\right) \tag{5.20}$$

for a final reflection off the air-sea interface, and

$$\phi_n^i = \tan^{-1}\left(\frac{x_o - x'_n}{z_o - z'_n}\right) + 2\phi_s \tag{5.21}$$

for a final reflection off the sea-seabed interface, where ϕ_s is the slope angle of the seabed. As mentioned earlier, an additional ϕ_s term is required for reflections off the sea-seabed interface because the sloping seabed modifies the angle of incidence.

The reflection coefficients, R_n for the n^{th} secondary reflection term (NB: n=1 is a primary reflection) can be constructed in the following manner for reflections that reach the observer after a final reflection off the air-sea interface (i.e. from clockwise images)

$$R_1 = R_{21}\left(\phi_1^i\right)$$

$$R_2 = R_{23}^s\left(\phi_2^i + 2\phi_s\right)R_{21}\left(\phi_2^i\right)$$

$$R_3 = R_{21}\left(\phi_3^i + 2\phi_s\right)R_{23}^s\left(\phi_3^i + 2\phi_s\right)R_{21}\left(\phi_3^i\right)$$

$$R_4 = R_{23}^s\left(\phi_4^i + 4\phi_s\right)R_{21}\left(\phi_4^i + 2\phi_s\right)R_{23}^s\left(\phi_4^i + 2\phi_s\right)R_{21}\left(\phi_4^i\right)$$

$$R_5 = R_{21}\left(\phi_5^i + 4\phi_s\right)R_{23}^s\left(\phi_5^i + 4\phi_s\right)R_{21}\left(\phi_5^i + 2\phi_s\right)R_{23}^s\left(\phi_5^i + 2\phi_s\right)R_{21}\left(\phi_5^i\right)$$

Similarly, the reflection coefficients for each secondary reflection that reach the observer after a final reflection off the sea-seabed interface (i.e. anti-clockwise images) can be constructed in the following manner

$$R_1 = R_{23}^s\left(\phi_1^i\right)$$

$$R_2 = R_{21}\left(\phi_2^i\right)R_{23}^s\left(\phi_2^i\right)$$

$$R_3 = R_{23}^s\left(\phi_3^i + 2\phi_s\right)R_{21}\left(\phi_3^i\right)R_{23}^s\left(\phi_3^i\right)$$

$$R_4 = R_{21}\left(\phi_4^i + 2\phi_s\right)R_{23}^s\left(\phi_4^i + 2\phi_s\right)R_{21}\left(\phi_4^i\right)R_{23}^s\left(\phi_4^i\right)$$

$$R_5 = R_{23}^s\left(\phi_5^i + 4\phi_s\right)R_{21}\left(\phi_5^i + 2\phi_s\right)R_{23}^s\left(\phi_5^i + 2\phi_s\right)R_{21}\left(\phi_5^i\right)R_{23}^s\left(\phi_5^i\right)$$

5.6 Correction factor for reflected lateral waves

As mentioned earlier (see Section 5.3), the modular approach adopted for the 3-layer sloping seabed model also excludes contributions from lateral wave interactions that involve reflections. Figure 5.13 shows the 'launching' and 'arrival' of lateral waves that are reflected once off the sea-seabed and air-sea interfaces, respectively.

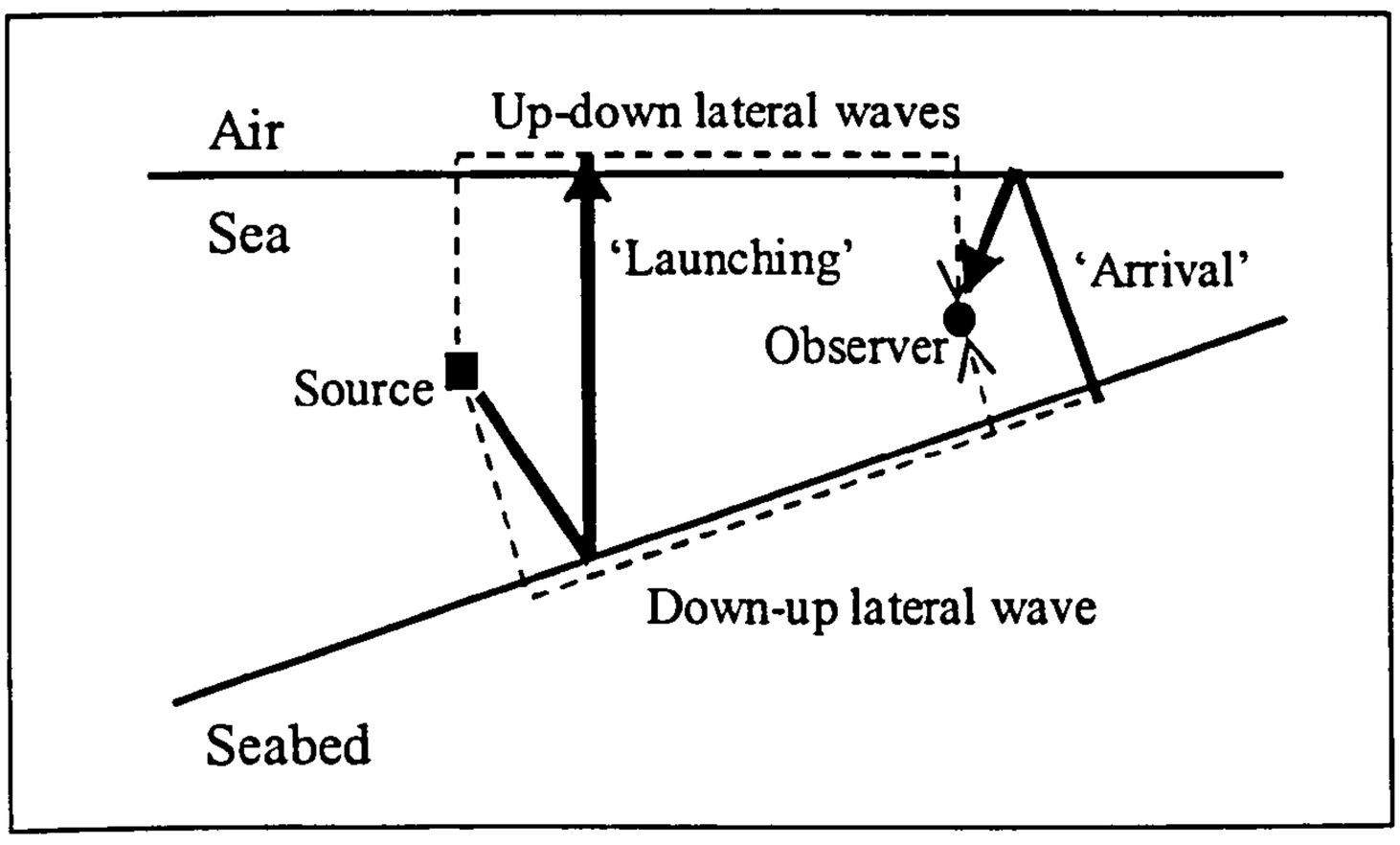

Figure 5.13: Interface interactions for lateral waves

This study has assumed that the critical angles (ϕ_c) associated with the launching and arrival of lateral waves are zero during the development of the correction factors for the lateral waves (see Figure 5.14).

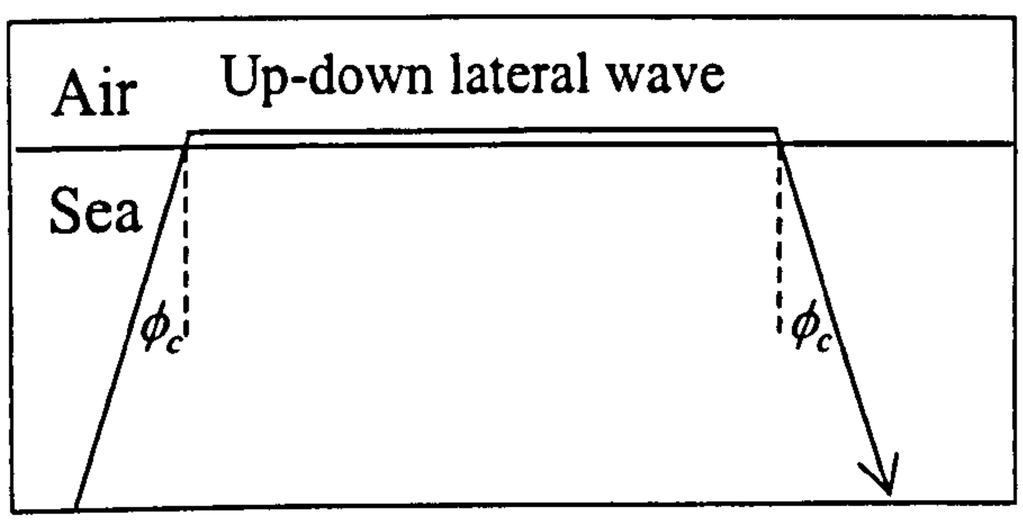

Figure 5.14: Schematic representation of critical angle

Given that a lateral wave propagates along the interface (i.e. ϕ=90°), Snell's law can be used to show that

$$\sin(\phi_c) = \frac{k_1}{k_2} \tag{5.22}$$

for the air-sea interface, and

$$\sin(\phi_c) = \frac{k_3}{k_2} \tag{5.23}$$

for the sea-seabed interface where $k_n = \sqrt{-i\omega\mu\sigma_n^*}$ and $\sigma_n^* = \sigma_n + i\omega\varepsilon_n$. Given that the air has a negligible conductivity, the critical angle will also be negligible.

In contrast, the conductivity ratio (i.e. σ_3/σ_2) for the sea and seabed can be sufficiently large to produce critical angles of a few degrees. In practice, the critical angle will only be significant in regions where the sedimentary layers are thick. Thick sedimentary layers are generally more common in deep ocean environments rather than shallow waters, where the tide-action tends to wash the loose sediments away. For example, the conductivity ratio for Weymouth Bay was estimated to be (0.05)/(3.4), thus giving a critical angle ϕ_c=0.84°.

The non-zero critical angles can cause a discrepancy in both the path length and reflection coefficient calculations. The 2-layer propagation models used in this study to calculate the contributions from the reflected lateral waves will automatically take care of this problem for the path lengths. This can be explained from the subtle fact that the imaging technique developed only determines the locations of the image-sources and image-observer points. The critical angles are thus modelled correctly using the 2-layer propagation models. However, the reflection coefficients associated with down-up lateral waves are calculated using a critical angle of zero, thus need to be corrected. This correction can be implemented by modifying the calculated angles of incidences from (ϕ_i) to (ϕ_i+ϕ_c) for the launching and (ϕ_i-ϕ_c) for the arrivals of reflected lateral waves. This should become clearer in the model implementation procedure detailed below.

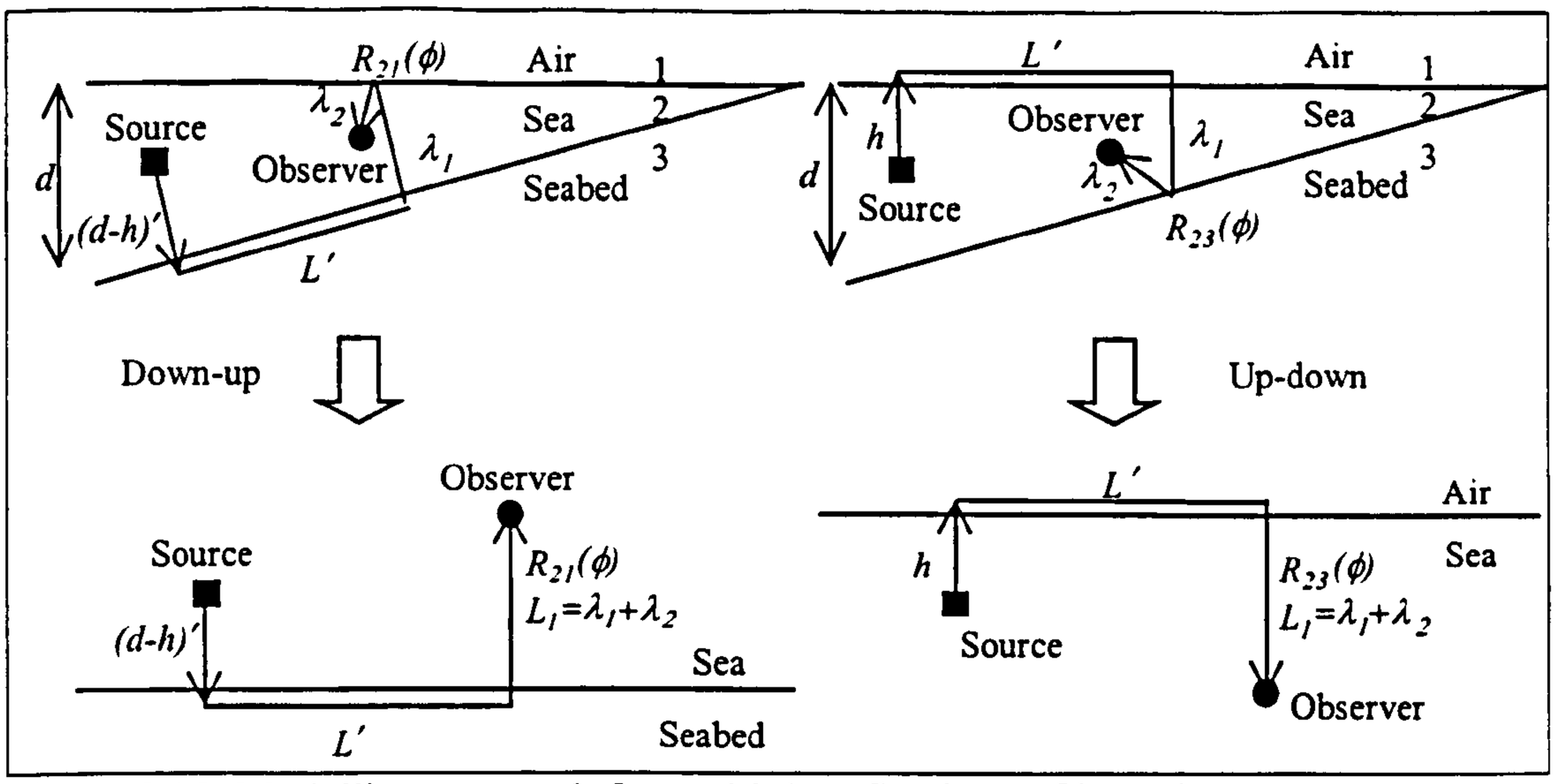

Figure 5.15: Modelling approach for multiple reflections of lateral waves

Figure 5.15 details how reflected lateral wave arrivals are approximated using a geometrical-optical approach in conjunction with a 2-layer propagation model. An analogous approach can be used for the launching of reflected lateral waves. The important factors required for the calculations are the path lengths within the sea layer (i.e. $(d-h)'$ and $\lambda_1 + \lambda_2$ for the down-up case), the path length along the interfaces (i.e. L') and the angles of incidence (i.e. ϕ) for each of the reflections (NB: $\phi=\phi_i-\phi_c$ for the down-up lateral wave interactions).

The path length along the interface is calculated using

$$L' = \sin(\phi_s)\left|S_n - O_n\right| \tag{2.24}$$

and

$$L' = \left|x'_s - x'_o\right| \tag{2.25}$$

for down-up and up-down lateral waves, respectively where

$$S_n = \left(z'_s + \frac{x'_s}{\tan(\phi_s)}\right) \tag{2.26}$$

and

$$O_n = \left(z'_o + \frac{x'_o}{\tan(\phi_s)} \right), \tag{2.27}$$

where (x_s', z_s') and (x_o', z_o') are the image-source[5] and image-observer[6] co-ordinates[7], respectively. S_n and O_n are the co-ordinates of two intersection points for straight lines that pass through the image-source and image-observer points, see Figure 5.16. The two lines are both parallel and have a gradient of $-1/\tan(\phi_s)$ i.e. they are normal to the sea-seabed interface.

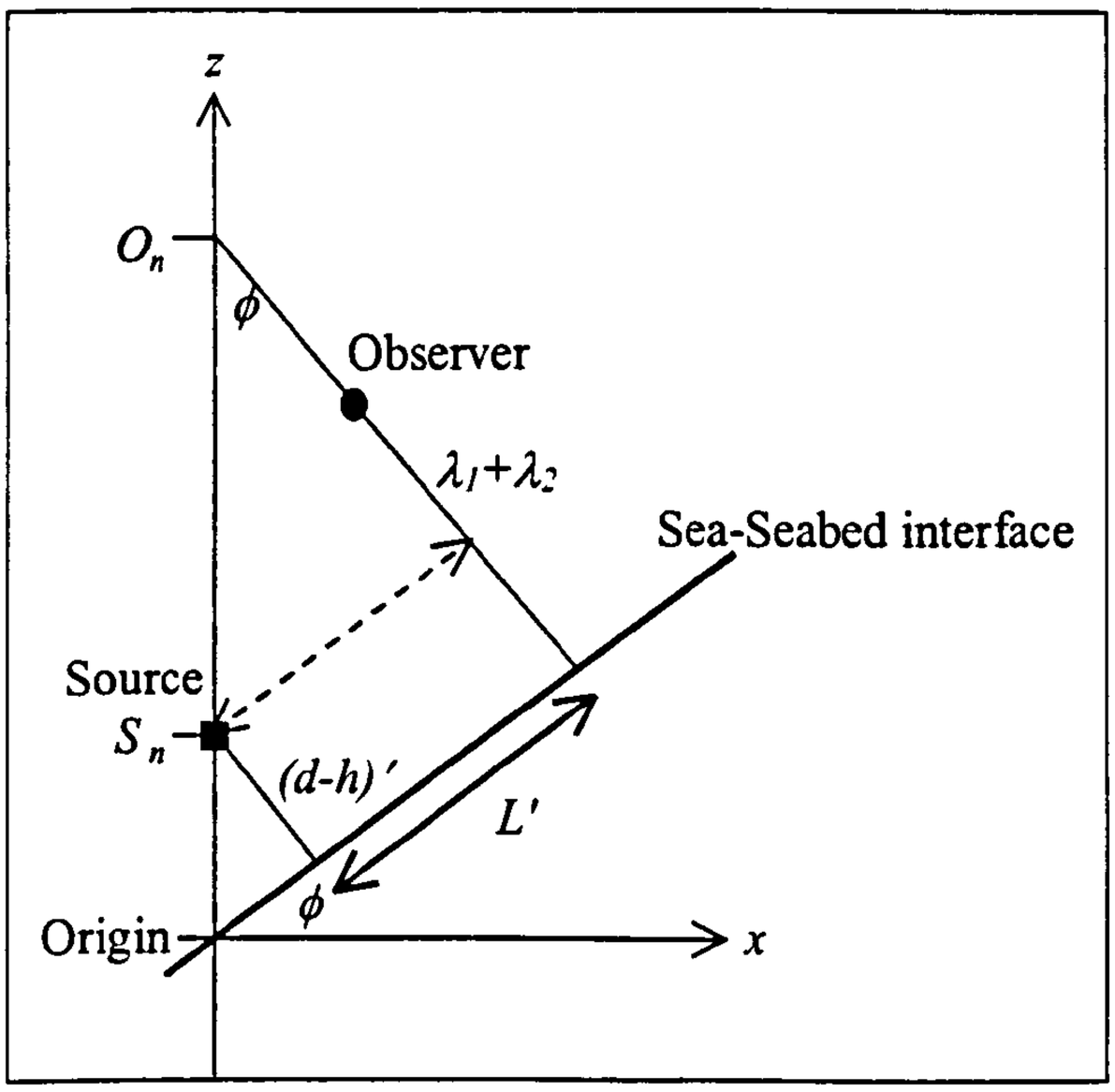

Figure 5.16: Schematic representation of intersection points

The choice of co-ordinate system used for these calculations is arbitrary, but should be consistent for both S_n and O_n. Figure 5.16 has the origin of the co-ordinate system on the sea-seabed interface, directly below the source.

---

[5] The real-source co-ordinates need to be used if the lateral wave is launched without reflecting of any boundaries.
[6] The real-observer co-ordinates need to be used if the lateral wave arrives without reflecting of any boundaries.
[7] The subscript *n* used to denote image source/observer co-ordinates has not been used in Equations (5.26) and (5.27) to maintain generality i.e. both the source and observers can be images.

The modelling technique detailed above describes how the geometrical-optical approach can be applied to reflected lateral waves. However, an imaging technique similar to that used for the secondary reflections needs to be employed to determine the 'path length' of the radiation in the seawater i.e. the λ_1 and λ_2 parameters in Figure 5.15. Strictly speaking, these are the distances of the image-sources or image-observers from the real air-sea or sea-seabed interfaces.

Figure 5.17 shows the new imaging technique applied to the launching of reflected lateral waves. Figure 5.17 shows the arrangement of image environments and image-sources generated using the same technique employed for the secondary reflections.

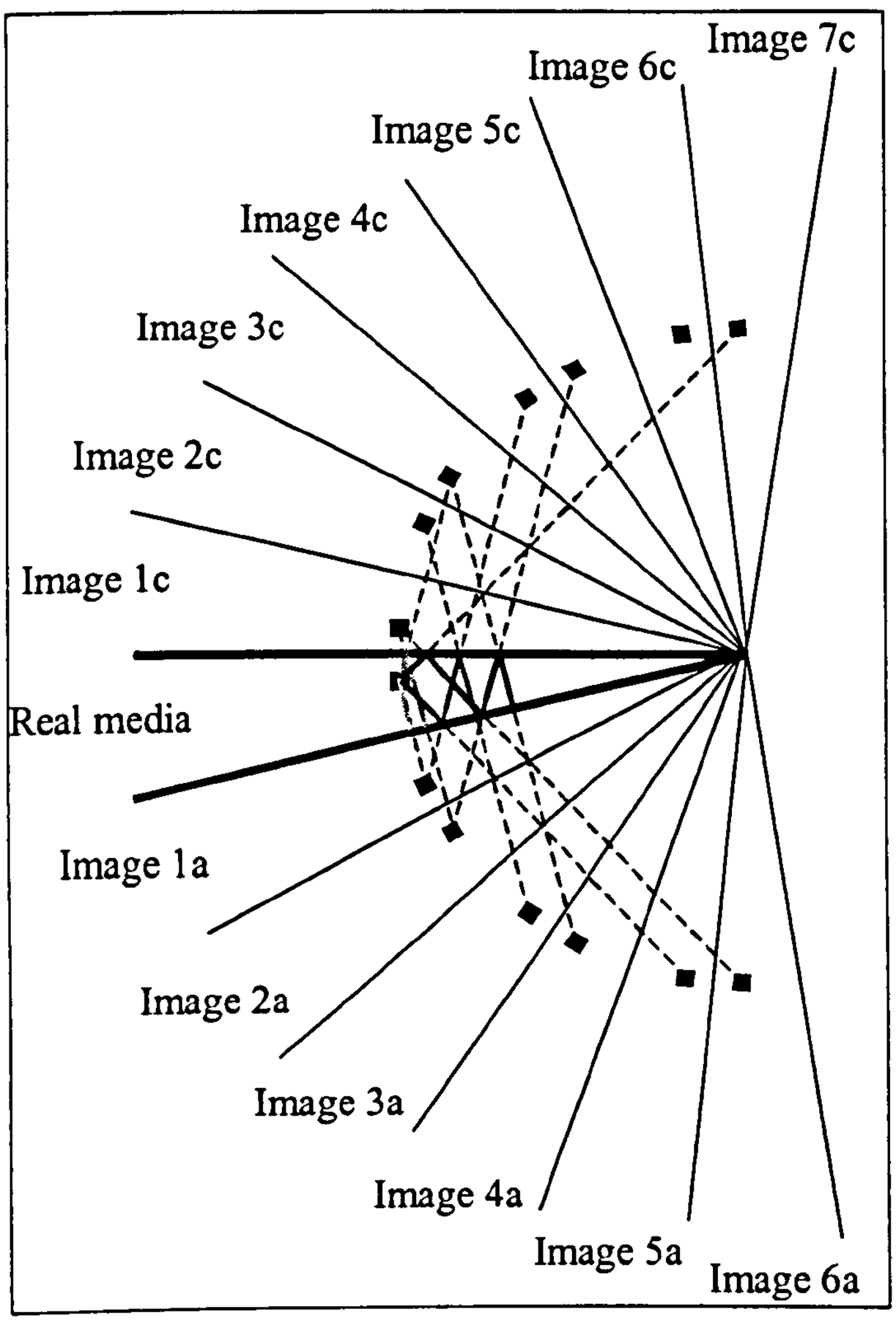

Figure 5.17: Lateral waves using imaging technique

The path length in the sea layer (prior to launching) is now equal to half the distance given by the real-source to image-source separation. For example, the path length for

the launching of the down-up lateral wave is given by half the real-source to image-1a separation. The path length for 1st reflected down-up lateral wave is given by half the real-source to image-3c separation (note: this is equivalent to half the image-1c to image-2a separation).

The 2nd reflected down-up lateral wave is given by half the real-source to image-5a separation (NB: this is also equivalent to half the image-2c to image-3a separation) and so on. Figure 5.18 shows a simplified version of Figure 5.17 to illustrate how image-sources are distributed symmetrically about the real sea-seabed interface for the down-up lateral wave calculations. There is also a corresponding distribution of image-sources about the air-sea interface for the up-down lateral wave calculations.

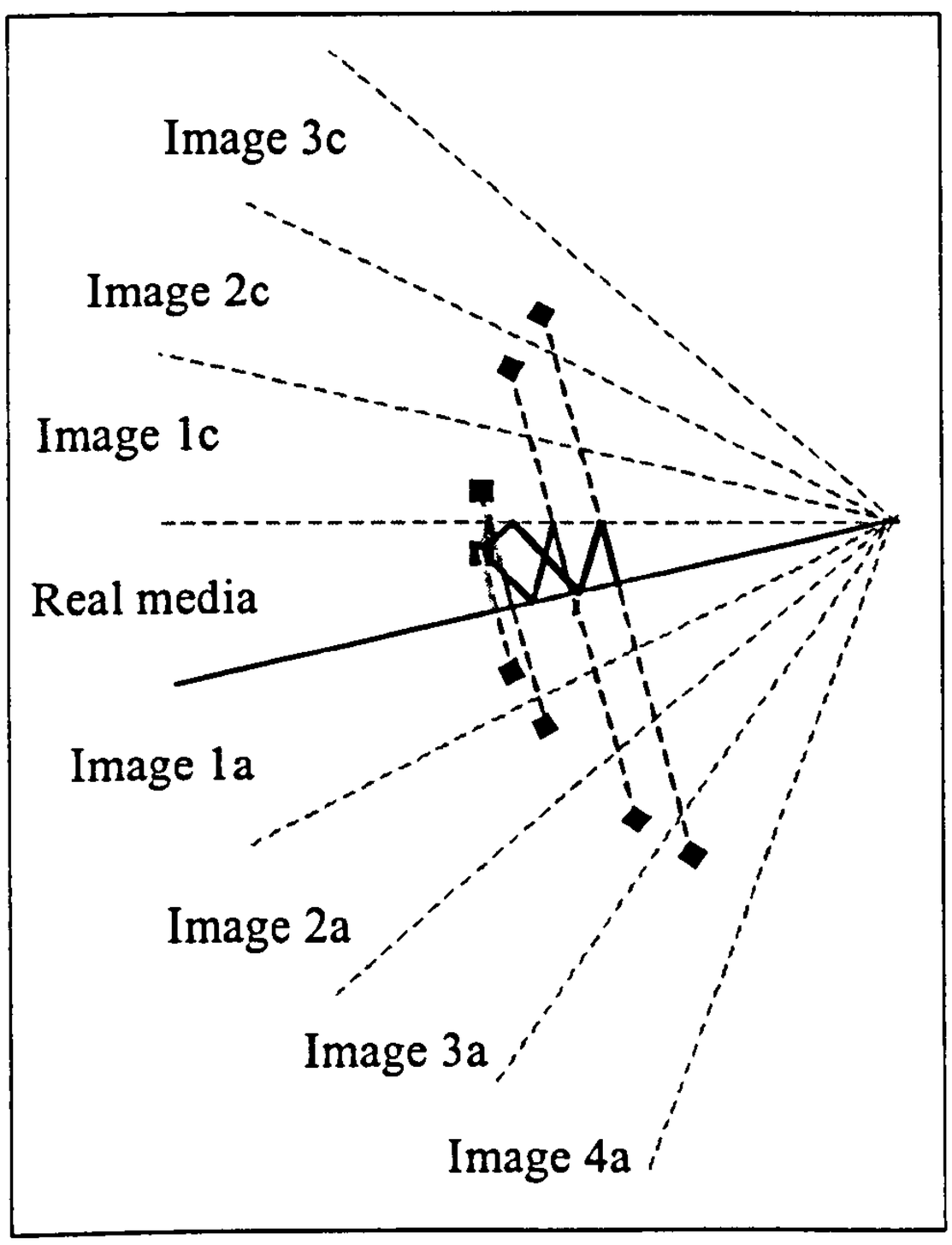

Figure 5.18: Simplified representation of imaging technique for lateral waves

The calculations for the path lengths and the angles of incidence with the interfaces are analogous to those carried for the secondary reflections. If ϕ_1 and ϕ_2 are defined relative to the source as shown in Figure 5.12, the image-sources for the down-up lateral wave can be calculated using Equations (5.16) and (5.17), and the following equation

$$\phi_n = -2n\phi_2 - 2(n-1)\phi_1 \tag{5.28}$$

for odd images, and

$$\phi_n = 2n\phi_1 + 2(n-1)\phi_2 \tag{5.29}$$

for even images. Similarly, the image-sources for the up-down lateral waves are calculated using

$$\phi_n = 2n\phi_1 + 2(n-1)\phi_2 \tag{5.30}$$

for odd images, and

$$\phi_n = -2n\phi_2 - 2(n-1)\phi_1 \tag{5.31}$$

for even images. The 'path length' for propagation in the seawater is given by Equation (5.32).

$$\mathrm{L_n} = \frac{\sqrt{(x_s - x'_n)^2 + (z_s - z'_n)^2}}{2} \tag{5.32}$$

The arrival of reflected lateral waves is modelled using exactly the same approach, the only difference is that the sources in Figures 5.17 and 5.18 are replaced by real and image-observers.

Chapter 6

FDTD sloping seabed model

This Chapter details the development of a new sloping seabed ELFE propagation model based on the finite-difference time-domain (FDTD) method (Bhakta, 2001).

The review of the existing sloping seabed models in Section 1.10 highlighted a number of shortfalls. The numerical models developed to date were only applicable to plane wave fields emanating from the upper atmosphere or were constrained to a 2-dimensional geometry. Although the 2-dimensional models have obvious computational benefits, they do not allow 3-dimensional source distributions or point sources to be modelled. Such complex source distributions are essential for representing the stray ELFE fields from naval vessels (see Section 1.4.2). Off-axis field predictions are also impossible using 2-dimensional models. This is also critical to naval applications where the threat can be situated anywhere with respect to the source.

The FDTD model developed in this study is 3-dimensional. The sources can be any three axes magnetic and/or electric dipoles, and can be situated in the sea layer. Additional features include the ability to describe up to ten arbitrary sea/seabed layers with smooth profiles, rather than simpler 'stair-case' approximations, and the direct evaluation of both the magnetic and electric field components.

6.1 General methodology

The FDTD model will work by transforming the sloping seabed environment into a horizontally plane-stratified environment, within a new co-ordinate system using a one-to-one mapping. This transformation is essential to simplify the process of

applying the boundary conditions across the media interfaces and will make the geometry of the problem conform to a regular grid.

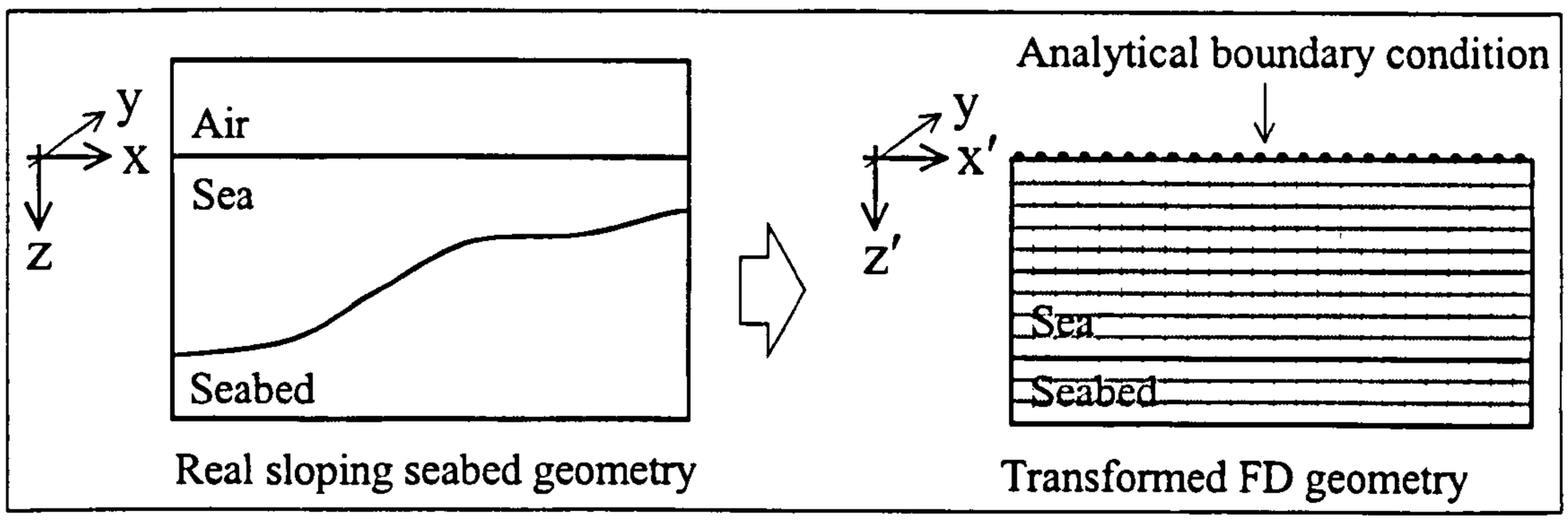

Figure 6.1: Transformation of sloping geometry

The FDTD method will only be applied to the conducting sea and seabed layers, because of the problems associated with modelling environments in which the EM propagation speeds differ widely using the FDTD method. The air-sea interface is therefore modelled using an analytical boundary condition. Two boundary condition formulations were tested; both developed by Leif Abrahamsson (1997, 2000).

6.2 Formulation of FDTD model

Yee's formulation (Yee, 1966) has been used to implement the FDTD model. The following Maxwell's equations

$$\nabla \times \mathbf{E} = -\mu \frac{\partial \mathbf{H}}{\partial t} - \mu \mathbf{M}(t) \tag{6.1}$$

$$\nabla \times \mathbf{H} = \sigma \mathbf{E} + \mathbf{J}(t) \tag{6.2}$$

are transformed one-to-one from a continuous domain to a new discrete space by allocating different spatial and temporal offsets to both the **E** and **H** fields, as shown schematically in Figure 6.2. **M**(t) and **J**(t) are the time-dependent magnetic dipole density and electric dipole density, respectively. This form of Maxwell's equations is

only applicable to good conductors since displacement currents are ignored in Equation (6.2).

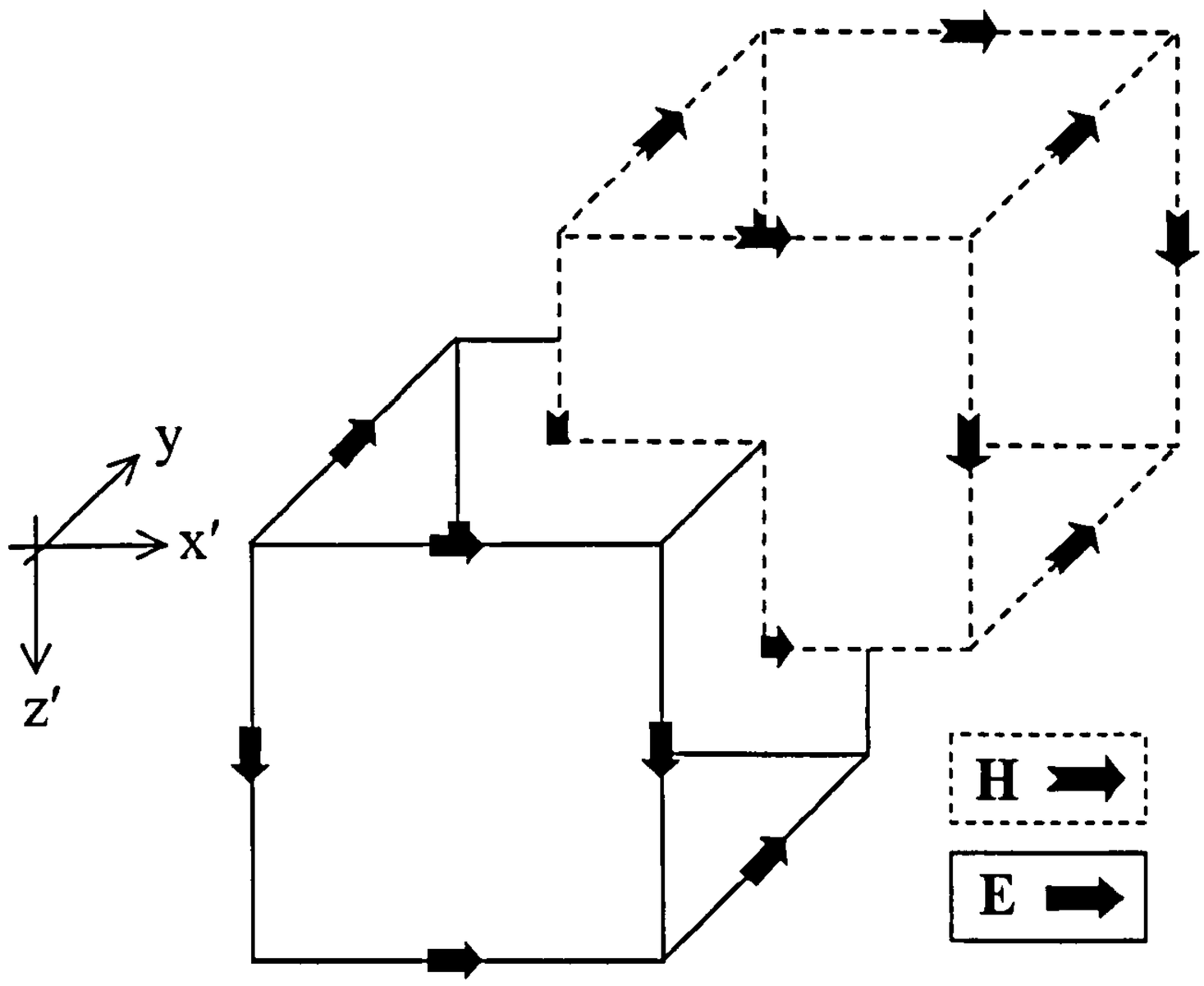

Figure 6.2: Yee unit cell.

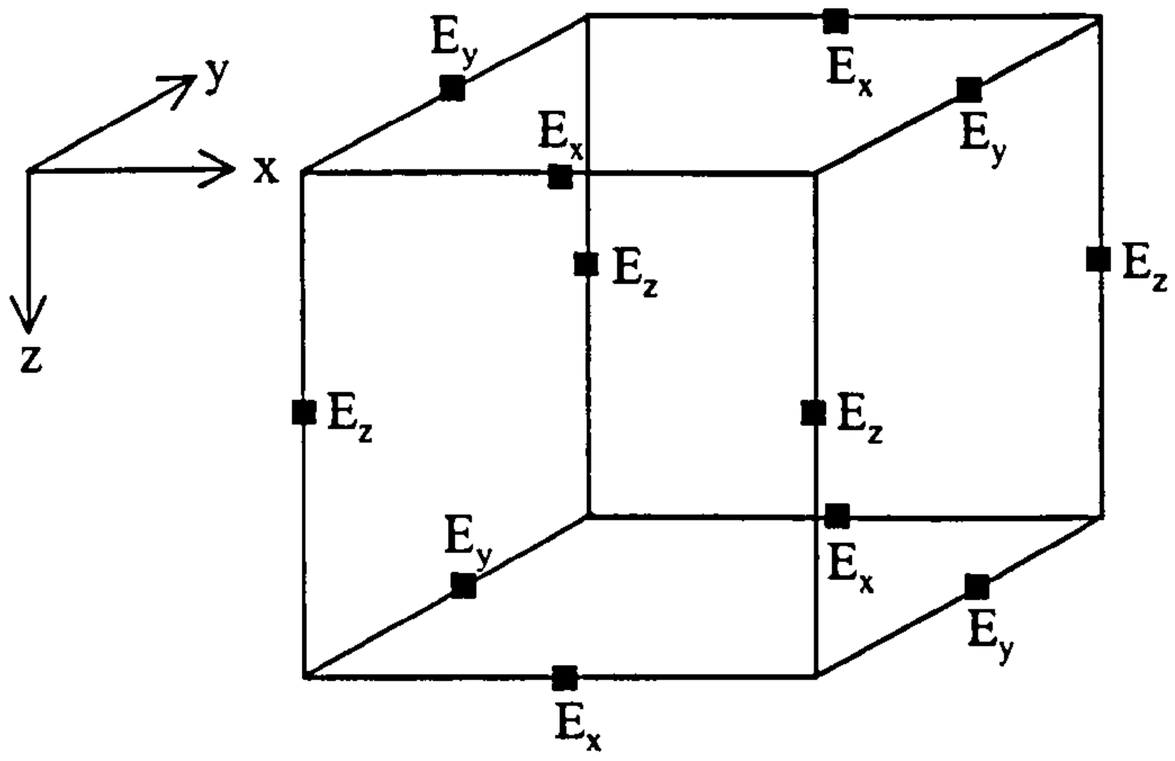

Figure 6.3: E-field portion of Yee unit cell

Figure 6.3 above shows how individual electric field components are positioned (on a cubic grid) within the Yee unit cell. All the field components lie at the midpoint of the edges. The magnetic field components are also positioned in the same manner on their cubic grid. Given that the two grids are spatially offset as shown in Figure 6.2, the magnetic field components will be positioned at the centre of the E-field's cube faces. Similarly, the electric fields are also positioned in the centre of the H-field's

cube faces. The method used to determine the size of the Yee unit cell is described in Section 6.8

This results in field components which are expressed in the form $Ex'(i+^1/_2,j,k,n)$, $Ey(i,j+^1/_2,k,n)$ and $Ez'(i,j,k+^1/_2,n)$ for the electric fields and similarly, $Hx'(i,j+^1/_2,k+^1/_2,n+^1/_2)$, $Hy(i+^1/_2,j,k+^1/_2,n+^1/_2)$ and $Hz'(i+^1/_2,j+^1/_2,k,n+^1/_2)$ for the magnetic field where the integers i, j and k denote spatial counters on the FD mesh in the x', y and z' directions, respectively. Adjacent nodes are spatially offset by a distance $\Delta x'$, Δy and $\Delta z'$ along the x', y and z' axes, respectively. The integer 'n' denotes the time counter, which is incremented by Δt to allow the solution to evolve with time.

6.3 Co-ordinate transformation

As mentioned earlier, this model works by transforming the sloping seabed geometry onto a new orthogonal co-ordinate system (x',y,z'). Hence, the differential operators used within Maxwell's equations must be applicable to a general co-ordinate system. This generality can be achieved by using the following Curl operators (Morse et al., 1953): -

$$\nabla \times \mathbf{E} = \frac{1}{b}\left[\frac{\partial}{\partial y}(bE_{z'}) - \frac{\partial}{\partial z'}E_y\right]\underline{x'}$$

$$+\frac{1}{ab}\left[\frac{\partial}{\partial z'}(aE_{x'}) - \frac{\partial}{\partial x'}(bE_{z'})\right]\underline{y}$$

$$+\frac{1}{a}\left[\frac{\partial}{\partial x'}E_y - \frac{\partial}{\partial y}(aE_{x'})\right]\underline{z'} \qquad (6.3)$$

$$\nabla \times \mathbf{H} = \frac{1}{b}\left[\frac{\partial}{\partial y}(bH_{z'}) - \frac{\partial}{\partial z'}H_y\right]\underline{x'}$$

$$+\frac{1}{ab}\left[\frac{\partial}{\partial z'}(aH_{x'}) - \frac{\partial}{\partial x'}(bH_{z'})\right]\underline{y}$$

$$+\frac{1}{a}\left[\frac{\partial}{\partial x'}H_y - \frac{\partial}{\partial y}(aH_{x'})\right]\underline{z'} \tag{6.4}$$

where the coefficients '*a*' and '*b*' are defined by

$$a^2(x',z') = \left[\left(\frac{\partial x}{\partial x'}\right)^2 + \left(\frac{\partial z}{\partial x'}\right)^2\right] \tag{6.5}$$

and

$$b^2(x',z') = \left[\left(\frac{\partial x}{\partial z'}\right)^2 + \left(\frac{\partial z}{\partial z'}\right)^2\right]. \tag{6.6}$$

The transformation of the sloping seabed environment into a horizontally plane-stratified medium as shown in Figure 6.1 is carried out using the '*ORTHO*' algorithm developed by L. Abrahamsson (1991) of FOI. This algorithm is capable of transforming most seabed geometries of interest, provided they are relatively 'smooth' with no abrupt features.

The *ORTHO* algorithm calculates all the '*a*' and '*b*' weighting factor at the requested grid points. The inputs to the algorithm are the grid points and the environmental profile describing the geometry of the interfaces. Figure 6.4 shows an example input environmental profile. This figure shows the geometry of the problem and an orthogonal grid in the transformed x and z co-ordinates. Figure 6.4 is based on the real x and z co-ordinates; hence the orthogonal grid is not rectangular.

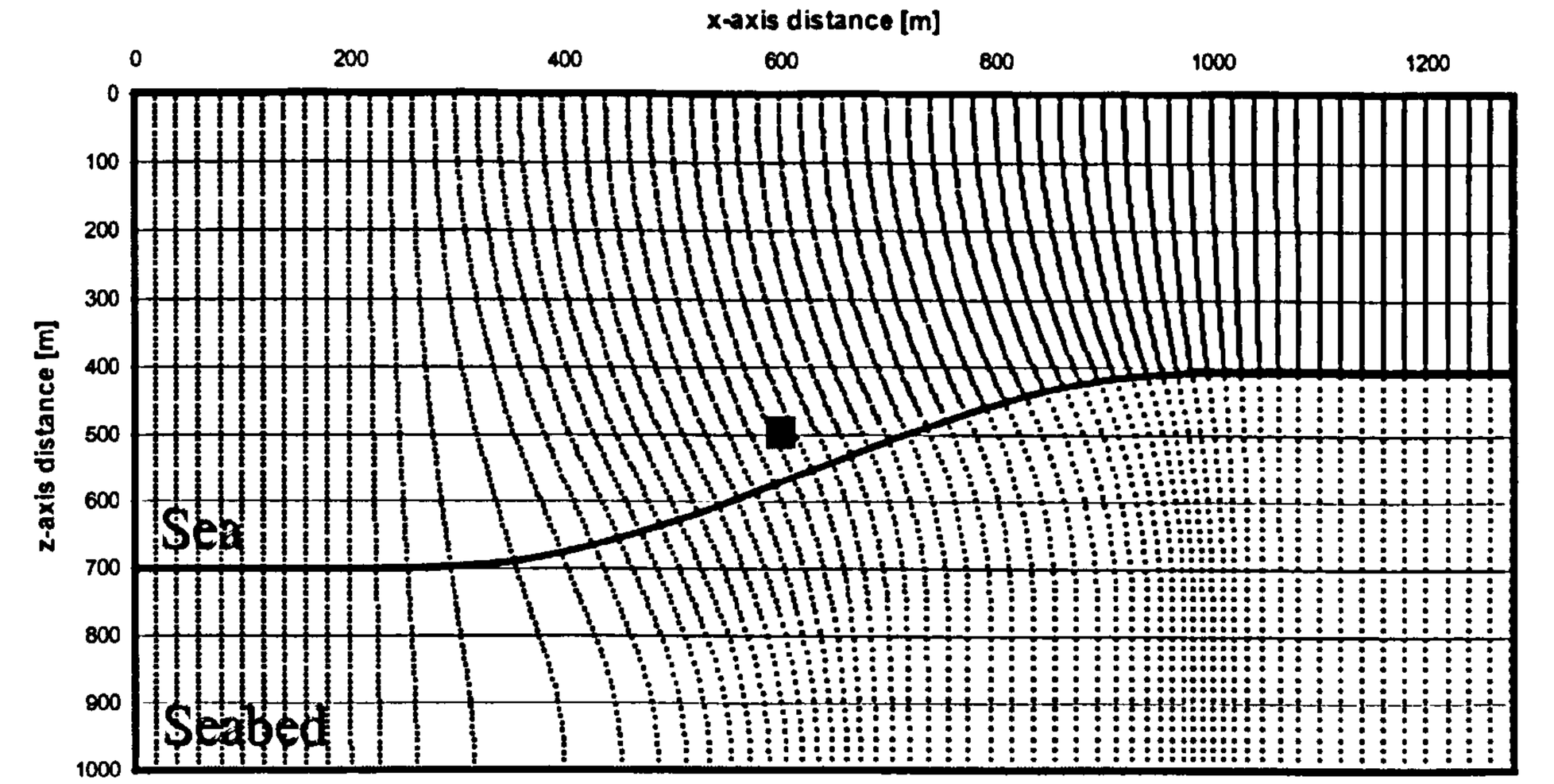

Figure 6.4: Orthogonal grid for input geometry

The orthogonal nature of the co-ordinate system is also visible. The dotted lines all intersect the boundaries at ninety degrees. Similarly, horizontal lines will intersect all the vertical lines at ninety degrees. The transformed geometry used for the FDTD calculations is shown in Figure 6.5. The orthogonal dotted lines are all mapped onto a regular grid. The vertical co-ordinates of each interface in the transformed space are defined by their initial value at x=0.0 within the real problem space.

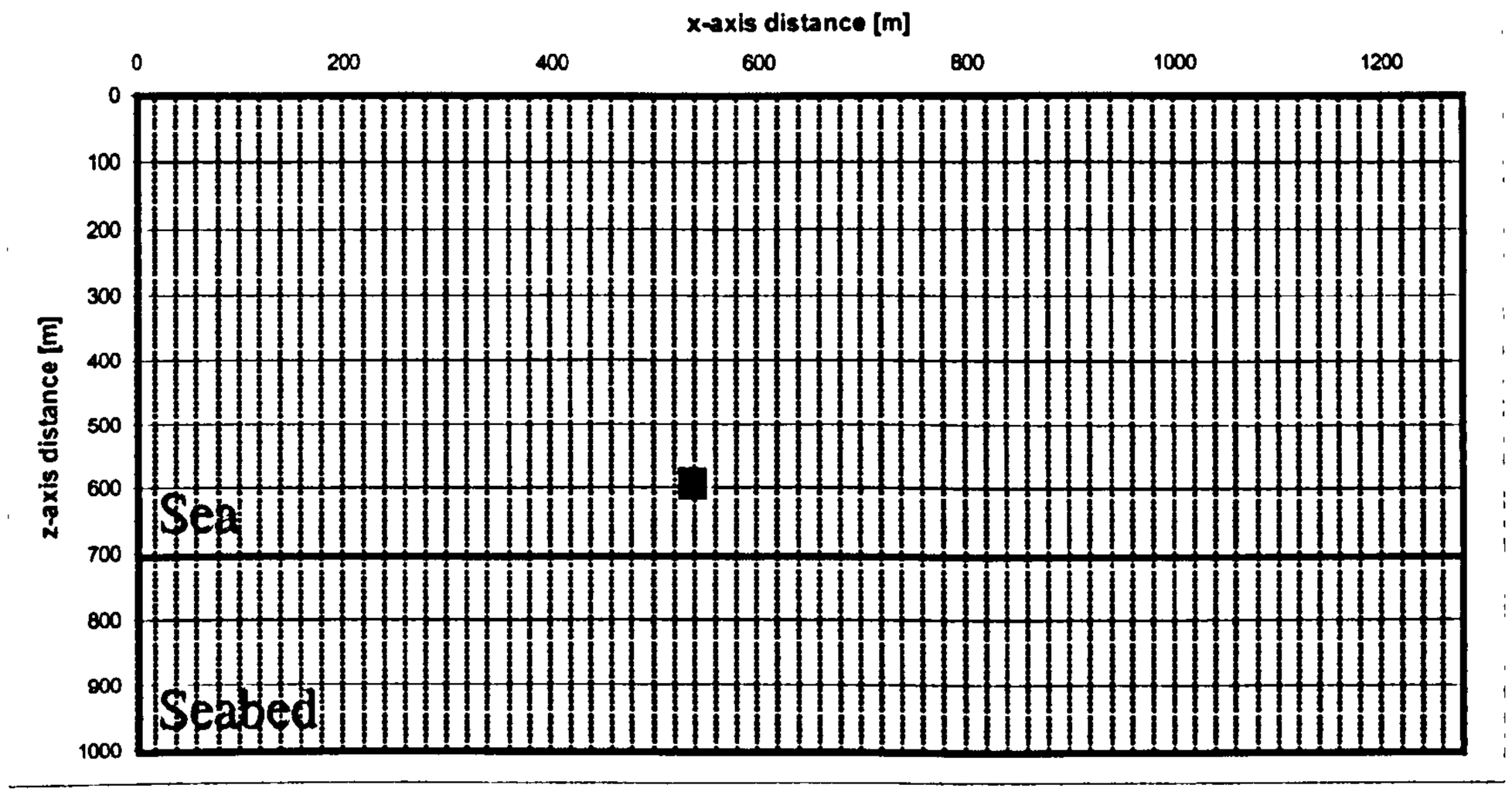

Figure 6.5: Transformed geometry

6.4 Finite-difference scheme

The Yee scheme, as implemented in this study, approximates continuous spatial and time derivative using the following discrete derivatives:

$$\frac{\partial H'_x}{\partial z'} = \frac{H'_x\left(i, j+\frac{1}{2}, k+\frac{1}{2}, n+\frac{1}{2}\right) - H'_x\left(i, j+\frac{1}{2}, k-\frac{1}{2}, n+\frac{1}{2}\right)}{\Delta z'}, \tag{6.7}$$

$$\frac{\partial H'_x}{\partial t} = \frac{H'_x\left(i, j+\frac{1}{2}, k+\frac{1}{2}, n+\frac{1}{2}\right) - H'_x\left(i, j+\frac{1}{2}, k+\frac{1}{2}, n-\frac{1}{2}\right)}{\Delta t}, \tag{6.8}$$

$$\frac{\partial E'_x}{\partial z'} = \frac{E'_x\left(i+\frac{1}{2}, j, k+1, n\right) - E'_x\left(i+\frac{1}{2}, j, k, n\right)}{\Delta z'}. \tag{6.9}$$

The FD operators are essentially the same in the general transformed co-ordinate system. However, the 'a' and 'b' weighting factors need to be included as indicated by Equations (6.3) and (6.4). The 'a' and 'b' weighting factors describe the local 'distortion' to the FD mesh, therefore will be different for each node of the mesh.

Equation (6.10) shows the same differential operator given by Equation (6.7), but for a general co-ordinate system. The 'a' and 'b' factors adopt the same spatial counters as the node point if they need to be differentiated or they adopt the average spatial counter values if they can be brought outside the differential operator. Equations (6.5) and (6.6) show that 'a' and 'b' are both a function of (x',z'), hence they can only be brought outside partial derivatives with respect to y.

$$\frac{1}{ab}\frac{\partial(aH'_x)}{\partial z'} = \frac{1}{a_{i,k}b_{i,k}} \frac{a_{i,k+\frac{1}{2}} H'_x\left(i, j+\frac{1}{2}, k+\frac{1}{2}, n+\frac{1}{2}\right) - a_{i,k-\frac{1}{2}} H'_x\left(i, j+\frac{1}{2}, k-\frac{1}{2}, n+\frac{1}{2}\right)}{\Delta z'} \tag{6.10}$$

All the finite difference approximations used in this model are generated using the methodology described above.

6.5 Homogeneous medium

The magnetic field components $\mathbf{H}(H_x', H_y, H_z')$ are calculated from Equation (6.1) using the general curl operator given by Equation (6.3). Equations (6.11) to (6.13) are obtained by separating this equation into its three scalar components.

$$\frac{1}{b}\left[\frac{\partial(bE_z')}{\partial y} - \frac{\partial E_y}{\partial z'}\right] = -\mu\frac{\partial H_x'}{\partial t} - \mu M_x' \tag{6.11}$$

$$\frac{1}{ab}\left[\frac{\partial(aE_x')}{\partial z'} - \frac{\partial(bE_z')}{\partial x'}\right] = -\mu\frac{\partial H_y}{\partial t} - \mu M_y \tag{6.12}$$

$$\frac{1}{a}\left[\frac{\partial E_y}{\partial x'} - \frac{\partial(bE_x')}{\partial y}\right] = -\mu\frac{\partial H_z'}{\partial t} - \mu M_z' \tag{6.13}$$

The differential operators in Equation (6.11) can be expressed as discrete operators using the methodology described earlier to give

$$\left[\frac{E_z'\left(i, j+1, k+\frac{1}{2}, n\right) - E_z'\left(i, j, k+\frac{1}{2}, n\right)}{\Delta y}\right]$$

$$-\frac{1}{b_{i,k+\frac{1}{2}}}\left[\frac{E_y'\left(i, j+\frac{1}{2}, k+1, n\right) - E_z'\left(i, j+\frac{1}{2}, k, n\right)}{\Delta z}\right]$$

$$= -\mu\frac{H_x'\left(i, j+\frac{1}{2}, k+\frac{1}{2}, n+\frac{1}{2}\right) - H_x'\left(i, j+\frac{1}{2}, k+\frac{1}{2}, n-\frac{1}{2}\right)}{\Delta t}$$

$$-\mu M_x'\left(i, j+\frac{1}{2}, k+\frac{1}{2}, n+\frac{1}{2}\right) \tag{6.14}$$

Equation (6.14) can be rearranged to take the H_x' component to be calculated (i.e. the newest value at $n+{}^1/_2$) to the left-hand side of the equation. All other terms are taken to the right-hand side as shown in Equation (6.15).

$$H'_x\left(i, j+\frac{1}{2}, k+\frac{1}{2}, n+\frac{1}{2}\right) = -H'_x\left(i, j+\frac{1}{2}, k+\frac{1}{2}, n-\frac{1}{2}\right) - \Delta t M'_x\left(i, j+\frac{1}{2}, k+\frac{1}{2}, n+\frac{1}{2}\right)$$

$$-\frac{\Delta t}{\mu}\left\{\left[\frac{E'_z\left(i, j+1, k+\frac{1}{2}, n\right) - E'_z\left(i, j, k+\frac{1}{2}, n\right)}{\Delta y}\right]\right.$$

$$\left.-\frac{1}{b_{i,k+\frac{1}{2}}}\left[\frac{E_y\left(i, j+\frac{1}{2}, k+1, n\right) - E_y\left(i, j+\frac{1}{2}, k, n\right)}{\Delta z'}\right]\right\} \quad (6.15)$$

The same method is used to formulate the expressions for the H_y and H_z' components. This gives

$$H_y\left(i+\frac{1}{2}, j, k+\frac{1}{2}, n+\frac{1}{2}\right) = -H_y\left(i+\frac{1}{2}, j, k+\frac{1}{2}, n-\frac{1}{2}\right) - \Delta t M_y\left(i+\frac{1}{2}, j, k+\frac{1}{2}, n+\frac{1}{2}\right)$$

$$-\frac{\Delta t}{\mu}\frac{1}{a_{i+\frac{1}{2},z+\frac{1}{2}} b_{i+\frac{1}{2},z+\frac{1}{2}}}\left\{\left[\frac{a_{i+\frac{1}{2},z+1} E'_x\left(i+\frac{1}{2}, j, k+1, n\right) - a_{i+\frac{1}{2},z} E'_x\left(i+\frac{1}{2}, j, k, n\right)}{\Delta z'}\right]\right.$$

$$\left.-\left[\frac{b_{i+1,k+\frac{1}{2}} E'_z\left(i+1, j, k+\frac{1}{2}, n\right) - b_{i,k+\frac{1}{2}} E'_z\left(i, j, k+\frac{1}{2}, n\right)}{\Delta x'}\right]\right\} \quad (6.16)$$

and

$$H'_z\left(i+\frac{1}{2}, j+\frac{1}{2}, k, n+\frac{1}{2}\right) = -H'_z\left(i+\frac{1}{2}, j+\frac{1}{2}, k, n-\frac{1}{2}\right) - \Delta t M'_z\left(i+\frac{1}{2}, j+\frac{1}{2}, k, n+\frac{1}{2}\right)$$

$$-\frac{\Delta t}{\mu}\frac{1}{a_{i+\frac{1}{2},z}}\left\{\left[\frac{E_y\left(i+1, j+\frac{1}{2}, k, n\right) - E_y\left(i, j+\frac{1}{2}, k, n\right)}{\Delta x'}\right]\right.$$

$$-\left[\frac{a_{i+\frac{1}{2},k}E'_x\left(i+\frac{1}{2},j+1,k,n\right)-a_{i,k+\frac{1}{2}}E'_x\left(i+\frac{1}{2},j,k,n\right)}{\Delta y}\right]\Bigg\}. \qquad (6.17)$$

The electric field components are also derived in a similar fashion using Equation (6.2) and the general curl operator defined by Equation (6.4). The three scalar components of this equation are

$$\frac{1}{b}\left[\frac{\partial(bH'_z)}{\partial y}-\frac{\partial H_y}{\partial z'}\right]=\sigma E'_x+J'_x, \qquad (6.18)$$

$$\frac{1}{ab}\left[\frac{\partial(aH'_x)}{\partial z'}-\frac{\partial(bH'_z)}{\partial x'}\right]=\sigma E_y+J_y \qquad (6.19)$$

and

$$\frac{1}{a}\left[\frac{\partial H_y}{\partial x'}-\frac{\partial(aH'_x)}{\partial y}\right]=\sigma E'_z+J'_z \qquad (6.20)$$

The derivatives in Equation (6.18) can be replaced by discrete operators to give

$$\left\{\left[\frac{H'_z\left(i+\frac{1}{2},j+\frac{1}{2},k,n+\frac{1}{2}\right)-H'_z\left(i+\frac{1}{2},j-\frac{1}{2},k,n+\frac{1}{2}\right)}{\Delta y}\right]\right.$$

$$\left.-\frac{1}{b_{i+\frac{1}{2},k}}\left[\frac{H_y\left(i+\frac{1}{2},j,k+\frac{1}{2},n+\frac{1}{2}\right)-H_y\left(i+\frac{1}{2},j,k-\frac{1}{2},n+\frac{1}{2}\right)}{\Delta z'}\right]\right\}$$

$$=\sigma E'_x\left(i+\frac{1}{2},j,k,n\right)+J'_x\left(i+\frac{1}{2},j,k,n+1\right) \qquad (6.21)$$

Equation (6.21) can be rearranged to take the E_x' component to be evaluated to the left-hand side with all remaining terms on the right-hand side to give

$$E'_x\left(i+\tfrac{1}{2},j,k,n\right)=-\frac{J'_x\left(i+\tfrac{1}{2},j,k,n+1\right)}{\sigma}$$

$$+\frac{1}{\sigma}\left\{\left[\frac{H'_z\left(i+\tfrac{1}{2},j+\tfrac{1}{2},k,n+\tfrac{1}{2}\right)-H'_z\left(i+\tfrac{1}{2},j-\tfrac{1}{2},k,n+\tfrac{1}{2}\right)}{\Delta y}\right]\right.$$

$$\left.-\frac{1}{b_{i+\frac{1}{2},k}}\left[\frac{H_y\left(i+\tfrac{1}{2},j,k+\tfrac{1}{2},n+\tfrac{1}{2}\right)-H_y\left(i+\tfrac{1}{2},j,k-\tfrac{1}{2},n+\tfrac{1}{2}\right)}{\Delta z'}\right]\right\} \quad (6.22)$$

The E_y and $E_z{}'$ components are generated using the same technique. This gives

$$E_y\left(i,j+\tfrac{1}{2},k,n\right)=-\frac{J_y\left(i,j+\tfrac{1}{2},k,n+1\right)}{\sigma}$$

$$+\frac{1}{\sigma}\left\{\frac{1}{a_{i,k}b_{i,k}}\left[\frac{a_{i,k+\frac{1}{2}}H'_x\left(i,j+\tfrac{1}{2},k+\tfrac{1}{2},n+\tfrac{1}{2}\right)-a_{i,k-\frac{1}{2}}H'_x\left(i,j+\tfrac{1}{2},k-\tfrac{1}{2},n+\tfrac{1}{2}\right)}{\Delta z'}\right]\right.$$

$$\left.-\left[\frac{b_{i,k}H'_z\left(i+\tfrac{1}{2},j+\tfrac{1}{2},k,n+\tfrac{1}{2}\right)-b_{i,k}H'_z\left(i-\tfrac{1}{2},j+\tfrac{1}{2},k,n+\tfrac{1}{2}\right)}{\Delta x'}\right]\right\} \quad (6.23)$$

and

$$E'_z\left(i,j,k+\tfrac{1}{2},n\right)=-\frac{J'_z\left(i,j,k+\tfrac{1}{2},n+1\right)}{\sigma}$$

$$+\frac{1}{\sigma}\left\{\frac{1}{a_{i,k+\frac{1}{2}}}\left[\frac{H_y\left(i+\tfrac{1}{2},j,k+\tfrac{1}{2},n+\tfrac{1}{2}\right)-H_y\left(i-\tfrac{1}{2},j,k+\tfrac{1}{2},n+\tfrac{1}{2}\right)}{\Delta x'}\right]\right.$$

$$-\left[\frac{H_x'\left(i,j+\frac{1}{2},k+\frac{1}{2},n+\frac{1}{2}\right)-H_x'\left(i,j-\frac{1}{2},k+\frac{1}{2},n+\frac{1}{2}\right)}{\Delta y}\right]\Bigg\}. \quad (6.24)$$

6.6 Boundaries across media interfaces

The boundary conditions required across the media interfaces are the familiar continuity requirements for the tangential field components. In this case, the E_x', H_x', E_y and H_y field components need to be continuous.

The most practical way of implementing this boundary condition is to place the nodes of the finite-difference mesh on the interface itself. This forces the continuity of the fields; i.e. the nodes are common to both sides of the interface. However, the spatial offsets between the field components means that both the magnetic and electric field components cannot both lie on the interface. This leads to the following arrangement[1] of nodes at the interfaces if the continuity of E_x' and E_y are to be enforced in this way.

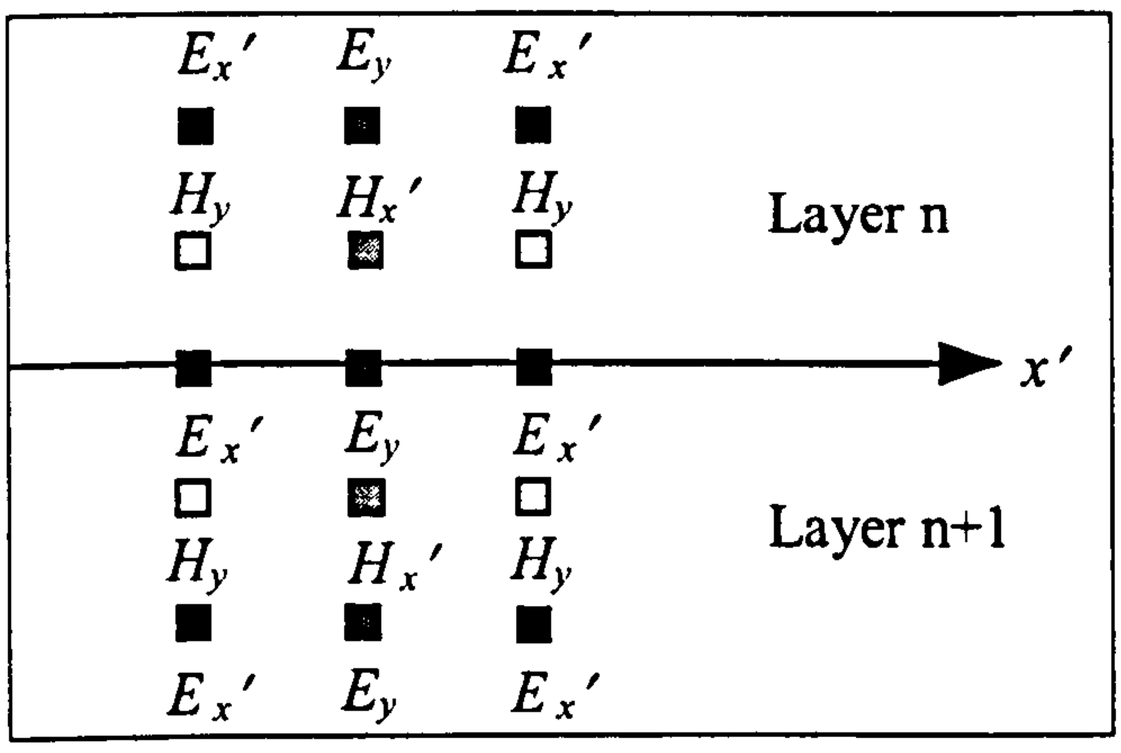

Figure 6.6: Schematic representation of tangential field components at interface

The general differencing scheme detailed in Section 6.5 is only applicable for homogeneous regions where all the nodes lie in the same medium. An alternative scheme is required to deal with conductivity discontinuities in the FD grid (i.e. the interfaces between two differing mediums). This new scheme only needs to be applied to the electric field nodes that lie on the interface between two conducting

[1] The x and y field components do not physically lie in the same plane.

mediums. The air-sea interface is treated separately in Section 6.7 due to the added complication of the non-conducting air medium.

Assuming there are no sources at the interface, Equations (6.18) and (6.19) can be used to show that the tangential electric fields are given by

$$E_x' = \frac{1}{\sigma}\left[\frac{\partial H_z}{\partial y} - \frac{1}{b}\frac{\partial H_y}{\partial z}\right] \tag{6.25}$$

and

$$E_y = \frac{1}{\sigma}\left[\frac{1}{ab}\frac{\partial (aH_x)}{\partial z} - \frac{1}{ab}\frac{\partial (bH_z)}{\partial x}\right] \tag{6.26}$$

There are two problems that complicate the application of Equations (6.25) and (6.26) to determine E_x' and E_y: The conductivity is discontinuous across the boundary and there is no method to enforce the continuity of the tangential magnetic field components. Using one of the conductivity values arbitrarily is not feasible, since the solution will be different depending on the conductivity value chosen. Similarly, setting the tangential magnetic field components to be the same on either side of the boundary is not useful. This is considered unrealistic due to the spatial offset of the nodes from the interface. It would also adversely affect the electric field calculations (i.e. the tangential electric fields would solely depend on the normal components of the magnetic field).

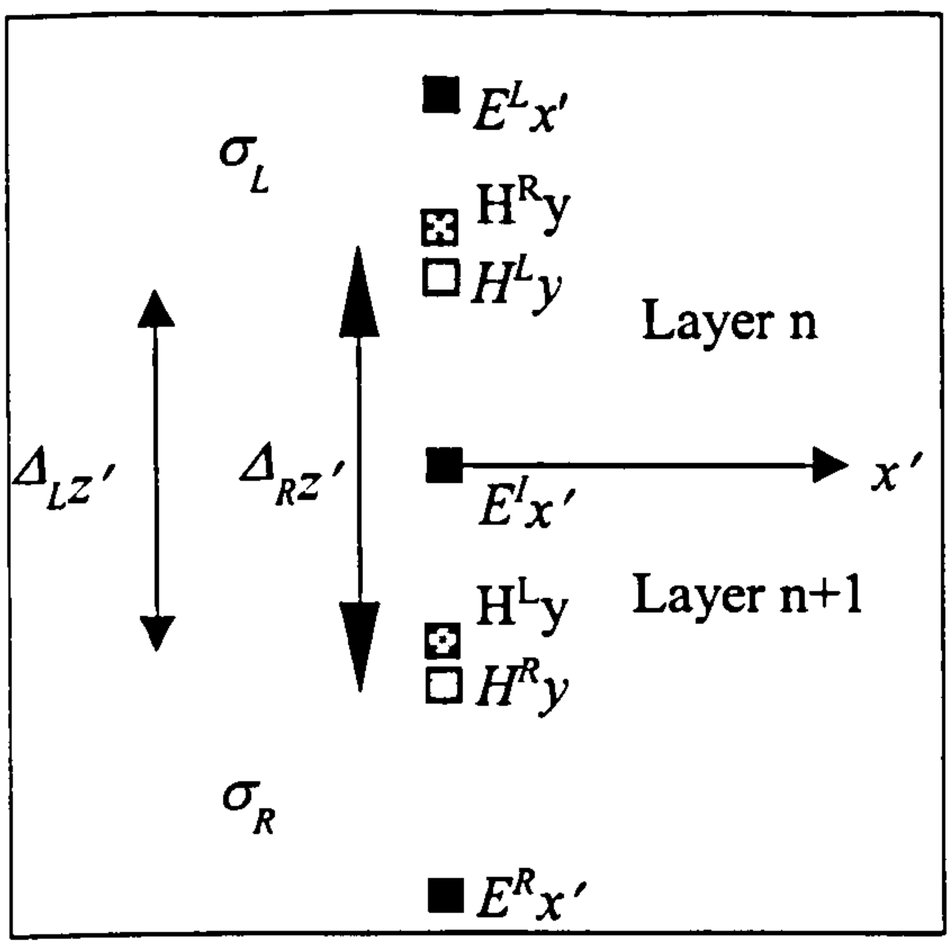

Figure 5.7: Arrangement of fictitious points for determining $E^I_x{}'$

Ideally, both the conductivity values would be used and the continuity of the tangential magnetic field components would be enforced in a more appropriate manner (i.e. average fields are continuous). Fortunately, this can be done if additional nodes representing the tangential magnetic fields are introduced near the interface. H^L_y and H^R_y are new 'fictitious' nodes placed on either side of the interface and $E^I_x{}'$ is the $E_x{}'$ field at the interface, see Figure 6.7 (Abrahamsson, 1997).

This approach relies on having different spatial step sizes (e.g. $\Delta_Z{}'$) on either side of the interface. To maintain the stability of the differencing scheme (see Section 6.9), the larger step size is used in the layer with the lower conductivity (i.e. longer wavelength). The different parameters used in the model are now denoted by a superscript L (left of interface i.e. above) and R (right of interface i.e. below).

Two equations can now be formulated for $E^I_x{}'$ using Equation (6.25), the first using H^L_y, H^L_y, Δ^L_z and σ_L, the second using H^R_y, H^R_y, Δ^R_Z and σ_R, see Equations (6.27) and (6.28).

$$E^I_{x'}\left(i+\tfrac{1}{2},j,k,n+1\right)=-\frac{1}{\sigma_L b_L \Delta_L z}\left(H^L_y - H^L_y\right)+$$

$$\frac{1}{\sigma_L \Delta y}\left[H^I_z\left(i+\tfrac{1}{2},j+\tfrac{1}{2},k,n+\tfrac{1}{2}\right)-H^I_z\left(i+\tfrac{1}{2},j-\tfrac{1}{2},k,n+\tfrac{1}{2}\right)\right]-\frac{J_x}{\sigma_L} \qquad (6.27)$$

$$E_{x'}^{I}\left(i+\frac{1}{2},j,k,n+1\right)=-\frac{1}{\sigma_R b_R \Delta_R z}\left(H_y^R-\mathrm{H_y^R}\right)+$$

$$\frac{1}{\sigma_R \Delta y}\left[H_z^I\left(i+\frac{1}{2},j+\frac{1}{2},k,n+\frac{1}{2}\right)-H_z^I\left(i+\frac{1}{2},j-\frac{1}{2},k,n+\frac{1}{2}\right)\right]-\frac{J_x}{\sigma_R} \quad (6.28)$$

If the continuity of H_y is approximated using

$$H_y \approx \frac{1}{2}\left(H_y^R+\mathrm{H_y^R}\right)=\frac{1}{2}\left(H_y^L+\mathrm{H_y^L}\right), \quad (6.29)$$

the resulting three equations can be used to solve for the three unknowns (i.e. $E_x^{I}{}'$, $\mathrm{H^R_y}$ and $\mathrm{H^L_y}$). Eliminating the two fictitious points by substitution gives

$$E_{x'}^{I}\left(i+\frac{1}{2},j,k,n+1\right)=\left\{-2\left(H_y^L\left(i+\frac{1}{2},j,k+\frac{1}{2},n+\frac{1}{2}\right)-H_y^R\left(i+\frac{1}{2},j,k-\frac{1}{2},n+\frac{1}{2}\right)\right)\right.$$

$$\left.+\left(b_R\Delta_R z'+b_L\Delta_L z'\right)\left[\frac{1}{\Delta y}\left(H_{z'}^{I}\left(i+\frac{1}{2},j+\frac{1}{2},k,n+\frac{1}{2}\right)-H_{z'}^{I}\left(i+\frac{1}{2},j-\frac{1}{2},k,n+\frac{1}{2}\right)\right)-Jx'\right]\right\}$$

$$/\left(\sigma_L b_L \Delta_L z'+\sigma_R b_R \Delta_R z'\right) \quad (6.30)$$

Similarly, two equations can now be formulated for E^{I}_{y}, the first using $\mathrm{H^L_{x}}'$, $H^{L}_{x}{}'$, $\Delta^{L}_{Z}{}'$ and σ_L, the second using $H^{R}_{x}{}'$, $\mathrm{H^R_{x}}'$, $\Delta^{R}_{Z}{}'$ and σ_R (see Figure 6.8).

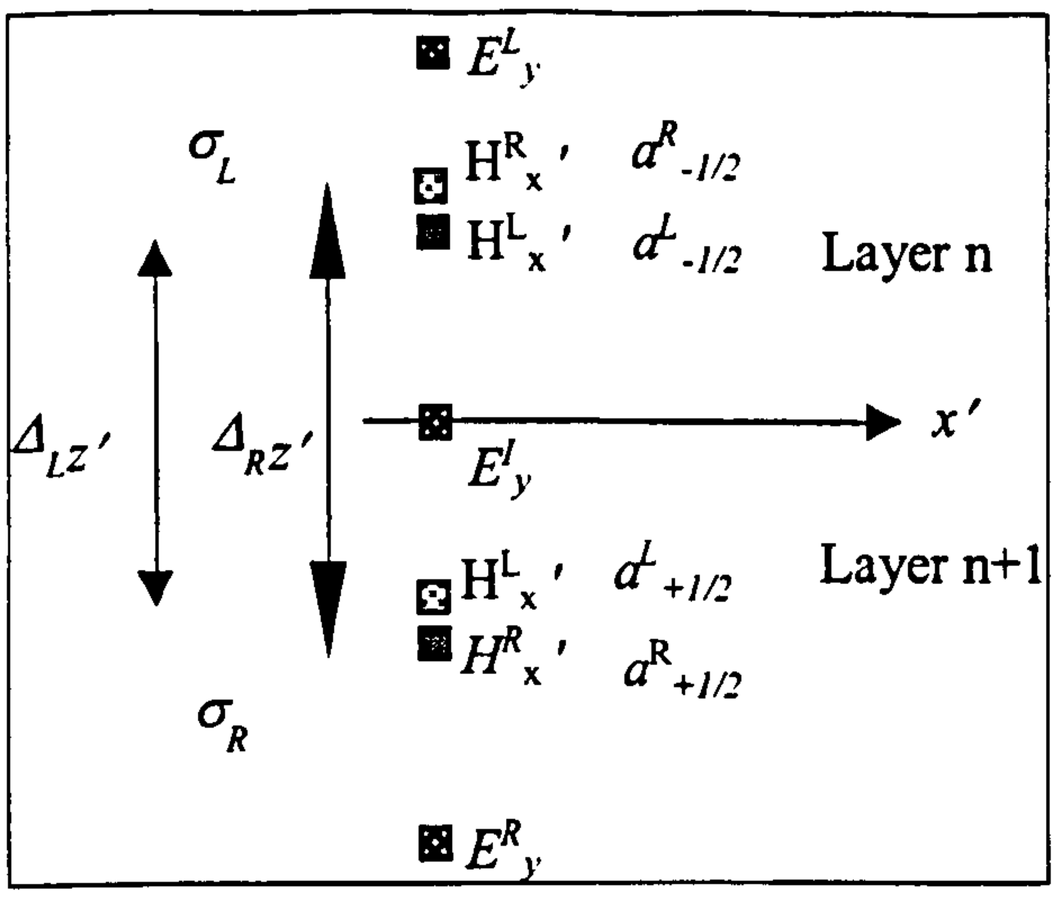

Figure 6.8: Arrangement of fictitious points for determining E^I_y

This results in the following expressions for E^I_y,

$$E_y^I(i,j+\tfrac{1}{2},k,n+1)=\frac{1}{\sigma_L a_L b_L \Delta_L z'}\left(a^L_{\frac{1}{2}}\mathrm{H}^{\mathrm{L}}_{\mathrm{x}'}-a^L_{-\frac{1}{2}}H^L_{x'}\right)-$$

$$\frac{1}{\sigma_L \Delta x}\left[b^L_{i+\frac{1}{2},k}H_z^I\left(i+\tfrac{1}{2},j+\tfrac{1}{2},k,n+\tfrac{1}{2}\right)-b^L_{i-\frac{1}{2},k}H_z^I\left(i-\tfrac{1}{2},j+\tfrac{1}{2},k,n+\tfrac{1}{2}\right)\right]-\frac{J_y}{\sigma_L} \tag{6.31}$$

and

$$E_y^I(i,j+\tfrac{1}{2},k,n+1)=\frac{1}{\sigma_R a_R b_R \Delta_R z'}\left(a^R_{\frac{1}{2}}H^R_{x'}-a^R_{-\frac{1}{2}}\mathrm{H}^{\mathrm{R}}_{\mathrm{x}'}\right)-$$

$$\frac{1}{\sigma_R \Delta x}\left[b^R_{i+\frac{1}{2},k}H_z^I\left(i+\tfrac{1}{2},j+\tfrac{1}{2},k,n+\tfrac{1}{2}\right)-b^R_{i-\frac{1}{2},k}H_z^I\left(i-\tfrac{1}{2},j+\tfrac{1}{2},k,n+\tfrac{1}{2}\right)\right]-\frac{J_y}{\sigma_R} \tag{6.32}$$

If the continuity of H_x' is approximated using Equation (6.33),

$$H_{x'}\approx\frac{1}{2}\left(H^L_{x'}+\mathrm{H}^{\mathrm{L}}_{\mathrm{x}'}\right)=\frac{1}{2}\left(H^R_{x'}+\mathrm{H}^{\mathrm{R}}_{\mathrm{x}'}\right) \tag{6.33}$$

the resulting three equations can be used to solve for the three unknowns (i.e. E^{I}_{y}, $H^{R}_{x'}$ and $H^{L}_{x'}$), thus giving

$$E_y^I\left(i,j+\tfrac{1}{2},k,n+1\right)=\frac{a^L_{-\frac{1}{2}}\left(a^R_{\frac{1}{2}}+a^R_{-\frac{1}{2}}\right)H^L_{x'}\left(i,j+\tfrac{1}{2},k+\tfrac{1}{2},n+\tfrac{1}{2}\right)-a^R_{\frac{1}{2}}\left(a^L_{\frac{1}{2}}+a^L_{-\frac{1}{2}}\right)H^R_{x'}\left(i,j+\tfrac{1}{2},k-\tfrac{1}{2},n+\tfrac{1}{2}\right)}{a\left(\sigma_L a^R_{\frac{1}{2}}b_L\Delta_L z'+\sigma_R a^L_{-\frac{1}{2}}b_R\Delta_R z'\right)}$$

$$-\frac{\left(f_1+J_y\right)a^R_{\frac{1}{2}}b_L\Delta_L z'+\left(f_2+J_y\right)a^L_{-\frac{1}{2}}b_R\Delta_R z'}{\left(\sigma_L a^R_{\frac{1}{2}}b_L\Delta_L z'+\sigma_R a^L_{-\frac{1}{2}}b_R\Delta_R z'\right)} \tag{6.34}$$

where

$$f_1=\frac{1}{\Delta x'}\left(b^L_{i+\frac{1}{2},k}H^I_{z'}\left(i+\tfrac{1}{2},j+\tfrac{1}{2},k,n+\tfrac{1}{2}\right)-b^L_{i-\frac{1}{2},k}H^I_{z'}\left(i-\tfrac{1}{2},j+\tfrac{1}{2},k,n+\tfrac{1}{2}\right)\right) \tag{6.35}$$

and

$$f_2=\frac{1}{\Delta x'}\left(b^R_{i+\frac{1}{2},k}H^I_{z'}\left(i+\tfrac{1}{2},j+\tfrac{1}{2},k,n+\tfrac{1}{2}\right)-b^R_{i-\frac{1}{2},k}H^I_{z'}\left(i-\tfrac{1}{2},j+\tfrac{1}{2},k,n+\tfrac{1}{2}\right)\right) \tag{6.36}$$

6.7 Boundary condition at air-sea interface

The boundary condition across the air-sea interface is implemented using an approximate analytical expression. This is coupled to the finite difference scheme, thus limiting the computational domain of the FDTD scheme to within the sea and seabed layers. The analytical expression is derived using a quasi-static field approximation in conjunction with the boundary conditions for the continuity of the tangential field components across the interface. This air-sea interface formulation is considered essential for modelling the propagation of up-down lateral waves.

The air-sea interface formulation used was developed by Leif Abrahamsson of FOI (Sweden), specifically for application in this model. One of the aims of this Ph.D. study was to investigate the validity of the formulation.

Two air-sea formulations were developed by Leif Abrahamsson during the course of this Ph.D. study. The first proved too unstable and could not model the correct propagation characteristics of the up-down lateral wave. This formulation is presented in Appendix B for completeness. The second proved to be successful, this formulation is presented below.

6.7.1 Air-sea interface formulation

The air-sea interface formulation presented in this chapter is fully 'discrete' in nature. Discrete in this context is akin to that of the finite difference method. All the continuous operators are expressed and evaluated in a discrete sense. In contrast, the original formulation presented in Appendix B was virtually 'continuous' in nature i.e. all the differentiations and integrations were evaluated analytically when possible using infinitesimal step sizes. It was concluded that the continuous nature of the formulation led to instabilities when coupled to the FDTD model.

For the reasons mentioned above, this formulation is derived by using the finite-difference equations as expressed in the Yee scheme. Maxwell's Equations in the following form are used as the starting point:

$$\nabla \times \mathbf{E} = -\mu \frac{\partial \mathbf{H}}{\partial t}; \tag{6.37}$$

$$\nabla \times \mathbf{H} = \varepsilon \frac{\partial \mathbf{E}}{\partial t}. \tag{6.38}$$

Equations (6.37) and (6.38) assume there are no conduction currents and no magnetic and electric sources in the air layer. These equations can be expanded into their scalar form as follows:

$$\frac{\partial E_z{}^n}{\partial y} - \frac{\partial E_y{}^n}{z} = -\mu \frac{H_x{}^{n+\frac{1}{2}} - H_x{}^{n-\frac{1}{2}}}{\Delta t} \tag{6.39}$$

$$\frac{\partial E_x{}^n}{\partial z} - \frac{\partial E_z{}^n}{\partial x} = -\mu \frac{H_y{}^{n+\frac{1}{2}} - H_y{}^{n-\frac{1}{2}}}{\Delta t} \tag{6.40}$$

$$\frac{\partial E_y{}^n}{\partial x} - \frac{\partial E_x{}^n}{\partial y} = -\mu \frac{H_z{}^{n+\frac{1}{2}} - H_z{}^{n-\frac{1}{2}}}{\Delta t} \tag{6.41}$$

$$\frac{\partial H_z{}^{n+\frac{1}{2}}}{\partial y} - \frac{\partial H_y{}^{n+\frac{1}{2}}}{\partial z} = \varepsilon \frac{E_x{}^{n+1} - E_x{}^n}{\Delta t} \tag{6.42}$$

$$\frac{\partial H_x{}^{n+\frac{1}{2}}}{\partial z} - \frac{\partial H_z{}^{n+\frac{1}{2}}}{\partial x} = \varepsilon \frac{E_y{}^{n+1} - E_y{}^n}{\Delta t} \tag{6.43}$$

$$\frac{\partial H_y{}^{n+\frac{1}{2}}}{\partial x} - \frac{\partial H_x{}^{n+\frac{1}{2}}}{\partial y} = \varepsilon \frac{E_z{}^{n+1} - E_z{}^n}{\Delta t} \tag{6.44}$$

The field components above are in the form[2] $E_x(i+{}^1/_2,j,k,n)$, $E_y(i,j+{}^1/_2,k,n)$ and $E_z(i,j,k+{}^1/_2,n)$ for the electric fields and similarly, $H_x(i,j+{}^1/_2,k+{}^1/_2,n+{}^1/_2)$,

[2] The air-sea interface is not transformed into a new co-ordinate system by the *ORTHO* algorithm, see Figure (6.4). Hence, there are no primed quantities or '*a*' and '*b*' weighting coefficients associated with this formulation.

$H_y(i+{}^1/_2,j,k+{}^1/_2,n+{}^1/_2)$ and $H_z(i+{}^1/_2,j+{}^1/_2,k,n+{}^1/_2)$ for magnetic fields. The differential operators on the left hand side of Equations (6.39) to (6.44) will be replaced by finite difference operators.

The field components in the horizontal *xy*-plane at the air-sea interface are Fourier transformed to couple the solution at each grid point. The following definitions are used for the forward and inverse 2-dimensional discrete Fourier transform (DFT): -

$$\hat{F}(\hat{i},\hat{j}) = \frac{1}{IJ}\sum_{i=0}^{I-1}\sum_{j=0}^{J-1} F(i,j) e^{-i2\pi\left(\frac{\hat{i}\cdot i}{I}+\frac{\hat{j}\cdot j}{J}\right)} \tag{6.45}$$

$$F(i,j) = \sum_{\hat{i}=0}^{I-1}\sum_{\hat{j}=0}^{J-1} \hat{F}(\hat{i},\hat{j}) e^{i2\pi\left(\frac{\hat{i}\cdot i}{I}+\frac{\hat{j}\cdot j}{J}\right)} \tag{6.46}$$

where $F(i,j)$ is a generic field component and $\hat{F}(\hat{i},\hat{j})$ is the transformed field component (i.e. all transformed variables are denoted by the hat symbol).

The DFT must be applied to each of the field points that make up the discrete operators in Equations (6.39) to (6.44). For example, the differentiation of E_x with respect to x is defined as follows within the Yee scheme

$$\frac{\partial E_x}{\partial x} = \frac{E_x\left(i+\frac{1}{2},j,k,n\right) - E_x\left(i-\frac{1}{2},j,k,n\right)}{\Delta x} \tag{6.47}$$

Applying the DFT to the difference operator above gives[3]

$$\frac{\partial \hat{E}_x}{\partial x} = \frac{\hat{E}_x(k,n) e^{i2\pi\left(\frac{\hat{i}\cdot\left(i+\frac{1}{2}\right)}{I}+\frac{\hat{j}\cdot j}{J}\right)} - \hat{E}_x(k,n) e^{i2\pi\left(\frac{\hat{i}\cdot\left(i-\frac{1}{2}\right)}{I}+\frac{\hat{j}\cdot j}{J}\right)}}{\Delta x}. \tag{6.48}$$

The exponents can be factorised (for future convenience) to give

$$\frac{\partial \bar{E}_x}{\partial x} = \frac{\bar{E}_x(k,n)e^{i2\pi\left(\frac{\hat{i}\cdot i}{I}+\frac{\hat{j}\cdot j}{J}\right)}}{\Delta x}\left(e^{i\left(\frac{2\pi\hat{i}}{I}\frac{1}{2}\right)} - e^{-i\left(\frac{2\pi\hat{i}}{I}\frac{1}{2}\right)}\right). \tag{6.49}$$

Given that $\frac{1}{2i}\left(e^{ix} - e^{-ix}\right) = \sin(x)$, Equation (6.49) becomes

$$\frac{\partial \bar{E}_x}{\partial x} = i\hat{E}_x\left(\hat{i},\hat{j}\right)\frac{2}{\Delta x}\sin\left(\frac{k_x}{2}\right)e^{i2\pi\left(\frac{\hat{i}\cdot i}{I}+\frac{\hat{j}\cdot j}{J}\right)}, \tag{6.50}$$

where k_x is defined by

$$k_x = \frac{2\pi\hat{i}}{I} \qquad 0 \le \hat{i} \le \frac{I}{2} \tag{6.51}$$

or

$$k_x = -\frac{2\pi\left(I-\hat{i}\right)}{I} \qquad \frac{I}{2} < \hat{i} \le (I-1). \tag{6.52}$$

The same approach can be applied to the following differential operator (i.e. y-component of field differentiated with respect to x):

$$\frac{\partial E_y}{\partial x} = \frac{E_x\left(i+1, j+\frac{1}{2}, k, n\right) - E_x\left(i, j+\frac{1}{2}, k, n\right)}{\Delta x}. \tag{6.53}$$

The application of the DFT to Equation (6.53) gives

---

[3] The $\hat{i}$ and $\hat{j}$ counters within the transformed field variables, has been dropped for brevity i.e. $\bar{F}\left(\hat{i},\hat{j},k,n\right)$ becomes $\bar{F}(k,n)$.

$$\frac{\partial \hat{E}_y}{\partial x} = \frac{\hat{E}_y(k,n)e^{i2\pi\left(\frac{\hat{i}\cdot(i+1)}{I}+\frac{\hat{j}\cdot\left(j+\frac{1}{2}\right)}{J}\right)} - \hat{E}_y(k,n)e^{i2\pi\left(\frac{\hat{i}\cdot i}{I}+\frac{\hat{j}\cdot\left(j+\frac{1}{2}\right)}{J}\right)}}{\Delta x}. \quad (6.54)$$

The exponents can be factorised to give

$$\frac{\partial \hat{E}_y}{\partial x} = \frac{\hat{E}_y(k,n)e^{i2\pi\left(\frac{\hat{i}\cdot\left(i+\frac{1}{2}\right)}{I}+\frac{\hat{j}\cdot\left(i+\frac{1}{2}\right)}{J}\right)}}{\Delta x}\left(e^{i\left(\frac{2\pi\hat{i}}{I}\frac{1}{2}\right)} - e^{-i\left(\frac{2\pi\hat{i}}{I}\frac{1}{2}\right)}\right). \quad (6.55)$$

Note the subtle difference in the factored exponents within Equations (6.49) and (6.55). Making use of the identity introduced above, $\frac{1}{2i}\left(e^{ix} - e^{-ix}\right) = \sin(x)$, gives

$$\frac{\partial \hat{E}_y}{\partial x} = i\hat{E}_y(\hat{i},\hat{j})\frac{2}{\Delta x}\sin\left(\frac{k_x}{2}\right)e^{i2\pi\left(\frac{\hat{i}\cdot\left(i+\frac{1}{2}\right)}{I}+\frac{\hat{j}\cdot\left(i+\frac{1}{2}\right)}{J}\right)}. \quad (6.56)$$

The application of the DFT therefore gives

$$\frac{\partial \hat{E}_x}{\partial x} = i\tilde{k}_x\hat{E}_x \quad (6.57)$$

for x-derivatives, and

$$\frac{\partial \hat{E}_y}{\partial y} = i\tilde{k}_y\hat{E}_y \quad (6.58)$$

for y–derivatives, where

$$\tilde{k}_x = \frac{2}{\Delta x}\sin\left(\frac{k_x}{2}\right), \quad (6.59)$$

$$\tilde{k}_y = \frac{2}{\Delta y}\sin\left(\frac{k_y}{2}\right) \tag{6.60}$$

and

$$k_y = \frac{2\pi\hat{j}}{J} \qquad 0 \le \hat{j} \le \frac{J}{2} \tag{6.61}$$

or

$$k_y = -\frac{2\pi(I-\hat{j})}{J} \qquad \frac{J}{2} < \hat{j} \le (J-1). \tag{6.62}$$

The application of the DFT to Equations (6.39) to (6.44) using the methodology described above will therefore give[4]: -

$$i\tilde{k}_y\hat{E}_z\left(k+\tfrac{1}{2},n\right) - \frac{1}{\Delta z}\left[\hat{E}_y(k+1,n) - \hat{E}_y(k,n)\right] = -\mu\frac{1}{\Delta t}\left[\hat{H}_x\left(k+\tfrac{1}{2},n+\tfrac{1}{2}\right) - \hat{H}_x\left(k+\tfrac{1}{2},n-\tfrac{1}{2}\right)\right] \tag{6.63}$$

$$\frac{1}{\Delta z}\left[\hat{E}_x(k+1,n) - \hat{E}_x(k,n)\right] - i\tilde{k}_x\hat{E}_z\left(k+\tfrac{1}{2},n\right) = -\mu\frac{1}{\Delta t}\left[\hat{H}_y\left(k+\tfrac{1}{2},n+\tfrac{1}{2}\right) - \hat{H}_y\left(k+\tfrac{1}{2},n-\tfrac{1}{2}\right)\right] \tag{6.64}$$

$$i\tilde{k}_x\hat{E}_y(k,n) - i\tilde{k}_y\hat{E}_x(k,n) = -\mu\frac{1}{\Delta t}\left[\hat{H}_z\left(k,n+\tfrac{1}{2}\right) - \hat{H}_z\left(k,n-\tfrac{1}{2}\right)\right] \tag{6.65}$$

$$i\tilde{k}_y\hat{H}_z\left(k,n+\tfrac{1}{2}\right) - \frac{1}{\Delta z}\left[\hat{H}_y\left(k+\tfrac{1}{2},n+\tfrac{1}{2}\right) - \hat{H}_y\left(k-\tfrac{1}{2},n+\tfrac{1}{2}\right)\right] = \varepsilon\frac{1}{\Delta t}\left[\hat{E}_x(k,n+1) - \hat{E}_x(k,n)\right] \tag{6.66}$$

$$\frac{1}{\Delta z}\left[\hat{H}_x\left(k+\tfrac{1}{2},n+\tfrac{1}{2}\right) - \hat{H}_x\left(k-\tfrac{1}{2},n+\tfrac{1}{2}\right)\right] - i\tilde{k}_x\hat{H}_z\left(k,n+\tfrac{1}{2}\right) =$$

[4] The exponential terms in the form $e^{i2\pi[\ldots]}$ all cancel each other out in the following equations.

$$\varepsilon \frac{1}{\Delta t}\left[\hat{E}_y(k,n+1)-\hat{E}_y(k,n)\right] \tag{6.67}$$

$$i\tilde{k}_x \hat{H}_y\left(k+\tfrac{1}{2},n+\tfrac{1}{2}\right)-i\tilde{k}_y \hat{H}_x\left(k+\tfrac{1}{2},n+\tfrac{1}{2}\right)=$$

$$\varepsilon \frac{1}{\Delta t}\left[\hat{E}_z\left(k+\tfrac{1}{2},n+1\right)-\hat{E}_z\left(k+\tfrac{1}{2},n\right)\right] \tag{6.68}$$

The finite difference scheme is implemented such that the tangential electric field components are situated at the air-sea interface (see Figure 6.9).

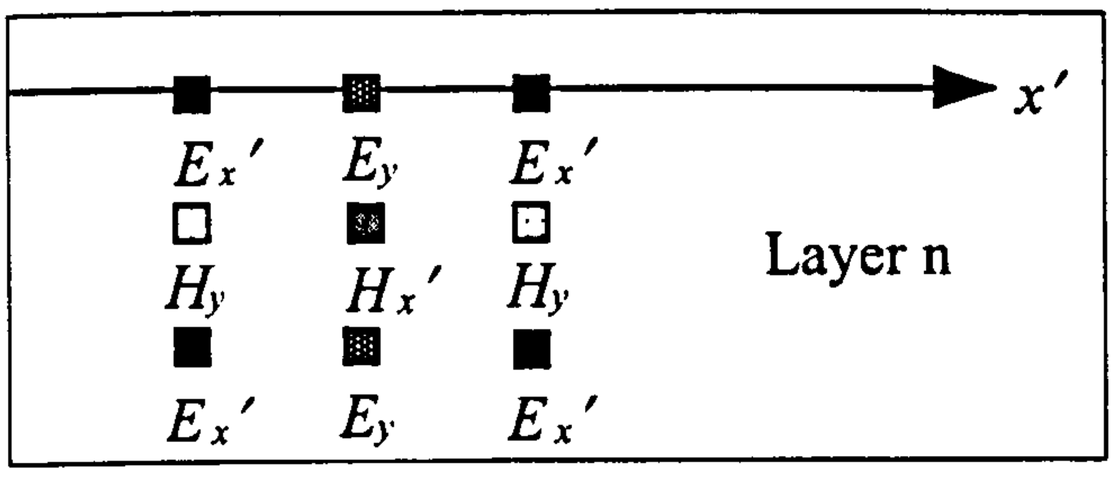

Figure 6.9: Nodes at air-sea interface

The magnetic field components can thus be eliminated by substitution. The substitution process can be facilitated by multiplying Equations (6.63) to (6.65) by $\varepsilon/\Delta z$, and multiplying Equations (6.66) to (6.68) by $\mu/\Delta t$.

$$-\frac{1}{\Delta z^2}\left[\hat{E}_x(k+1,n)-2\hat{E}_x(k,n)+\hat{E}_x(k-1,n)\right]+i\tilde{k}_x \frac{1}{\Delta z}\left[\hat{E}_z\left(k+\tfrac{1}{2},n\right)-\hat{E}_z\left(k-\tfrac{1}{2},n\right)\right]+$$

$$\tilde{k}_y^2 \hat{E}_x(k,n)-\tilde{k}_x\tilde{k}_y \hat{E}_y(k,n)=-\mu\varepsilon \frac{1}{\Delta t^2}\left[\hat{E}_x(k,n+1)-2\hat{E}_x(k,n)+\hat{E}_x(k,n-1)\right] \tag{6.69}$$

$$-\frac{1}{\Delta z^2}\left[\hat{E}_y(k+1,n)-2\hat{E}_y(k,n)+\hat{E}_y(k-1,n)\right]+i\tilde{k}_y \frac{1}{\Delta z}\left[\hat{E}_z\left(k+\tfrac{1}{2},n\right)-\hat{E}_z\left(k-\tfrac{1}{2},n\right)\right]+$$

$$\tilde{k}_x^2 \hat{E}_y(k,n)-\tilde{k}_x\tilde{k}_y \hat{E}_x(k,n)=-\mu\varepsilon \frac{1}{\Delta t^2}\left[\hat{E}_y(k,n+1)-2\hat{E}_y(k,n)+\hat{E}_y(k,n-1)\right] \tag{6.70}$$

$$\left(\tilde{k}_x^2+\tilde{k}_y^2\right)\hat{E}_z\left(k+\tfrac{1}{2},n\right)+i\tilde{k}_x \frac{1}{\Delta z}\left[\hat{E}_x(k+1,n)-\hat{E}_x(k,n)\right]+i\tilde{k}_y \frac{1}{\Delta z}\left[\hat{E}_y(k+1,n)-\hat{E}_y(k,n)\right]=$$

$$-\mu\varepsilon\frac{1}{\Delta t^2}\left[\hat{E}_z\left(k+\tfrac{1}{2},n+1\right)-2\hat{E}_z\left(k+\tfrac{1}{2},n\right)+\hat{E}_z\left(k+\tfrac{1}{2},n-1\right)\right] \quad (6.71)$$

Equations (6.69) to (6.70) can be simplified by using the quasi-static approximation (i.e. ε=0) and by forcing the divergence of the electric field to be zero. The divergence in discrete form (after the application of the DFT) is given by Equation (6.72).

$$\frac{1}{\Delta z}\left[\hat{E}_z\left(k+\tfrac{1}{2},n\right)-\hat{E}_z\left(k-\tfrac{1}{2},n\right)\right]+i\tilde{k}_y\hat{E}_y(k,n)+i\tilde{k}_x\hat{E}_x(k,n)=0 \quad (6.72)$$

This gives the following expressions for $\hat{E}_x$ and $\hat{E}_y$

$$\frac{1}{\Delta z^2}\left[\hat{E}_x(k+1,n)-2\hat{E}_x(k,n)+\hat{E}_x(k-1,n)\right]=\left(\tilde{k}_x^2+\tilde{k}_y^2\right)\hat{E}_x(k,n), \quad (6.73)$$

$$\frac{1}{\Delta z^2}\left[\hat{E}_y(k+1,n)-2\hat{E}_y(k,n)+\hat{E}_y(k-1,n)\right]=\left(\tilde{k}_x^2+\tilde{k}_y^2\right)\hat{E}_y(k,n) \quad (6.74)$$

and

$$\hat{E}_z\left(k+\tfrac{1}{2},n\right)=\frac{1}{\tilde{k}_x^2+\tilde{k}_y^2}\left\{-i\tilde{k}_x\frac{1}{\Delta z}\left[\hat{E}_x(k+1,n)-\hat{E}_x(k,n)\right]\right.$$
$$\left.-i\tilde{k}_y\frac{1}{\Delta z}\left[\hat{E}y(k+1,n)-\hat{E}y(k,n)\right]\right\} \quad (6.75)$$

for $\hat{E}_z$ in terms of $\hat{E}_x$ and $\hat{E}_y$.

The solution to Equations (6.73) is postulated to be in the form of Equation (C.16); where χ is a real variable and k is an integer representing the vertical counter in the FDTD grid.

$$\hat{E}x(k,n)=\chi^k\hat{E}x(0,n). \quad (6.76)$$

This form of the solution is based on the derivation detailed in Appendix C for the same problem solved directly from Maxwell's equations. Substituting Equation (6.76) into Equation (6.73) yields

$$\frac{1}{\Delta z^2}\left[\chi^{k+1} - 2\chi^k + \chi^{k-1}\right]\tilde{E}x(0,n) = \left(\tilde{k}_x^2 + \tilde{k}_y^2\right)\chi^k\,\tilde{E}x(0,n), \tag{6.77}$$

which simplifies to

$$\frac{1}{\Delta z^2}\left[\chi^2 - 2\chi + 1\right] = \left(\tilde{k}_x^2 + \tilde{k}_y^2\right)\chi\,. \tag{6.78}$$

when k=1. This can be rearranged into the quadratic form $a\chi^2 + b\chi + c = 0$ to give

$$\left[\chi^2 - \chi\left(2 + \Delta z^2\left(\tilde{k}_x^2 + \tilde{k}_y^2\right)\right) + 1\right] = 0\,, \tag{6.79}$$

which has a solution given by

$$\chi = \frac{-b \pm \sqrt{b^2 - 4ac}}{2a}. \tag{6.80}$$

Thus, giving the following solution for χ if the positive root is chosen

$$\chi = 1 + \frac{1}{2}\Delta z^2\left(\tilde{k}_x^2 + \tilde{k}_y^2\right) + \sqrt{\Delta z^2\left(\tilde{k}_x^2 + \tilde{k}_y^2\right) + \frac{1}{4}\Delta z^4\left(\tilde{k}_x^2 + \tilde{k}_y^2\right)^2}\,. \tag{6.81}$$

The same process can also be used for $\tilde{E}_y$. This will result in a solution for χ identical to Equation (6.81). The boundary conditions for the continuity of the tangential magnetic fields across the interface can be exploited to couple the discrete analytical formulation with the finite difference scheme. The continuity of H_x and H_y can be expressed as follows using Equation (6.1),

$$\frac{\partial {E_x}^A}{\partial z} - \frac{\partial {E_z}^A}{\partial x} = \frac{\partial {E_x}^W}{\partial z} - \frac{\partial {E_z}^W}{\partial x} \tag{6.82}$$

and

$$\frac{\partial E_z{}^A}{\partial y} - \frac{\partial E_y{}^A}{\partial z} = \frac{\partial E_z{}^W}{\partial y} - \frac{\partial E_y{}^W}{\partial z}. \tag{6.83}$$

The '*A*' and '*W*' superscripts in Equations (6.82) and (6.83) denote fields in the air and water at infinitesimal distances from the interface. Given that the electric field components for E_x and E_y lie on the interface, and E_z is ½ a step size above and below the interface, the Fourier transform of the boundary conditions yields

$$i\tilde{k}_y \hat{E}_z\left(-\tfrac{1}{2},n\right) - \frac{1}{\Delta z}\left[\hat{E}_y(0,n) - \hat{E}_y(-1,n)\right] =$$

$$i\tilde{k}_y \hat{E}_z\left(\tfrac{1}{2},n\right) - \frac{1}{\Delta z}\left[\hat{E}_y(1,n) - \hat{E}_y(0,n)\right] \tag{6.84}$$

and

$$\frac{1}{\Delta z}\left[\hat{E}_x(0,n) - \hat{E}_x(-1,n)\right] - i\tilde{k}_x \hat{E}_z\left(-\tfrac{1}{2},n\right) =$$

$$\frac{1}{\Delta z}\left[\hat{E}_x(1,n) - \hat{E}_x(0,n)\right] - i\tilde{k}_x \hat{E}_z\left(\tfrac{1}{2},n\right). \tag{6.85}$$

All the electric field points in Equations (6.84) and (6.85) need to be expressed in terms of field points (or FDTD nodes) in the seawater (i.e. within the FDTD mesh). Equations (6.76) and (6.81) can be used to map field points in the air to field points on the sea surface. This gives rise to the following substitutions: -

$$\frac{\hat{E}_x(0,n) - \hat{E}_x(-1,n)}{\Delta z} = \frac{1-\chi^{-1}}{\Delta z}\hat{E}_x(0,n); \tag{6.86}$$

$$\frac{\hat{E}_y(0,n) - \hat{E}_y(-1,n)}{\Delta z} = \frac{1-\chi^{-1}}{\Delta z}\hat{E}_y(0,n); \tag{6.87}$$

$$\hat{E}_z\left(-\tfrac{1}{2},n\right) = \frac{1}{\tilde{k}_x^2 + \tilde{k}_y^2}\left\{-i\tilde{k}_x\left(\frac{1-\chi^{-1}}{\Delta z}\right)\hat{E}_x(0,n) - i\tilde{k}_y\left(\frac{1-\chi^{-1}}{\Delta z}\right)\hat{E}_y(0,n)\right\}. \tag{6.88}$$

The two resulting boundary conditions can now be expressed in the form of Equation (6.89) and solved for the two unknowns, $\tilde{E}_x$ and $\tilde{E}_y$.

$$\begin{bmatrix} a_{11} & a_{12} \\ a_{21} & a_{22} \end{bmatrix} \begin{bmatrix} \tilde{E}_x(0,n) \\ \tilde{E}_y(0,n) \end{bmatrix} = \begin{bmatrix} f_1 \\ f_2 \end{bmatrix} \tag{6.89}$$

The terms within the matrix Equation (6.89) are defined as follows: -

$$a_{11} = \frac{1}{\Delta z} + \frac{1-\chi^{-1}}{\Delta z}\left(1 - \frac{\tilde{k}_x^2}{\tilde{k}_x^2 + \tilde{k}_y^2}\right); \tag{6.90}$$

$$a_{12} = -\left(\frac{1-\chi^{-1}}{\Delta z}\right)\frac{\tilde{k}_x \tilde{k}_y}{\tilde{k}_x^2 + \tilde{k}_y^2}; \tag{6.91}$$

$$a_{21} = -\left(\frac{1-\chi^{-1}}{\Delta z}\right)\frac{\tilde{k}_x \tilde{k}_y}{\tilde{k}_x^2 + \tilde{k}_y^2}; \tag{6.92}$$

$$a_{22} = \frac{1}{\Delta z} + \frac{1-\chi^{-1}}{\Delta z}\left(1 - \frac{\tilde{k}_y^2}{\tilde{k}_x^2 + \tilde{k}_y^2}\right); \tag{6.93}$$

$$f_1 = \frac{1}{\Delta z}\hat{E}_x(1,n) - i\tilde{k}_x \hat{E}_z\left(\frac{1}{2},n\right); \tag{6.94}$$

and

$$f_2 = \frac{1}{\Delta z}\hat{E}_y(1,n) - i\tilde{k}_y \hat{E}_z\left(\frac{1}{2},n\right). \tag{6.95}$$

6.8 Spatial steps

The FDTD approach requires that the problem space is discretised into small cubic elements, the dimensions of which can affect the accuracy of the solution. The spatial step size is usually chosen to be around 20 steps per wavelength. Given that the

wavelength is dependent on the conductivity of the medium, the shortest wavelength within the problem space is typically within the sea layer.

This corresponds to approximately 3 steps over one skin depth (i.e. wavelength $\lambda = 2\pi\delta$). This is considered adequate to describe an exponentially decaying solution in space. Figure 6.10 shows a comparison between an analytical function decaying exponentially over one skin depth (i.e. from 1.0 to 0.3678) and the same function approximated linearly using 3 steps.

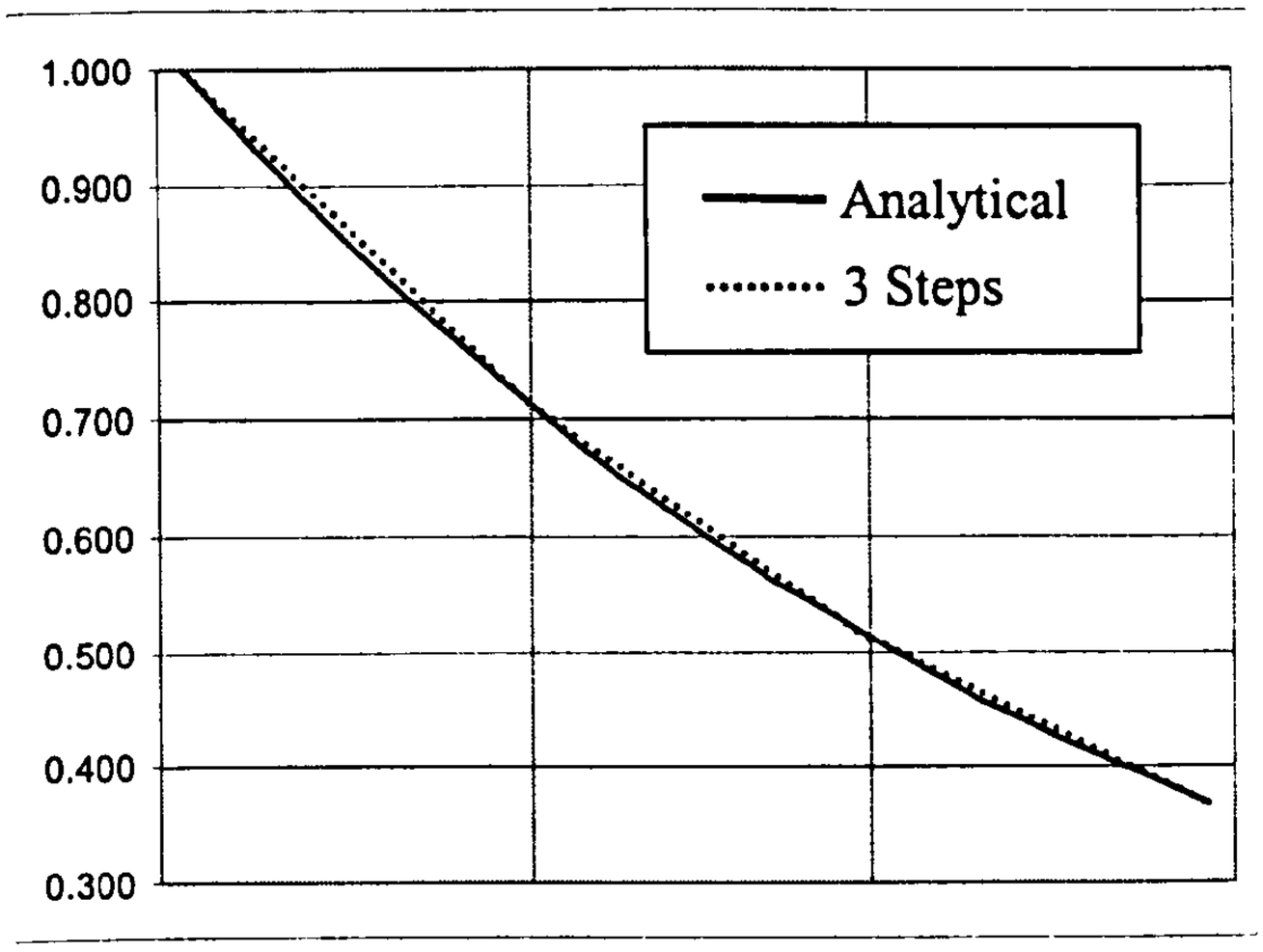

Figure 6.10: Approximating exponential decay

6.9 Stability / time steps

The time step used to increment the FDTD solution is currently determined using a modified version of the Courant stability criterion, which is defined by

$$\Delta t\left(\frac{1}{\Delta x'^2}+\frac{1}{\Delta y^2}+\frac{1}{\Delta z'^2}\right)^{\frac{1}{2}} \leq \frac{1}{2}\sigma\mu \qquad (6.96)$$

The Courant stability criterion can be used to calculate the largest possible time step that can be used whilst maintaining a stable scheme given the spatial step sizes and the media parameters.

Equation (6.96) has been modified to take account of the spatial distortion arising from the co-ordinate transformation. This requires the 'a' and 'b' weighting factors to be taken into account. The stability criterion used is defined as

$$\Delta t \leq \frac{1}{2}\sigma\mu(\Delta x')\left(\frac{a^2b^2}{a^2+a^2b^2+b^2}\right)^{\frac{1}{2}}. \tag{6.97}$$

Equation (6.97) assumes the spatial step sizes are all equal (i.e. $\Delta x' = \Delta y = \Delta z'$). The time step is calculated using the lowest conductivity from all the layers (i.e. normally the seabed) and is used globally throughout the scheme. In practice, the time step is chosen to be typically half that given by Equation (6.97) to 'guarantee' stability.

6.10 Model implementation

The FDTD formulations presented in this chapter are all implemented within a single FORTRAN90 program, which is executable on most personal computers and workstations. The program operation mainly consists of looping through all the i,j,k and n counters, applying different formulations when required (i.e. at interface boundaries and the air-sea interface). The most complex aspect of the program is accounting for all the variables and ensuring they are initialised correctly as the program jumps to different formulations.

The *ORTHO* algorithm that performs the co-ordinate transformations was supplied by FOI (Sweden). This has been integrated into two separate programs that calculate the 'a' and 'b' weighting factors for each mesh point and the rotation angle of the source. The co-ordinate transformation distorts the space around the source, thus forcing it to change orientation. The rotation angle is used to resolve the source into components parallel (i.e. HED source) and perpendicular (i.e. VED source) to the x'-axis.

Several programs are used in total to perform all the necessary calculations and in some cases to check to consistency of the input data (i.e. validity of spatial steps). The consistency of data can be critical, since it can take up to five days of continuous computations before numerical instabilities become apparent.

Chapter 7

Validation

This Chapter details the validation of the approximate analytical and numerical FDTD sloping seabed models. The validation process focused on testing the main components of each model. The components addressed are as follows for each of the models

Analytical model:

- Geometrical-imaging technique
- Geometrical-optical approach

FDTD model:

- Interface boundary condition
- Air-sea interface boundary condition
- Co-ordinate transformation

The tests were all carried such that the results could be compared against known data sets. The data sets were all generated using the *NLAYER* propagation developed by FOI of Sweden. The *NLAYER* model has been validated extensively against the experimentally validated KCL model *LAYER*. *NLAYER* was used because it could produce time-domain results and is computationally more efficient.

The validation of the co-ordinate transformation exploited by the FDTD code was performed by cross-validating the two sloping seabed models with each other. The comparison was unfortunately restricted to the deep-water case, thus neglected the contribution from the interface interactions. Shallow water results proved to be computationally too expensive (approximately one month per run). The underlying reasons leading to this problem are described in the discussions.

7.1 Validation of geometrical-imaging technique

The geometrical-imaging technique developed for the 'wedge-like' sloping seabed environment is the first of its kind. This section aims to demonstrate the validity of the imaging technique by comparing the path length and angles of incidence predictions for a secondary reflection calculated with those obtained using analytical expressions. It is assumed that this test will also be sufficient to validate the imaging technique employed for modelling reflected lateral wave interactions. Since the same methodology is applied to determine the location of the image sources and observers.

The problem geometry and the secondary reflection considered are shown in Figure 7.1. The location of the image-source is also indicated relative to the real environment.

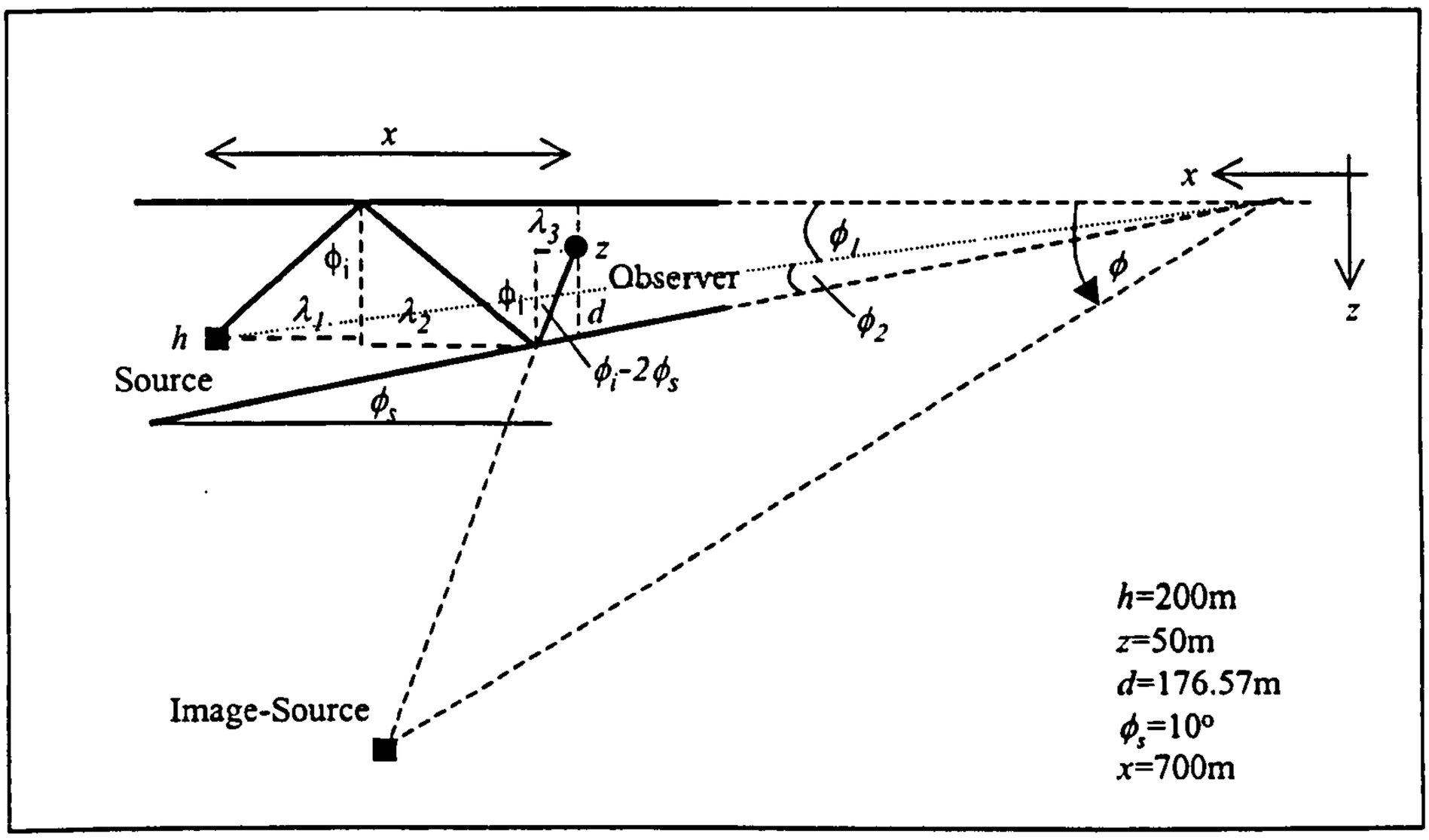

Figure 7.1: Schematic representation of secondary reflection

7.1.1 Analytical method

The horizontal source-observer separation can be expressed as

$$x = \lambda_1 + \lambda_2 + \lambda_3, \tag{7.1}$$

where λ_1, λ_2 and λ_3 are the lengths for one of the triangle's sides as shown in Figure 7.1. These triangles are formed by dividing the path length of the secondary reflection into three parts and using the angles of incidence with the interfaces. The analytical expressions for λ_1, λ_2 and λ_3 are

$$\lambda_1 = h\tan(\phi_i), \tag{7.2}$$

$$\lambda_2 = \left[\frac{(d-z)\cos(\phi_s)}{\cos(\phi_i - \phi_s)}\cos(\phi_i - 2\phi_s) + z\right]\tan(\phi_i), \tag{7.3}$$

and

$$\lambda_3 = \frac{(d-z)\cos(\phi_s)}{\cos(\phi_i - \phi_s)}\sin(\phi_i - 2\phi_s). \tag{7.4}$$

Equation (7.1) can be solved iteratively to determine the value of ϕ_i that gives a horizontal separation of x=700m. Figure 7.2 shows how x varies with ϕ_i for a small range of angles.

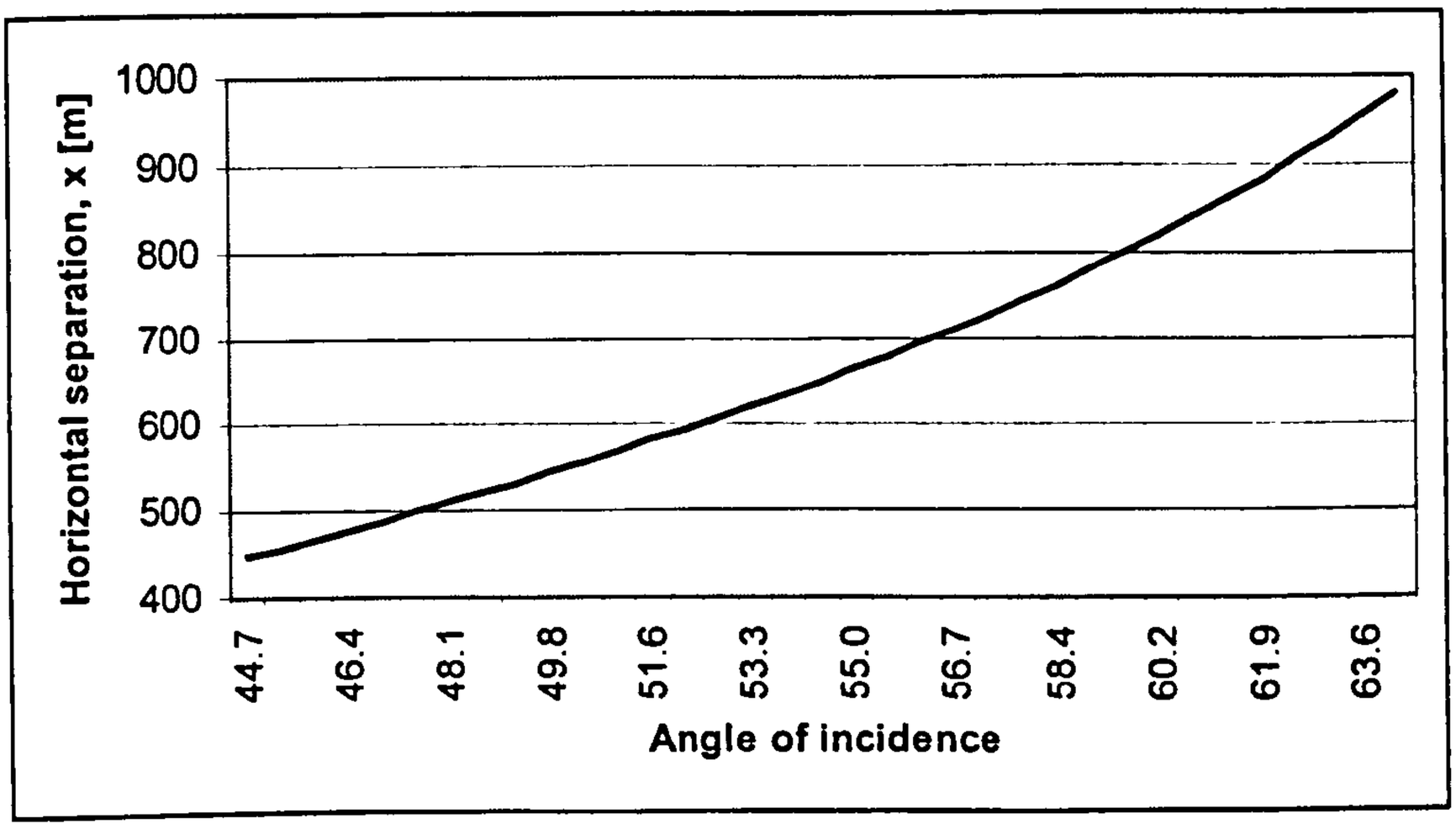

Figure 7.2: The horizontal separation, x as a function of ϕ_i

The iterative solution gives an angle of incidence of ϕ_i=56.31°. This can be used to calculate the geometrical path length for the secondary reflection using Equation 7.5, which is also determined using the geometry of the triangles shown in Figure 7.1. Substituting ϕ_i=56.31° into Equation 7.5 gives a path length of L=893.31m.

$$L = \frac{h}{\cos(\phi_i)} + \frac{l}{\cos(\phi_i)}\left[\frac{(d-z)\cos(\phi_s)}{\cos(\phi_i - \phi_s)}\cos(\phi_i - 2\phi_s) + z\right] + \frac{(d-z)\cos(\phi_s)}{\cos(\phi_i - \phi_s)} \qquad (7.5)$$

7.1.2 Imaging technique

The wedge apex was used as the origin of the co-ordinate system to make all the geometrical-imaging calculations, see Figure 7.1. The real-source and real-observer co-ordinates are (1701.39m, 200.0m) and (1001.39m, 50.0m) respectively, within this co-ordinate system.

The real-source is thus r=1713.1m from the origin i.e. $r = \sqrt{x^2 + z^2}$. The co-ordinates of the image-source can be calculated using

$$x' = r\cos(\phi) \qquad (7.6)$$

$$z' = r\sin(\phi) \qquad (7.7)$$

where the angle ϕ is given by

$$\phi = \phi_1 + 2(\phi_1 + \phi_2) \qquad (7.8)$$

Figure 7.1 can be used to show that ϕ_1=6.70°, ϕ_2=3.30°, hence ϕ=26.70°. The image-source co-ordinates are thus (1530.37m, 769.85m). The angles of incidence and the path length can now be calculated using Equations 7.9 and 7.10 and the real-observer co-ordinates (x_o,z_o).

$$\phi_i = \tan\left(\frac{x' - x_o}{z' - z_o}\right) + 2\phi_s \tag{7.9}$$

$$L = \sqrt{(x' - x_o)^2 + (z' - z_o)^2} \tag{7.10}$$

The angle of incidence equals ϕ_i=56.31° and the path length equals L=893.31m.

7.1.3 Summary of results

The analytical calculations and the geometrical-imaging technique have produced identical results to two decimal places. This result demonstrates the validity of the imaging technique employed to determine the path length and the angles of incidence for the secondary reflections. It also validates the method used to determine the location of the image-sources and image-observers for the reflected lateral waves.

	Angle of incidence	Path-length
Analytical method	56.31°	893.31m
Geometrical-Imaging technique	56.31°	893.31m

Table 7.1: Summary of geometrical-imaging results

7.2 Validation of geometrical-optical approach

This Section details the validation of the geometrical-optical approach used to model the secondary reflections and the reflected lateral waves. Results obtained using the approximate techniques were cross-validated against the solution obtained using the *NLAYER* propagation model.

7.2.1 Modular solution

The results presented in this Section are generated by considering a VED source. Only the peak positive E_z field from the Ricker pulse (see Section 7.3 for more details) is plotted.

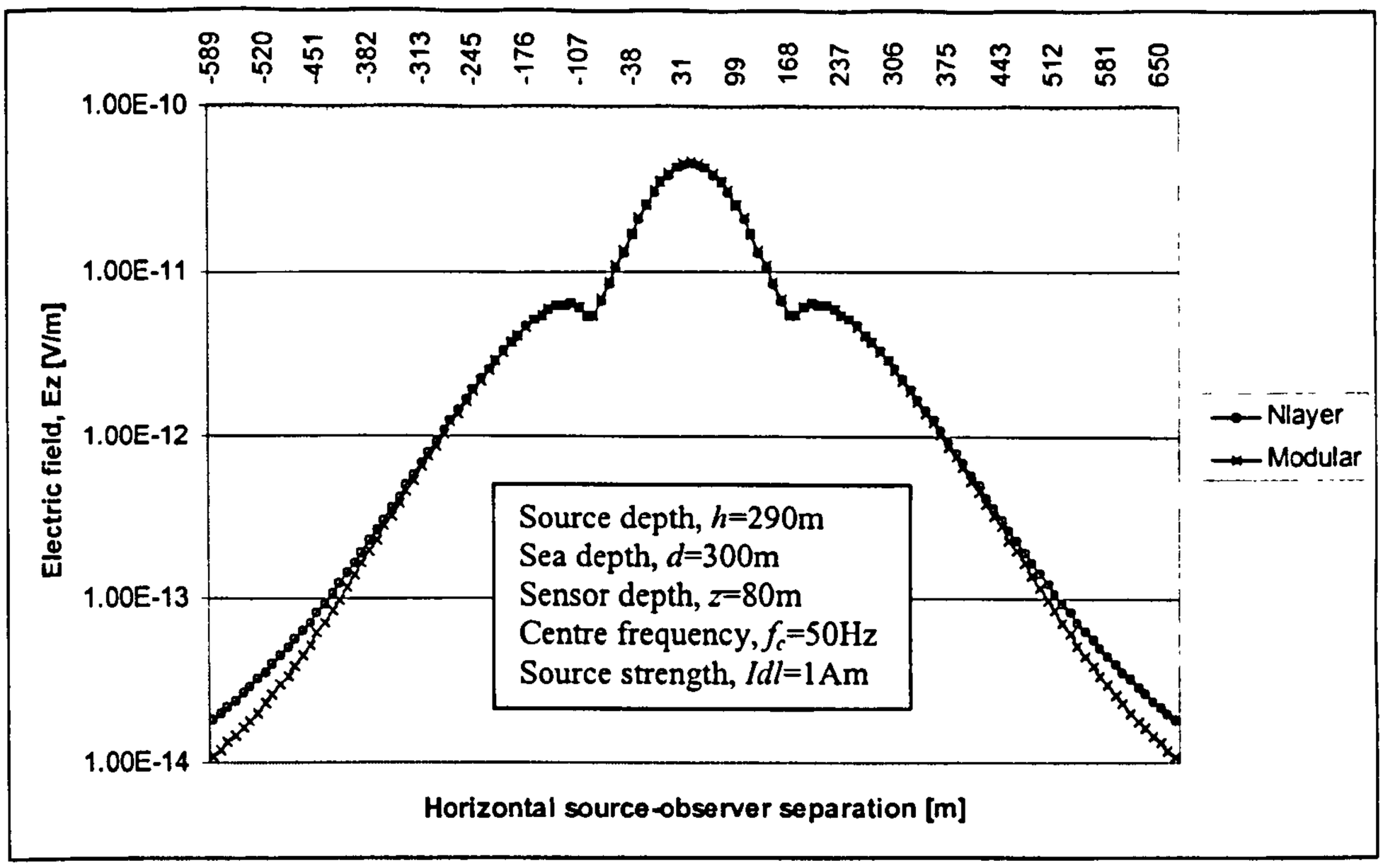

Figure 7.3: Comparison between *NLAYER* and modular solution

Figure 7.3 shows there are significant differences between the full solution obtained using *NLAYER* and the modular solution. These differences are attributed to the omission of the interface interactions.

7.2.2 Interface interactions

Figure 7.4 shows schematic representation of the two most significant interface interactions.

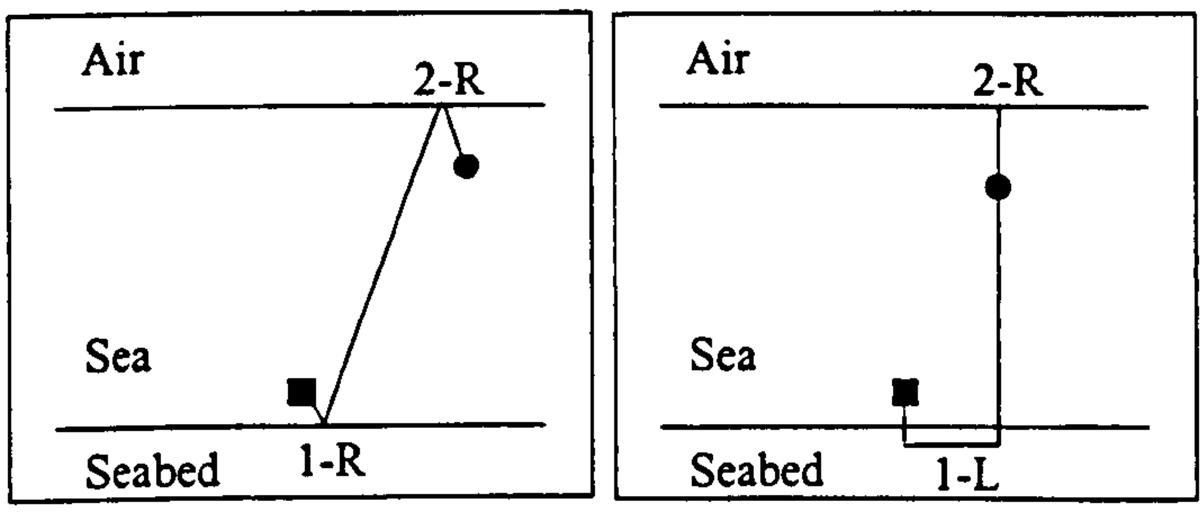

Figure 7.4: Schematic representation of interface interactions

The interface interactions are denoted by the order in which the interactions occur (1=1st or 2=2nd) and the type of interaction (R=reflection or L=lateral wave) in the

form 'order-type'. The left-hand figure shows a secondary reflection and the right-hand figure shows the arrival of a reflected lateral.

Figure 7.5 shows the relative contribution of each of these modes compared to the original *NLAYER* solution. In practice, there will be a larger, but finite number of interface interactions. However, these tend to progressively contribute less and less to the overall field levels, due to the increased attenuation as the radiation bounces between the interfaces.

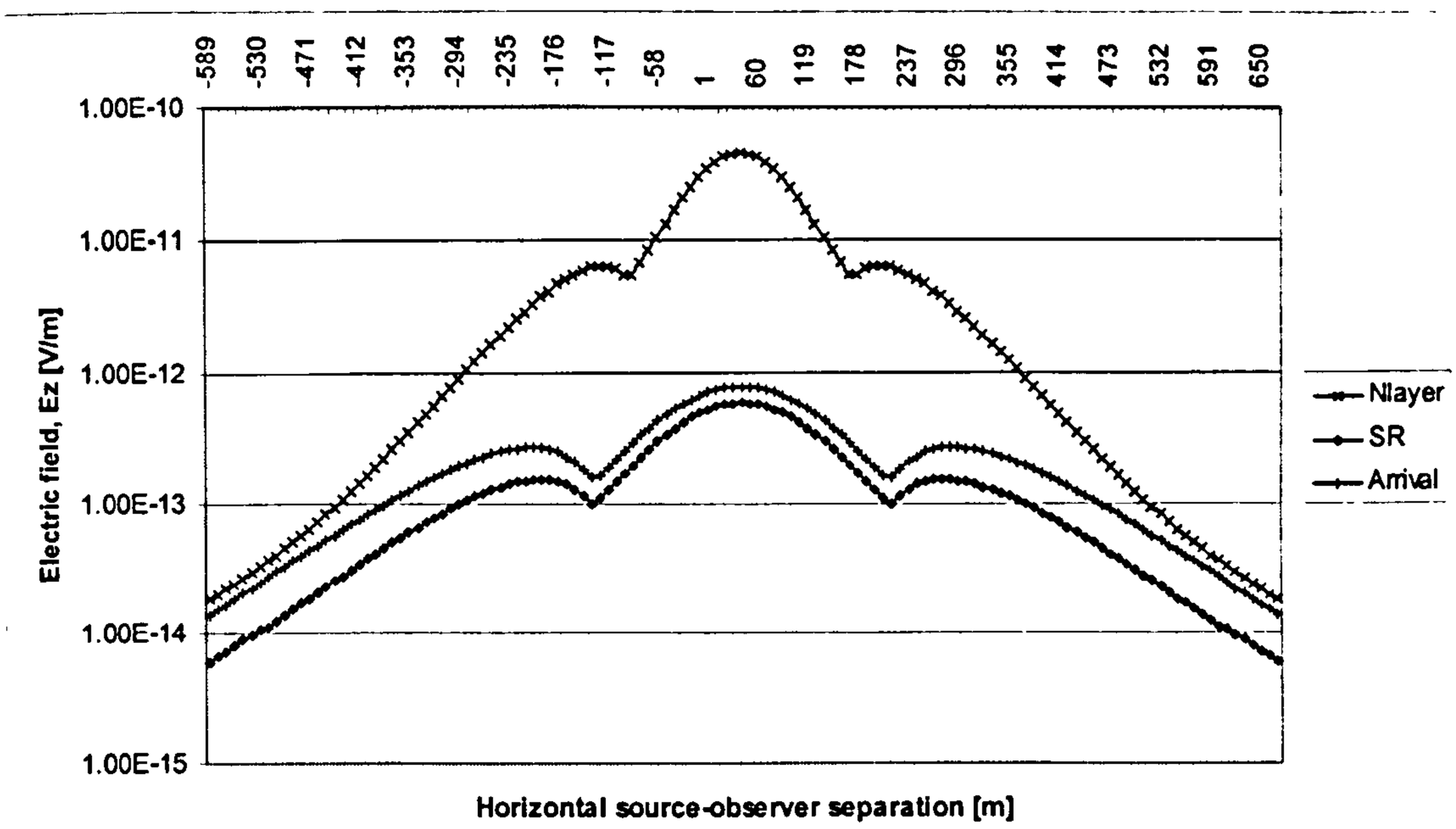

Figure 7.5: Contribution of interface interactions

7.2.3 Corrected modular solution

Figure 7.6 shows how the corrected solution (i.e. modular solution plus the interface interactions) compares to the *NLAYER* and modular solutions. The percentage difference between the field predictions obtained using *NLAYER* and the modular approach has been reduced from 40% to 0.41% at x=640m. The average percentage difference has been reduced from 12% to 3.2%. This difference can be reduced further by including more interface interactions.

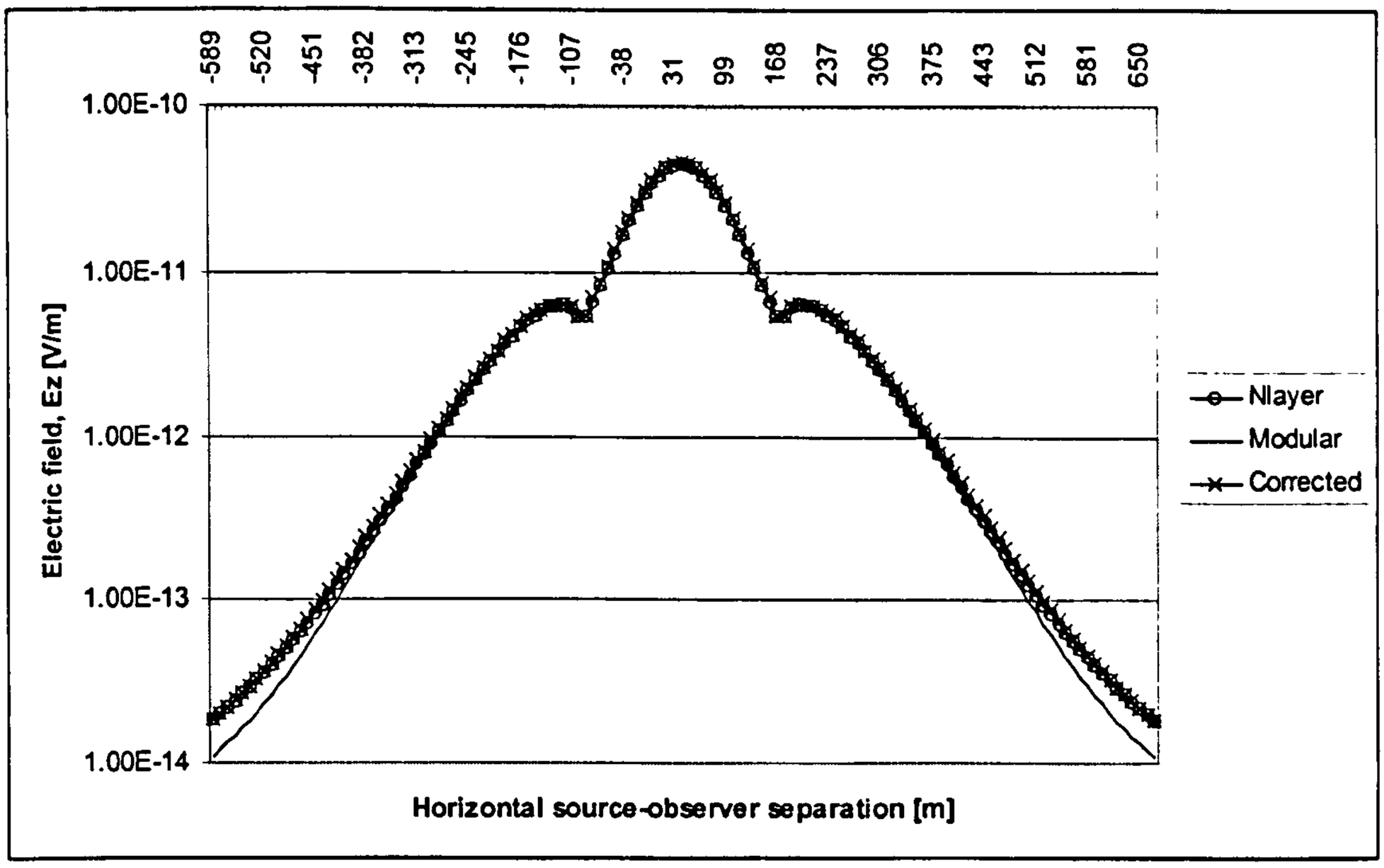

Figure 7.6: Comparison between *NLAYER* and corrected solution

7.2.4 Summary of results

The results show that the modular solution can be improved by including additional corrections for the interface interactions. The corrected solution was in good agreement with the solution produced using *NLAYER*, thus demonstrating the validity of the geometrical-imaging technique.

The number of interface interactions required to improve the accuracy of the solution will depend on both the frequency and the slope angle. At lower frequencies, more corrections are required. At greater slope angles, the number of total interface interactions possible will fall.

7.3 Transient pulse

The field predictions used for the validation process were obtained using horizontal (HED) and vertical electric dipole (VED) sources excited with a transient pulse (see below).

The transient signal used to excite the FDTD source throughout this study was the 'Ricker' pulse (Abrahamsson, 2000). This is defined by

$$r(t) = \left(2\frac{t^2}{\tau^2} - 1\right)\exp\left(-\frac{t^2}{\tau^2}\right) \tag{7.11}$$

where t is time, $\tau = 1/\pi f_c$ and f_c is the centre frequency of the pulse. This pulse was chosen due to its narrow 'window' in both time and frequency. A transient signal was preferred over a sinusoidal signal due to the 'start-up' problems associated with the latter. The start-up problems refer to the introduction of additional frequency components, particularly those with low frequencies. The additional frequencies are generated because the sinusoidal signal starts abruptly at $t=0$ i.e. the sinusoid is convoluted with a step[1] function. This problem can be overcome if the number of time steps is increased such that the FDTD code is allowed to run for several periods of the sinusoidal wave. This ensures the unwanted frequency components have had sufficient time to decay away. However, this option was computationally unacceptable for most the problems addressed in this study. Figure 7.7 shows a Ricker pulse with a centre frequency of 300Hz and Figure 7.8 shows the Fourier transform of this pulse. The pulse is offset by letting t equal $(t-q\Delta t)$, where is Δt is the FDTD spatial time step and q is an arbitrary constant used to offset the pulse in time.

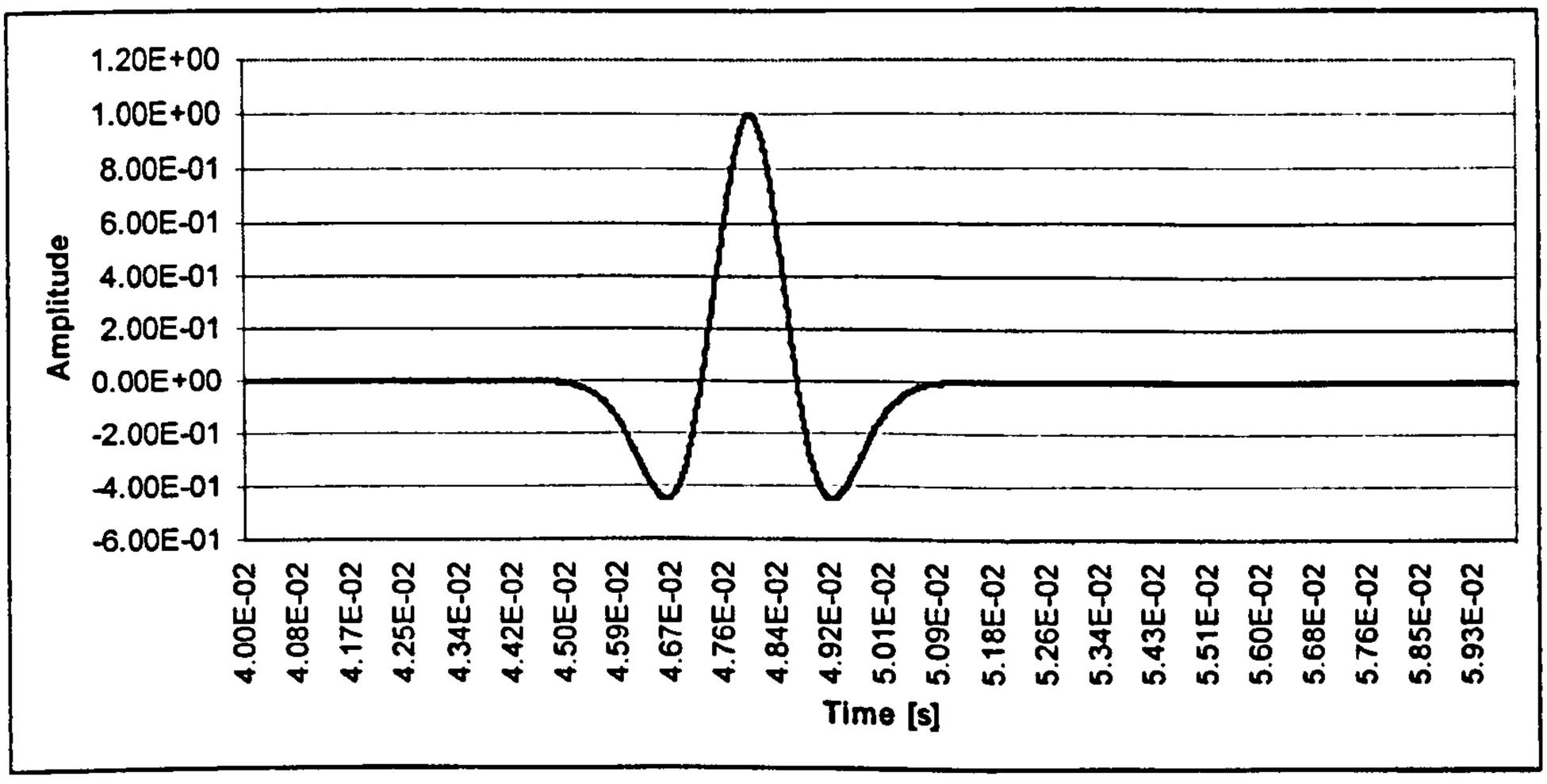

Figure 7.7: Ricker pulse (Δt=1.0E-05, f_c=300Hz, n_{max}=8192)

The energy of the pulse is greatest at the centre frequency, f_c=300Hz. The energy distribution of the pulse tends to zero at both 0Hz and approximately $3f_c$.

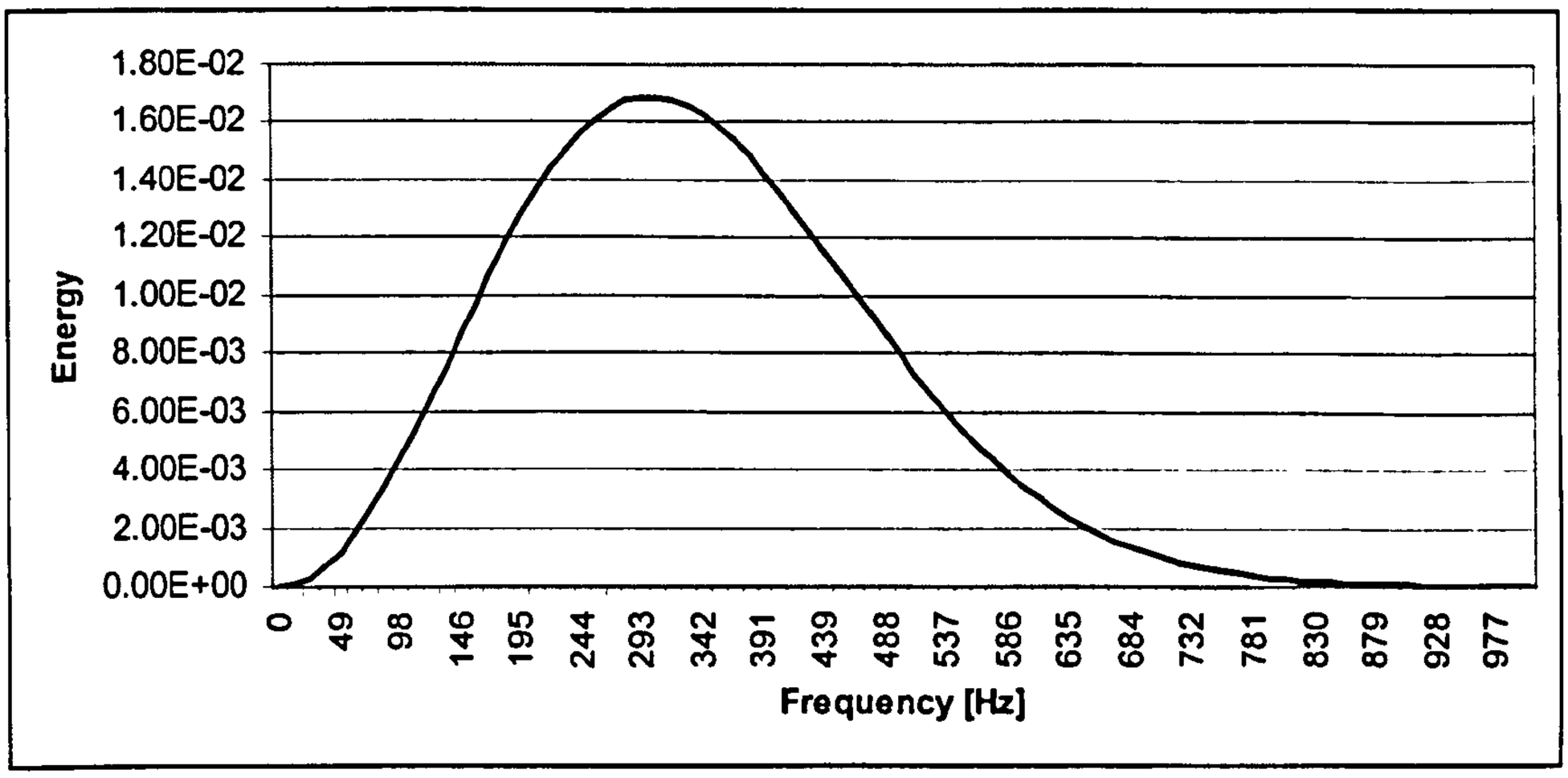

Figure 7.8: Fourier transform of Ricker pulse showing frequency content of signal

Time-domain results also have the added benefit that they can be Fourier transformed to generate a number of frequency-domain results. The critical factor governing the frequency resolution will be $1/(n_{max}*\Delta t)$, where n_{max} is the maximum number of time steps (Δt) i.e. $t=n*\Delta t$ where n is an integer. For example, if Δt=1.0E-05 seconds, n_{max} must be 100,000 to achieve a frequency resolution of 1Hz. Unfortunately, increasing the number of time steps increases the computational time. Hence, there is a compromise between the solution time and the frequency resolution.

7.4 Validation of interface boundary conditions

The interface boundary conditions are applied to all the interfaces between conducting layers (i.e. sea-sea or sea-seabed). The FDTD model can incorporate up to ten arbitrary sloping layers, thus allowing conductivity profiles within the sea and seabed layers to be modelled.

---

[1] The step function, $f(t)$ is defined such $f(t)$=0.0 when t<0 and $f(t)$=1 when $t\geq$0.

Figures 7.9 to 7.12 show a comparison between field predictions from the FDTD code and the *NLAYER* propagation model. The results correspond to HED and VED sources in a 2-layer sea-seabed horizontally stratified environment. The source and observer are both 10m above the seabed, with horizontal separations of 50m (thin black line in figures) and 75m (thick grey line in figures).

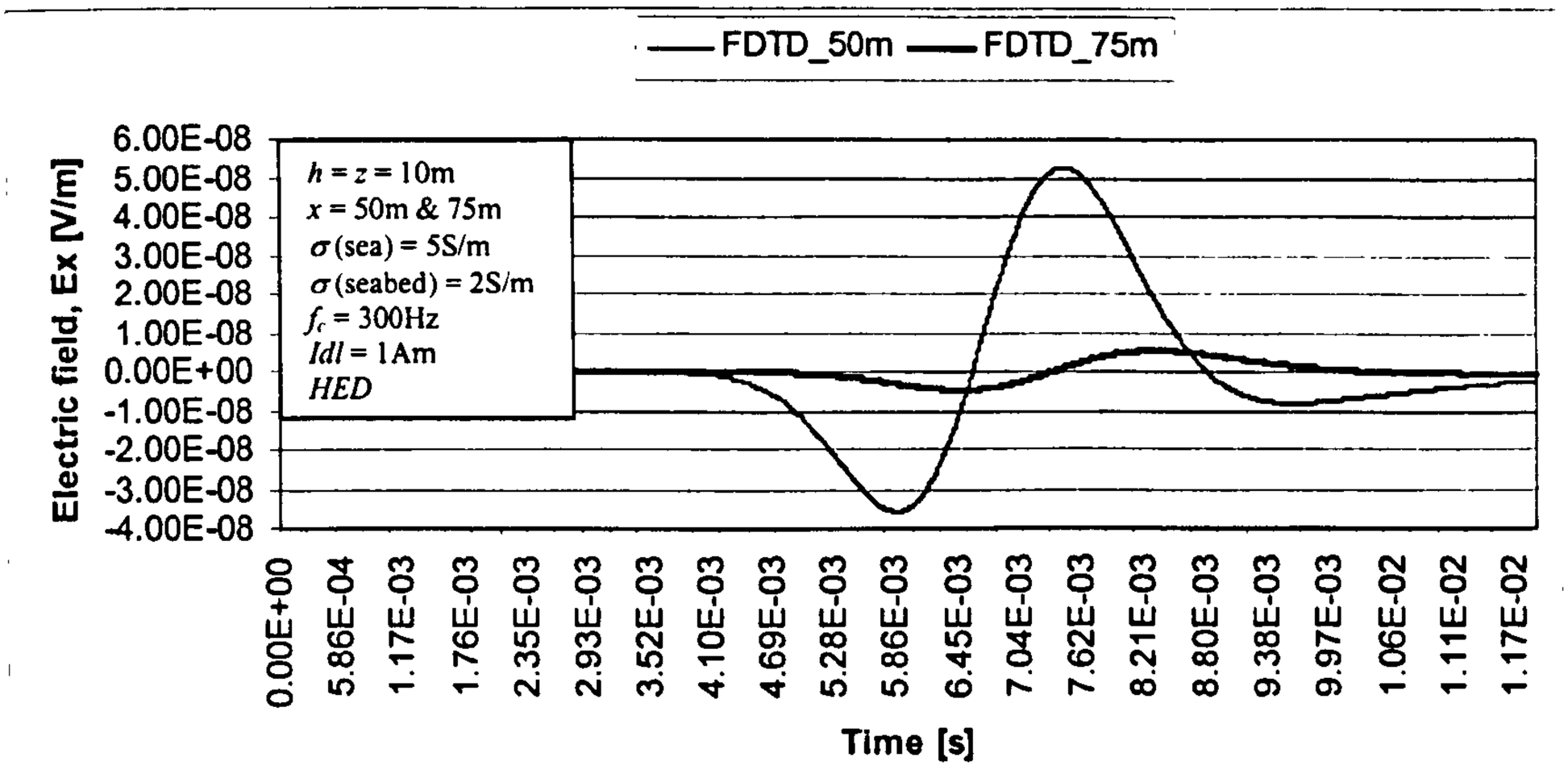

Figure 7.9: FDTD result for sea-seabed interface boundary condition (HED)

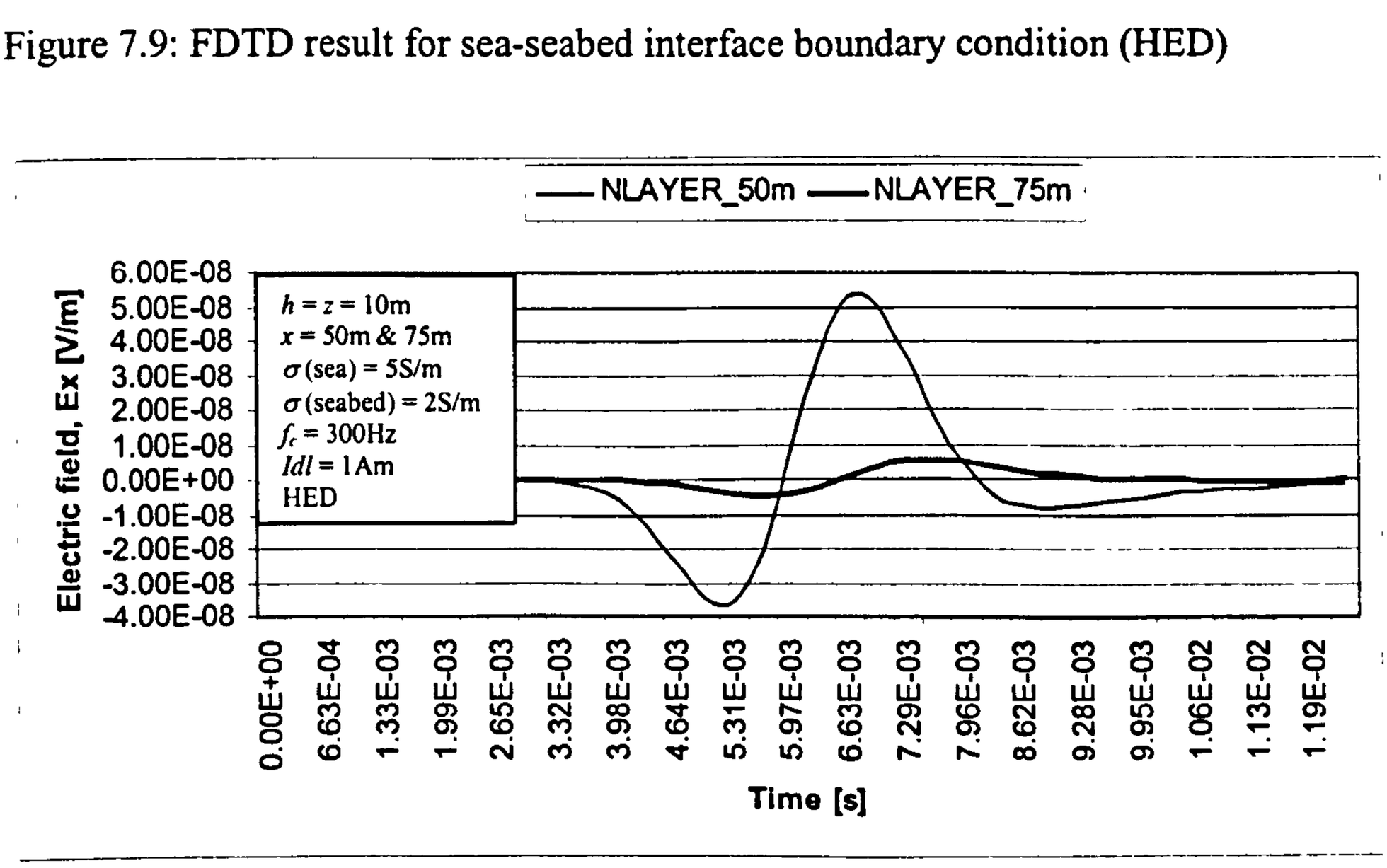

Figure 7.10: *NLAYER* result for sea-seabed interface boundary condition (HED)

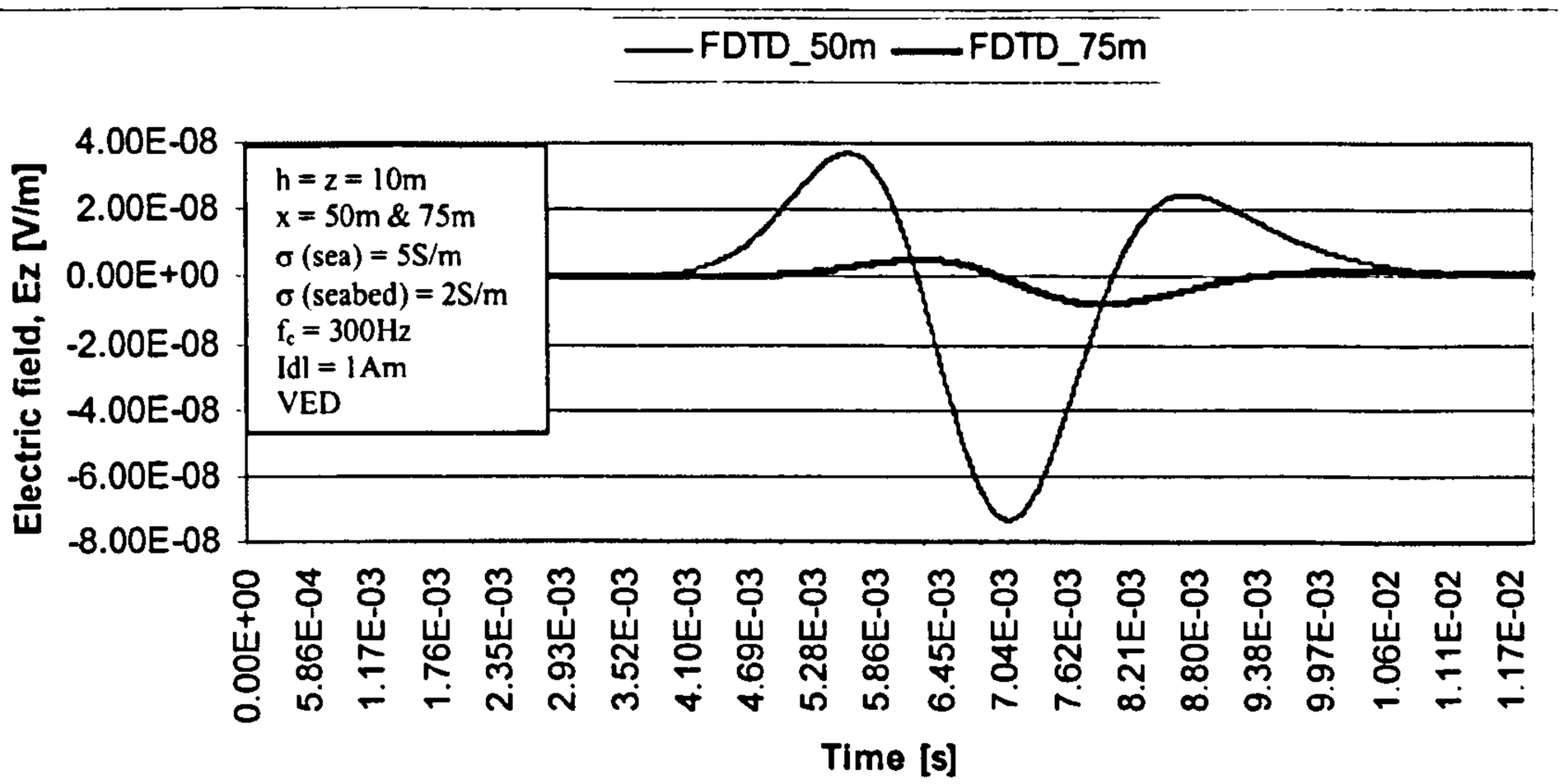

Figure 7.11: FDTD result for sea-seabed interface boundary condition (VED)

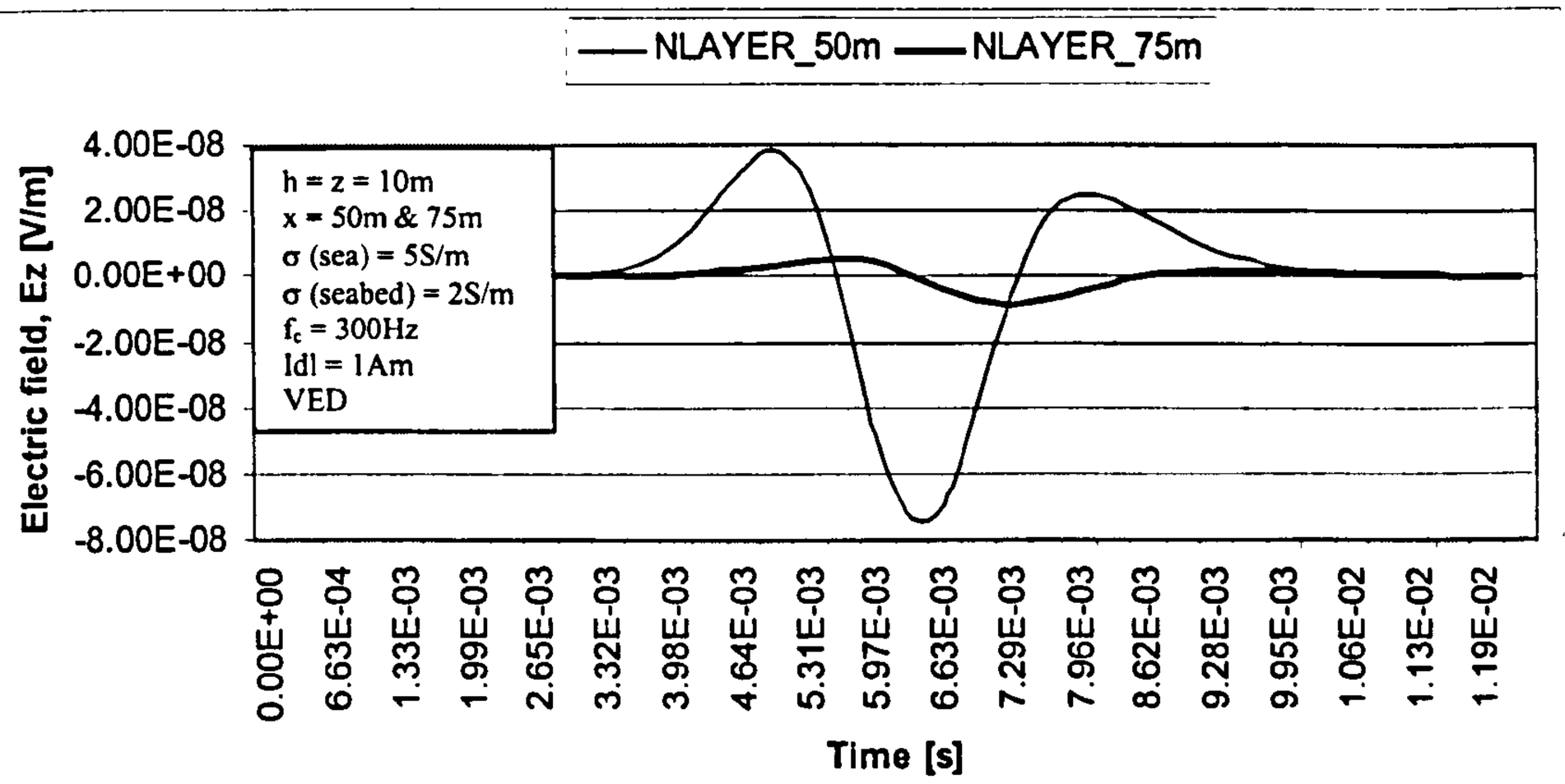

Figure 7.12: *NLAYER* result for sea-seabed interface boundary condition (VED)

The results show that the fields amplitudes are in good agreement at both 50m and 75m, see Table 7.2. The temporal[2] distribution of the field predictions is also in good agreement. This indicates that both the propagation speed and dispersion of the Ricker pulse are modelled correctly in each of the mediums.

[2] NLAYER calculates the time-domain results by automatically selecting the pulse start time. Hence, only the pulse duration is synchronised in Figures 7.10 and 7.12.

	FDTD	NLAYER	% mismatch
HED – 50m separation	5.27E-08V/m	5.33E-08V/m	1.13%
HED – 75m separation	5.33E-09V/m	5.38E-09V/m	0.93%
VED – 50m separation	-7.32E-08V/m	-7.37E-08V/m	0.7%
VED – 75m separation	-8.22E-09V/m	-8.5E-09V/m	3.3%

Table 7.2: Percentage mismatch for peak fields

7.5 Validation of air-sea interface formulation

The analytical boundary condition at the air-sea interface is an essential requirement for using the FDTD method to address ELFE propagation in the marine environment. The spatial time step (Δt) required for maintaining a stable scheme would need to be minute to take account of propagation in air, thus making it impractical for addressing propagation in conducting media as well. The validity of the air-sea interface formulation is demonstrated by checking that the following conditions are met: -

- The lateral waves exhibit the correct behaviour
- The symmetry of the solution is preserved
- The field predictions are of the correct magnitude and distribution

These conditions can only be met if the analytical boundary condition correctly models the behaviour of horizontally and vertically polarised radiation. In particular, the propagation characteristics of the up-down lateral wave associated with horizontally polarised radiation.

7.5.1 Lateral waves

The up-down lateral wave exhibits two features that result from propagation at the air-sea interface. These are low attenuation and high propagation speeds. Figure 7.13 shows the configuration of three observer points (A, B and C) used for determining if the lateral waves were displaying the correct characteristics.

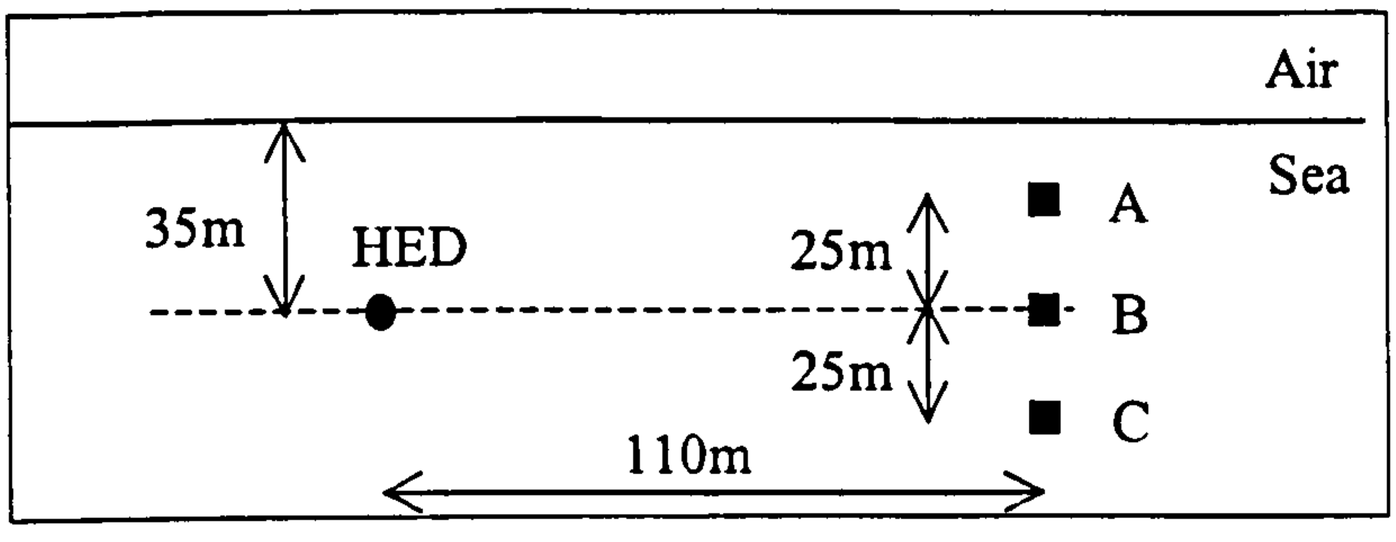

Figure 7.13: Spatial configuration of lateral wave test

The reason for selecting this configuration stems from a consideration of the different paths lengths the radiation can follow in each of the mediums. The propagation path taken by the radiation can be determined by analysing the field magnitudes, and the dispersion and arrival times of the pulse at points A, B and C. This allows contributions from the direct waves, primary reflections and lateral waves to be identified. Figures 7.14 and 7.15 show the field predictions at the three points calculated using the FDTD code and the *NLAYER* propagation model. Note that the pulse start times are not synchronised.

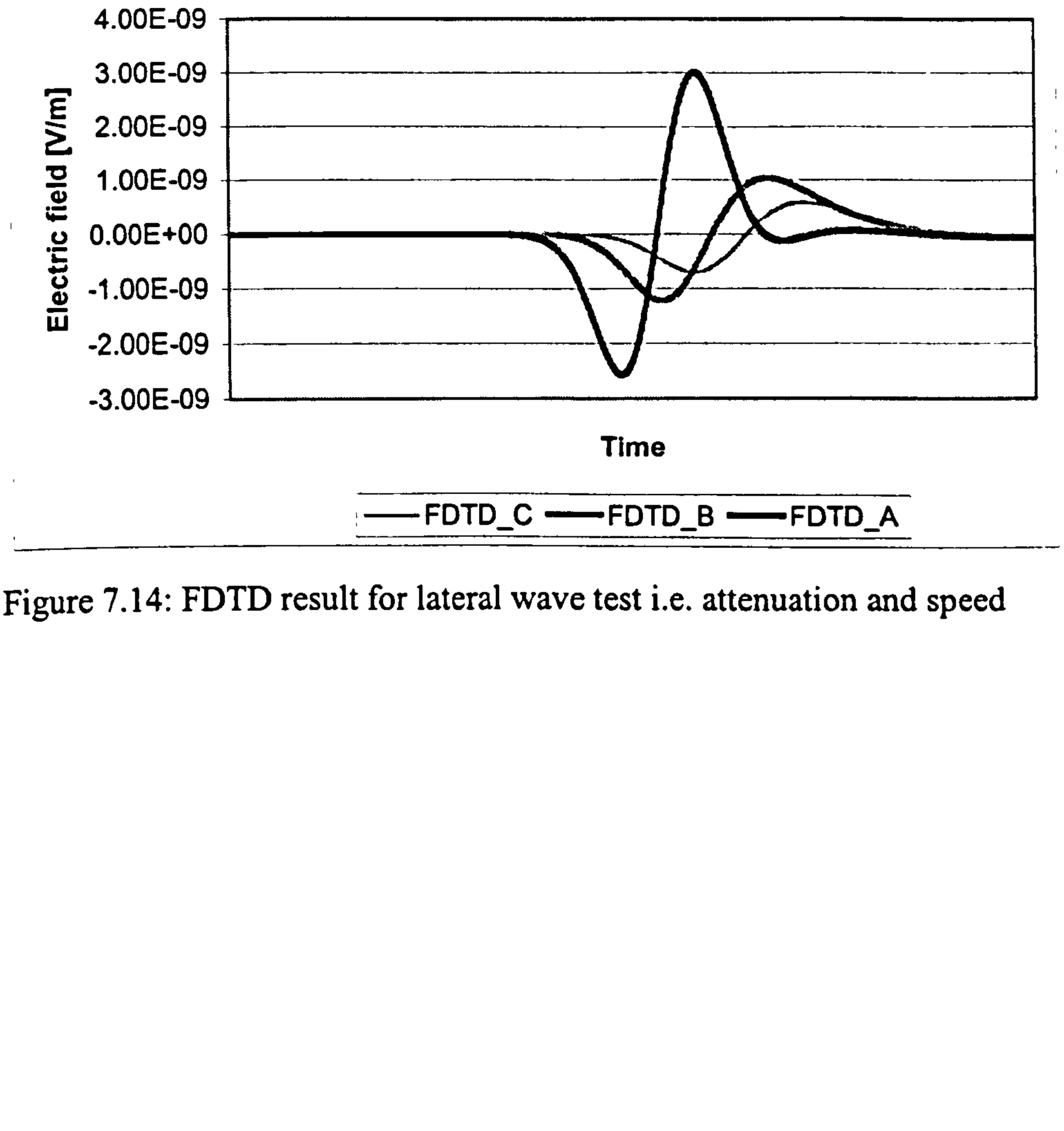

Figure 7.14: FDTD result for lateral wave test i.e. attenuation and speed

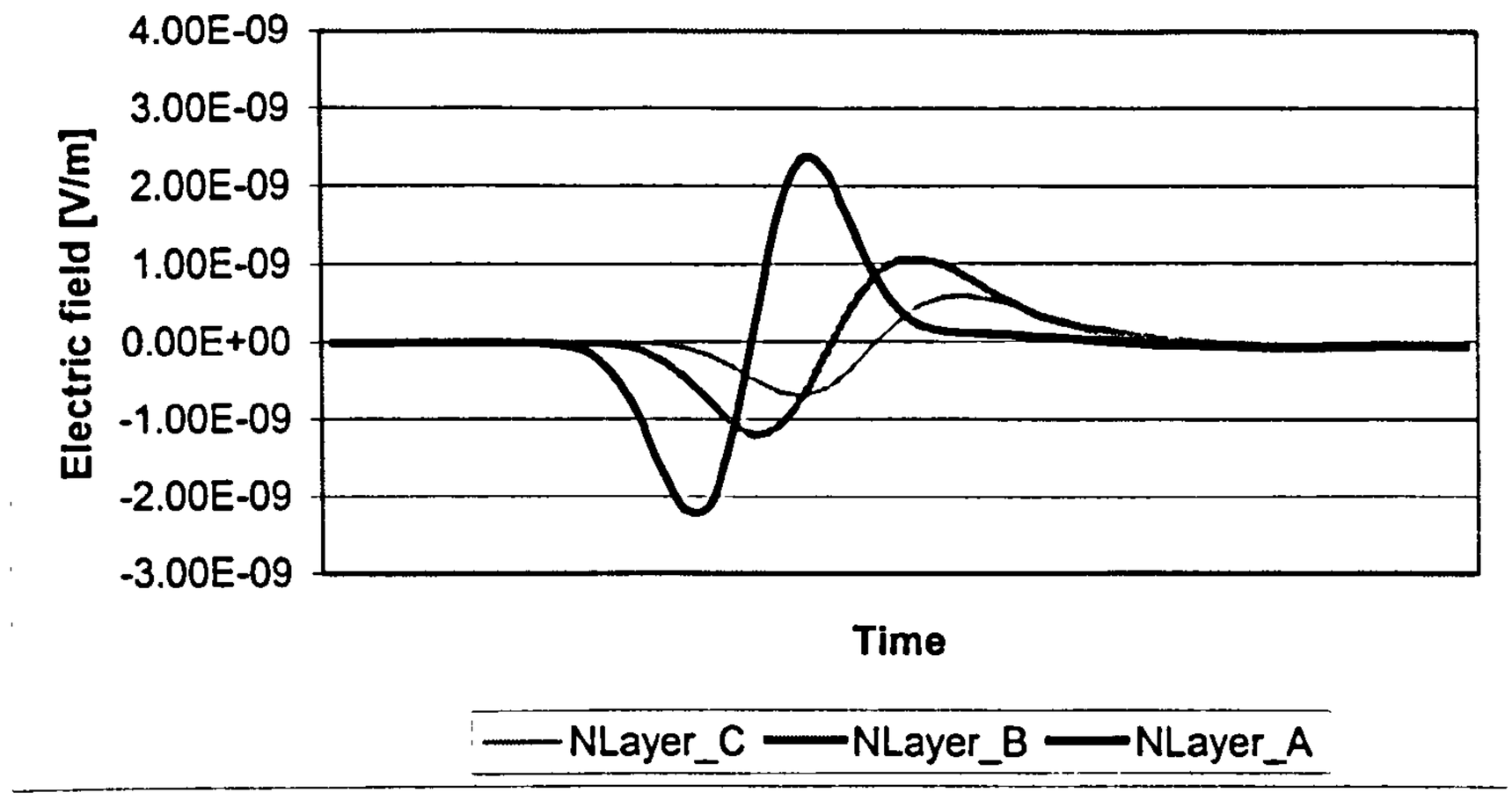

Figure 7.15: *NLAYER* result for lateral wave test i.e. attenuation and speed

A visual comparison between the results shows they are in very good agreement. The relative field magnitudes, dispersion and arrival times are all closely correlated and consistent with the presence of lateral waves. However, there are differences between the field magnitudes, particularly at point A, and small discrepancies in the pulse shapes. These are attributed to boundary effects due to the finite extent of the air-sea interface in the horizontal plane and the non-ideal nature of the source. The latter effect is responsible for the over estimation of the field values, since the source only behaves as a point source at distances greater than ten step sizes. The finite extent of the air-sea interface will result in radiation being reflected back into the region of interest, thus interfering with the solution.

7.5.2 Symmetry

It is well known that the electromagnetic fields from dipole sources display a high degree of symmetry. Figure 7.16 shows the spatial location of four adjacent quadrants centred on a HED source in the horizontal *xy*-plane, for both the E_x (left) and E_z (right) field components. The '+' and '-' symbols denote the sign of the fields above the dipole source in each quadrant. The longitudinal fields are all the same sign and magnitude, whereas the vertical fields are the same magnitude but have opposing signs for the quadrants on the left (i.e. negative *x*-axis) and right (i.e. positive *x*-axis) hand sides.

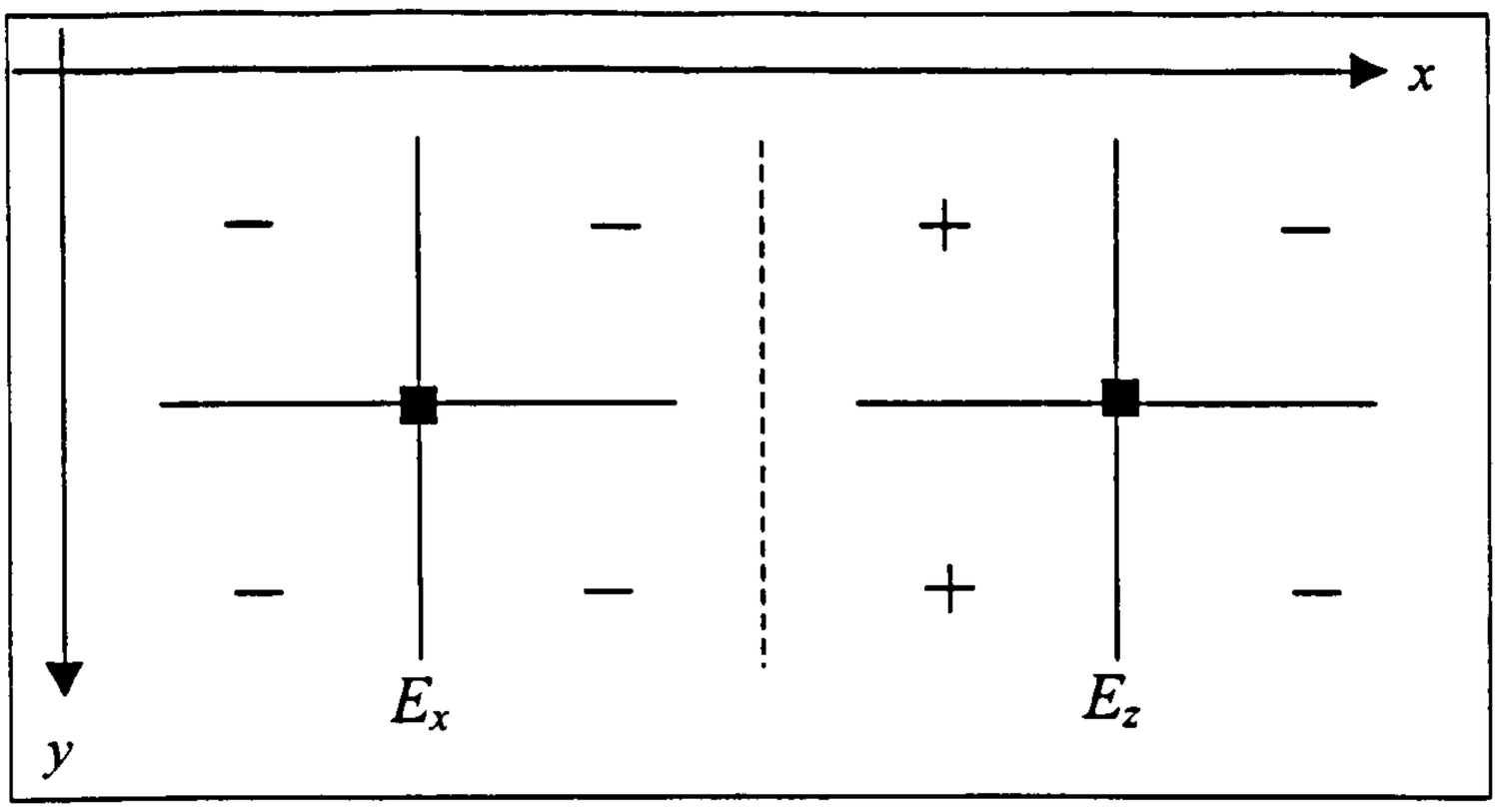

Figure 7.16: Schematic representation of symmetry zones

Figure 7.17 shows that the air-sea interface scheme maintains the symmetry for the E_x field from the HED source. The field at each of the four points is equal in magnitude and has the same sign as expected (i.e. four overlapping curves present in figure).

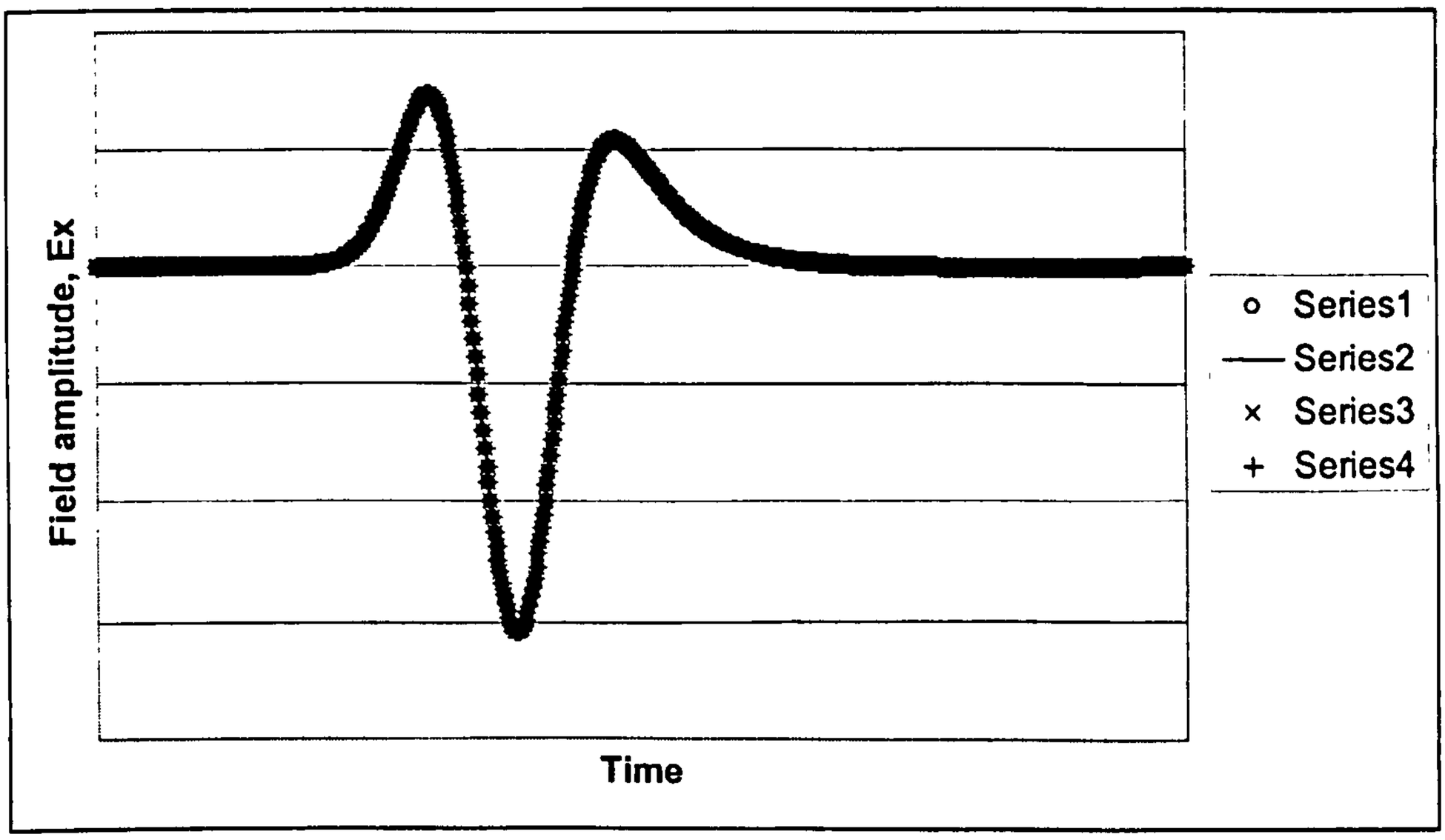

Figure 7.17: E_x symmetry for HED source

Figure 7.18 shows that the symmetry for the E_z field is also maintained by the air-sea formulation.

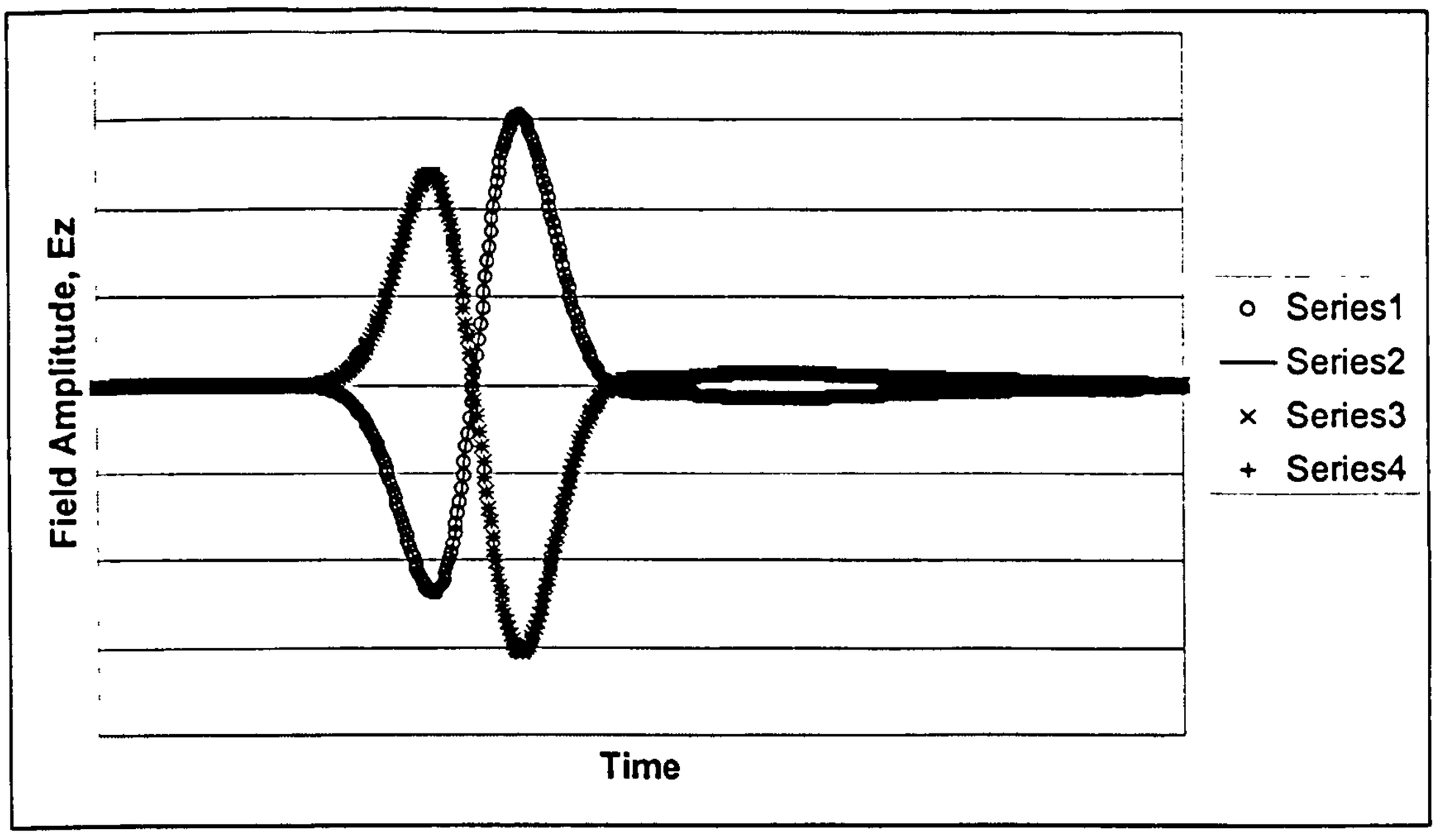

Figure 7.18: E_z symmetry for HED source

7.5.3 Field amplitudes

The final test for the air-sea interface formulation was its ability to accurately predict the electromagnetic field from both VED and HED sources. In order to allow useful field comparisons using the time-domain data, only the peak positive fields at each of the grid point were stored during these computations. The results thus indicate the peak field over the length of the FDTD mesh, in the plane of the source, due to the exciting Ricker pulse.

Figure 7.19 shows the longitudinal field for a VED source predicted using the FDTD code and the *NLAYER* propagation model is in excellent agreement. As expected, there are no lateral waves launched by the VED at the air-sea interface.

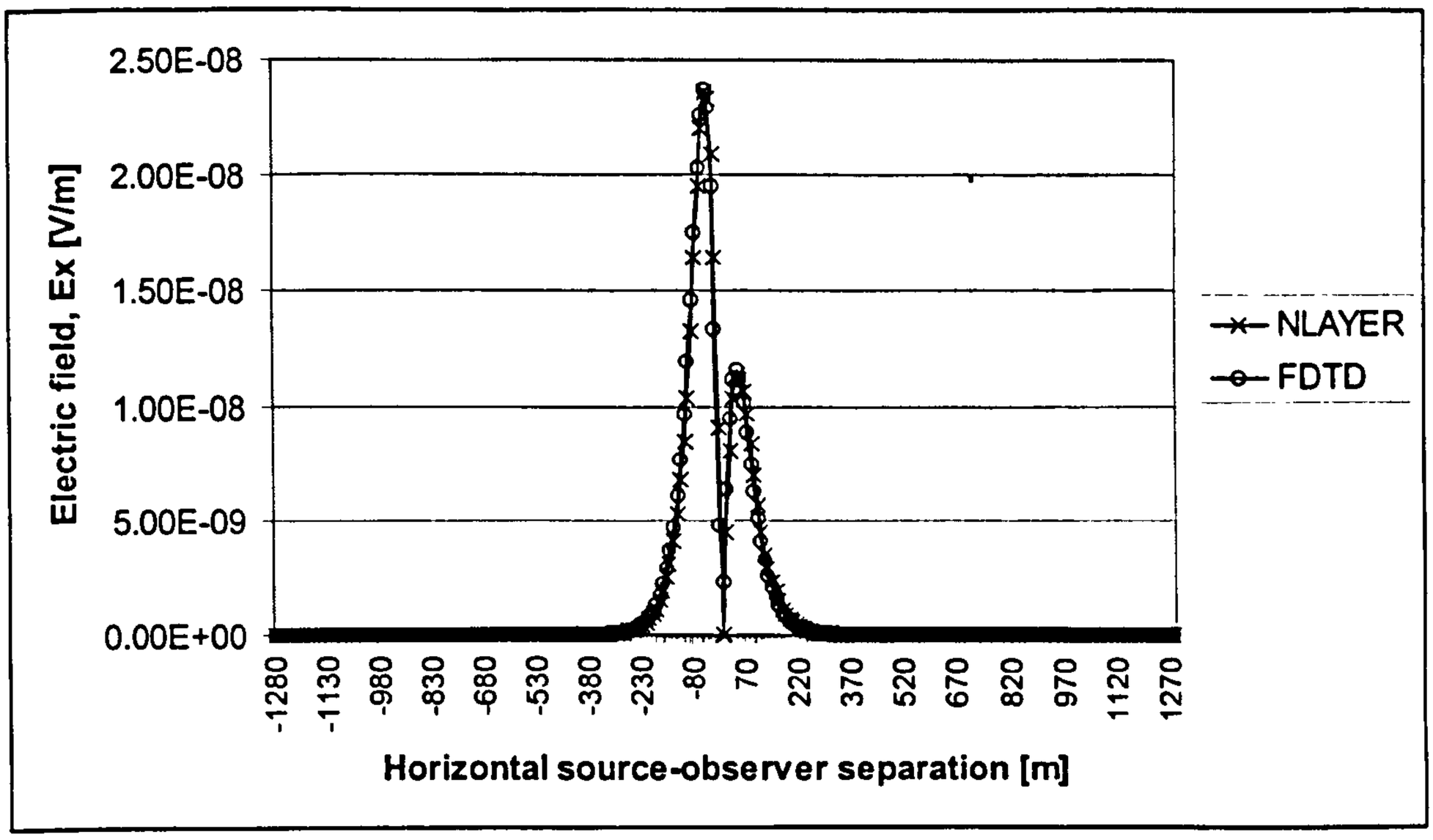

Figure 7.19: Fields from a VED near the air-sea interface

Figure 7.20 shows the longitudinal field for a HED source predicted using the FDTD code and *NLAYER* are in good agreement. The field distributions follow the same decay rates, thus suggesting all the different propagation modes are modelled correctly.

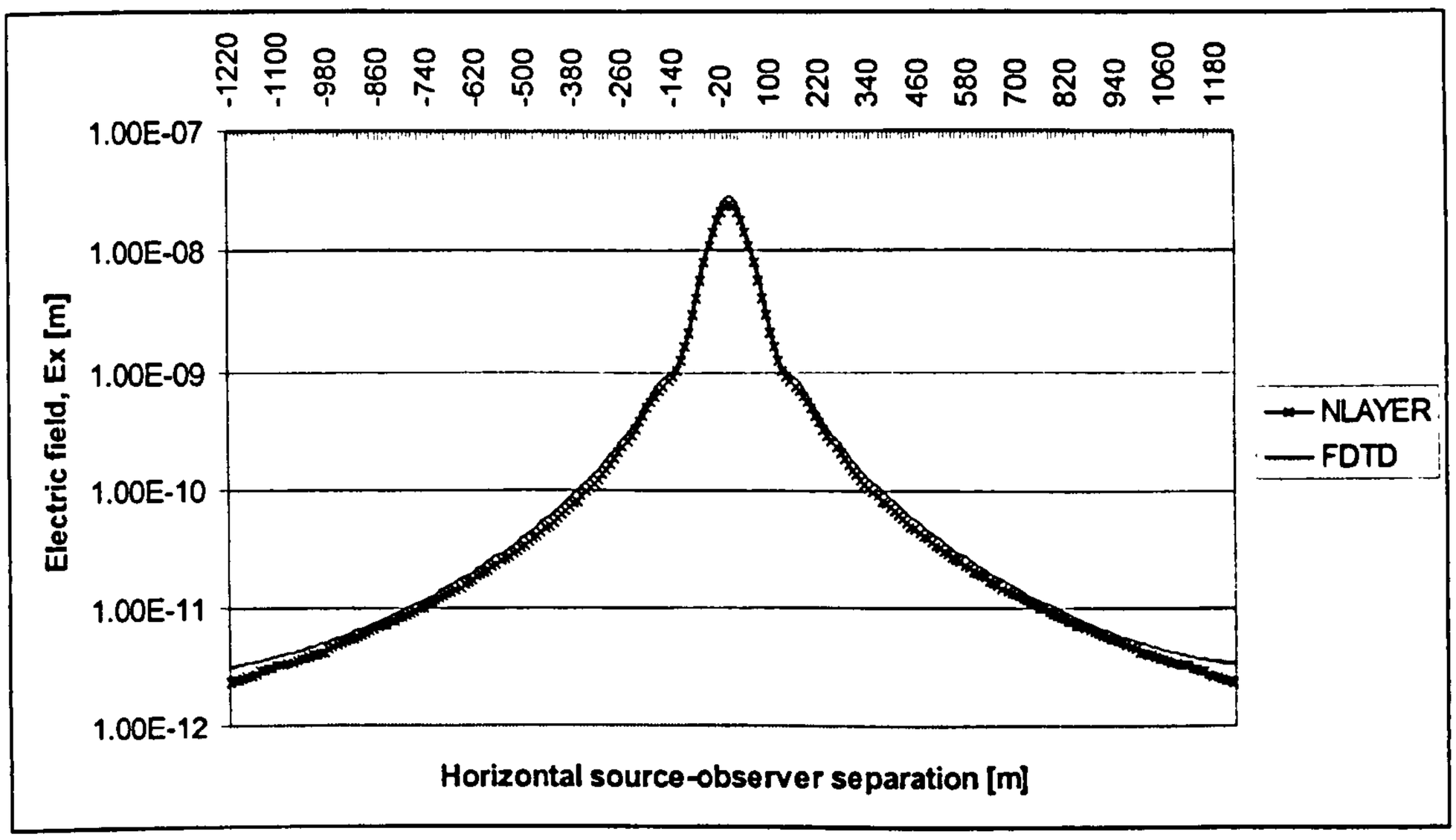

Figure 7.20: Fields from a HED near the air-sea interface

However, the FDTD code has over predicted the field levels by approximately 17.0%, over the entire source-observer range. This means that the contributions from the direct wave, primary reflections and the lateral waves are all affected by the same amount. This implies a problem with the source scaling rather than any problems modelling the air-sea interface. This scaling problem is attributed to the non-ideal nature of the source.

The small anomalies at the ends of the field predictions are 'edge' effects due to the finite extent of the FDTD mesh. The mesh used in these calculations consisted of 256x256x100 nodes, thus making it a very large problem (i.e. 6.5 million nodes!). This large mesh was essential to minimise the edge effects.

7.5.4 Discussion

The results presented in this Section have demonstrated that the FDTD code is modelling all the propagation modes correctly. The field amplitudes, the spatial and temporal field distributions, signal dispersion and decay rates have all shown good agreement with the predictions obtained from the *NLAYER* propagation model. However, there were a number of small discrepancies in the results caused by reflections from the mesh boundaries and the non-ideal nature of the source. In theory, these errors can be reduced by increasing the problem size and reducing the spatial step sizes respectively, albeit at the expense of increased processing time. In practice, it was not feasible to perform calculations of this magnitude for the reasons discussed below.

Before discussing the main issues, it is worth noting that the spatial step size is determined by the highest conductivity present in the marine environment i.e. the sea conductivity. The time step is governed by the spatial step size and the smallest conductivity present i.e. the seabed conductivity. This will result in smaller time steps for marine environments with large conductivity discontinuities[3]. Hence, a large number of time steps are required to allow the field to propagate the extent of the problem domain.

[3] Large conductivity discontinuities at the sea-seabed interface also increase the significance of the contribution from the down-up lateral wave.

The minimum size of the computational domain is also restricted by the slowly decaying up-down lateral waves i.e. they only suffer from spreading losses, no attenuation occurs. Hence, the number of elements (n) in each of the horizontal axes must be increased if smaller spatial steps are used, if the overall size of the computational domain is to be maintained.

The FDTD model is currently implemented such that the computational processing time required to solve a problem increases dramatically when attempts are made to either increase the size of the computational domain or to reduce the spatial step size. The number of spatial steps in the xy-plane must be 2^n x 2^n, where n is an integer. This restriction[4] is imposed by the method used to apply the discrete Fourier transform (DFT) for the air-sea interface boundary condition.

For the reasons mentioned above, the author has found it extremely difficult[5] to obtain a large number of data sets using the FDTD code. Particularly, results containing strong lateral wave effects at the air-sea interface. Most of the results presented in this thesis will focus on electrically deep waters with the source near the seabed. Unfortunately, this also minimises the contribution of the interface interactions (i.e. secondary reflections and reflected lateral wave).

This section has been used to demonstrate the validity of the FDTD using results from horizontally plane-stratified environments. No mention has been made of the co-ordinate transformations that maps the sloping seabed into a horizontally stratified seabed. This aspect of the FDTD model is considered one of the most important new features of this model. Other important features include its ability to model 3-dimensional problems and source/observer configurations within the sea layer. The validation of the mapping process will be detailed below.

---

[4] This restriction can be overcome in a number of ways (see recommendations for future work). However, the risks involved in changing the FDTD code were considered too great at the time of writing this thesis.

[5] The FDTD models typically required around 7 days processing time.

7.6 Validation of co-ordinate transformation

This section details the cross-validation of the analytical and numerical sloping seabed models. The focus will be on demonstrating the validity of the co-ordinate transformation used to map the sloping seabed into a horizontally stratified seabed within the FDTD computational domain. This will be performed by comparing the field predictions from each of the two models. The models are both formulated using different techniques; hence, the comparison constitutes an independent test.

7.6.1 Problem geometry

The environmental geometry chosen for the comparisons was a constant gradient seabed. This geometry was dictated by the approximate analytical model, which can only address seabed profiles with a constant gradient. Figure 7.21 shows the problem geometry with the interfaces and the source location marked. The seabed has horizontal segments near the boundaries to maintain the rectangular nature of the computational domain, see Section 7.6.3. However, the seabed does have a constant gradient for the majority of the region of interest.

The dotted lines show the pattern of the orthogonal grid lines generated by the *ORTHO* algorithm. The grid lines will be distorted to form a regular grid within the transformed co-ordinate system.

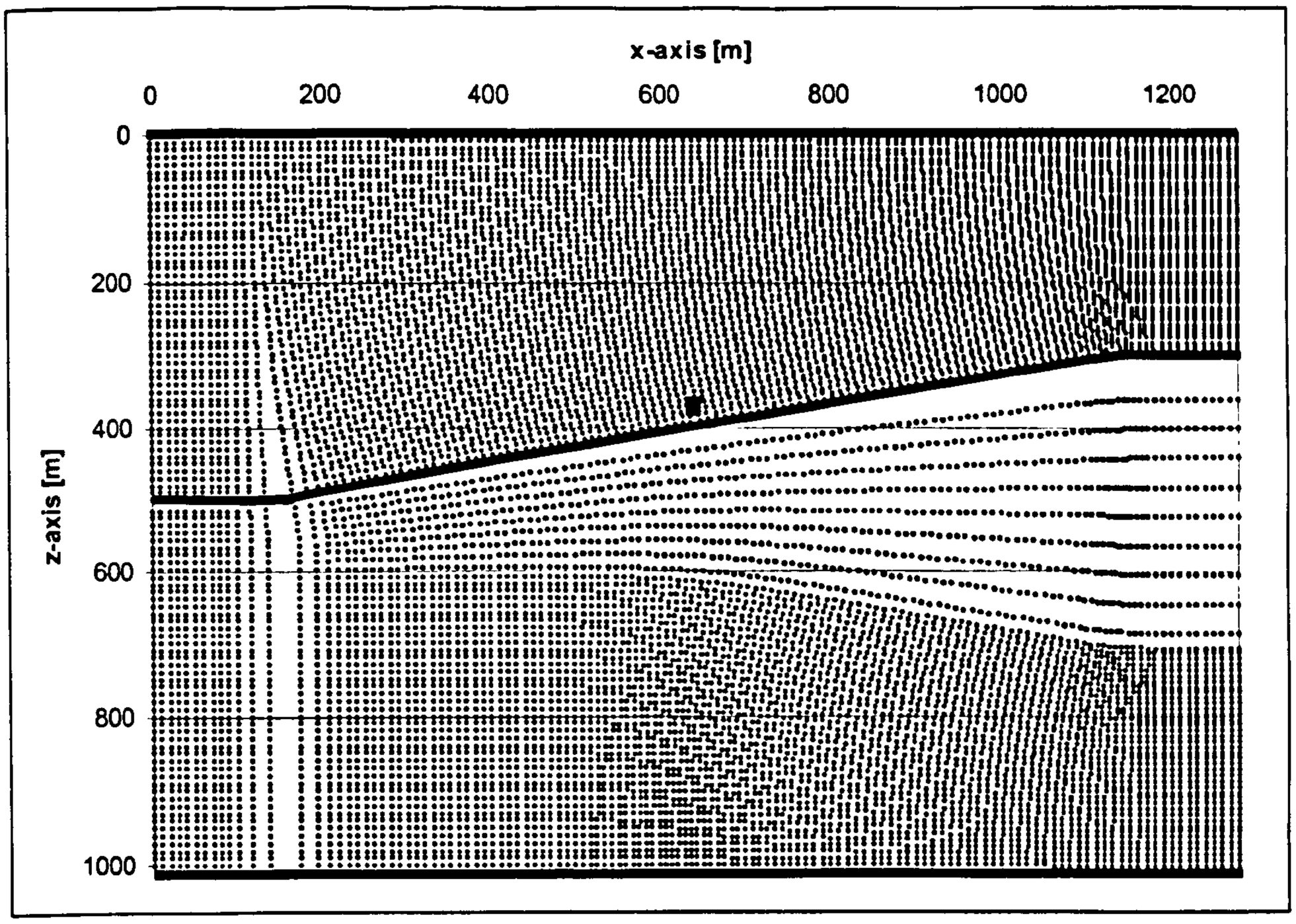

Figure 7.21: Cross-validation problem geometry in original co-ordinate system

Table 7.3 shows the parameters used to generate the sloping seabed profile shown in Figure 7.21. The *ORTHO* algorithm requires the vertical co-ordinate for each specified x-co-ordinate. Five x-co-ordinates are specified in Table 7.3 to create the desired geometry. Interface-1 denotes the air-sea interface, Interface-2 denotes the sea-seabed interface, Interface-3 denotes a 'virtual' interface (see below) to control the weighting coefficients and Interface-4 denotes the bottom of the FDTD mesh.

	x=0m	x=150m	x=640m	x=1130m	x=1280m
Interface-1	0	0	0	0	0
Interface-2	500m	500m	400m	300m	300m
Interface-3	600m	600m	600m	700m	700m
Interface-4	1005m	1005m	1005m	1005m	1005m

Table 7.3: Sloping seabed parameters

A virtual interface can be introduced to control the 'a' and 'b' weighting coefficients generated by the orthogonal transformation program. There are no conductivity discontinuities associated with virtual interfaces. The conductivity is the same on

both sides of the interface. The FDTD model is therefore unaware of their presence. Virtual interfaces are employed to control the size of the time step, Δt, which is a function of 'a' and 'b', see Equation 6.97. This can significantly reduce the computational time required to solve a problem. It is also worth noting that the seabed geometry shown in Figure 7.21 could not be transformed without the inclusion of this virtual interface.

The field measurements are made along a straight line in the transformed problem space. However, this does not relate to a straight line within the original co-ordinate system. Figure 7.22 shows the co-ordinates of the 128 measurement points, for both the HED and VED sources. The measurements are made along distorted lines that follow the distortion pattern created by the sea-seabed interface.

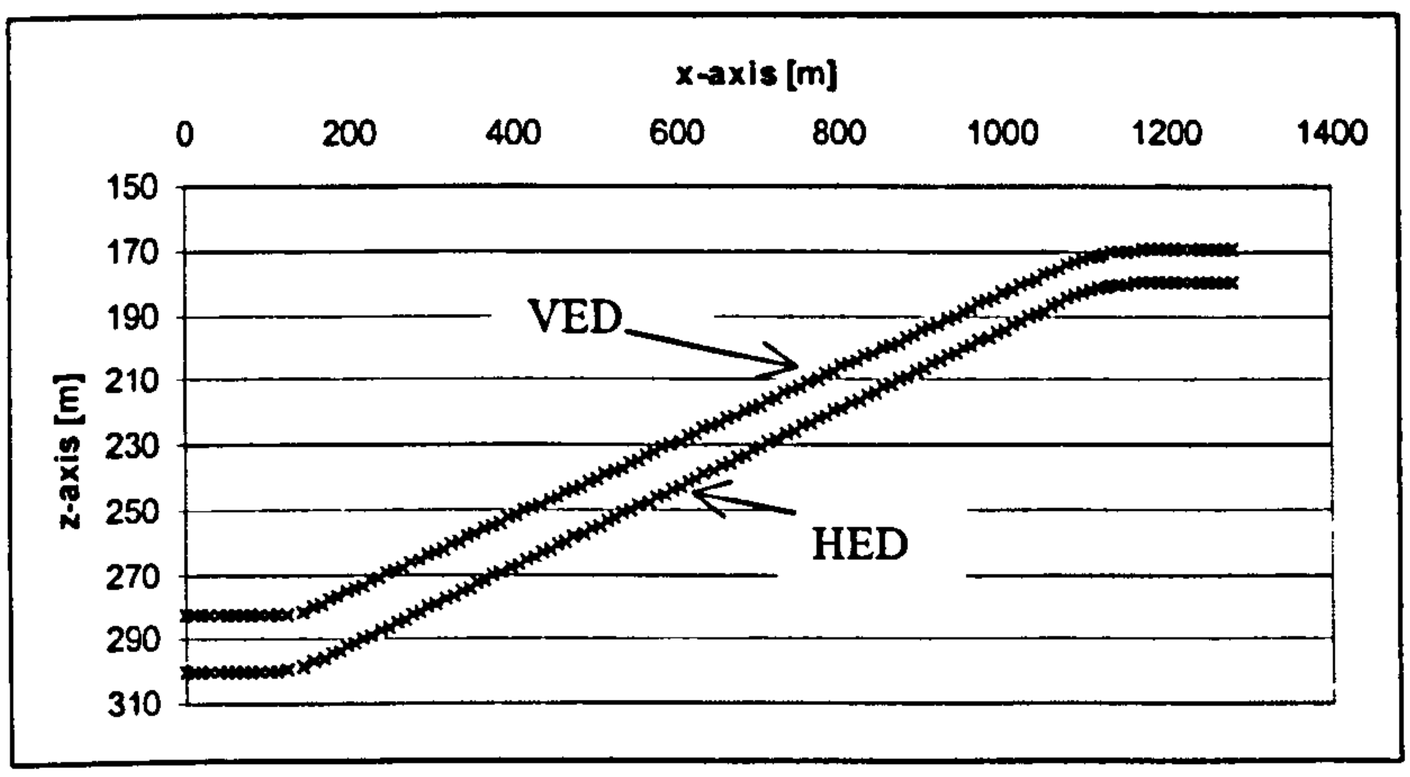

Figure 7.22: Field measurement points

7.6.2 Cross-validation results

Figure 7.23 shows a field comparison for the HED source above a sloping seabed. The peak longitudinal electric (E_x) field from the Ricker pulse (f_c=50Hz) is plotted. The source is located at (637.3m, 384.2m). Three results are presented on this figure:

- The analytical solution obtained using the approximate 3-layer model;
- The numerical solution obtained using the FDTD model;
- The *NLAYER* solution for a horizontally plane-stratified seabed at 400m depth[6].

[6] NB: The average sea depth for the sloping seabed environment is 400m.

The *NLAYER* solution has been included to provide a useful measure of the impact of the sloping seabed on the field distribution.

Figure 7.23 shows that the two sloping seabed results are correlated much more closely to each other than with the horizontally plane-stratified result. The percentage differences between the curves over the entire source-observer range and for the peak signature are summarised in Table 7.4.

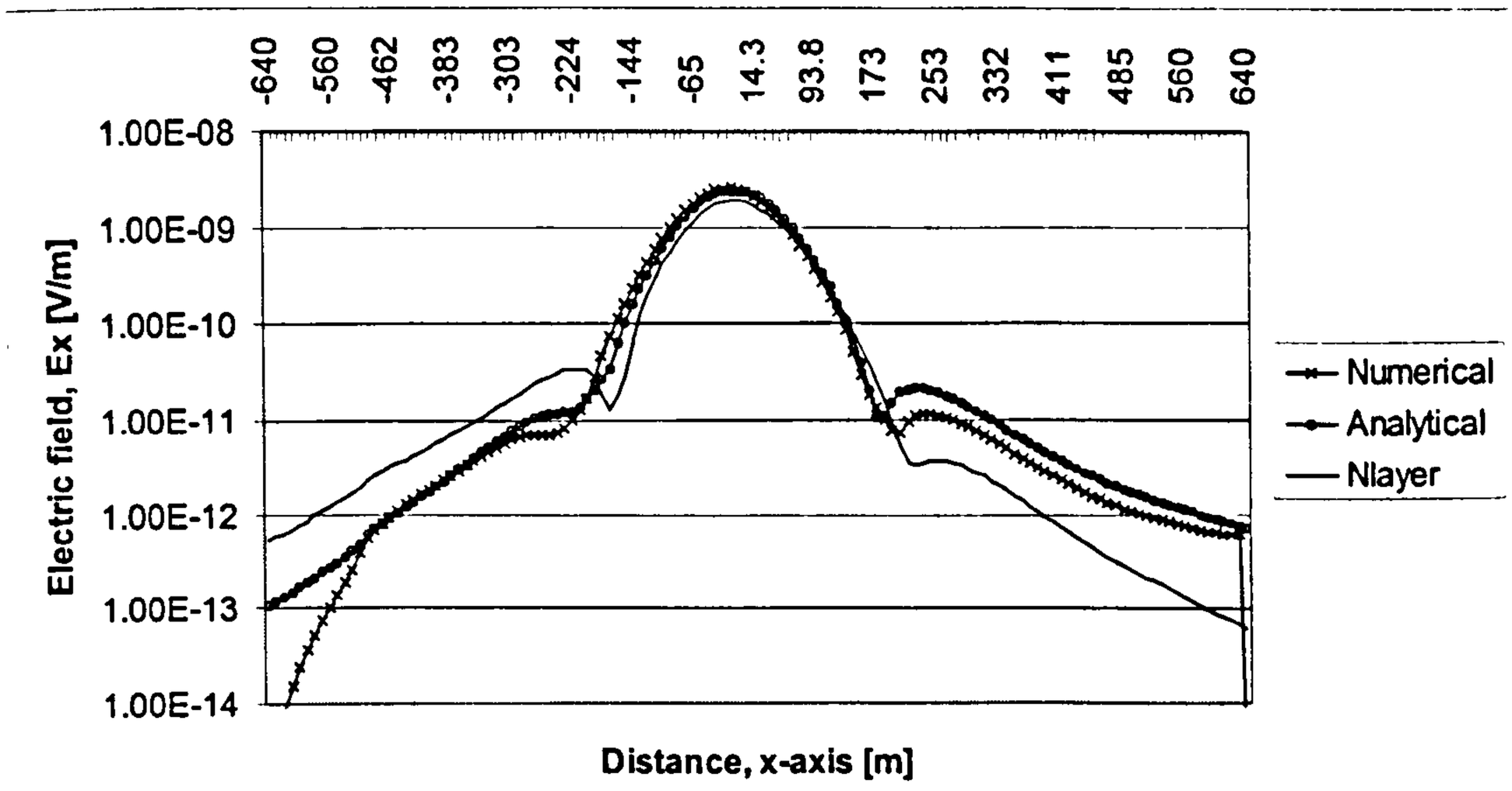

Figure 7.23: Numerical and analytical sloping seabed model comparison (HED)

	Average field	Peak field
Numerical-Analytical	31%	4%
Numerical-NLAYER	115%	21%
Analytical-NLAYER	739%	24%

Table 7.4: Percentage difference between field predictions (HED)

Figure 7.24 shows the corresponding result for a VED source. The peak vertical electric (E_z) field from the Ricker pulse (f_c=50Hz) is plotted. The source is located at (637.3m, 384.2m). The two sloping seabed results are also correlated much more closely to each other than with the horizontally plane-stratified result. The percentage difference between the curves is summarised in Table 7.5.

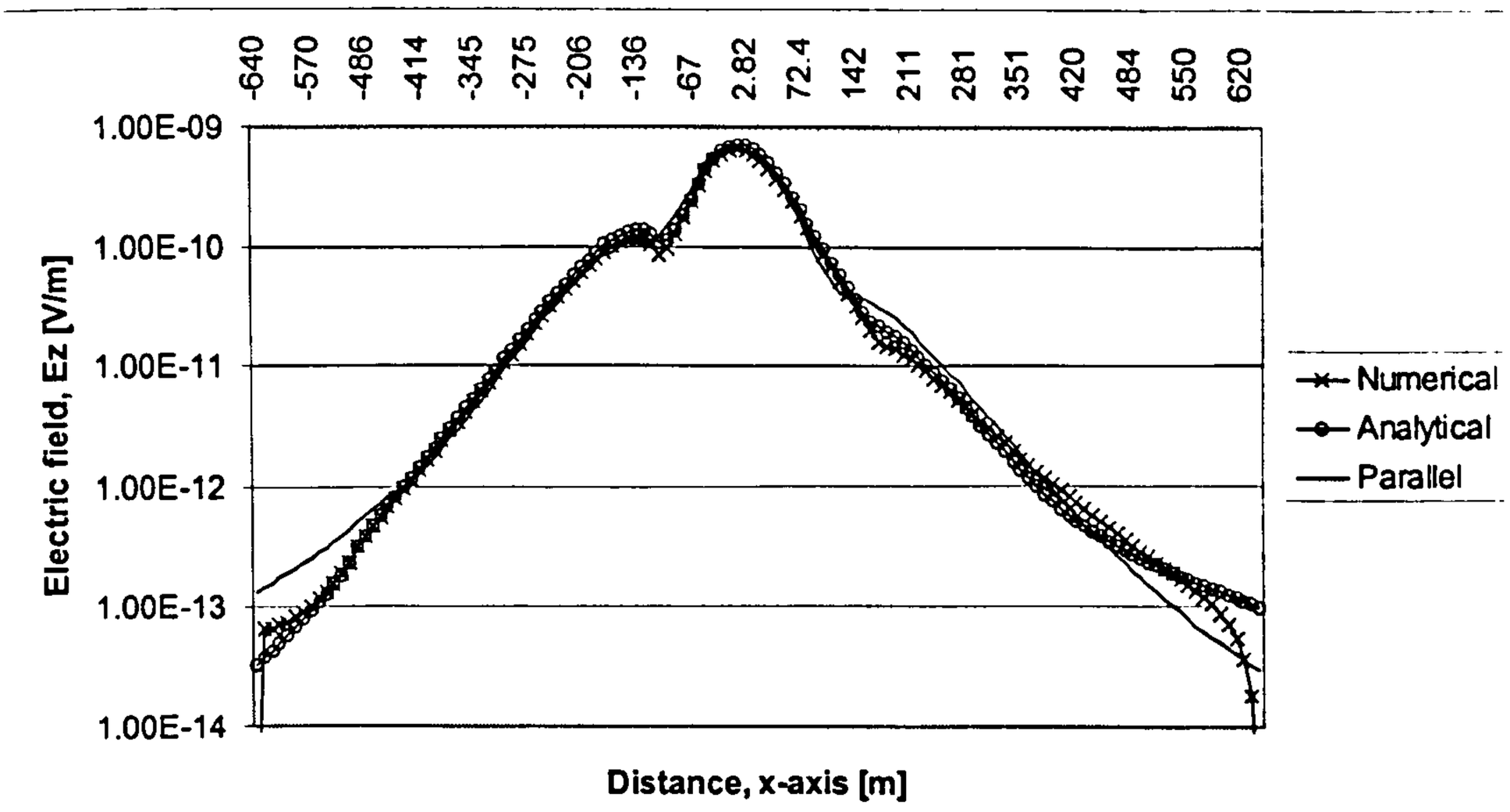

Figure 7.24: Numerical and analytical sloping seabed model comparison (VED)

	Average field	Peak field
Numerical-Analytical	16%	9%
Numerical-NLAYER	134%	11%
Analytical-NLAYER	43%	1%

Table 7.5: Percentage difference between field predictions (VED)

7.6.3 Discussion

The cross validation results appear to demonstrate the validity of the approximate analytical and the numerical FDTD sloping seabed models. The percentage mismatch between the field predictions was, on average, at least three times less than the mismatch between the sloping seabed models and the *NLAYER* solution. The two sloping seabed models produced field predictions that correlated well with each other. The field amplitudes and field distributions (i.e. decay rates) were in good agreement

over most the source-observer range. However, there were some differences between the results, particularly near the boundaries for both sources, and for x>810m for the HED source. These differences must be accounted for, before the validity of the two models is confirmed.

In practice, some differences between the field predictions from the sloping seabed models were inevitable, due to the inherent errors associated with numerical methods. These errors can be attributed to a range of factors, including poor discretisation of the problem space, the non-ideal nature of the source, numerical dispersion and so on. The approximate nature of the boundary conditions at the air-sea and sea-seabed interface would have also been an additional source of errors in the FDTD model developed in this study.

The most prominent field differences in Figures 7.23 and 7.24 are attributed to boundary effects at the external faces of the FDTD mesh. The boundary conditions implemented on the mesh faces forces the tangential field components to be zero; thus making the mesh faces behave as perfect reflectors. Fields that reach the boundary are simply reflected back into the computational domain where they can interfere with the solution.

These problems can be overcome by using a larger computational domain; therefore ensuring the fields decay to negligible levels by the time they reach the boundary. However, this option is computationally very inefficient and significantly increases the memory (i.e. RAM) requirements of the computer. The alternative is to implement special 'absorbing' or 'transparent' boundary conditions that, as the names suggest, absorb any incident radiation, thus behaving as transparent boundaries. However, these can be difficult to implement for problems where the interfaces between different materials, extends all the way to the mesh faces.

Excluding boundary effects, the field comparison for the VED source is promising, despite the relatively small differences between the sloping seabed solution and the parallel interfaces solution. In contrast, there is a significant discrepancy in the field comparison for the HED, for source-observer separations of x>810m. This

discrepancy is attributed to errors introduced by the boundary condition across the sea-seabed interface.

Two factors indicate that this is the most likely candidate. Firstly, the problem only affects the HED source, which produces a strong[7] down-up lateral wave. Secondly, the spatial distortion in the FDTD mesh becomes increasingly severe in the seabed as x increases, see Figure 7.21. The combined effect of these two factors is to introduce an error into the down-up lateral wave calculation for the HED source when x>810m. The direct wave and primary reflections dominate when 470m<x<810m and the lateral wave dominates when 470m>x>810m (NB: this is indicated by the change in the decay rates of the field distribution).

The down-up lateral wave is affected by the distorted elements because the boundary condition at the sea-seabed interface enforces the continuity of the tangential magnetic fields using Equations 6.29 and 6.33. These relationships become increasingly invalid as $\Delta z'$ increases. The spatial step sizes used in the FDTD model are typically chosen such that $\Delta z'_{n+1}=1.1\Delta z'_n$, where n denotes the layer (i.e. n=1 for the sea and n=2 for the seabed). However, the orthogonal transformation has spatially deformed the seabed to produce elongated elements that are much greater than those in the sea layer i.e. $\Delta z'_{n+1}>2\Delta z'_n$. This will result in field predictions that are under estimated i.e. the continuity of the tangential magnetic field is approximated by averaging the fields at $\Delta z'_n$ above and $2\Delta z'_n$ below the interface.

Figure 7.21 shows that the seabed profile used within the FDTD model does not have a constant gradient seabed for all source-observer ranges. The seabed is flat near the boundaries to prevent the problem space from being distorted as shown in Figure 7.25. Both these geometries were investigated. They produced 'similar' results and suffered from the same problems mentioned above. Figure 7.26 shows the numerical results for the VED. A qualitative[8] inspection of this result shows the same boundary effects are present.

---

[7] The down-up lateral wave associated with the VED source is not significant over the source-observer ranges considered in this example

[8] The source and observer locations are slightly different to those used in Figure 7.21.

However, the HED results obtained using the geometry shown in Figure 7.25 suffered from significant boundary effects from the mesh bottom due to the shallower seabed modelled (i.e. z=600m).

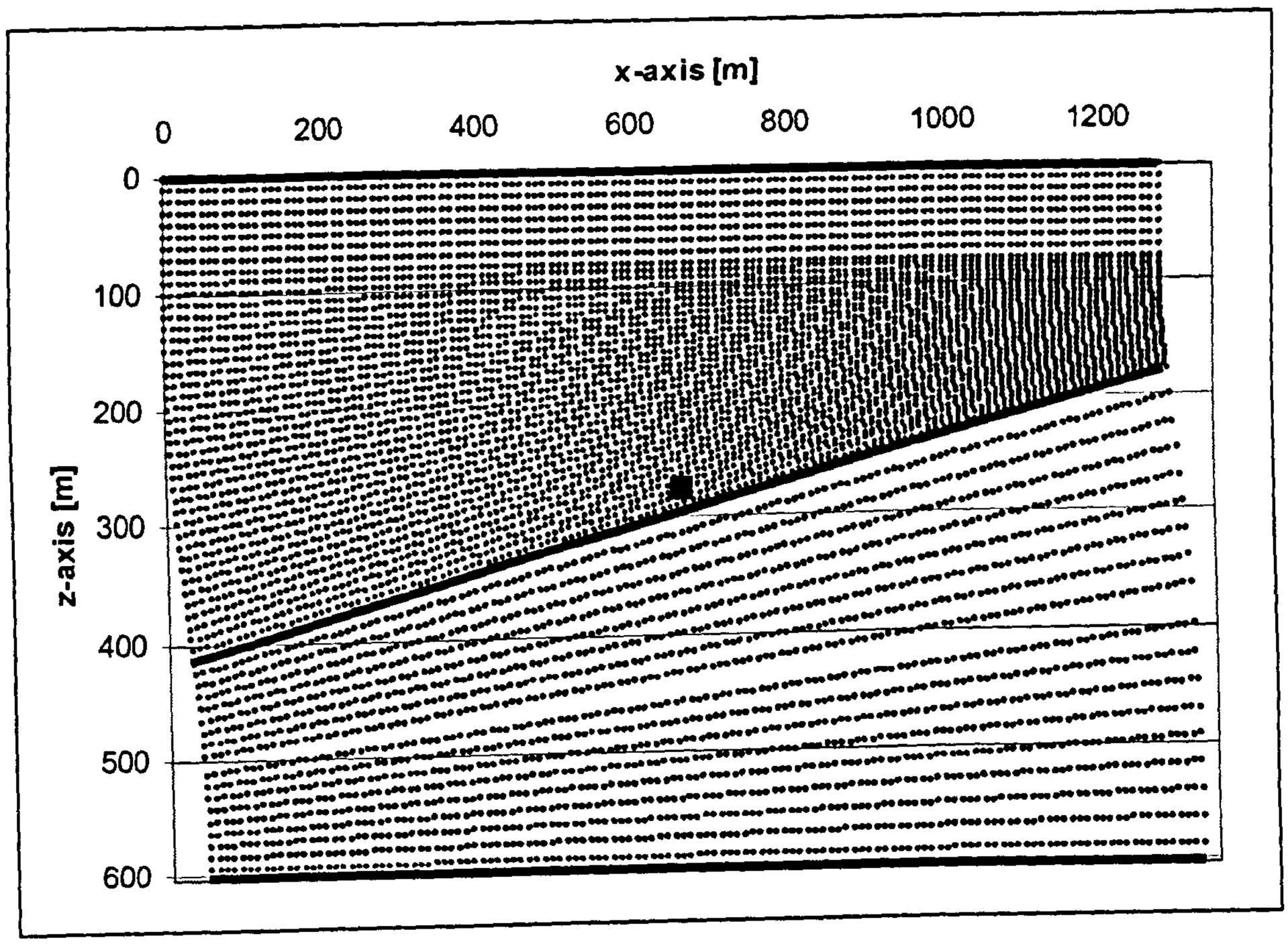

Figure 7.25: A sloping seabed mesh with a constant gradient

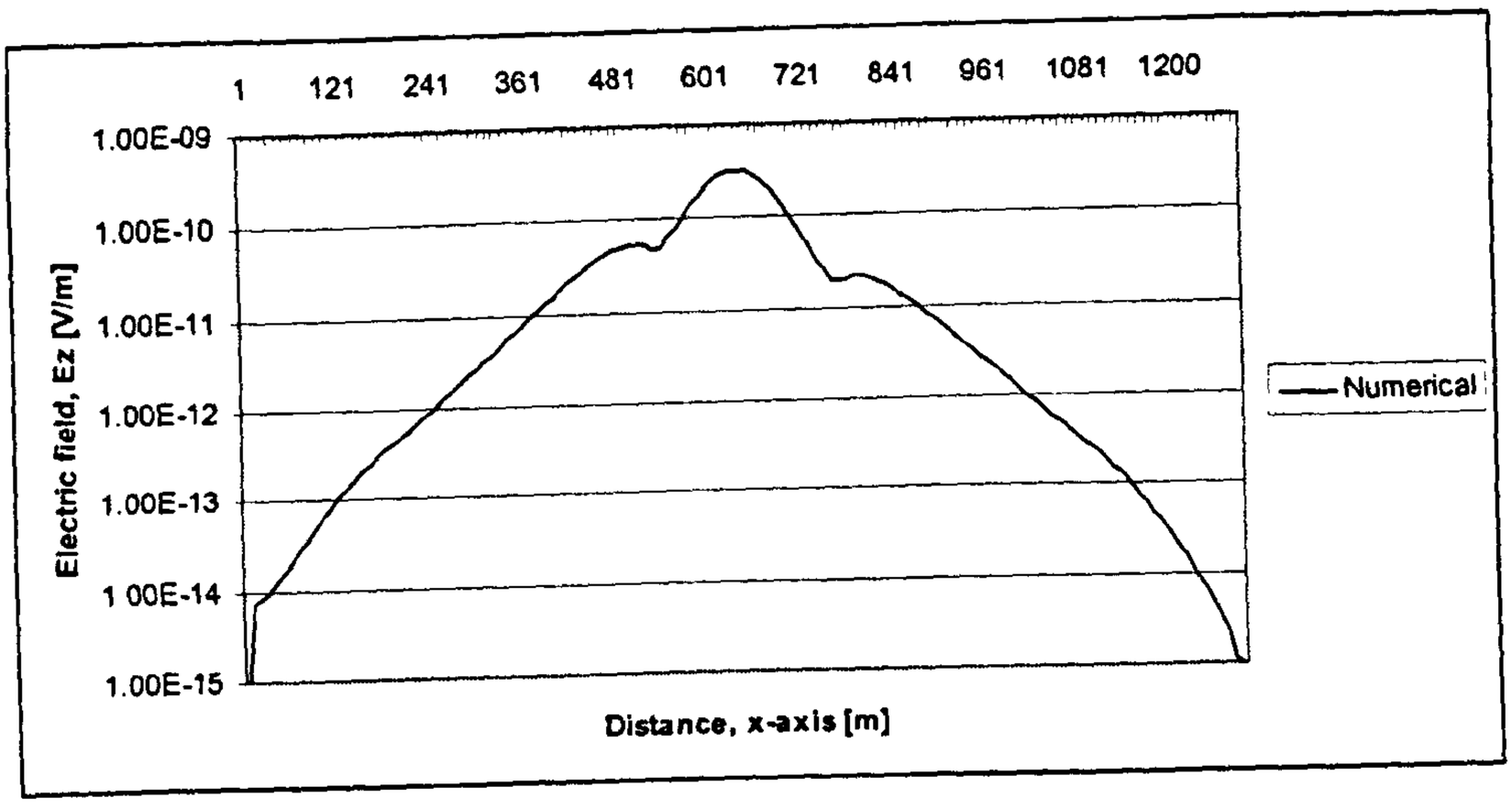

Figure 7.26: Numerical sloping seabed result for VED

In practice, the geometry used to produce the FDTD results has not adversely affected the field predictions close to the boundary. In most cases, reflections from the mesh faces have dominated the behaviour of the solution in these regions.

The explanations detailed above can account for the majority of differences observed between the field predictions from the two sloping seabed models. The remaining differences were due to 'numerical errors' and the approximate nature of the boundary conditions. Some of these can be reduced by increasing the level of discretisation, but at great computational costs. It is therefore concluded that the cross-validation results have successfully demonstrated that the validity of the two models and the co-ordinate transformations employed.

Chapter 8

Results

This chapter investigates the propagation characteristics of ELFE radiation in a sloping seabed environment. The results presented in this chapter are produced using the approximate analytical model detailed in Chapter 5 and the numerical model detailed in Chapter 6.

The focus will be on using the analytical models to investigate the impact of the source location and the slope angle (ϕ_s) of the seabed on ELFE propagation. The results mainly address situations in which the interaction between the two interfaces is negligible. However, some low frequency data is presented where interface interactions are significant. These interface interactions were modelled using the imaging techniques detailed in Chapter 5.

8.1 Geometry of problem

Figure 8.1 shows the geometry used to generate all the analytical results. The seabed is sloping such that the sea depth decreases, as x becomes increasingly positive. The field measurements are made from x=–950m to +950m, in steps of 5m, 50m below the air-sea interface. The average sea depth will be d=450m in all the analytical cases presented (i.e. this is the depth of the seabed in the yz-plane containing the source). The source depths and the slope angles will be the only variables; all other parameters will remain fixed.

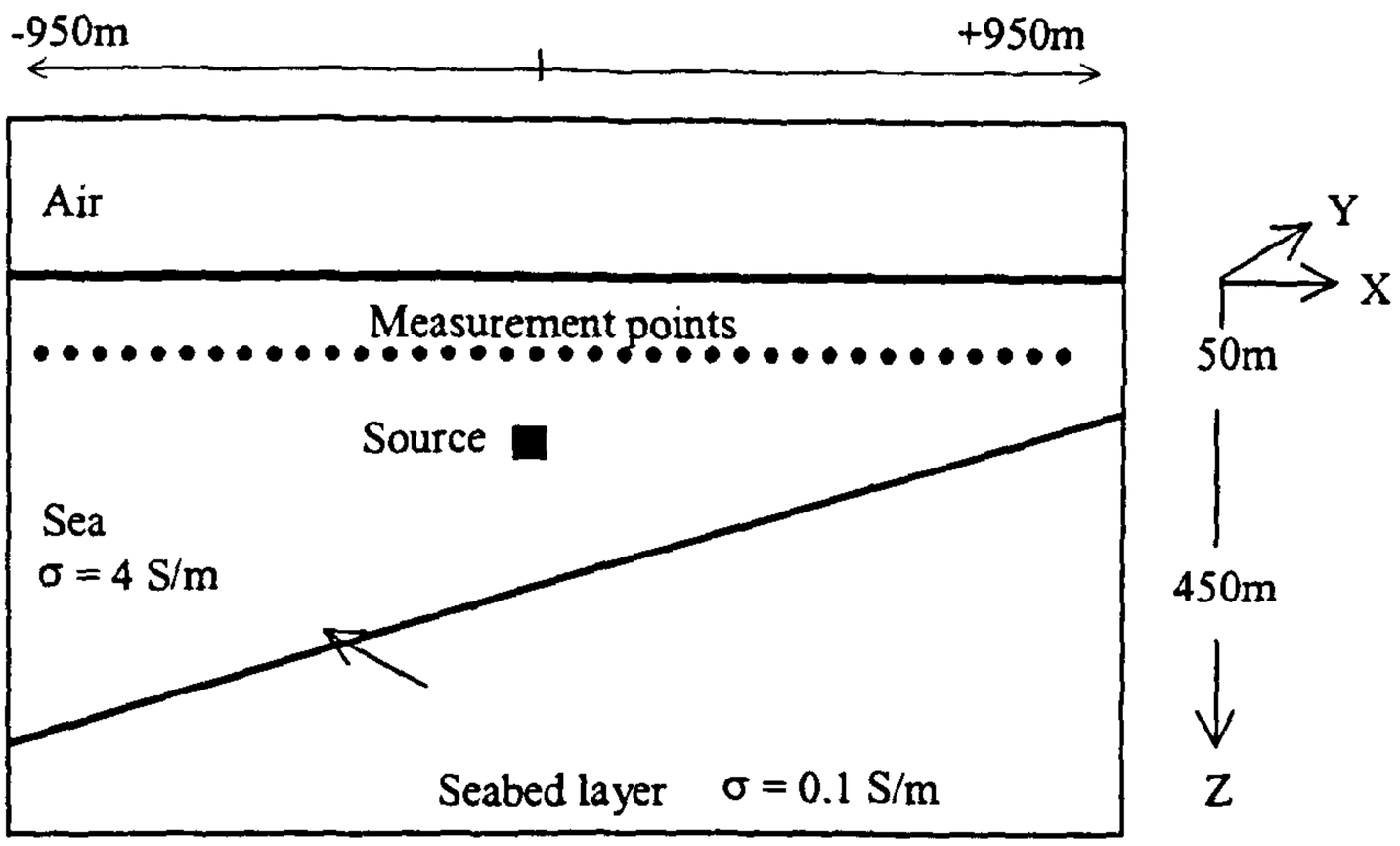

Figure 8.1: Geometry of sloping seabed modelled

8.2 Varying the slope angle

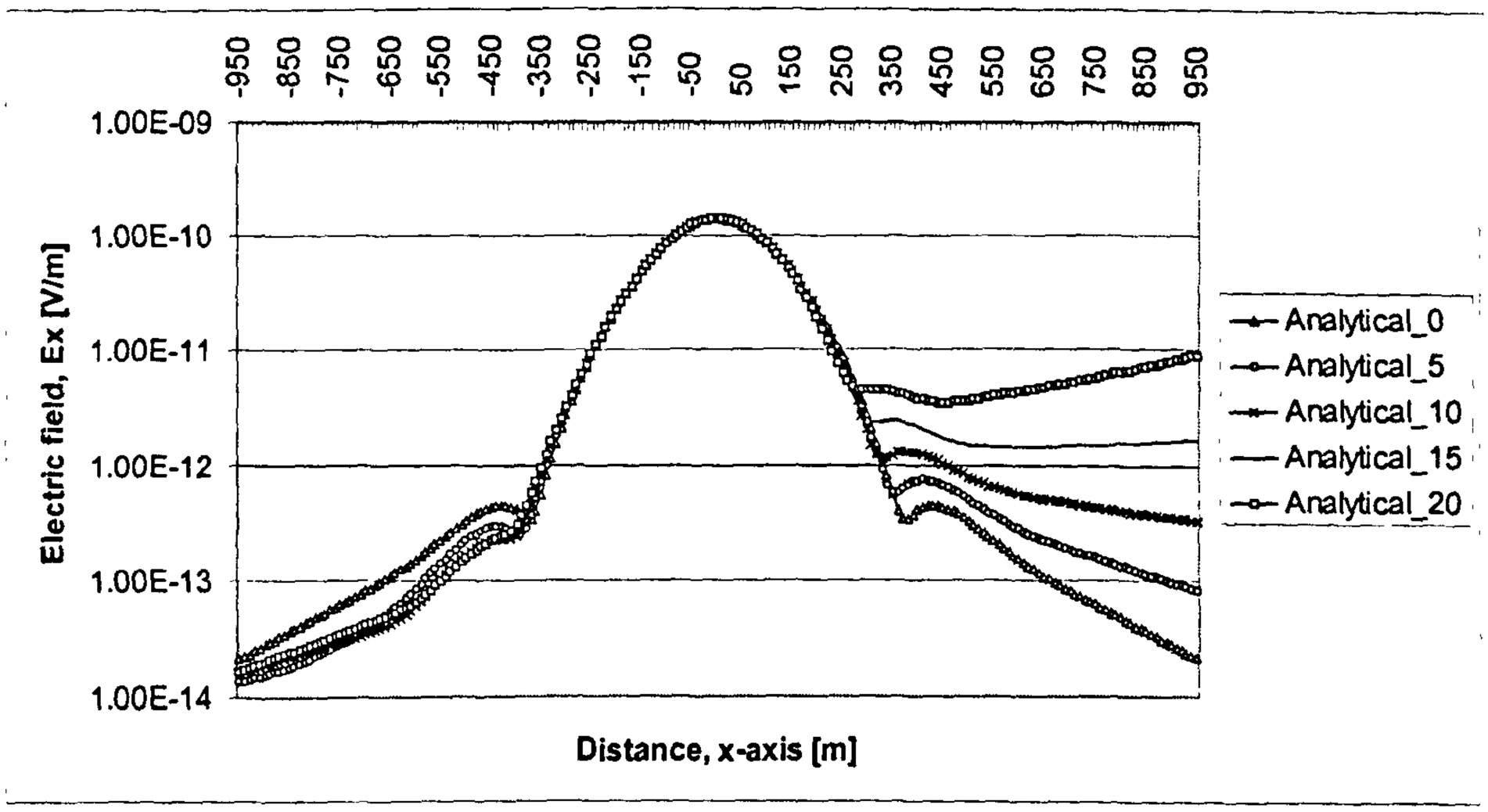

Figure 8.2: Sloping seabed results for different slope angles (HED)

Figure 8.2 shows the longitudinal electric field components for a HED source. The source frequency is 25Hz (sinusoidal), the source depth h=250m and the source strength is 1.0Am. Four results are presented pertaining to different seabed slope angles ϕ_s=5°, 10°, 15° and 20°, and the horizontally plane-stratified case (i.e. ϕ_s=0°) is included for comparative purposes.

Figure 8.2 shows that the horizontally plane-stratified solution is symmetrical about x=0.0, whereas the sloping seabed solutions show various degrees of asymmetry. The field predictions for x<-450m are lower in magnitude compared to the parallel interfaces solution. The largest difference was 0.6 (i.e. 60%) for ϕ_s=10° at x=-650m. The field predictions at x>450m were significantly greater than the parallel interfaces solution. The field increases at x=950m were by factors of 3, 14, 78 and 433 for ϕ_s=5°, 10°, 15° and 20°, respectively. In contrast, the field differences observed for –350m<x<250m were negligible, typically less than 1%. Results for ϕ_s=15° and 20° also showed that the field amplitude was increasing as the source-observer separation increased for x>450m.

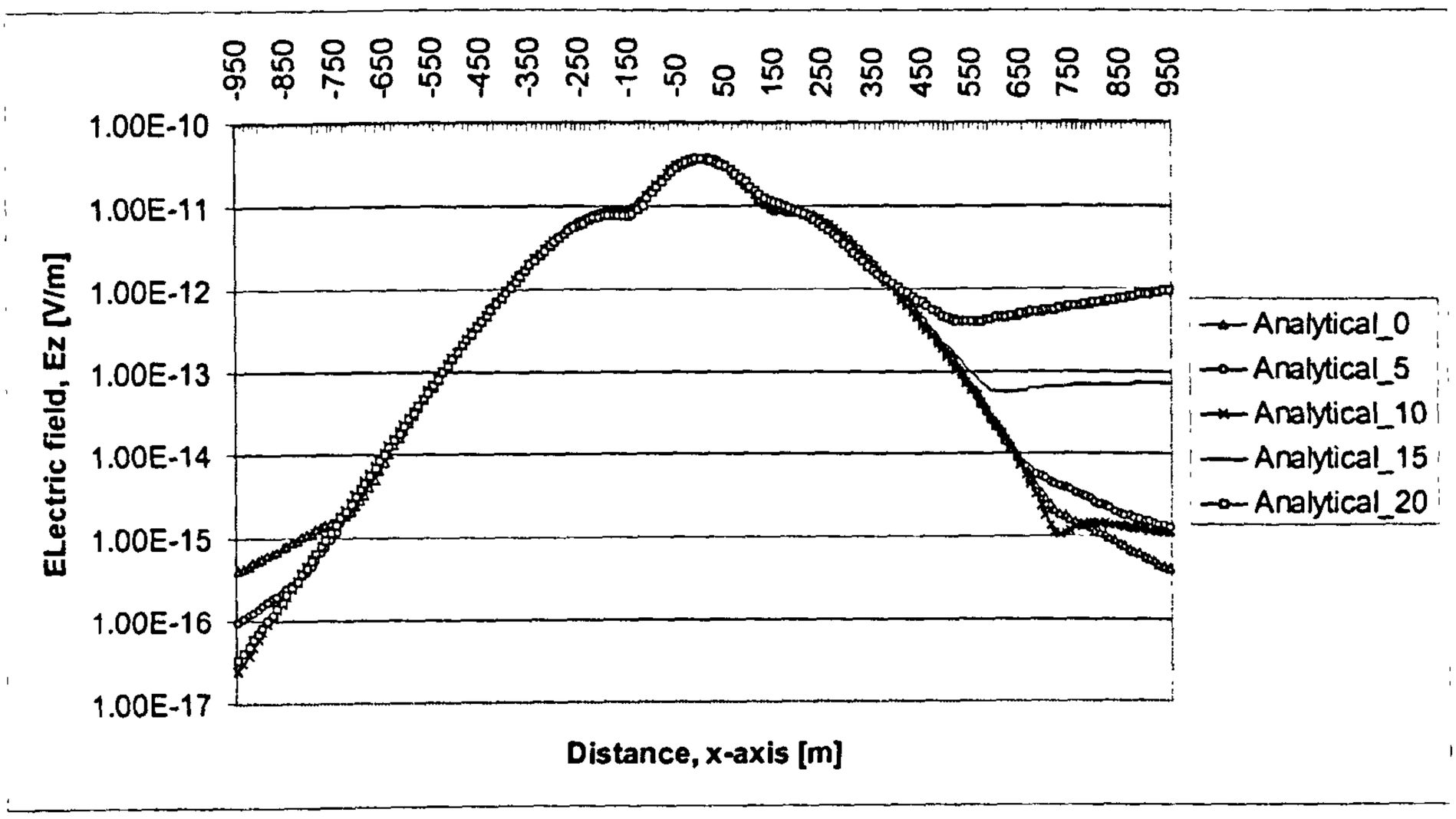

Figure 8.3: Sloping seabed results for different slope angles (VED)

Figure 8.3 shows the vertical electric field components for a VED above a sloping seabed. The results display the same behaviour seen with the HED source, particularly for large slope angles. The field predictions for x<-650m are lower in magnitude compared to the parallel interfaces solution. The largest difference was 0.95 (i.e. 95%) for ϕ_s=10° at x=-950m. The field predictions at x>450m were significantly greater than the parallel interfaces solution. The field increases at x=950m were by a factor of 2.2, 1.7, 181 and 2354 for ϕ_s=5°, 10°, 15° and 20°, respectively. In contrast, the field differences observed for –350m<x<250m were

small, typically less than 15%. Results for ϕ_s=15° and 20° also showed that the field amplitude was increasing as the source-observer separation increased for x>450m.

8.3 Low frequency result

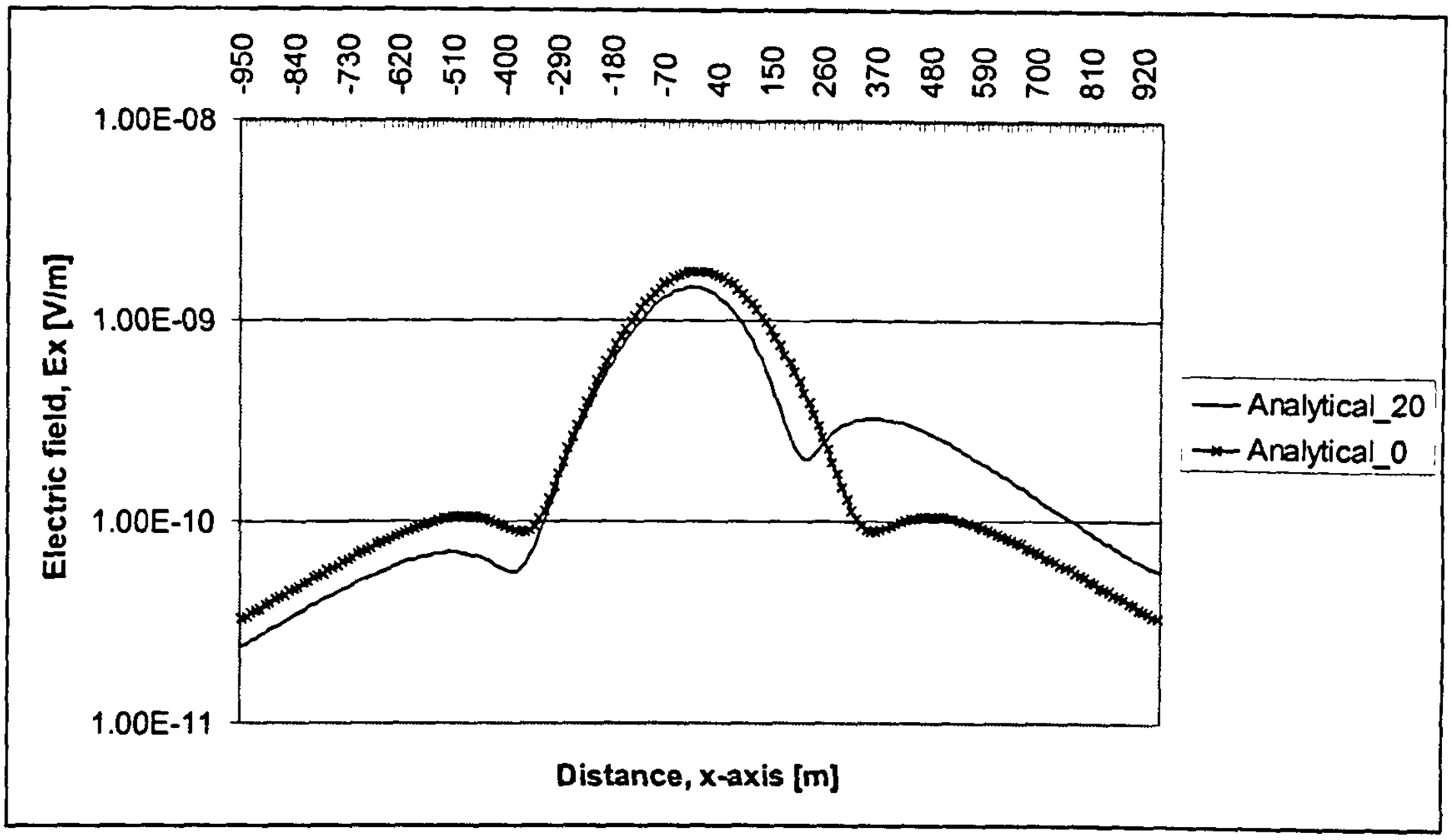

Figure 8.4: Low frequency sloping seabed result

Figure 8.4 shows the low frequency solution obtained at 1Hz. The source depth was 350m and the slope angle was 20°. The field levels are significantly greater for x>250m and significantly lower for x<-350m. The low frequency result also shows a significant near-field effect.

8.4 Varying the source depth

Figure 8.5 shows the relationship between the source depth and the resulting impact of the sloping seabed. The source depth is denoted by the curve name i.e. 'Analytical_*source depth*'. All the results are presented for a slope angle of 20°. The results show that the sloping seabed effect becomes less pronounced as the source depth decreases. The results also show various interference effects; the most interesting of which occurs when the source is at a depth of 100m.

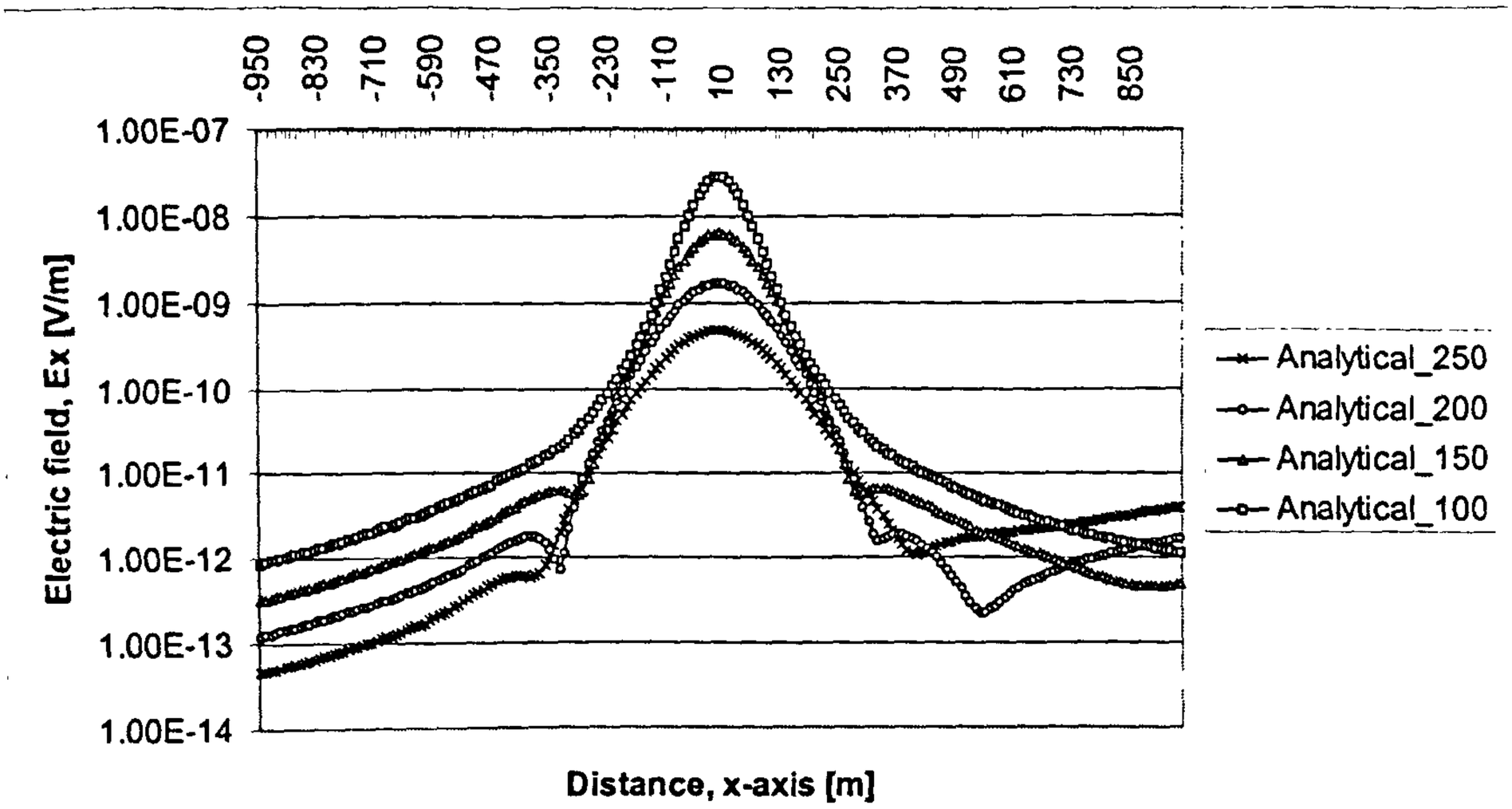

Figure 8.5: Sloping seabed results with different source heights

8.5 Sloping seabed profiles with curvature

Figures 8.6 and 8.7 show a 2-dimensional cross section through the *zx*-plane of the FDTD grid. A 3-layer medium consisting of air ($z<0$), sea and seabed is modelled with a electric dipole situated at (800m,500m). The sea-seabed interface extends from (0,400m) to (1200m,600m) and is marked by a black line. The contour map shows the peak positive field (*Ex*) in V/m over the time history of the excitation pulse. The excitation is by a Ricker pulse with a centre frequency of f_c=25Hz.

Figures 8.6 and 8.7 show the results from VED and HED sources respectively. Both figures show that the field in the sea layer increases as the sea depth decreases. This behaviour is in agreement with the analytical results and is attributed to the same effect. Figure 8.6 also shows that the fields of a given magnitude propagate further along the sea-seabed interface to the left of the source (i.e. x is less than 800m). No significant asymmetry is observable for the HED source, since the interference effects are less significant for this particular case.

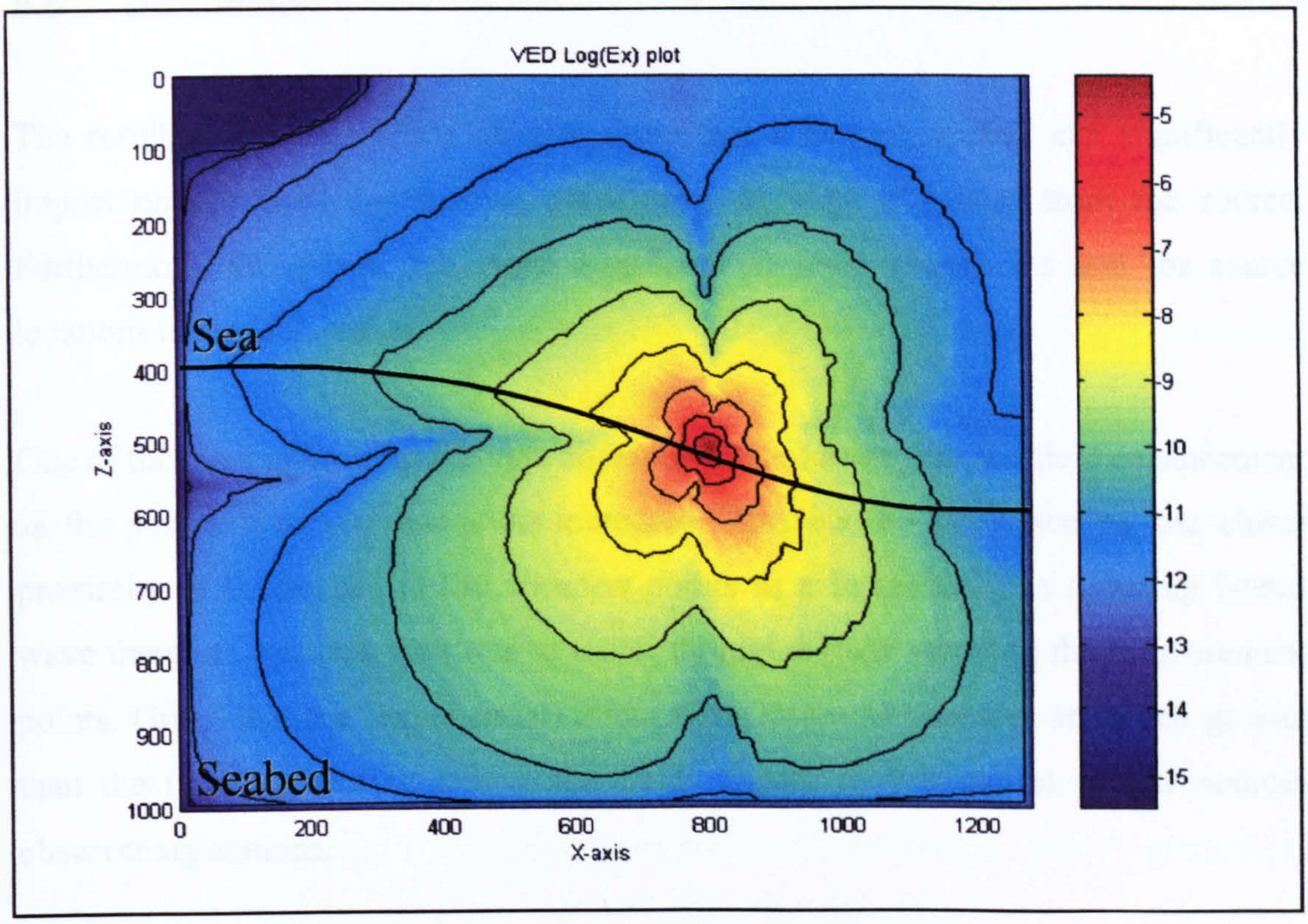

Figure 8.6: Log(*Ex*) plot for VED above sloping seabed

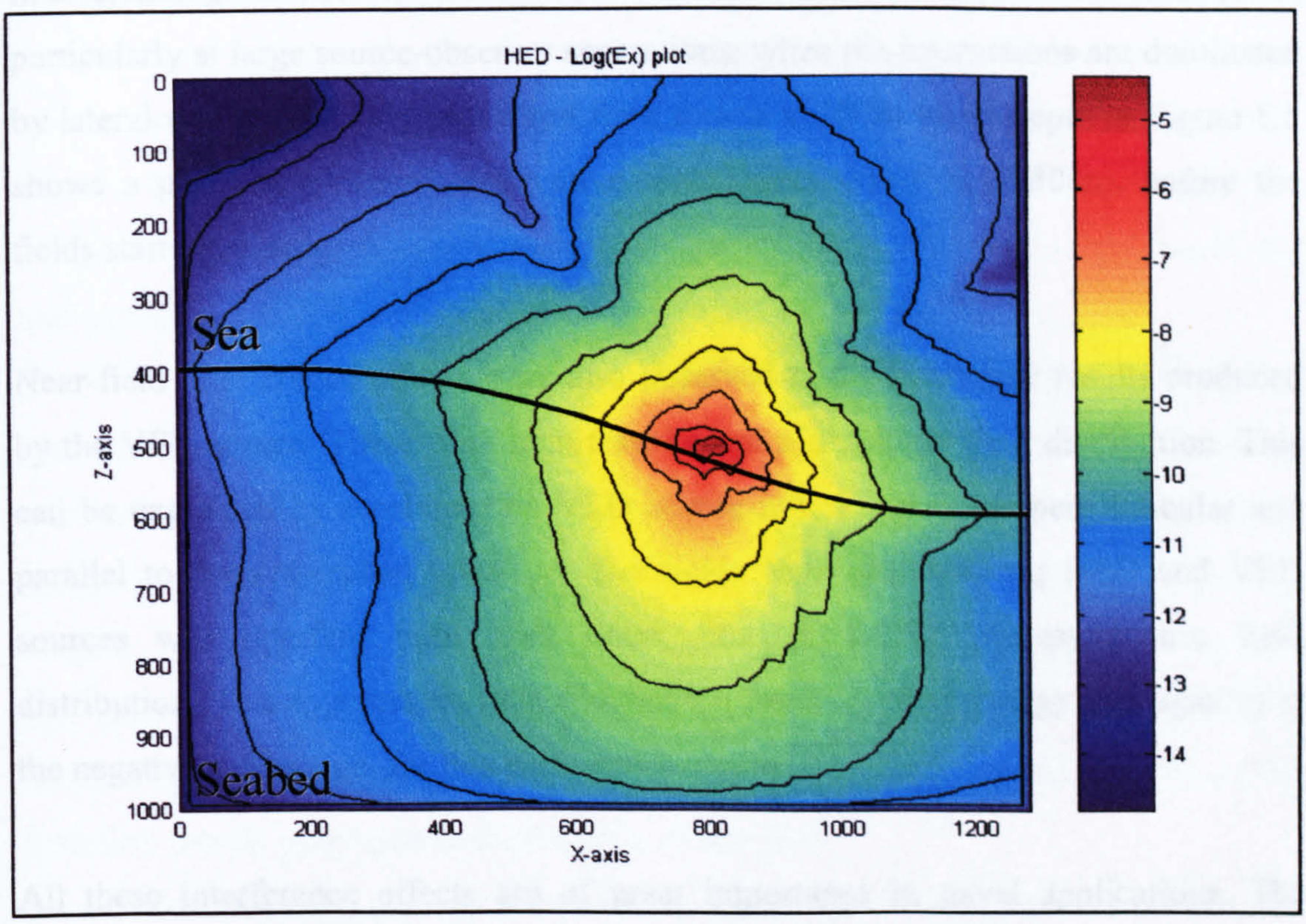

Figure 8.7: Log(Ex) plot for HED above sloping seabed

8.6 Discussion

The results presented in this chapter show that a sloping seabed can significantly impact on the field distribution, particularly at large distances from the source. Furthermore, the effects are more significant at high frequencies and for source locations is near the seabed.

One of the most interesting features observed in the results was the field enhancement as the source-observer separation increased. This can be explained by the closer proximity of the seabed to the observer points as x increases. The down-up lateral wave therefore has less seawater to travel through before reaching the measurement points. Given that the (exponential) attenuation losses in seawater are much greater than the $(1/R^3)$ spreading losses, the fields appear to increase at greater source-observer separations.

Another important observation is the interference produced by the interaction between the different propagation modes. The constructive and destructive interference gives rises to the detailed structure within the field distribution plots, particularly at large source-observer separations, when the interactions are dominated by lateral waves. The field prediction for a source at 100m water depth in Figure 8.5 shows a particularly strong destructive interference effect at x=500m, before the fields start increasing.

Near-field interference effects were also observed in the numerical results produced by the VED source. These were manifested as an asymmetric field distribution. This can be explained by resolving the VED source into components perpendicular and parallel to the sea-seabed interface. The fields from the resulting HED and VED sources will interfere with each other, thus producing an asymmetric field distribution. This asymmetric field distribution leads to more energy propagating in the negative x-direction, for this particular scenario.

All these interference effects are of great importance in naval applications. The features have advantages and disadvantages, depending on the friend or foe

perspective, for both detecting naval platforms and determining the optimum location of sensors.

The sloping seabed effects are more pronounced for sources near the seabed because more energy is supplied to the down-up lateral wave mode. Similarly, less energy arrives at the measurement points from the other propagation modes, thus increasing the relative importance of the down-up lateral wave mode.

The low frequency sources did not produce any order of magnitude field increases, since a significant proportion of the energy could still propagate as an up-down lateral wave. For example, the average sea depth for the geometry used in this chapter was 1.6δ at 1Hz. This means that the total attenuation and spreading losses suffered by the down-up and up-down lateral waves can be comparable when calculated over their respective path lengths. The dominant lateral wave contribution will be determined by the frequency, source location and the seabed conductivity.

The results produced in this thesis have consistently shown that the impact of a sloping seabed is relatively small near the source at high frequencies. This can be attributed to the dominance of the direct wave mode at small source-observer separations. In most cases, the peak fields are reduced by a few percent by the sloping seabed. However, there can be a significant difference in the near-field at low frequencies. This difference can manifest itself in the form of lower field amplitudes and asymmetry in the field distribution.

The asymmetry and lower field levels are attributed to the fact that a sloping seabed will reflect the fields incident upon it such that the angle of reflection $\phi_r=\phi_i-2\phi_s$, where ϕ_i is the angle of incidence, see Figure 8.8. Figure 8.8 also shows that the infinite medium solution (E_x-component) contains a narrow peak directly above/below the source; hence, most the energy from the E_x field component is directed vertically above/below the source. The reflected energy off the seabed will therefore mostly propagate in the negative x-direction.

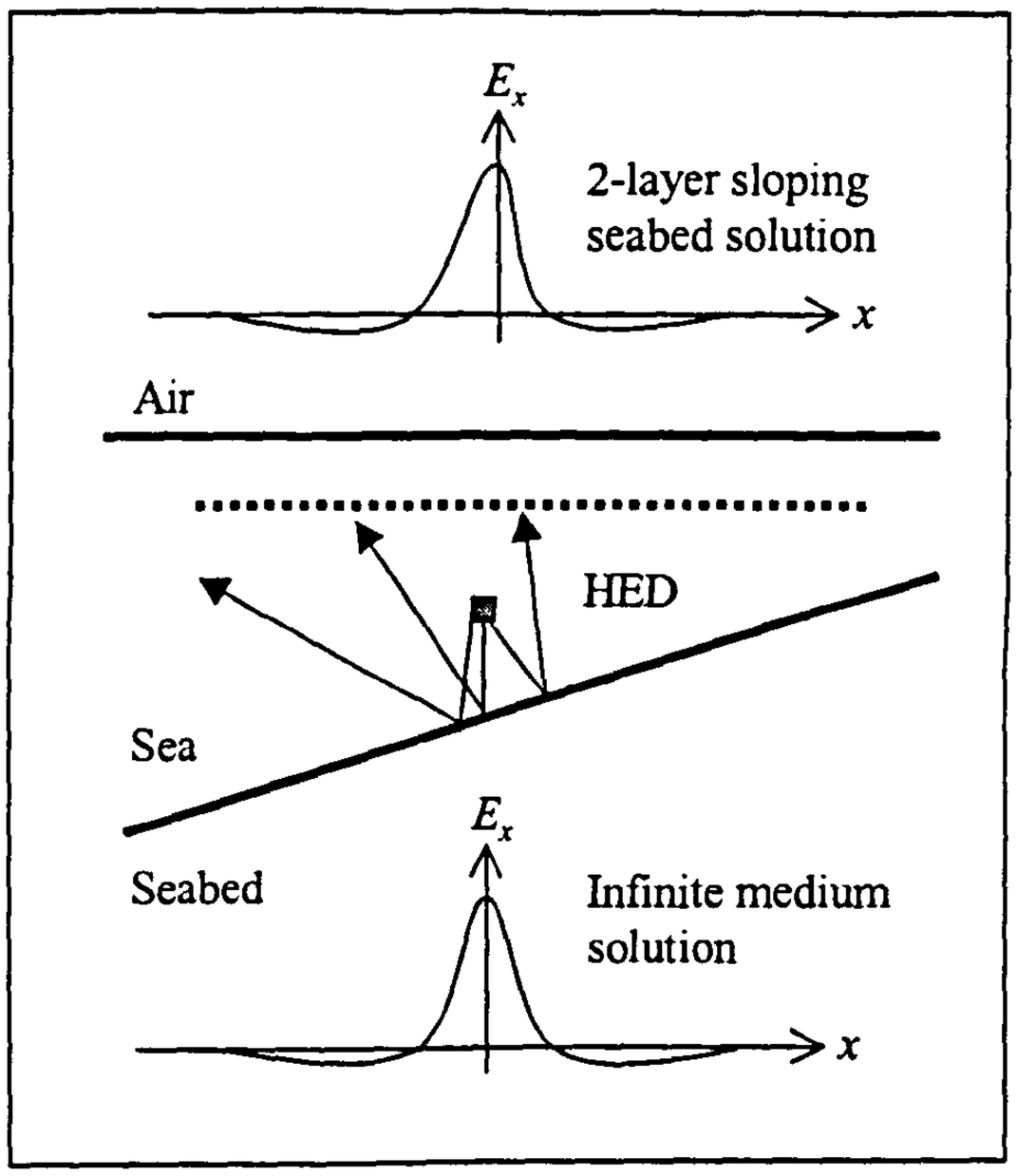

Figure 8.8: Asymmetry in near-field results

Chapter 9

Conclusions

This thesis has focused on the development of ELFE propagation models for littoral environments where the seabed is sloping. An approximate analytical model and a numerical FDTD model were developed and validated.

ELFE propagation models have widespread applications in the field of naval stealth, where the propagation of EM radiation in seawater can be exploited. A significant amount of research is undertaken to optimise the performance of these models, but very little work addresses the development of complex models that can be applied to the littoral environment. Recent research efforts have focused on the development of *n*-layer propagation models, where *n* is an integer $n \geq 3$. A handful of sloping seabed models have been developed over the years. These are generally implemented using numerical techniques due to the difficulty in obtaining analytical solutions. However, the models tend to be restricted to a 2-dimensional problem space and in most cases, only consider excitations from plane waves emanating in the upper atmosphere. A distribution of three-axis point dipole sources is typically required to characterise complex sources in naval applications. Hence, existing models are unsuitable for such applications.

Given that ELFE propagation models are critical for naval applications, it is vital to ensure all models are validated where possible using experimental data. This thesis presented the work undertaken to validate the 3-layer propagation model developed by Kings College London (KCL). The results showed that the KCL model could accurately model all the different propagation modes in a shallow water environment. The conductivity values for the sea and seabed were calculated using the experimental data, and represented 'effective' values required to approximate the real

environment using a 3-layer model. Further work also included the extension of the KCL 3-layer model to a 5-layer model i.e. ionosphere-air-sea-sediment-bedrock.

The focus of this thesis has been on the development of two sloping seabed models. The models developed in this study are the first to address complex 3-dimensional source distributions (composed of point sources) in seawater. The approximate analytical model is based on a modular approach to the solution, where the air-sea and sea-seabed interfaces are modelled separately. This model becomes very accurate at high frequencies where the interactions between the interfaces are negligible. Geometrical-optical techniques are used to model the neglected interface interactions by calculating attenuation and phases changes over the geometrical path travelled. The reflections are then approximated using plane wave theory (i.e. Fresnel reflection coefficients) and the lateral wave interactions are modelled using a 2-layer propagation model. A new geometrical-imaging technique has been developed to identify all the secondary reflections and the reflected lateral wave interactions. Simple geometrical transformations can be used to calculate the new image-source or image-observer points. This analytical model is computationally very efficient (i.e. based on 2-layer propagation models) and can produce accurate results across the whole ELFE spectrum. In fact, the interface interactions only need to be included when the sea depth is electrically shallow (i.e. less than five skin depths deep).

The numerical FDTD model was primarily intended as a research tool for addressing complex seabed profiles with curvature. The FDTD model uses the well-known Yee scheme and can address magnetic and electric sources. The FDTD model exploits co-ordinate transformations to map the sloping seabed geometry into a horizontally plane-stratified geometry. This simplifies the process of applying the boundary conditions to the familiar continuity requirements on the tangential field components along parallel interfaces. It also makes the problem space conform to a regular grid, thus simplifying the FDTD scheme itself. This also allows curved interfaces to be modelled accurately, rather than by using rectangular girds (i.e. a 'stair-case' approximation). Two analytical boundary conditions, both developed by L. Abrahamsson, were investigated to model propagation at the air-sea interface. The second formulation was developed to overcome the problems associated with the

original formulation. The problems were attributed to poor 'coupling' between the continuous analytical formulation and the discrete FDTD mesh.

Both the models developed in this study have undergone extensive validation tests. In most cases, the models were tested against horizontally plane-stratified propagation models (i.e. *LAYER* and *NLAYER*), where the latter models were all validated against experimental data.

The key components of the analytical model were the geometrical-optical method and the geometrical-imaging technique. These were compared against *NLAYER* and alternative analytical methods, respectively. Both showed very good agreement, thus demonstrating the validity of this modelling approach. The key components of the FDTD model were the boundary conditions between conducting media and at the air-sea interface, and the co-ordinate transformation used to map the geometry. The boundary conditions were successfully validated using *NLAYER*. All the propagation modes were being modelled correctly. The co-ordinate transformation was cross-validated by comparing results with the analytical sloping seabed model. The results were generally in good agreement. All the discrepancies in the results could be attributed to the small computational domain (i.e. reflections from the boundaries) and the distorted problem space. The latter caused the underlying assumption used to approximate the continuity of the tangential magnetic field components to become invalid, within the boundary condition formulation. Both these problems could be overcome by enlarging the problem space and using virtual interfaces to control the distortion in the mesh.

The validation process highlighted some of the shortfalls in the implementation of the FDTD model, which made it increasingly difficult to model large problems; due to the computational penalty involved.

Results obtained using the analytical sloping seabed have shown a number of interesting features. These include large field increases near coastlines and significant near-field effects at low frequencies. The large field increases were attributed to lower attenuation losses for the down-up lateral wave, as the observer points become closer to the seabed. The near-field changes were attributed to the seabed reflecting

energy away from the vertical *yz*-plane containing the source. The results also showed that the impact of the sloping seabed was greatest for high frequencies and for when the source is closer to the seabed. These two effects were necessary to increase the energy entering the seabed and to increase the relative contribution of the down-up lateral wave to the observed field levels. A number of interesting interference effects was also observed due to the interaction of the different propagation modes.

The numerical results were limited in number, but produced results that were consistent with the analytical results. Particularly the large field increases as the sea depth decreases and the interference effects.

In conclusion, the analytical and numerical sloping seabed models developed in this study have been validated for addressing this complex propagation problem. The models are suitable for the naval applications considered and have produced a number of interesting results. These have all been consistent with results obtained by other researchers such as Tyler *et al.*, (1999); thus providing confidence in the predictions. Further analysis using these models, specific to the scenarios of interest, will reveal the full impact of the sloping seabed. The focus of this will be complex source distributions and field predictions in the horizontal *xy*-plane (i.e. those cases not addressable by other sloping seabed models).

Recommendations for future work

There are a number of improvements that can be made to the sloping seabed models developed in this study. These are summarised below: -

FDTD model

- Implementation of absorbing boundary conditions to help reduce the computational domain of the FDTD mesh.
- The exploitation of symmetry about the vertical *zx*-plane may be possible for some dipole sources. This can reduce the computational requirements for sources directed in the *x* and *z*-directions.
- The removal of the 2^n x 2^n node restriction in the horizontal *xy*-plane of the FDTD mesh. This can be achieved by using a more general discrete Fourier transform (DFT) algorithm or padding out the unused 2^n x 2^n array with zeros.
- The co-ordinate transformation used to map the sloping seabed geometry into a horizontally plane-stratified geometry could be made fully 3-dimensional.

Approximate analytical model

- To extend the geometrical-imaging technique developed in this study to a fully 3-dimensional method. This will allow more accurate field predictions to be made in the horizontal *xy*-plane.

Other areas of future work could address the following

- The experimental validation of the sloping seabed models.
- The development of a coastline model
- Enhancements to the models to allow field predictions to be made in the air

Appendix A

Evaluation of commercial finite element method package

The section summarises the work undertaken to determine the feasibility of using a commercial finite-element method (FEM) package for tackling ELFE propagation problems in complex environments. This investigation was considered to be a prudent step before attempting to developing new models specifically for this application.

A.1 Introduction

The result presented in this section was obtained using the *MEGA* FEM package developed by the Electrical Engineering Department at the University of Bath, England. Attempts were made to use *MEGA* to model both static and alternating electric sources.

Unfortunately, the FEM software was unable to model alternating electric sources situated in the sea layer. The numerical model suffered from convergence problems, which prevented any solutions being obtained. The so-called $\mathbf{A}V$ formulation was the only suitable candidate for this application implemented within *MEGA* since the other formulations were only applicable at high frequencies (i.e. MHz and above) or for 2-dimensional problems.

This section thus presents a result showing the field distribution from a static electric source within a complex coastal environment. This result is still considered useful since it gives a good indication to the results expected at ultra low frequencies (ULF) i.e. 1Hz and below.

An overview of the formulations implemented within *MEGA* (Bath University, 1995) is presented in an annex at the end of this chapter.

A.2 Results

Figure A.1 shows a grey-scale contour plot of the horizontal electric (E_x) field at the mesh surface (white to black represents high to low field levels). The problem space shown has dimensions of 2km x 2km x 0.8km. The source is a HED directed towards the coastline.

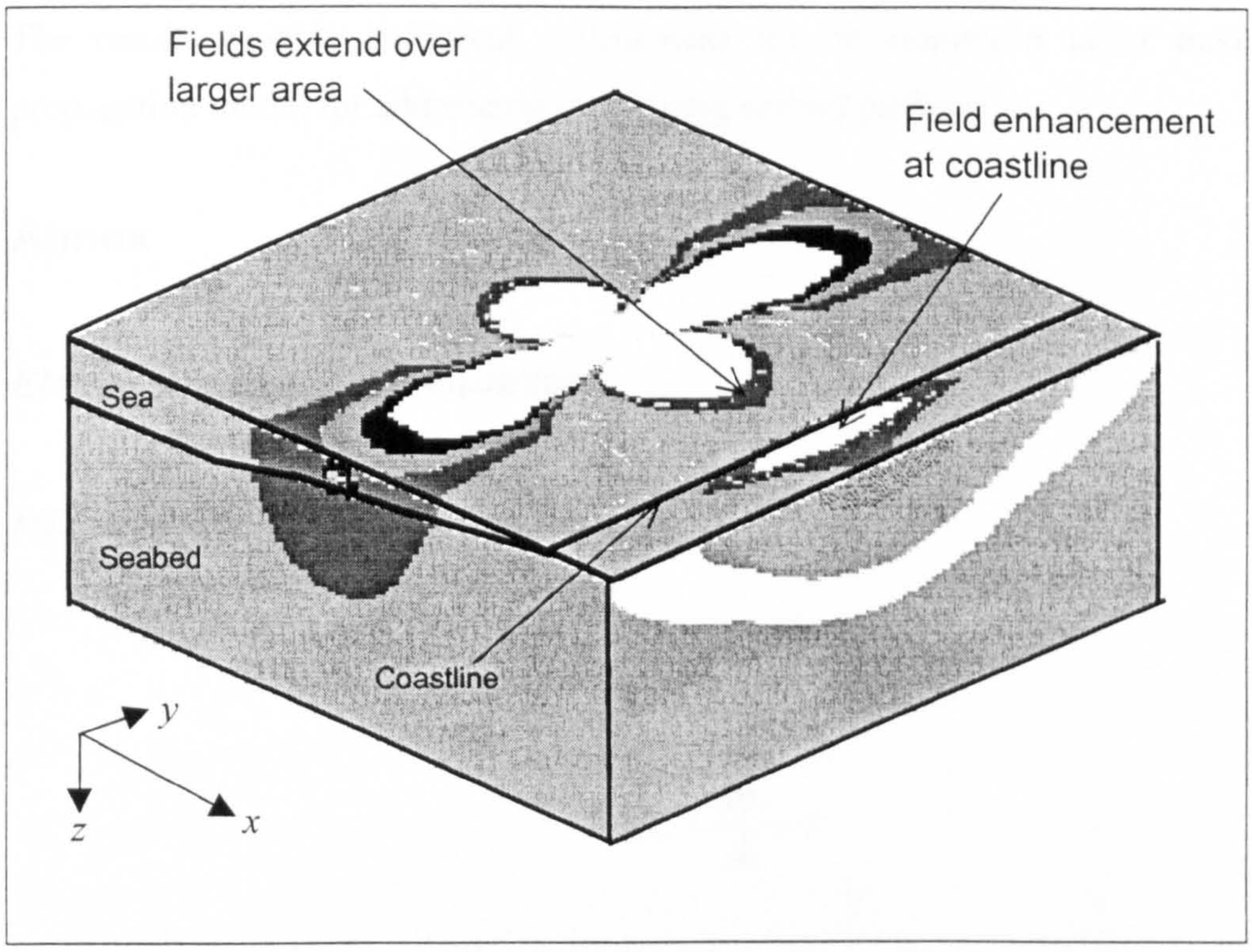

Figure A.1: Sloping seabed with coastline (static result)

This result shows qualitatively that the electric fields appear to extend over greater distances as the sea depth decreases. Thus indicating there is a larger contribution from energy propagating within the seabed. There is also a significant enhancement of field levels at the coastline. This is also attributed to energy emanating from the seabed.

A.3 Discussion

This study has shown that *MEGA*, the commercial FEM package, is currently unable to solve the ELFE propagation problems considered in this study. However, *MEGA*

did cope extremely well with DC problems involving electric dipoles in various complex environments.

The DC results are considered important since they can provide a good indication of how ELFE signatures behave at low frequencies (i.e. approaching the DC limit). The results show enhanced field levels as the sea depth decreases and at the coastline.

The results provide sufficient justification for developing a tailor made ELFE propagation model for addressing the sloping seabed problem.

Annex

Electromagnetic field equations

MEGA is based on the following equations: -

$$\nabla \times \mathbf{H} = \mathbf{J} \tag{A.1}$$

$$\nabla \times \mathbf{E} + \frac{\partial \mathbf{B}}{\partial} = 0 \tag{A.2}$$

$$\mathbf{B} = \mu \mathbf{H} \tag{A.3}$$

$$\mathbf{J} = \sigma \mathbf{E} \tag{A.4}$$

where **H** is the magnetic field intensity, **J** is the free current density, **E** is the electric field, **B** is the magnetic flux density, σ is the electrical conductivity, μ is the magnetic permeability and t denotes time.

Electrostatic problems

When considering electrostatic problems, the equations solved by *MEGA* are:

$$\nabla.\mathbf{D} = \rho \tag{A.5}$$

and

$$\nabla.\varepsilon\nabla V = -\rho \tag{A.6}$$

where **D** is the displacement field, ε is the permittivity, V is the electrostatic potential and ρ is the charge density. The electric field can then be determined using the following relationship:

$$\mathbf{E} = -\nabla V\,. \tag{A.7}$$

This type of problem requires prescribed voltages or charges for the source, with the materials properties expressed in terms of the dielectric constants for the media.

AV formulation

The so-called **A***V* formulation is a method of representing electromagnetic fields using the magnetic vector potential **A** and the electric scalar potential *V*. This formulation is currently under investigation for modelling alternating electric dipoles. Although there are some problems associated with using this formulation, it appears to be the only suitable formulation implemented in *MEGA* at present.

One of the main problems with this formulation is that it leads to more unknowns than equations. A secondary problem is that the vector potential needs to be gauged to ensure a unique solution is obtained, however this can cause problems with the equations becoming over-constrained.

The magnetic vector potential **A** is used to determine the magnetic flux density using the following relationship

$$\mathbf{B} = \nabla \times \mathbf{A}\,. \tag{A.8}$$

The electric field can be expressed using both **A** and the electric scalar potential V by

$$\mathbf{E} = -\frac{\partial \mathbf{A}}{\partial t} - \nabla V \tag{A.9}$$

It should be noted that a knowledge of **B** and **E** does not uniquely define **A** and V. Additional conditions are required to impose a "gauge" on **A**. This gauging problem tends to make the use of the electric scalar potential unattractive for most applications. However, the *MEGA* program does have the capability to use this formulation either un-gauged or with a penalty term to define the divergence of **A**.

The partial differential equation (PDE) to be solved is derived by substituting equations (A.4), (A.8) and (A.9) into equation (A.1), resulting in the following expression

$$\nabla \times \frac{1}{\mu} \nabla \times \mathbf{A} + \sigma \left(\frac{\partial \mathbf{A}}{\partial t} + \nabla V \right) = 0 . \tag{A.10}$$

This equation leaves **A** without a gauge (and also leads to more unknowns than equations). To overcome this problem an augmented set of equations can be solved,

$$\nabla \times \frac{1}{\mu} \nabla \times \mathbf{A} - \left\{ \frac{1}{\mu_0} \nabla \nabla . \mathbf{A} \right\} + \sigma \left(\frac{\partial \mathbf{A}}{\partial t} + \nabla V \right) = 0 \tag{A.11}$$

$$\nabla . \sigma \left(\frac{\partial \mathbf{A}}{\partial t} + \nabla V \right) = 0 \tag{A.12}$$

The term within braces {} is optionally added as a penalty term constraining the divergence of **A** to be zero.

Furthermore, to ensure the solution is unique the additional constraint shown below can be applied on the boundary of regions where **A** is defined

$$\mathbf{A} . \hat{\mathbf{n}} = 0 \tag{A.13}$$

where $\hat{\mathbf{n}}$ is a unit vector normal to the surface.

Appendix B

'Continuous' air-sea interface formulation

This appendix details the original air-sea interface formulation developed by Leif Abrahamsson (1997), of FOI (Sweden). As mentioned in Chapter 6, this formulation suffered from stability problems and could not accurately model the propagation of up-down lateral waves. This formulation was therefore abandoned and a new formulation was developed. For completeness, this formulation is detailed below. However, the formulation has been simplified from that originally proposed by L. Abrahamsson. This simplification was essential to overcome the stability problems encountered i.e. the solution always increased exponentially!

Chapter 6 indicated that the most probable cause for the problems experienced with this formulation was the incompatibility between the continuous nature of the boundary condition and the discrete nature of the FDTD method. It is anticipated that this formulation could be applied to other models or could be modified to resolve this problem.

The author also acknowledges that the problems may have also arisen from the incorrect implementation of the model. However, this is considered unlikely, as the implemention was extensively review by the author and Leif Abrahamsson.

B.1 Fields in air

The equations governing the behaviour of the electric fields in air are simply postulated such that they satisfy the divergence condition for a source free region (i.e. Div**E**=0). The three components of the electric field in air (i.e. denoted by superscript A) are given by

$$E_x^A = -2 \iint_{z=0} E_x^A(x', y') \frac{\partial g}{\partial z'} dx' dy' \tag{B.1}$$

$$E_y^A = -2 \iint_{z=0} E_y^A(x', y') \frac{\partial g}{\partial z'} dx' dy' \tag{B.2}$$

$$E_z^A = 2 \iint_{z=0} \left[E_x^A(x', y') \frac{\partial g}{\partial x'} + E_y^A(x', y') \frac{\partial g}{\partial y'} \right] dx' dy' \tag{B.3}$$

The arrangement of the tangential electric field nodes on the air sea interface can be used to explicitly enforce the boundary conditions. The continuity of E_x and E_y is assured since the nodes are common to both sides of the interface, see Figure B.1.

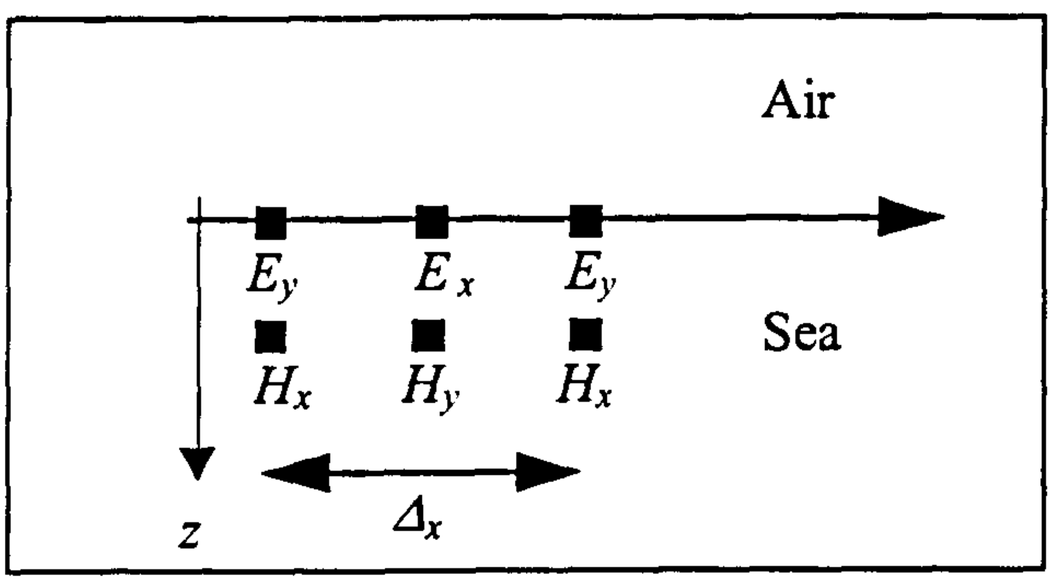

Figure B.1: Nodes at air-sea interface

Given that $\mu \frac{\partial H_x}{\partial t}$ and $\mu \frac{\partial H_y}{\partial t}$ also need to be continuous across the interface, Equation (6.1) can be used to show that

$$\left(\nabla \times E^A\right) = \left(\nabla \times E^W\right) \tag{B.4}$$

must also be continuous, where E^A and E^W are the electric fields in the air and seawater (i.e. denoted by superscript W) mediums, respectively.

The analytical boundary condition at the air-sea interface can be derived by substituting Equations (B.1) to (B.3) into Equation (B.4) and assuming $E_x^A = E_x^W$ and $E_y^A = E_y^W$ (e.g. tangential field components are continuous), thus giving

$$\frac{\partial E_x^w}{\partial z} - \frac{\partial E_z^w}{\partial x} = 2 \iint_{z=0} \left(E_x^w \left(\frac{\partial g}{\partial x \partial x'} + \frac{\partial g}{\partial z \partial z'} \right) + E_y^w \frac{\partial g}{\partial x \partial y'} \right) dx' dy' \qquad \text{(B.5)}$$

and

$$\frac{\partial E_z^w}{\partial y} - \frac{\partial E_y^w}{\partial z} = 2 \iint_{z=0} \left(E_x^w \frac{\partial g}{\partial y \partial x'} + E_y^w \left(\frac{\partial g}{\partial y \partial y'} + \frac{\partial g}{\partial z \partial z'} \right) \right) dx' dy' \qquad \text{(B.6)}$$

where x, y and z are variables of the Cartesian co-ordinate system, the primed[1] and unprimed variables denote the source and observer co-ordinates, respectively and

$$g(\underline{r}, \underline{r}') = \frac{1}{4\pi |\underline{r} - \underline{r}'|}. \qquad \text{(B.7)}$$

Equations (B.5) and (B.6) are both integral equations with hyper-singular kernel, which makes their evaluation very difficult.

B.2 Approximating differential operators

The differential terms on the left hand side (LHS) of Equations (B.5) and (B.6) can be approximated using a Taylor series expansion up to and including first order terms, see Equation (B.8).

$$f(z) = f(a) + (z-a) f'(a) + \frac{(z-a)^2}{2!} f''(a) + \ldots \qquad \text{(B.8)}$$

[1] The finite difference operators have x' and z' to denote they are transformed variables. This should not be confused with the primed quantities in the air/sea formulation that are simply source co-ordinates. The FDTD code is implemented such that the grid points on the air-sea interface are not transformed into the new co-ordinate system.

The Taylor series can be used to generate the following differential approximations for points on or near the air-sea interface, where 'z' is 1 or $^1/_2$ and 'a' is zero (i.e. on the interface).

$$\frac{E_x^{n+1}\left(i+\frac{1}{2},j,1\right)-E_x^{n+1}\left(i+\frac{1}{2},j,0\right)}{\Delta z}=\frac{\partial E_x^{n+1}\left(i+\frac{1}{2},j,0\right)}{\partial z} \tag{B.9}$$

$$\frac{E_z^{n+1}\left(i+1,j,\frac{1}{2}\right)-E_z^{n+1}\left(i,j,\frac{1}{2}\right)}{\Delta x}=\frac{\partial E_z^{n+1}\left(i+\frac{1}{2},j,\frac{1}{2}\right)}{\partial x}=\frac{\partial E_z^{n+1}\left(i+\frac{1}{2},j,0\right)}{\partial x} \tag{B.10}$$

$$\frac{E_y^{n+1}\left(i,j+\frac{1}{2},1\right)-E_y^{n+1}\left(i,j+\frac{1}{2},0\right)}{\Delta z}=\frac{\partial E_y^{n+1}\left(i,j+\frac{1}{2},0\right)}{\partial z} \tag{B.11}$$

$$\frac{E_z^{n+1}\left(i,j+1,\frac{1}{2}\right)-E_z^{n+1}\left(i,j,\frac{1}{2}\right)}{\Delta y}=\frac{\partial E_z^{n+1}\left(i,j+\frac{1}{2},\frac{1}{2}\right)}{\partial y}=\frac{\partial E_z^{n+1}\left(i,j+\frac{1}{2},0\right)}{\partial y} \tag{B.12}$$

The LHS of Equations (5.21) and (5.22) can now be expressed as

$$\frac{\partial E_x}{\partial z}-\frac{\partial E_z}{\partial x}=\frac{E_x^{n+1}\left(i+\frac{1}{2},j,1\right)-E_x^{n+1}\left(i+\frac{1}{2},j,0\right)}{\Delta z}-\frac{E_z^{n+1}\left(i+1,j,\frac{1}{2}\right)-E_z^{n+1}\left(i,j,\frac{1}{2}\right)}{\Delta x} \tag{B.13}$$

and

$$\frac{\partial E_z}{\partial y}-\frac{\partial E_y}{\partial z}=\frac{E_z^{n+1}\left(i,j+1,\frac{1}{2}\right)-E_z^{n+1}\left(i,j,\frac{1}{2}\right)}{\Delta y}-\frac{E_y^{n+1}\left(i,j+\frac{1}{2},1\right)-E_y^{n+1}\left(i,j+\frac{1}{2},0\right)}{\Delta z} \tag{B.14}$$

B.3 Convolution integrals

The integral expressions on the right hand side (RHS) of Equations (B.5) and (B.6) can be easily solved because they are in the form of convolution integrals. Recognising this relationship is critical for simplifying the derivation of the solution. Hence, Equation (B.5) becomes

$$\frac{\partial E_x}{\partial z}-\frac{\partial E_z}{\partial x}=-2\iint_{z=0}\left[E_x\left(\frac{\partial^2 g}{\partial z\partial z'}+\frac{\partial^2 g}{\partial x\partial x'}\right)+E_y\frac{\partial^2 g}{\partial x\partial y'}\right]dx'\,dy'$$

$$=-2E_x^{n+1}\left(i+\tfrac{1}{2},j,0\right)\otimes\left(\frac{\partial^2 g}{\partial z\partial z'}+\frac{\partial^2 g}{\partial x\partial x'}\right)-2E_y^{n+1}\left(i,j+\tfrac{1}{2},0\right)\otimes\frac{\partial^2 g}{\partial x\partial y'} \qquad \text{(B.15)}$$

and Equation (B.6) becomes

$$\frac{\partial E_z}{\partial y}-\frac{\partial E_y}{\partial z}=2\iint_{z=0}\left[E_x\frac{\partial^2 g}{\partial x'\partial y}+E_y\left(\frac{\partial^2 g}{\partial y\partial y'}+\frac{\partial^2 g}{\partial z\partial z'}\right)\right]dx'\,dy'$$

$$=2E_x^{n+1}\left(i+\tfrac{1}{2},j,0\right)\otimes\frac{\partial^2 g}{\partial x'\partial y}+2E_y^{n+1}\left(i,j+\tfrac{1}{2},0\right)\otimes\left(\frac{\partial^2 g}{\partial y\partial y'}+\frac{\partial^2 g}{\partial z\partial z'}\right) \qquad \text{(B.16)}$$

The two analytical expressions for the E_x^{n+1} and E_y^{n+1} fields at the air-sea interface can now be written in full as

$$2E_x^{n+1}\left(i+\tfrac{1}{2},j,0\right)\otimes\frac{\partial^2 g}{\partial x'\partial y}+2E_y^{n+1}\left(i,j+\tfrac{1}{2},0\right)\otimes\left(\frac{\partial^2 g}{\partial y\partial y'}+\frac{\partial^2 g}{\partial z\partial z'}\right)-\frac{1}{\Delta z}E_y^{n+1}\left(i,j+\tfrac{1}{2},0\right)$$

$$=\frac{E_z^{n+1}\left(i,j+1,\frac{1}{2}\right)-E_z^{n+1}\left(i,j,\frac{1}{2}\right)}{\Delta y}-\frac{1}{\Delta z}E_y^{n+1}\left(i,j+\tfrac{1}{2},1\right) \qquad \text{(B.17)}$$

and

$$-2E_x^{n+1}\left(i+\tfrac{1}{2},j,0\right)\otimes\left(\frac{\partial^2 g}{\partial x\partial x'}+\frac{\partial^2 g}{\partial z\partial z'}\right)+\frac{1}{\Delta z}E_x^{n+1}\left(i+\tfrac{1}{2},j,0\right)$$

$$-2E_y^{n+1}\left(i,j+\tfrac{1}{2},0\right)\otimes\frac{\partial^2 g}{\partial x\partial y'}=\frac{1}{\Delta z}E_x^{n+1}\left(i+\tfrac{1}{2},j,1\right)$$

$$-\frac{E_z^{n+1}\left(i+1,j,\tfrac{1}{2}\right)-E_z^{n+1}\left(i,j,\tfrac{1}{2}\right)}{\Delta x} \qquad \text{(B.18)}$$

B.4 Full solution

Explicit expressions for E_x^{n+1} and E_y^{n+1} can be obtained from Equations (B.17) and (B.18) if they are Fourier transformed and rewritten in matrix form as shown in Equation (B.19). Fourier transforming Equations (B.17) and (B.18) replaces the convolutions by simple multiplications.

$$\begin{bmatrix} a_{11} & a_{12} \\ a_{21} & a22 \end{bmatrix}\begin{bmatrix} \hat{E}_x^{n+1} \\ \hat{E}_y^{n+1} \end{bmatrix}=\begin{bmatrix} f_1 \\ f_2 \end{bmatrix} \qquad \text{(B.19)}$$

The new Fourier transformed variables are all denoted with by the hat symbol. a_{11}, a_{12}, a_{21}, a_{22}, f_1 and f_2 are given by

$$a_{11}=2\frac{\partial^2\hat{g}}{\partial x'\partial y}, \qquad \text{(B.20)}$$

$$a_{12}=2\left(\frac{\partial^2\hat{g}}{\partial y\partial y'}+\frac{\partial^2\hat{g}}{\partial z\partial z'}\right)-\frac{1}{\Delta z}, \qquad \text{(B.21)}$$

$$a_{21}=-2\left(\frac{\partial^2\hat{g}}{\partial x\partial x'}+\frac{\partial^2\hat{g}}{\partial z\partial z'}\right)+\frac{1}{\Delta z}, \qquad \text{(B.22)}$$

$$a_{22}=-2\frac{\partial^2\hat{g}}{\partial x\partial y'}, \qquad \text{(B.23)}$$

$$f_1 = \frac{1}{\Delta y}\left[\hat{E}_z^{n+1}\left(i, j+1, \frac{1}{2}\right) - \hat{E}_z^{n+1}\left(i, j, \frac{1}{2}\right)\right] - \frac{1}{\Delta z}\hat{E}_y^{n+1}\left(i, j+\frac{1}{2}, 1\right), \qquad \text{(B.24)}$$

and

$$f_2 = \frac{1}{\Delta z}\hat{E}_x^{n+1}\left(i+\frac{1}{2}, j, 1\right) - \frac{1}{\Delta x}\left[\hat{E}_z^{n+1}\left(i+1, j, \frac{1}{2}\right) - \hat{E}_z^{n+1}\left(i, j, \frac{1}{2}\right)\right]. \qquad \text{(B.25)}$$

Equation (B.7) can also be differentiated and Fourier transformed to give the following expressions

$$\frac{\partial^2 \hat{g}}{\partial x \partial y'} = -2\pi \frac{k_x k_y}{\sqrt{k_x^2 + k_y^2}} \qquad \text{(B.26)}$$

$$\frac{\partial^2 \hat{g}}{\partial x' \partial y} = -2\pi \frac{k_x k_y}{\sqrt{k_x^2 + k_y^2}} \qquad \text{(B.27)}$$

$$\frac{\partial^2 \hat{g}}{\partial x \partial x'} = -2\pi \frac{k_x^2}{\sqrt{k_x^2 + k_y^2}} \qquad \text{(B.28)}$$

$$\frac{\partial^2 \hat{g}}{\partial y \partial y'} = -2\pi \frac{k_y^2}{\sqrt{k_x^2 + k_y^2}} \qquad \text{(B.29)}$$

$$\frac{\partial^2 \hat{g}}{\partial z \partial z'} = 2\pi\sqrt{k_x^2 + k_y^2} \qquad \text{(B.30)}$$

where k_x and k_y are wave numbers in the x and y directions as defined in Chapter 6, see Equations (6.51), (6.52), (6.61) and (6.62).

Equations (B.19) to (B.30) were originally implemented in the FDTD scheme. After calculated $\hat{E}_x^{n+1}$ and $\hat{E}_y^{n+1}$, they were both inverse Fourier transformed to produce E_x^{n+1} and E_y^{n+1}.

B.5 Validation

The air-sea interface formulation was tested by comparing the results obtained using the FDTD model and the *NLAYER* propagation model. The field predictions were taken from a HED source excited by a Ricker pulse with a centre frequency of f_c=300Hz (see Section 7.3).

Figures B.2 and B.3 show the longitudinal electric field from a HED source in an infinite medium with conductivity σ=3S/m. The measurements were both made 50m directly above the source.

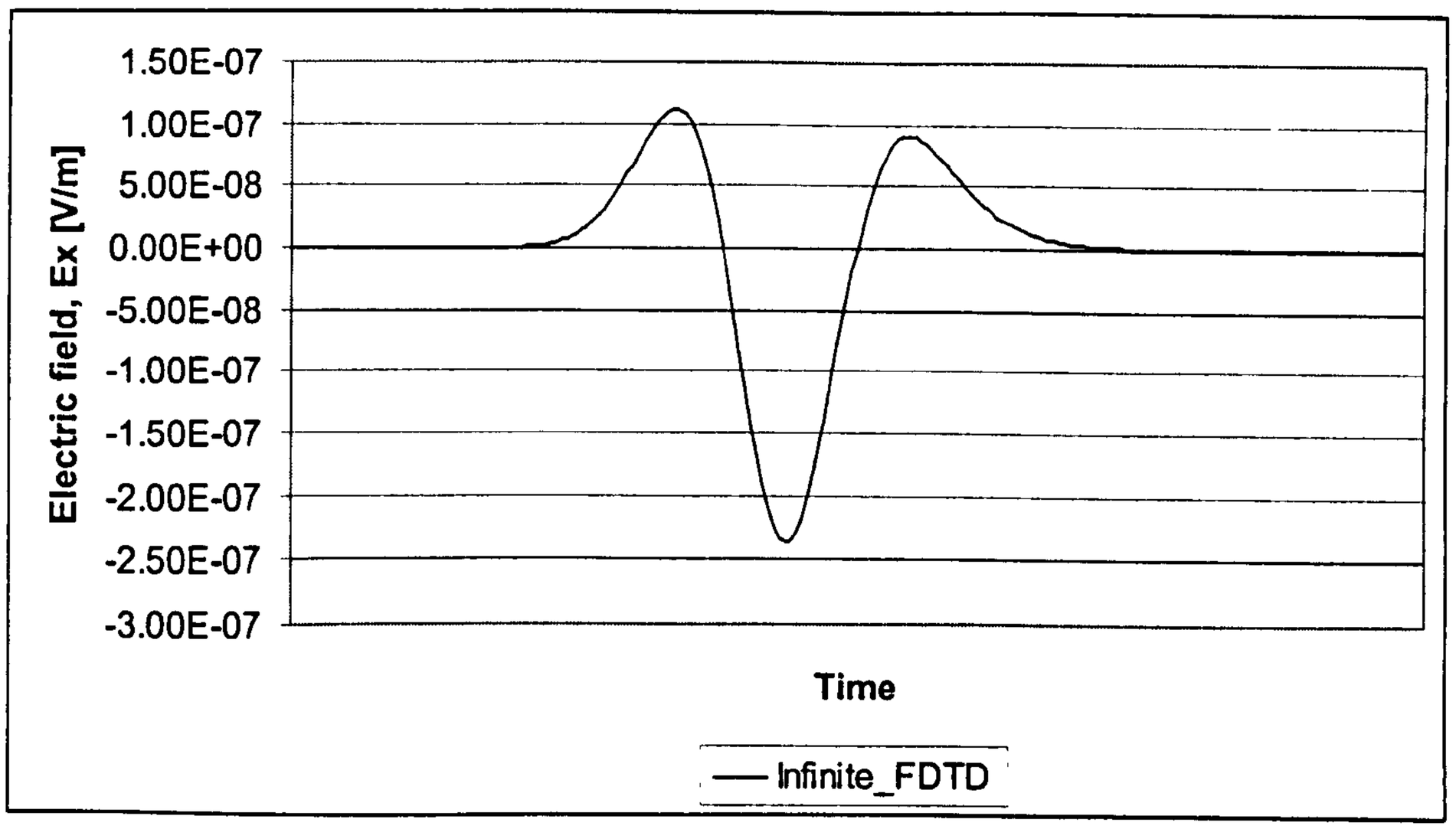

Figure B.2: FDTD solution for HED source in infinite medium

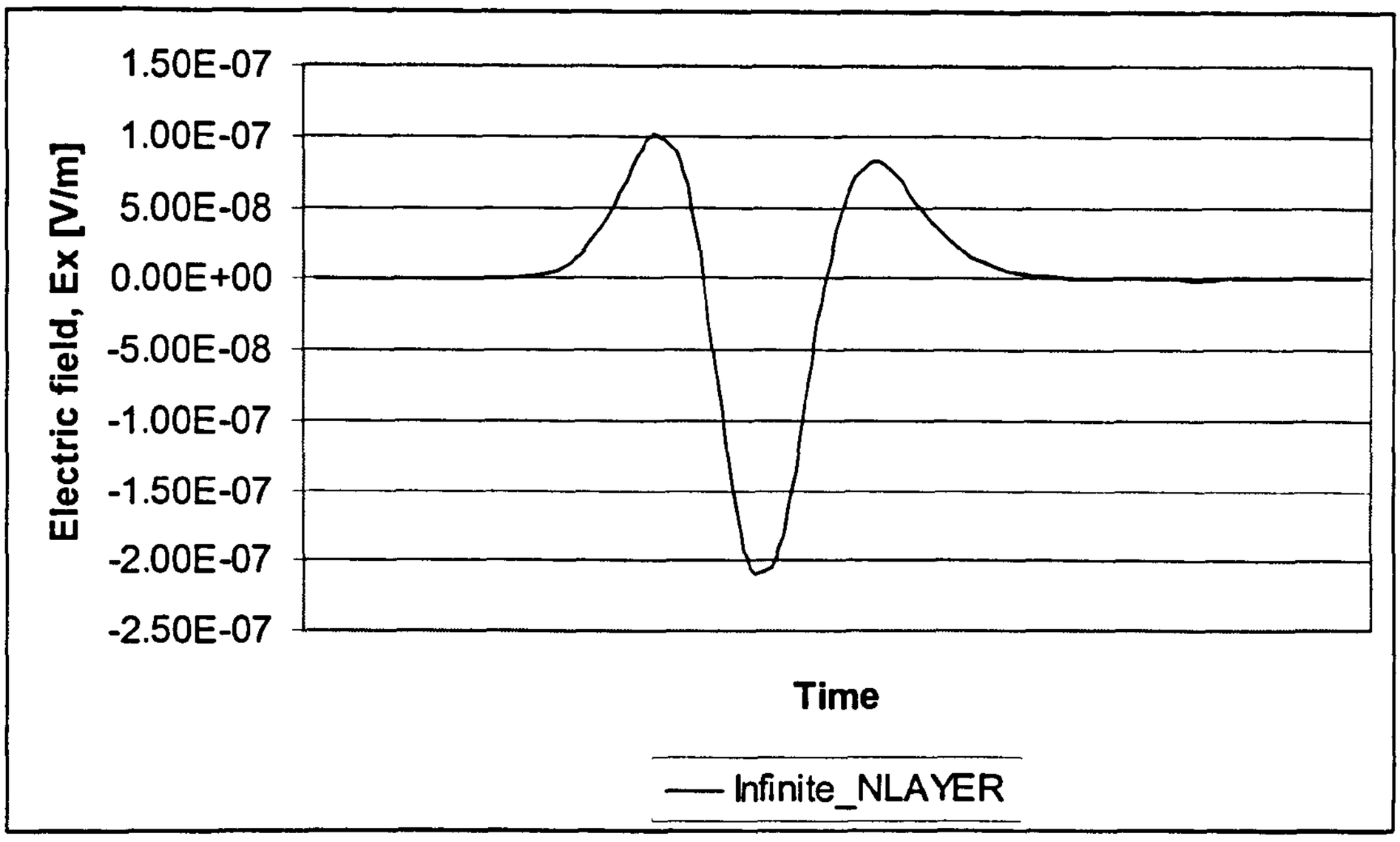

Figure B.3: *NLAYER* solution for HED source in infinite medium

The field predictions are generally in good agreement. However, there was a difference in the amplitudes of the field levels (approximately 13% difference). This was expected due to the non-ideal nature of the source i.e. the source only behaves like a point source at distances greater than ten step sizes.

Figures B.4 and B.5 shows the field predictions for a HED source located 50m below the air-sea interface in seawater with a conductivity of σ=3S/m. The observer is now situated 110m away at the air-sea interface. Figure B.5 corresponds to the 'benchmark' solution from *NLAYER* and Figure B.4 is the FDTD prediction.

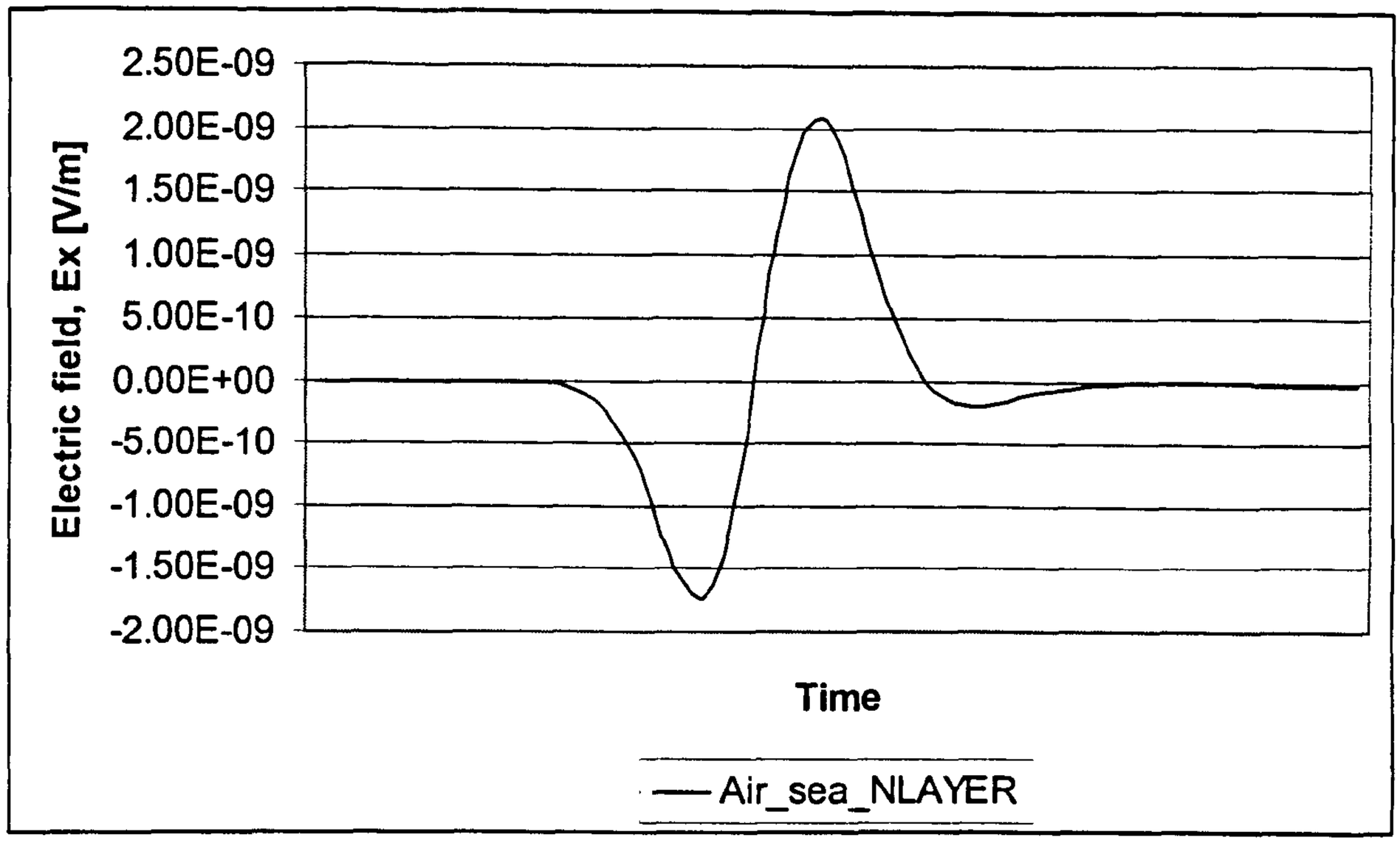

Figure B.4: *NLAYER* solution for HED source at air-sea interface

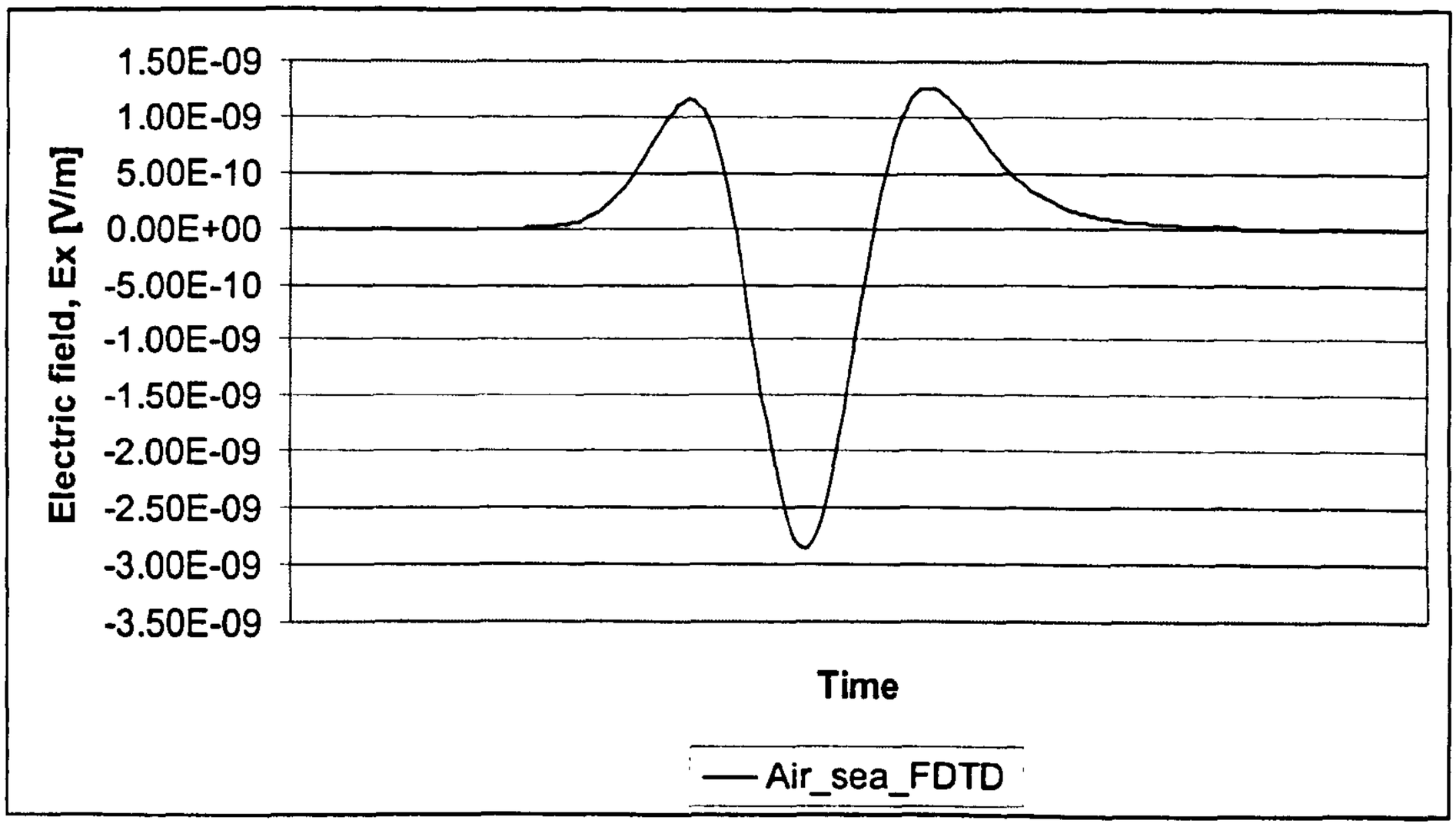

Figure B.5: FDTD solution for HED source at air-sea interface

The field predictions are in poor agreement. The field magnitudes and field distributions are significantly different. This indicates that the air-sea formulation has not correctly modelled the propagation of the up-down lateral wave.

The field magnitudes are of the correct order of magnitude; thus suggesting that a propagation mode that only suffered spreading losses was modelled. The peak field

would have been approximately E_x=2.5E-10V/m if the attenuation due to seawater was modelled over the entire path length (i.e. one order of magnitude lower than the levels predicted).

The most significant difference between Figures B.4 and B.5 is the field distribution. The FDTD results for the infinite medium and the 2-layer air-sea model show very little difference.

Based on the results presented above, the field predictions from the air-sea interface formulation were rejected and a new formulation was developed. The new formulation is presented in Chapter 6.

Appendix C

Initial 'discrete' formulation

This formulation is derived using Equation (C.1), which is obtained by combining Equations (6.37) and (6.38) for a source free region and eliminating **H** by substitution.

$$\nabla \times (\nabla \times \mathbf{E}) = -\mu\varepsilon \frac{\partial^2 \mathbf{E}}{\partial t^2} \tag{C.1}$$

This equation can be expanded to give the following scalar equations if the quasi-static approximation (ε=0) is used: -

$$\frac{\partial}{\partial x}(\nabla \cdot \mathbf{E}) - \nabla^2 E_x = 0 \tag{C.2}$$

$$\frac{\partial}{\partial y}(\nabla \cdot \mathbf{E}) - \nabla^2 E_y = 0 \tag{C.3}$$

$$\frac{\partial}{\partial z}(\nabla \cdot \mathbf{E}) - \nabla^2 E_z = 0 \tag{C.4}$$

Given that the two-dimensional discrete Fourier transform (DFT) is defined by

$$\hat{E}(\hat{x}, \hat{y}) = \sum_{x=0}^{X-1} \sum_{y=0}^{Y-1} E(x, y) e^{i2\pi\left(\frac{\hat{x}\cdot x}{X} + \frac{\hat{y}\cdot y}{Y}\right)} \tag{C.5}$$

where x and y are spatial variables for E, and $\hat{E}(\hat{x},\hat{y})$ is the transformed electric field variable. Differentiating Equation (C.5) with respect to x and y is equivalent to replacing the differential operator with ik_x and ik_y, respectively; where k_x and k_y are defined: -

$$k_x = \frac{2\pi\hat{i}}{I} \qquad 0 \le \hat{i} \le \frac{I}{2} \tag{C.6}$$

or

$$k_x = -\frac{2\pi(I-\hat{i})}{I} \qquad \frac{I}{2} < \hat{i} \le (I-1). \tag{C.7}$$

and

$$k_y = \frac{2\pi\hat{y}}{Y} \qquad 0 \le \hat{j} \le \frac{J}{2} \tag{C.8}$$

or

$$k_y = -\frac{2\pi(I-\hat{j})}{J} \qquad \frac{J}{2} < \hat{j} \le (J-1). \tag{C.9}$$

Applying the DFT to Equations (C.2) to (C.3) will therefore give

$$-k_x^2\hat{E}_x - k_xk_y\hat{E}_y + ik_x\frac{\partial\hat{E}_z}{\partial z} + \left(k_x^2+k_y^2\right)\hat{E}_x - \frac{\partial^2\hat{E}_x}{\partial z^2} = 0 \tag{C.10}$$

$$-k_xk_y\hat{E}_x - k_y^2\hat{E}_y + ik_y\frac{\partial\hat{E}_z}{\partial z} + \left(k_x^2+k_y^2\right)\hat{E}_y - \frac{\partial^2\hat{E}_y}{\partial z^2} = 0 \tag{C.11}$$

$$ik_x\frac{\partial\hat{E}_x}{\partial z} + ik_y\frac{\partial\hat{E}_y}{\partial z} + \frac{\partial^2\hat{E}_z}{\partial z^2} + \left(k_x^2+k_y^2\right)\hat{E}_z - \frac{\partial^2\hat{E}_z}{\partial z^2} = 0 \tag{C.12}$$

Equation (C.12) can be rearranged to show that

$$\hat{E}_z = \frac{1}{k_x^2 + k_y^2}\left(-ik_x \frac{\partial \hat{E}_x}{\partial z} - ik_y \frac{\partial \hat{E}_y}{\partial z}\right). \tag{C.13}$$

Equations (C.10) and (C.11) can be simplified to

$$\frac{\partial^2 \hat{E}_x}{\partial z^2} = \left(k_x^2 + k_y^2\right)\hat{E}_x \tag{C.14}$$

and

$$\frac{\partial^2 \hat{E}_y}{\partial z^2} = \left(k_x^2 + k_y^2\right)\hat{E}_y \tag{C.15}$$

by enforcing the condition that the divergence of the field is zero for a charge free region. This leads to the following solutions: -

$$\hat{E}_x(k_x,k_y,z) = e^{z\sqrt{k_x^2+k_y^2}}\,\hat{E}_x(k_x,k_y,0); \tag{C.16}$$

$$\hat{E}_y(k_x,k_y,z) = e^{z\sqrt{k_x^2+k_y^2}}\,\hat{E}_y(k_x,k_y,0); \tag{C.17}$$

$$\hat{E}_z(k_x,k_y,z) = \frac{1}{\sqrt{k_x^2+k_y^2}}\left(-ik_x\hat{E}_x\left(k_x,k_y,0\right) - ik_y\hat{E}_y\left(k_x,k_y,0\right)\right). \tag{C.18}$$

References

Abrahamsson, L., 'Orthogonal grid generation for two-dimensional ducts', Journal of Computational and Applied Mathematics, Vol. 34, No 3, pp305-314. 1991.

Abrahamsson, L., Unpublished technical notes on boundary conditions for FDTD problems. 1997

Abrahamsson, L., Unpublished technical notes on air-sea interface formulation for FDTD problems. 2000

Akindinov, V. V., Naryshkin, V. I., and Ryazantsev, A. M., 'Electromagnetic waves in sea water (review)', Radio Eng. Ele., Vol. 21, No. 5, Pages 1-26, 1978.

Ash, A. D., 'Noise and noise reduction techniques for airborne magnetic measurements at sea', Proc. Int. Conf. Marine Electromagnetics (Marelec'97), London, 1997.

Barr, R., Jones, D. L. and Rodgers, C. J., 'ELF and VLF Radio Waves', J. Atmospheric and Solar-Terrestrial Phys., Vol. 62, (N° 17-18), pp. 1689-1718, (Nov) 2000.

Bath University, Electrical Engineering Department, User guide and tutorials for *MEGA*, 1995.

Bhakta, N., 'Experimental validation of the of the DERA ELFE propagation model', Proc. Int. Conf. Marine Electromagnetics (Marelec'97), London, 1997.

Bhakta, N., 'ELFE Propagation – Sloping Seabeds', MPhil. to Ph.D. viva report submitted to King's College London, 51 pages, Nov 1998.

Bhakta, N., 'ELFE propagation in marine environments with non-parallel interfaces', Proc. Int. Conf. Marine Electromagnetics (Marelec'01), Stockholm, 2001

Bruxelle, J. Y., 'Electromagnetic response of the coastal zone to a low frequency emission', Proc. Int. Conf. Marine Electromagnetics (Marelec'97), London, 1997.

Burke, C. P., and Jones, D. L., 'Radio propagation in deep and shallow sea water', King's College London, Technical report RP940101, 53 pages, Feb 1994.

Burrows, M. L., 'ELF communications Antennas', IEE Electromagnetic Waves Series 5, published by Peter Peregrinus Ltd, 1978.

Certenais, J. and Periou, J. J., 'Electromagnetic measurements at sea', Proc. Int. Conf. Marine Electromagnetics (Marelec'97), London, 1997.

Dunbar, R. M., 'Experimentally validated heuristic models for submerged electromagnetic wave antennas', Proc. Int. Conf. Marine Electromagnetics (Marelec'97), London, 1997.

Holtham, P. M. and Jeffrey, I. G., 'ELF signature control', Underwater Defence Technology Conf. Proc. (UDT'96), London, pp486-489, July 1996.

Hubbard, J. C., Dr Stopher, I. M., 'Predicting the ELFE signatures', Proc. Int. Conf. Marine Electromagnetics (Marelec'97), London, 1997.

Ireland, R. C., Coles, P. C., Rodgers, D. and Leonard, P. J., 'Low frequency electromagnetic scattering by a submerged finite length cylinder', Proc. Int. Conf. Marine Electromagnetics (Marelec'97), London, 1997.

Jones, D. L., 'Sending signals to submarines', New Scientist, July 1985.

Kraichman, M. B., 'Handbook of electromagnetic propagation in conducting media', U.S. Government Printing Office, Washington, DC., 1976.

Le Coat, G., Foggia, A., Bongiraud, J. P. and Le Thiec, P., 'Electromagnetic stray fields of a propulsion induced machine', Proc. Int. Conf. Marine Electromagnetics (Marelec'97), London, 1997.

Morse, P. M. and Feshback, H., 'Methods of theoretical physics - Part 1', McGraw Hill, Library of Congress Catalogue Card Number: 52-11515, pp42

Ogawa, T., 'The lightning current', In: Volland, H. (Ed.), CRC Handbook of Atmospherics, Vol. 1, 23-63, CRC Press, Boca Raton, Florida, USA, 1982.

Peddell, J. B., and Garnett, G. W., 'Review of electromagnetic field research in an ocean environment', Proc Int. Conf. Marine Electromagnetics (Marelec'97), London, 1997.

Pickworth, G., 'The very long waves', Parts 1-5, Maplins, Electronics and beyond, 2000.

Orr, A. M. W., 'Computational techniques for evaluating extremely low frequency electromagnetic fields produced by a horizontal electric dipole in sea water', Ph.D. thesis, University of London, King's College, Jun 2000.

Rawlins, P. G. and Davidson, S. J., 'Modelling of AC vessel signatures using time dependent dipoles', Proc Int. Conf. Marine Electromagnetics (Marelec'99), Brest, 1999.

Schlak, G. A., and Wait., J. R., 'Electromagnetic wave propagation over nonparallel stratified conducting medium', Can. J. Phys., Vol. 45, Pages 3697-3720, 1967.

Sommerfeld, A. N., 'Partial differential equations in physics', Academic Press, New York, 1949

Tyler, R. H., Sanford, T. B, and Unsworth, M. J., 'Propagation of electromagnetic fields in the coastal ocean with applications to underwater navigation and communication', Proc. Int. Conf. Marine Electromagnetics (Marelec'99), Brest, 1999.

Wait, J. R., 'Electromagnetic waves in stratified media', Pergamon Press, New York, 1962 (3rd edition printed by IEEE/OUP, IEEE Press, 1996).

Weaver, J. T., and Agarwal, A. K., 'Three-dimensional modelling of the electromagnetic induction in the ocean', Proc Int. Conf. Marine Electromagnetics (Marelec'97), London, 1997.

Yee, K. S.,'Numerical solution of the initial boundary value problems involving Maxwell's Equations in isotropic media', IEEE AP-14, pp.302-307, 1966.